

Recharge Source and Groundwater Dynamics in the Southern Sections of the Western Afar Rift Margin and Associated Rift Floor

Dereje Gidafie

A thesis submitted to the School of Earth Science

Addis Ababa University

For the partial fulfillment of the Requirement for the Degree of Doctor of Philosophy in Geological Engineering (Hydrogeology)

Addis Ababa, Ethiopia

June, 2025

Advisors	**Signature**	**Date**
Dr. Dessie Nedaw	_____	_____
Dr. Tilahun Azagegn	_____	_____
Prof. Bekele Abebe	_____	_____

Addis Ababa University,

College of Natural and Computational Science

School of Earth Science

As members of the Examining Committee for the final PhD defense, we hereby certify that we have thoroughly reviewed and evaluated the dissertation titled "Recharge Source and Groundwater Dynamics in the Southern Sections of Western Afar Rift Margin and Associated Rift Floor" by Dereje Gidafie Amedie. After careful consideration, we confirm that the dissertation complies with the academic regulations of the university and meets the highest standards of originality, scholarly rigor, and quality. Accordingly, we recommend its acceptance in fulfillment of the requirements for the award of the Doctor of Philosophy degree.

Signed by the Examining Committee:

Prof. Tenalem Ayenew (Internal Examiner) _____ _____

Signature Date

Prof. Nata Tadesse (External Examiner) _____ _____

Signature Date

Dr. Behailu Berehanu (Chairman) _____ _____

Signature Date

Abstract

This study employs a multidisciplinary approach integrating geological, hydrogeological, hydro-meteorological, hydrochemical, and isotopic analyses, supported by GIS and remote sensing tools, along with steady-state groundwater flow modeling to assess groundwater dynamics in the study area. Lithostratigraphic correlations indicate that the columnar-jointed lower basalt exhibits a continuous extension from the plateau to the rift margin; however, it is not present on the rift floor. Transverse structures trending NW-SE, NE-SW, and W-E connect the plateau, Western Afar rift margin, and rift floor. Hydrochemical analyses reveal that most of the groundwater samples from the plateau and northern rift escarpment are predominantly Ca-(Mg)-HCO3-type waters with low total dissolved solids (TDS). The stable isotope compositions plot near and along the Local Meteoric Water Line (LMWL). Integrating the hydrochemical and isotope results, these water groups represent early-stage geochemical evolution with limited water-rock interaction and have been recharged primarily from modern precipitation and local groundwater flow systems. Highland springs along escarpments have comparable water types, relatively depleted isotope signatures, and a high yield with the continuous flow from small catchments demonstrating that the influx of groundwater from the adjacent plateau through transverse structures supplemented by local precipitation is the main source of recharge. The deep groundwater from the north western plateau and western Afar rift margin have Na-Ca-HCO3 and Na-HCO3 water type and depleted isotope content but with a moderate increase of TDS towards the groundwater flow directions. In the rift floor, the groundwater from the shallow aquifers exhibits Ca-HCO3 water type, isotopically enriched, and low radon values, indicating evaporation-affected local recharge with minimal water-rock interaction. In contrast, the deep groundwater source is Na-HCO_3/SO_4^{2-}/Cl^- water type, isotopically depleted, with high radon and mineralization distinct from shallow systems, indicating separate recharge sources and mechanisms. Integrating the geological, lithostratigraphic correlations, hydrochemical and isotope analysis; deep circulating groundwater flow from the plateau area is the main source of recharge for the deep aquifer systems of the Western Afar rift margin and associated rift floor. The main controlling mechanisms are the columnar jointed lower basalt and transverse structures that connect the plateau to the rift margin, and finally to the rift floor which can be taken as preferential pathways. Hence, the plateau area serves as the primary source of groundwater recharge for the deep aquifers for both the rift margin and rift floor. Hydro meteorological study quantifies groundwater recharge by employing Water balance, WetSpass modeling, Chloride Mass Balance, and Baseflow separation controlled by radon measurement. Accordingly, the estimation of groundwater recharge using the WetSpass and Base-flow separation methods highlights that the rift margin has a significantly higher recharge rate than the rift floor. Similarly, the groundwater potential map delineated through GIS and RS techniques shows that

the rift floor has a very low to low groundwater potential than the rift margin. However, from the geological, hydrochemical, and isotope analysis, groundwater flows from the rift margin to the rift floor due to the presence of preferential pathways. Hence, the rift floor can have moderate groundwater recharge, leads moderate groundwater potential. In addition, the GIS and RS tools have shown that structures and geology are the determinants of thematic layers for the occurrence of groundwater both in the rift floor and rift margin. Steady-state groundwater flow modeling in the Jewuha–Robit catchment confirms substantial plateau-derived groundwater influx. Sensitivity analysis identifies hydraulic conductivity as the most influential parameter, while abstraction has minimal impact on flow dynamics.

Key Words: Afar depression, Transverse structures, Columnar jointed basalt, Groundwater dynamics

Acknowledgments

First and foremost, I want to express my gratitude to the Addis Ababa University, School of Earth Sciences for providing the facilities and the chance to conduct the study. I am most grateful to my supervisors Dr. Dessie Nedaw, Dr. Tilahun Azagegn, and Prof. Bekele Abebe for their remarkable support during the study. I also want to express my gratitude to Prof. Tenalem Ayenew, Dr. Mebatsion Shawel, and Dr. Behailu Berehanu for their insightful remarks and evaluation of the study's progress. I also want to thank all of the Earth science school members who supported me in one way in another throughout the study. Special thanks to Mr. Dagmawi Shiferaw, for his valuable guidance and support for sampling and related laboratory works.

I want to sincerely thank Water Well Drilling Enterprise (WWDE) for sponsoring and organizing the logistics of the fieldwork for the geological and hydrogeological studies as well as the collection of water samples. For the hydrochemical and isotope laboratory analyses, I am extremely grateful to the IHE-UNESCO Institute for Water Studies in the Netherlands. I am thankful to the Ministry of Water and Energy, the Ethiopian Meteorological Agency, the Ethiopian Engineering Corporation (EEC), and Afar Water Works Construction Enterprise for providing the necessary data for the successful accomplishment of the study. Many institutions and organizations deserve special recognition for providing pertinent data.

I would like to thank the local government administrations both in the Amhara and Afar regions of the study area, for their comprehensive support during the fieldwork. Special thanks are extended to all those who assisted me at different levels throughout this study. I am especially grateful to Mr. Mulugeta Belayhun, G/Manager of G6 Water Well Drilling and Construction Company, for his unwavering support in every way during the study.

Last but not least, I would like to express my sincere gratitude to my dear wife, Medina Yusuf, who has been my inspiration and source of strength. Her unwavering love, support, and encouragement have helped me tremendously in my academic career and lifted my spirits while I studied. My sincere gratitude also goes out to my entire family for their support. My achievement can be attributed in large part to their spiritual and moral support.

Table of Contents

Abstract ii

Acknowledgments iv

List of Figures ix

List of Tables xi

Chapter One: Introduction 1

1.1Background 1

1.2Literature Review and Data collection 2

1.3Statement of the problem 9

1.4Objectives 12

1.4.1 General objective 12

1.4.2 Specific Objectives 12

1.5Expected results and applications 12

1.6Methodology 13

1.6.1 Geological and Hydrogeological characterization 13

1.6.2 Hydrochemical and Environmental Isotopes analysis and interpretations 14

1.6.3 Multivariate statistical analysis of hydrochemical data 17

1.6.4 Different Recharge Estimation tools 17

1.6.5 Integrated Remote Sensing and GIS overlay analysis 17

1.6.6 Development of Numerical groundwater flow model for selected catchment 18

1.7 Materials 18

1. 8 Software 19

Chapter Two: Description of the study area 20

2.1Location and accessibility 20

2.2Climate 21

2.3 Physiography and Drainage 22

2.3.1 Physiography 22

2.3.2 Drainage System 23

2.4 Geology 24

2.4.1 Regional Geology 24

2.4.2 Local Geology 27

2.4.2.1 Columnar Jointed (Aiba) basalt 27

2.4.2.2 Alaji formations (Rhyolites and Ignimbrites) 28

2.4.2.3 Tarmaber (Upper) basalt 29

2.4.2.4 Balchi Rhyolite and Ignimbrite....30
2.4.2.5 Dalha Basalt....30
2.4.2.6 Afar Startoid Series....30
2.4.2.7 Lacustrine Deposit....31
2.4.2.8 Sub Recent to Recent Basalt....31
2.4.2.9 Alluvial Deposits....32
2.5 Structures....32
Chapter Three: Evaluation of the source and mechanisms of Groundwater Recharge....36
3.1General....36
3.2Results and Discussions....36
3.2.1 Preferential orientation of highland springs and Source of recharge....36
3.2.2 Lithostratigraphic Correlations, Source and Mechanisms of Recharge....37
3.2.2.1 A-A′ Correlation....39
3.2.2.2 B-B′ Correlation....41
3.2.2.3 C-C′ Correlation....43
3.2.3 Hydrochemical and Environmental Isotope analysis....45
3.2.3.1 Hydrochemical Interpretations....45
3.2.3.1.1 Data Quality Control....45
3.2.3.1.2 Distribution of Water Types....46
3.2.3.1.2.1 Ca-(Mg)-HCO3....47
3.2.3.1.2.2 Ca-Na-HCO3 and Ca-(Mg)-Na-HCO3....47
3.2.3.1.2.3 Na-Ca-HCO3 and Na-HCO3....48
3.2.3.1.2.4 Na-HCO3-SO4 and Na-HCO3-Cl....48
3.2.3.1.3 Geochemical Process....51
3.2.3.1.4 Weathering Process....53
3.2.3.1.5 Ion Exchange Process....54
3.2.3.1.6 Total Alkalinity (TA) Analysis....56
3.2.3.1.7 Summary of the Hydrochemical analysis and Interpretations....57
3.2.3.2 Isotopic Signatures....57
3.2.3.2.1 Stable Isotopes....57
3.2.3.2.1.1 Graphical Presentations....58
3.2.3.2.1.2 Determination of Isotopic Ratios....63
3.2.3.2.1.3 Correlation of Slope and D-Excess along the Plateau, Rift margin and Rift floor....66
3.2.3.2.1.4 Correlation of Isotopic Results with Recharge Elevation....67
3.2.3.2.1.5 Summary of Isotopic interpretations....67
3.2.3.2.2 Radon Isotopes....68

3.2.3.2.2.1 General....68
3.2.3.3.2.2 Data Interpretations....68
3.2.4 Multivariate Statistical Analysis....70
3.2.4.1 General....70
3.2.4.2 Hierarchal Cluster Analysis (HCA)....71
3.2.4.3 Statistical Correlation and Principal Component Analysis (PCA)....75
3.2.5 Structural analysis and their role in transferring groundwater....79
3.3 Summary of the Source and Mechanisms of Groundwater Recharge....80
Chapter Four: Groundwater Recharge Estimations....83
4.1 General....83
4.2 Data Processing....83
4.2.1 Determination of areal depth of precipitation....83
4.2.2 Temperature....87
4.2.3 Sunshine hours....88
4.2.4 Wind Speed....88
4.2.5 Relative Humidity....89
4.2.6 Land use and land cover....89
4.2.7 Soil....90
4.2.8 Slope....92
4.3 Estimation of Hydro meteorological Variables....93
4.3.1 Potential Evapotranspiration (PET)....93
4.3.2 Actual Evapotranspiration (AET)....95
4.3.3 Surface Runoff:....100
4.3.4 Groundwater Recharge....103
4.3.4.1 Water Balance Method....103
4.3.4.2 WetSpass Model....104
4.3.4.3 Chloride Mass Balance (CMB) method....107
4.3.4.4 Base flow separation method supported by Radon measurement analysis....109
4.3.4.5 Comparison of Results and their limitations....112
Chapter Five: Integrated Remote Sensing (RS) and Geographic Information System (GIS) overlay analysis for groundwater potential evaluation....114
5.1 General....114
5.2 Selection, Reclassification, and Ratings of Thematic Layers....116
5.2.1 Geology....116
5.2.2 Lineament Density....118

5.2.3 Slope 119
5.2.4 Drainage Density 119
5.2.5 Soil 120
5.2.6 Land use 121
5.2.7 Recharge 122
5.2.8 Topographic Wetness Index (TWI) 124
5.3 Assigning Percentage of Influence (Weight) for the Thematic Layers 125
5.4 Delineation of Groundwater Potential Zones (GWPZ) 127
5.5 Validation of Groundwater Potential Map (GWPM) 129
5.5.1 Validation using Well Discharge 130
5.5.2 Validation using Groundwater flow direction 130
5.5.3 Validation using Specific Capacity and Transmissivity 131
5.6 Sensitivity Analysis 132
5.7 Limitations of the study 134
Chapter Six: Steady-state Groundwater Flow Modeling: Jewuha-Robit Catchment 136
6.1 General 136
6.2 Conceptual Model 136
6.3 Numerical Model 137
6.3.1 Model Design 137
6.3.2 Model Selection and Governing Equations 137
6.3.3 Boundary Conditions 138
6.3.4 Input parameters and flow packages 139
6.3.4.1 Hydraulic heads 139
6.3.4.2 Horizontal hydraulic conductivity 139
6.3.4.3 General Head boundary 139
6.3.4.4 Recharge 140
6.3.4.5 Well package 140
6.3.4.6 River package 140
6.4 Model Simulation 141
6.5 Model Results and Calibration 141
6.5.1 Evaluation of Calibration Results 142
6.5.1.1 Qualitative evaluation 142
6.5.1.2 Quantitative evaluation 143
6.6 Model Sensitivity 147
6.7 Scenario analysis 148
Chapter Seven: Conclusions and Recommendations 151

7.1 Conclusions....151
7.2Recommendations....154
Reference....155
Appendices....189
Appendices 1: Borehole Data....189
Appendices 2: Hydrochemical analysis data....194
Appendices 3: Stable Isotope analysis data....198
Appendices 4: Radon values and Distribution....200
Appendices 5: Areal rainfall determination using arithmetic method....201
Appendices 6: Areal rainfall determination using Thiessen Polygon method....202
Appendices 7: Areal rainfall Determination using Isohyetal method....203
Appendices 8: Max, Min and Mean Temperature of the study area....203
Appendices 9: Mean monthly sun shine hours (hrs/d)....204
Appendices 10: Mean monthly and annual wind speed (m/s). 204
Appendices 12: Published papers 206

List of Figures

Figure 1: Sampling distributions along the plateau, rift margin, and associated rift floor....14
Figure 2: Insitu water quality measurement (A) and Sampling from hand-fitted pump wells (B)....15
Figure 3: Radon measurement: (A) Awash Adaitu (Rift floor), (B) Telalak River (Rift margin), and (C) Lake Yardi (Rift floor)....16
Figure 4: Afar Depression modified from Zwaan, Corti, Sani, et al., 2020 and Reference therein....20
Figure 5: Location map of the study area 21
Figure 6: Profile of the study area (Plateau -Rift Margin-Rift floor)....23
Figure 7: Drainage map of the study area....23
Figure 8: Geological map of the Afar Depression (a) (Beyene & Abdelsalam, et al., 2005, Tefera et al., 1996) ..26
Figure 9: Columnar jointed basalt exposed towards the rift floor (A) & at the beds of the tributaries (B) 27
Figure 10: Fractured ignimbrite bounding the graben (A), poorly welded rhyolite cut by basaltic dyke (B) 28
Figure 11: Tilted rhyolite beds in the margin/rift border (A), Rhyolite breccia with intense faulting (B) 29
Figure 12: Contact between the Alaji rhyolite and Termaber basalt 29
Figure 13: Blocks of Dalha basalt between RM and RF (A), Overlying weathered Ashangie basalt (B)....30
Figure 14: Welded lacustrine deposit (A), Layered lacustrine deposit around Meteka area (rift floor) (B)....31
Figure 15: Sub-recent to recent basalt (A), Stratoid basalt (B)....31
Figure 16: Digital elevation model of eastern Africa and Arabia showing the location of the MER, Red Sea, Afar Rift, and Gulf of Aden Rift modified from Tesfaye et al,2003(A), and Ethiopian physiography including NW Plateau, Afar Depression and SE Plateau(B). 33
Figure 17: Major normal fault bounding a marginal graben along the escarpment dipping towards the rift 33
Figure 18: Schematic geological cross sections across the western (A)....34
Figure 19: Geological map of the study area....35
Figure 20: Preferential orientations of Highland springs....37
Figure 21: Hydrogeological map of the study area....39

Figure 22: A-A′ (I: Lithostratigraphy, II: Correlation along the Plateau-Rift Margin-Rift floor) 41
Figure 23: B-B′ (I: Lithostratigraphy, II: Correlation along the Plateau-Rift Margin-Rift floor).....42
Figure 24: C-C′ (I: Lithostratigraphy, II: Correlation along the Plateau-Rift Margin-Rift floor).....44
Figure 25: Ionic balance error distribution in the hydrochemical data 46
Figure 26: Piper plot of water samples 49
Figure 27: Durov diagram of water samples.....50
Figure 28: Gibbs Ratio I: (Na+/Na+Ca2+) VS TDS 52
Figure 29: Gibbs Ratio II: ($Cl^-/Cl^-+HCO_3^-$) VS TDS.....53
Figure 30: Plot of Ca^{2+}/Na^+ vs HCO_3^-/Na^+.....54
Figure 31: Ca^{2+}/Na^+ vs Mg^{2+}/Na^+.....54
Figure 32: Mean Chloro-Alkaline Indices (CAI-I).....55
Figure 33: Total Alkalinity (A) and PH (B) along Plateau-Rift margin –Rift floor 56
Figure 34: Box plot of ^{18}O isotopic signatures along the plateau, Rift margin, and Rift floor (A), Mean and Median Correlations (B) 59
Figure 35: Plateau samples Vs LMWL and GMWL 61
Figure 36: Rift margin samples Vs LMWL and GMWL.....62
Figure 37: Rift floor samples vs LMWL and GMWL 63
Figure 38: Isotopic Ratio (Plateau-Rift margin -Rift floor).....65
Figure 39: D-Excess and Slope along plateau-rift margin and Rift floor 67
Figure 40: Measured Radon values and distribution 70
Figure 41: Histogram plots of water samples 72
Figure 42: Dendrogram diagram of water samples.....74
Figure 43: Piper plots of all clusters 75
Figure 44: Na^+ vs Ca^{2+} correlation along the plateau, Rift margin, and Rift floor 76
Figure 45: Principal component plots.....78
Figure 46: Transverse structures from plateau to Rift margin, Rift margin to the Rift floor.....80
Figure 47: Conceptual groundwater flow model 82
Figure 48: Thiessen Polygon Map 84
Figure 49: Isohyetal Map.....85
Figure 50: Mean monthly rainfall distribution (A): Spatial rainfall distribution (B).....87
Figure 51: Mean Monthly max, min, and Mean temperature of the study area vs. Months 87
Figure 52: Mean monthly sunshine hour 88
Figure 53: Mean monthly wind speed (m/sec) 88
Figure 54: Mean monthly and annual Relative Humidity (%).....89
Figure 55: Land Use and Land Cover map of the study area 90
Figure 56: Soil map of the study area 91
Figure 57: Slope map of the study area 92
Figure 58: PET vs. Months 95
Figure 59: Spatial distribution of AET 98
Figure 60: Distribution of AET with soil coverage 99
Figure 61: Distribution of AET with LULC 99
Figure 62: Spatial distribution of surface runoff.....102
Figure 63: Distribution of runoff with soil coverage 102
Figure 64: Distribution of runoff with land use land cover 102
Figure 65: Distribution of Recharge, Evapotranspiration, and Surface runoff with Soil coverage 106
Figure 66: Distribution of Recharge, Evapotranspiration, and Surface Runoff with respective LULC 106
Figure 67: Rainy season recharges (A), Dry season recharge (B), Annual recharges(C).....107
Figure 68: River gauging station at Awash Adaitu, and Borkena outlet (Left to Right) 111

Figure 69: Base flow separation for Awash Ataye using RAP (Version 3.0.3) (A), Radon and Wtd Baseflow correlations along the gauging stations (B) 111
Figure 70: Geological map (A), Reclassified geological map (B)....117
Figure 71: Classified Lineament Density (A), Reclassified Lineament Density (B), Rose Diagram (C) 118
Figure 72: Classified Slope (A), Reclassified Slope (B) 119
Figure 73: Classified Drainage Density (A), Reclassified Drainage Density (B)....120
Figure 74: Classified soil (A), Reclassified soil (B)....121
Figure 75: Classified LULC (A), Reclassified LULC (B)....122
Figure 76: Classified Recharge (A), Reclassified Recharge (B) 123
Figure 77: Classified Topographic Wetness Index (A), Reclassified Topographic Wetness Index (B)....124
Figure 78: Normalized weights of parameters using AHP and FAHP 127
Figure 79: Groundwater potential Zones (GWPZ) Using the AHP (A), & the FAHP (B) methods 129
Figure 80: Scatter plot of Discharge VS t Groundwater potential Zone Map (GWPZM)....130
Figure 81: Groundwater flow directions map....131
Figure 82: Scatter plot of Transmissivity VS the Groundwater Potential Zone map (GWPZM)....132
Figure 83: Scatter plot of Specific capacity VS the Groundwater potential Zone map (GWPZM) 132
Figure 84: Mapping removal sensitivity analysis index 134
Figure 85: Location map of the model area (Jewuha-Robit catchment)....137
Figure 86: Model result....141
Figure 87: Simulated hydraulic heads (m)....142
Figure 88: Observed hydraulic heads 142
Figure 89: Observed vs simulated heads (m)....144
Figure 90: Sensitivity graph....148
Figure 91: Graph showing scenario analysis with increasing abstractions....150

List of Tables

Table 1: Summary of identified geological formation and their coverage 32
Table 2: Major water type distribution along the plateau –Rift Margin (RM) –Rift floor (RF)....46
Table 3: Summary of the relation between water type, TDS, & Lithology along all physiography 51
Table 4: Mean Chloro-Alkaline Indices (CAI)....55
Table 5: Mean Total Alkalinity (TA) along the physiography 56
Table 6: Statistical summary of ^{18}O Isotope results....59
Table 7: Summary of Isotopic Ratios 65
Table 8: D-Excess and Slope along Plateau-Rift margin and Rift floor....66
Table 9: KMO and Bartlett's Test....71
Table 10: Physical and chemical composition of water samples....72
Table 11: Summary of the mean hydrochemical composition of sub-groups (Clusters) (EC in µS/cm), all others in mg/l)....73
Table 12: Summary of interpretation for the HCA major groups and Subgroups/clusters....73
Table 13: Correlation matrix of variables....76
Table 14: Principal Component classifications....78
Table 15: Classification scheme of monthly rainfall values (Source: Daniel Gemechu, 1977). 86
Table 16: Rainfall characteristics....86
Table 17: Land use land cover and their area coverage....89
Table 18: Slope and its area coverage....92
Table 19: Determination of Potential Evapotranspiration using Thornthwaite method 93
Table 20: PET calculation using the Penman method 94
Table 21: Average PET....94

Table 22: Calculated AET using soil water balance method for clay soil covered with shallow deep rotted cereal crops &available water capacity of the root zone 50mm. All values in the table are in mm. 96
Table 23: Calculated AET using soil water balance method for clay silt and Silty clay soil covered with shallow deep rotted cereal crops & available water capacity of the root zone 100mm. All values in the table are mm. 96
Table 24: Calculated AET using soil water balance method for Loam soil covered with shallow deep rotted cereal crops and available water capacity of the root zone 150mm. All values in the table are in mm. 96
Table 25: Calculated AET using soil water balance method for Sandy clay soil covered with pasture and shrub lands and available water capacity of the root zone 250mm. All values in the table are in mm. 97
Table 26: Calculated AET using soil water balance method for Sandy soil covered with Matured forest and available water capacity of the root zone 350mm. All values in the table are in mm. 97
Table 27: Weighted Actual Evapotranspiration (Wtd AET) 97
Table 28: Distribution of Evapotranspiration with Soil Coverage 99
Table 29: Distribution of Evapotranspiration with land use and land cover....99
Table 30: AET summary....99
Table 31: Runoff calculation using the Runoff Coefficient method....100
Table 32: Distribution of Surface runoff with respective Soil coverage 101
Table 33: Distribution of Surface runoff with respective Land use land cover 103
Table 34: Average Surface Runoff 103
Table 35: Recharge Estimation using the Water Balance Method 104
Table 36: Distribution of Recharge, Evapotranspiration, and Surface runoff with soil distribution 106
Table 37: Distribution of Recharge, Evapotranspiration, and Surface runoff with LULC....106
Table 38: Annual recharge from the CMB method 108
Table 39: Base flow estimation at the rift margin and rift floor 110
Table 40: Assigned Rates and Groundwater occurrence suitability classification 116
Table 41: Reclassified geological formations for the occurrence of groundwater potentiality. 117
Table 42: Soil coverage and Reclassified based on the Groundwater occurrence suitability....120
Table 43: Reclassified LULC based on the suitability for Groundwater (GW) occurrence. 122
Table 44: Analytic Hierarchy Approach (AHP) normalized Pairwise matrix of the thematic layers....126
Table 45: Fuzzy Analytic Hierarchy Approach (FAHP) normalized Pairwise matrix of the layers 126
Table 46: Groundwater potential zones (GWPZ) coverage variation with AHP and FAHP methods 128
Table 47: Well classification based on their yield 130
Table 48: Mapping removal sensitivity analysis index....133
Table 49: Groundwater potential areal distribution with the removal of lineament and drainage density 134
Table 50: Summary of calibration errors 144
Table 51: Observed vs simulated heads....144
Table 52: Water budget of the entire model 145
Table 53: Water budget of sub-region-I....146
Table 54: Water budget of sub region-II....147
Table 55: Water budget of sub region-III 147
Table 56: Sensitivity Parameters 148
Table 57: Scenario analysis with different abstraction rates....149

List of Acronyms

AAU	Addis Ababa University
AET	Actual Evapotranspiration
AAZ	Arcuate Accommodation Zone
BFS	Base flow Separation
Bq/m3	Becquerel per cubic meter
CMB	Chloride Mass Balance
CBE	Charge Balance Error
CR	Consistency Ratio
DEM	Digital Elevation Model
EC	Electrical Conductivity
FAO	Food and Agriculture Organization
GHB	General head boundary
GMWL	Global Meteoric Water Line
GPS	Global Positioning System
GSE	Geological Surveys of Ethiopia
GWPZ	Groundwater Potential Zone
Hrs/d	Hours per day
l/s	liters per second
LTG	Lake Tana Graben
LMWL	Local Meteoric Water Line
m.a.s.l.	meters above sea level
m/s	meters per second
m3/s	meter cubic per second
MAE	Meteorological Agency
meq/l	Mili-equivalent per liter
MER	Main Ethiopian Rift
mg/l	Milligram per liter
Mm3	Million-meter cube
MoWE	Ministry of Water, and Energy
NWP	North Western Plateau
PET	Potential Evapotranspiration
RAP	River Analysis Package
RH	Relative Humidity
SEP	South Eastern Plateau
SMD	Soil Moisture Deficit
SRTM	Shuttle Radar Topography Mission
SSH	Sun shine Hour
SWL	Static Water Level
TDS	Total Dissolved Substances
WWDSE	Water Works Design and Supervision Enterprise
YTVL	Yerer Tulu Volcanic Lineaments

Chapter One: Introduction

1.1 Background

Groundwater, as it is less affected by climate change and anthropogenic activities(Pazhuparambil Jayarajan et al., 2022, Mekonen et al., Mohammadi et al., 2014), is the world's primary source of water supply for domestic, irrigation, and industry(Ali Rahmani et al., 2017, Calvo-Alvarado, 1986, S. Mohan & Pramada, 2023). Due to this recently the resource has been a top development priority, especially in regions with arid and semiarid climates(Ikirri et al., 2023, S. Das & Pardeshi, 2018). To meet the aforementioned needs sustainably, an integrated water resource management strategy must be implemented as well as groundwater recharge and aquifer extraction must be balanced(Barua et al., 2021, Bera, A. and Das, S. et al., 2021). For this purpose, credible groundwater resource evaluation, conservation, management, and proper budgeting and balancing estimations are essential(Chung et al., 2016, Ebrahim et al., 2020). Accordingly, in the past few years identifying the source and mechanisms of groundwater recharge, as well as quantification for a certain basin is thought to be an essential component for modeling and protecting groundwater systems from overexploitation and contamination (Galliari et al., 2021, Scanlon et al., 2002), especially in arid and semi-arid regions (Huang & Wang, 2017, Cook al., 2017, Galliari et al., 2021). It's critical to do this to accurately describe the aquifer system, flow circumstances, and groundwater resource management(Glynn & Plummer, 2005, Berhanu et al., 2017, Fetter 2001, Scanlon, Healy, and Cook 2002, Kresic, n.d.,2009, Le Mesnil et al. 2020).

In this regard, in the upper Awash basin of Ethiopia, there have been numerous works carried out to identify the source and mechanisms of groundwater recharge to the rift aquifers based on geological, hydrogeological, hydrogeochemical, and environmental isotopes studies(Ayenew, et al., 2008; Bretzler et al., 2011; Kebede et al., 2005, 2008, Azagegn, 2014; Baye, 2009). Accordingly, groundwater flow from the adjacent Blue Nile Basin is the main source of recharge for the Awash Basin rift aquifers, due to the presence of hydrogeologic window mainly the lower basalt that connects the two basins and the transverse structures. However, the source and mechanisms of groundwater recharge for the Southern sections of the western Afar rift margin and associated rift floor aquifers, located on the eastern side of the Blue Nile basin has not been properly studied. As a result, it is difficult to confirm whether the northwest plateau has contributed groundwater both to the western Afar rift margin and the rift floor aquifers or not. This issue has been a topic of debate among scholars for several reasons due to the highly variable spatial distribution of groundwater occurrence resulting from different reasons.

1.2 Literature Review and Data collection

Considerable documents have been retrieved and reviewed from the previous works which deal with identifying the source and mechanisms of groundwater recharge, groundwater potential evaluation, estimating the rate of recharge of the upper, middle, and lower Awash River basins, as well as any other materials about the research area in general or a topic related to the research problem in particular. In addition, sources including meteorological data were obtained from the National Meteorological Agency of Ethiopia (NME), which includes rainfall, temperature (minimum, maximum, mean), relative humidity, sunshine hours, and wind speed. The stations have daily records from 1980 to 2000. Of the available meteorological stations, 34 and 33 stations have rainfall and temperature data, respectively, while 13, 12, and 11 stations provide data on sunshine hours, relative humidity, and wind speed, respectively. River flow data of the selected 7(seven) gauging stations covering 20 years of record from 1980 to 2000, were collected from the Ministry of Water and Energy. Well data, which includes the lithologic log, pumping test result, and aquifer parameters were collected from the Ministry of Water and Energy (MoWE), drilling companies, regional water bureaus, and governmental and private consultants. Besides, secondary hydrochemical, and isotope results both from the study area and adjacent plateau were also collected from different organizations. Classified soil and land use data of the Awash River basin in both vector and raster formats were compiled from various global and national data sources such as the Ministry of Water and Energy; Awash River Basin Integrated Master Plan studies (Awash Basin Authority, 2017), Semera University, Agricultural Transformation Agency(ATA), Wollo University, Food and Agriculture Organization (FAO) global soil and land use database (FAO, 2009a, FAO, 2009b), Ministry of Agriculture and other local feasibility project studies (ADSWE,2010, WWDSE, 2017, WWDSE, 2018)**.** Besides, sentinel images with a resolution of 10 meters in raster formats were adapted to the study area using the GIS platform. The geological map(1:250,000) acquired from the Geological Survey of Ethiopia (GSE, 2010) was harmonized using ArcGIS software and correlated with the drilling logs. Visual interpretation of land Sat-8imagery from open USGS satellites (https://earthexplorer.usgs.gov/) was performed to better delineate geologic features. Other remote sensing data such as the Digital Elevation Model (DEM) with a resolution of 30m was downloaded from the Shuttle Radar Topography Mission (SRTM). Some of the literatures that have been reviewed includes the following:

Kebede et al. (2005)

Kebede et al. (2005) conducted a study on groundwater recharge, circulation, and geochemical evolution in the source region of the Blue Nile River using environmental Isotopes of water (both stable and unstable) and hydrochemical data. According to the study, samples collected from the low TDS

groundwater from the basaltic plateau have appreciable concentrations of ^{3}H. Whereas the thermal and the high TDS groundwater from the YTVL (Yerer Tulu Volcanic Lineaments) and the LTG (Lake Tana Graben) contain low ^{3}H concentrations. With regards to the stable isotopes of water, highly depleted $\delta^{18}O$ composition of the high TDS Na–HCO3 springs of the YTVL and the LTG were found. However, the $\delta^{18}O$ of present-day highest altitude cold springs is not as depleted as the $\delta^{18}O$ of the high TDS waters. Using the hydrochemical and isotope analysis, the study has concluded that recharge of the high TDS Na-HCO_3 waters (rift aquifers) probably took place under a colder climate regime than today. In addition, the absence of an appreciable amount of ^{3}H in high TDS waters also testifies to a lack of any modern-day meteoric water mixing with them. So these waters must have followed deeper circulation pathways before they emerged as low-temperature thermal waters. Finally, the study has concluded that there is groundwater continuity between the western plateau and the rift floor aquifers in the upper Awash basin. The most important controlling factor for such conditions to be favorable is the geological architecture of the interface zone formed due to the intersection of the NE-SW trending rift and the E-W trending structure of Yerer Tulu Welle Volcanic lineaments (YTVL) and can be called "hydrogeologic window". However, unlike the Western Blue Nile Basin, the groundwater of the Ethiopian Rift Valley, which is east of the Blue Nile basin, is relatively enriched in $\delta^{18}O$ when compared to the groundwater of the neighboring highlands. This implies that there is not a strong connection between the plateau in the eastern part of the Blue Nile basin and the shallow Rift Valley aquifers.

Kebede et al. (2008)

Kebede et al. (2008) have conducted a study on groundwater origin and flow along selected transects in Ethiopian rift volcanic aquifers, using environmental Isotope and hydrochemical data. For this specific study, the transect approach is used, which is important to investigate geochemical evolution and isotopic variations in groundwater along a given topographic section or along groundwater flow lines. Accordingly, the research area is divided into 2(two) transects, namely Transect 1 and Transect 2, where Transect 1 is found in the western part of the Blue Nile basin, namely called upper Awash, and Transect 2 is the Eastern part of the Blue Nile basin. Based on the isotopic analysis conducted, in transect 1, the $\delta^{18}O$ and δD are depleted, while these kinds of waters are rare in transect 2. The difference in the degree of $\delta^{18}O$ and δD depletion in the two transects is related to the origin of the waters. This shows that ground waters in transect 2(the eastern part of the Blue Nile Basin) are distinct from the waters of transect 1(the Western part of the Blue Nile Basin). Generally, according to the research, in Transect 1, the intersection between the NNE rift structures and the E–W ridges forms a ‘hydrogeologic window’ that channels groundwater from the mountain to the rift. In transect 2, due to the presence of marginal grabens like Borkena grabens and faults bounding the rift, which act as a major groundwater barrier, groundwater is not flowing from the plateau to the rift aquifers. As a result, the principal sources of recharge in the rift

floor aquifers in the Eastern part of the Blue Nile basin are channel loss and local rainfall, not the plateau, which is unlike the western plateau margin. In contrast to the shallow sources, the δD and the $\delta^{18}O$ variations of all the thermal springs and deep cold wells in the marginal grabens and rift in Transect 2 do not fit into the enrichment trend.

Bretzler et al., 2011

Bretzler et al. (2011) conducted research on groundwater origin and flow dynamics in active rift systems – A multi-isotope approach in the Main Ethiopian Rift, upper and Middle Awash basin. The research has also included the Eastern escarpment of the Main Ethiopian Rift Valley (MERV). In this work, the concept has been elaborated and justified more with the help of a multi-isotope approach other than the transect approach. With this approach, the analysis of new hydrochemical and isotopic data of groundwater in the upper and middle Awash Basin has been used and contributed to gaining further understanding of the hydrochemical evolution of groundwater in the MER and the effect that structural controls have on groundwater dynamics in active rift systems. Besides the study has also shown the nature of groundwater flow dynamics at the different physiographic parts (escarpment, escarpment-rift transition zone, rift floor) using a multi-isotope approach. Generally, it has led to the improvement of previous; transect-based models (e.g. Kebede et al. (2008) of groundwater circulation in the MER. According to the research, based on the hydrochemical analysis, there is a hydrochemical change from the escarpment to the rift, Ca-Mg-Na-HCO3 to Na-HCO, due to the dissolution of Na-feldspars from the rhyolitic rocks which is aided by the high amount of CO_2 from the mantle. The cation exchange of Ca^{2+} for Na^{+} on clay minerals is another process that may be responsible for a change in relative cation contents in groundwater. According to the isotope analysis conducted at the escarpments, the study found that the tritium value was highly similar to the local precipitation of both the Eastern and Western escarpments. This suggests that precipitation during the main rainy season, which runs from July to September, is the primary source of groundwater recharge in the escarpment. Additionally, the groundwater recharge on both escarpments has the same temporal and spatial moisture source, as indicated by the δ2H and δ18O values in the eastern escarpments. According to the research, several meteorological conditions (such as a change in the supply of air moisture) during the period of groundwater recharge are the cause of isotopic depletion. Stable isotope signatures (δ2H, δ18O) show regional variability in the research area, suggesting that groundwater has multiple recharge areas and/or was recharged at different elevations or under different climatic circumstances. Groundwater from deep boreholes on the rift floor and escarpments typically has no detectable tritium, according to the tritium analysis, while there are few sites where this isn't the case, particularly in the lowland areas that received irrigation. According to the study's final findings, rift floor aquifers exhibit the opposite of short groundwater residence time, while

higher tritium concentrations, along with other isotopic and hydrochemical parameters found in the rift escarpment (such as low pH, low electrical conductivity, and depleted 13C), indicate shorter stays.

Ayenew et al. (2008)

Ayenew et al. (2008) conducted Environmental isotopes and hydrochemical studies applied to surface water and groundwater interaction in the Awash River basin in conjunction with hydrogeological principles. For the accomplishment of the research, samples were taken from highlands, escarpments, and rifts from cold springs and rainfall, lakes, thermal waters, wells, and rivers. In this study, two important issues have been addressed and concluded. These are river groundwater interactions and identification of the source and mechanisms of groundwater for the rift aquifer found at the western and eastern part of the Blue Nile River using isotope data analysis, hydrogeology like piezometric survey, and hydrograph separation methods. Accordingly, using isotopic data and hydrogeological surveys like a piezometric measurement in the middle and lower Awash River basin, the river is feeding the groundwater and at other locations, the reverse is true. Using the hydrograph separation method, the study has concluded that the Awash River has a sustained base flow and important surface runoff component during the rainy season. On an annual basis, the base flow is greater than the surface runoff, indicating the importance of groundwater in the discharge of Awash on the scale of the basin width. However, in the lower reaches, much river water feeds the aquifer. Regarding the source and mechanisms of recharge for the rift aquifer, the research has concluded that, in the case of the upper Awash (Western Blue Nile Basin), there is groundwater continuity between the Blue Nile Basin and upper Awash. The most important factor that controls the groundwater flow continuity between the high rainfall region in the plateau and the rift floor aquifers is the geological setting of the transitional escarpment. Accordingly, in the cases where the rift margin is cross-cut by transverse fault zones, the plateau-type waters are channeled into the rift valley. In this case, there is the likelihood of a higher component of indirect recharge from the plateau, channeled through large regional faults. In contrast, in the northwest section of the Awash basin (i.e. Eastern of the Blue Nile basin), the isotopically depleted highland water does not reach the volcanic aquifers of the rift directly because of the marginal graben and the fault forming the rift; rather, indirect recharge from rivers predominates in the alluvial and fractured aquifers of the Awash valley. Instead of reaching the rift aquifers, the waters that seep into the plateau appear in the alluvial deposits or re-enter the mountain streams. As a result, local direct recharge from seasonal floods or infiltration from river beds takes precedence over subsurface mountain recharge in the rift floor aquifers as the main source of sustained recharge in the lower and middle Awash valley. However, the study has shown that there is no discernible difference between the rift's deeper or shallower aquifers and the plateau-type water where the escarpment's rocks are permeable and the mountain and valley floor are

close together, indicating that there might be flow continuity. In addition, studies have revealed that a large number of deep cold wells and rift geothermal systems are linked to more depleted groundwater with extremely low ^{3}H, suggesting the presence of older, deeper systems that are not in direct contact with the shallow fresh groundwater.

Berehanu et al., 2017

Berehanu et al., 2017, has conducted Inter-Basin Groundwater transfer and Multiple Approach Recharge Estimation of the Upper Awash Aquifer System. The methods applied to estimate the recharge of the upper Awash are the Water Balance Method (WBM), Chloride Mass Balance Method (CMB), hydrograph separation system, and Hydrus1D infiltration model. Consequently, using these methods recharge estimated for the Upper Awash basin ranges from 51.5 mm/ year to 157 mm/ year, and for the two southern left- bank sub-basins of the Middle Blue Nile basin (Mugher and Jema) ranges from 86 mm/ year to 239 mm/ year. Accordingly, yearly average volumetric recharge in the Upper Awash and yearly groundwater flux from the portion of the Blue Nile sub-basins to the Upper Awash aquifer system are estimated to be 983 Mm3 and 365 Mm3 respectively. The significant flux joining the Upper Awash groundwater system from part of the Middle Blue Nile basin, which is nearly 37 of the total annual recharge to the Upper Awash basin, makes this part of the Middle Blue Nile basin an important recharge zone for the Upper Awash groundwater. To consider for and see the effect of geomorphology, settlement, lineament density, and slope, spatially distributed recharge has been determined using the Kriging interpolation approach in Arc GIS for the point recharge determined by Hydrus1D. In addition to considering spatial diversity of the most important factors governing recharge between any two points, the spatial distribution of recharge produced by ordinary interpolations, the recharge ASCII grid has been imported in processing Modflow and superimposed with the geomorphology, lineament density, slope, and settlement matrixes. The matrix performing from overlaying recharge and geomorphology is eventually exported to SURFER10 and converted to ArcGIS-compatible format (Surfer GRD format). From this, recharge zones constrained by geomorphology, slope, lineament density, and settlement variations were produced for the Upper Awash and part of the Middle Blue Nile basins. Besides, groundwater flow modeling for the three layers under steady- state conditions was also conducted. Consequently, model sensitivity analysis and scenario analysis for different abstraction rates were duly discussed. The modeling work can be a good management tool, especially for the Addis Ababa Water and Sanitation Authority (AAWSA).

Baye et.al (2009)

Baye et al (2009) have conducted Ph.D. research to characterize the hydrogeological system of the upper Awash basin by giving special emphasis on inter-basin water transfer across the Blue Nile and upper Awash River basin water shade boundary using geological, hydrogeological, environmental isotopes, and geochemistry. Consequently, using the litho- hydro stratigraphic relationship identified from the drilling data coupled with the geological structures, groundwater movement could be connected through the permeable and porous Scoraceous lower basaltic aquifer from the Blue Nile Plateau to the upper Awash.

Hence, the Scoraceous Tarmaber and/ or Aiba formation together with the tectonic structures are allowed to be responsible for conveying the recharge from the adjacent Blue Nile plateau to the Upper Awash groundwater system. From the chemical analysis result, the author has classified the waters into five major groups of chemical facies Ca- Mg- HCO3, Ca – Na – HCO3, Na- Ca- Mg- HCO3, Na- HCO3, and Ca – HCO3. Ca- Mg- HCO3 water type is substantially found in the shallow systems (springs, rivers, and shallow wells) in all three physiographic regions of the area, having dilute chemistry (TDS<340mg/l). Moderately mineralized waters (TDS< 500mg/ l) have Ca – Na – HCO3 facies that are substantially distributed to the transition and rift part and are associated substantially with intercalations of acidic rocks. The stable isotopic results(δ18O and δ 2H) of different water sources revealed further substantiation for the ideas concluded from the litho- stratigraphic connections obtained from lithologic logs and chemical analysis. Consequently, Water wells tapping the lower aquifer (i.e. lower basalt) in all three physiographic regions show relatively depleted in its heavy isotopic signatures when compared to present- day rainfall of the area. Deep wells from the Blue Nile Plateau, wells from the transitional part of the rift, and wells from the rift part scatter in the same group. The groundwater from the lower aquifer system generally has lower values of δ2H, δ18O, and d-excess indicating a colder climatic signal during recharge. So, the analogous isotopic results of the deep system in all three physiographic regions of the study area mirrors a comparable origin of recharge and the presence of hydraulic connectivity, there by inter-basin transfer across the watershed boundary of the two basins, Blue Nile and Awash. Besides, the tritium data from the deep aquifers is set up to be veritably low in all the physiographies, which strengthens the ideas attained from the litho- hydro stratigraphic connections and the stable isotopic signatures. Eventually, from all the converging methodologies and substantiation, the research has concluded that there's deep circulating water inflow coming from the Blue Nile Plateau towards the Upper Awash River basin due to the presence of the north- south running fault systems that dissect the E-W trending fault and the lower Scoraceous basalt aquifer which connects the Blue Nile Basin and the Upper Awash basin and serve as a hydrogeological window to connect the two basins.

Azagegn (2014)

Azagegn (2014) has conducted a Ph.D. research entitled Groundwater Dynamics in the Left Bank Catchments of the Middle Blue Nile and the Upper Awash River Basins, Central Ethiopia. For the accomplishment of the study, the author has used integrated geological, geophysical, hydrogeological, hydrogeochemical, and environmental isotopic studies with a simple regional groundwater flow model which helps to conceptualize aquifer distribution, groundwater dynamics, and the relationship between the aquifer systems of the Middle Blue Nile and the Upper Awash basins. Accordingly, the geological, hydrogeological, and geophysical investigations which are supported and correlated with litho stratigraphy, have outlined that two basic conditions are vital for the groundwater circulation in the Blue

Nile as well as Upper Awash basins. The first one is the NW-SE trending horsts which is beneath thick Tertiary volcanic layers and ridges that control aquifer distribution in the Middle Blue Nile basin. The other one is the E-W trending impermeable mudstone capped horst underlying the volcanic aquifers that control aquifer distribution and constitutes a groundwater divide between the Blue Nile and the Upper Awash basins, channeling recharged water from the Blue Nile to the upper Awash basins. These conclusions have been supported by hydrochemical and isotope (both stable and unstable) analyses. From the hydrochemical analysis, groundwater evolves from low TDS, Ca-HCO3 type, and negative residual alkalinity to high TDS, Na-HCO3 facies with positive residual alkalinity. From the analysis of stable isotopes of water (δ^2H & $\delta^{18}O$) in the deep wells found at both basins, the isotopic concentration was found to be depleted. Using unstable Isotopes, ^{14}C, the old waters located very close to the water divide between the Blue Nile and the Upper Awash basin support the conceptual hydrogeological model which shows groundwater transfer from the Blue Nile basin to the Upper Awash basin. In addition, to see the interaction between Awash River and groundwater, ^{222}Rn measurement was conducted at some selected sites of Awash River and its tributaries. Accordingly, the ^{222}Rn measured values show that tributary streams of the Awash River that cross the high lineament density zone flowing through highly permeable rocks have a clear connection with local groundwater flows. On the other hand, the Awash River and its tributary streams are poorly connected to the groundwater within rocks having low permeability, at a low lineament density zone.

Furi, 2012

Furi, 2012 conducted Ph.D. research in the Middle Awash River basin to characterize aquifer systems, mode of groundwater movement, and performing with volcanic materials as well as estimate the interaction of groundwater with surface waters. According to the study, two distinctive aquifer systems have been found which are linked to geology and physiographic position. The first rock types are basalt, ignimbrite and trachy basalt from aquifers in the mountain region are Ca- alkaline rich as a result groundwater circulating in the upland areas is slightly mineralized, and is Ca- Na- HCO3 type. The second rock types are Na- alkaline rocks which include scoria, pumice, tuff, and volcano clastics are the main aquifers set up in the rift floor resulting in the water type being Na- HCO3- Cl and is highly mineralized as well as containing a high amount of fluoride. Regarding the recharge mechanisms of the area, the author has concluded that the plateau region with high rainfall is contributing water to the aquifer whereas the rift floor area due to its high evapotranspiration and low rainfall is considered zero recharge to the aquifer. Therefore, further localized indirect recharge could do in the rift floor through geological structures.

Water Works Design and Supervision Corporation, 2019

In 2019, the corporation conducted Kobo-Chefa groundwater resource evaluation and assessment project. For the accomplishment of the project, geological, hydrogeological, and geophysical investigations were conducted. Based on the integrated investigations, test wells were drilled at the selected sub-basins. As a result, areas with high groundwater potential were selected, recharge for the selected catchments was determined and resource evaluations were also conducted for the selected sub-basins.

Amhara Design and Supervision Works Enterprise, 2010

In 2010, the Enterprise conducted the Eastern Amhara Development Corridor (Kobo-Robit-Minjar) groundwater potential assessment project. The main objective of the project was to identify groundwater potential well fields using geological, hydrogeological, and geophysical methods. Finally, test wells were drilled in selected areas. Accordingly, geological units, structures, and geomorphological situations of the area were identified. In addition, areas with high groundwater potential were selected, recharge for the selected catchments was determined, and resource evaluation was also conducted for the selected sub-basins.

Other governmental studies

Water supply and Irrigation projects were initiated by the government over the years (BCEOM, 1999); Regional Hydrogeological Investigations of Northern Ethiopia conducted by the Geological Survey of Ethiopia (GSE) (Bayessa Asfaw. et. al. 2002), where the main objective of conducting the study is to serve as planning for the development of water resources in the area for the future.

1.3 Statement of the problem

As has been well discussed in the literature review section above, in the upper Awash basin of Ethiopia, which is located on the western side of the Blue Nile basin, there have been numerous studies carried out to identify the source and mechanisms of groundwater recharge, determination of recharge rate and identification of groundwater boundary zones through different scholars based on geological, hydrogeological, hydrogeochemical, and environmental isotopes(Ayenew, et al., 2008; Bretzler et al., 2011; Kebede et al., 2005, 2008, Azagegn, 2014; Baye, 2009). However, the source and mechanisms of groundwater recharge for the southern sections of the western Afar rift margin and associated rift floor, which is located on the eastern side of the Blue Nile basin has not been properly studied. Hence, it is difficult to confirm whether the northwest plateau has contributed groundwater to the western Afar rift margin and the rift floor aquifers or not. As a result, the issue has been a topic of debate among scholars for several reasons due to the highly variable spatial distribution of groundwater occurrence and the complex geological and structural conditions. In the first case, the acidic horst created by the antithetic normal faults that form the western margin rifts on the eastern side(Agostini et al., 2011, Augustin et al.,

2014, ArRajehi et al., 2010) could form closed and isolated hydrogeological systems(marginal grabens) that separate it from the rift floor (Ayenew, et al., 2008, Bretzler et al., 2011 and Kebede et al., 2008). Furthermore, the rift ward tilted Tertiary flood basalt aquifers on the western margin do not continue until the rift floor(Abbate et al., 1995, Abbate et al., 2015 Corti et al., 2015, Rooney, 2017), as it is assumed that the flood basalts are interrupted by chains of silicic volcanic ridges and deep-seated rift faults (Abebe et al., 2010, Barberi et al., 1974, Bastow et al., 2018, Fentaw et al., 2024, Beutel et al., 2010), which may prevent the continuity of hydraulic conductivity across the formation. Based on these assumptions, the deep groundwater flow from the western marginal grabens to the Afar rift floor is impeded by the silicic volcanic ridges that surround the marginal grabens. Accordingly, few hydrogeological works done by Ayenew, et al., 2008; Bretzler et al., 2011; and Kebede et al., 2008, concluded that the main source of recharge to the shallow aquifer systems of the rift floor is channel losses and streams, conversely, deeper cold wells and rift geothermal systems are linked to more depleted groundwater with extremely low ^{3}H, without mentioning the source and mechanisms of recharge. These findings have shown that the deep and shallow aquifers in the rift floor have different sources and mechanisms of groundwater recharge. Recent studies conducted by Fentaw et al., 2024, in the central Afar Rift, concluded that the deep aquifers in the rift floor have received recharge from the northwestern plateau due to the presence of connection zones. However, there have been no detailed scientific studies to identify the source and mechanisms of groundwater recharge for the deep aquifers in the southern section of the western Afar rift margin and rift floor. In addition, in the western Afar rift margin particularly in the uplands of rift escarpments, highly discharged springs (30-70lit/sec) with preferential orientations are emerging from the foot of the NE- SW, and NW-SE trending volcanic mountains, mainly from upper basalt and ignimbrite. These springs flow all year round which the local recharge system cannot provide. In addition, recently deep wells have been drilled in the marginal grabens to a depth of 600 m, yielding up to 100 l/s with insignificant drawdown and acceptable water quality. Therefore, the presence of high-yield springs and deep wells on the southern sections of the western margin of the Afar rift might support groundwater inflow from the adjacent plateau, but this remains to be investigated in detail. Through the application of geological, hydrogeological, hydrochemical, and isotopic principles, this study attempts to fill the gaps in the identifications of the source and mechanisms of groundwater recharge for the Southern sections of the western Afar rift margin and associated rift floor deep aquifers.

Besides, in the study area, hydro-meteorological investigations with special emphasis on the estimation of groundwater recharge were conducted by the federal and regional governments(ADSWE, 2010, WWDSE, 2017). However, since the rift margin particularly the grabens were the main focus of the recharge estimation, the groundwater recharge rate of the rift floor and its surroundings was not

considered or determined. Moreover, the estimated recharge rate in the rift margin does not reveal the spatial and temporal distribution. Another significant gap in the estimation of the recharge rate at this particular location was the use of a single technique without comparison or calibration with alternative approaches. This is because, the groundwater recharge estimated using a single method at certain locations will not accurately represent the rate for the entire study area due to variations in soil characteristics, topography, climate, geology, tectonics, and land use, the different spatiotemporal applicability between various methods, as well as the inherent errors and uncertainties involved in all recharge estimation methods(Baye et.al, 2009, Berhanu et al., 2017, Schilling et al., 2021). Therefore, to fill the aforementioned gaps in the determination of groundwater recharge in the study area, the estimations should be carried out both in the rift margin and rift floor using a range of approaches, and the results should be calibrated and compared(Afrifa et al., 2017, Duah et al., 2021, Healy & Cook, 2002).

Furthermore, in the western Afar rift margin particularly at the marginal grabens, various methods including geological, hydrogeological, and geophysical investigations, including the drilling of test wells and groundwater modeling were conducted to identify and exploit the available groundwater resources. Although these conventional methods of groundwater investigation techniques are the most effective and widely used (Cooper et al, 2010, Gebeyehu et al., 2023, Mallick et al., 2015), they require a lot of resources both financial and human and are time-consuming(Arshad et al., 2020, Gintamo et al., 2017, Nampak et al., 2014). As a result, previous groundwater investigations in the study area were limited mainly to the rift margin, especially along the grabens, and covered a narrow area for the placement of well sites, failing to cover and display the groundwater's spatial distribution of the rift margin as well as the rift floor. Sometimes, the aforementioned exploration methods may also not take into account important regulating factors that can influence the occurrence and movement of groundwater(Srivastava & Bhattacharya, 2006, Rane et al., 2023). The frequent failure rate of well production, mainly in the rift floor, is due to the significant gap in knowledge regarding the key governing elements that govern groundwater occurrence and distribution(Andualem & Demeke et al., 2019, Godfrey & Hailemichael et al., 2016). In general, there is a lack of up-to-date data that shows spatially distributed groundwater potential in all areas, particularly in the rift floor and surrounding margins. This leads to a gap in the intensive exploitation, utilization, and overall development of the region's groundwater resources, especially on the rift floor, and results in frequent drought. Therefore, to fill these gaps a complete assessment and evaluation of the groundwater potential both in the rift margin and rift floor using integrated remote sensing (RS) and Geographic Information Systems (GIS) tools will be applied. This is because, as the technique is the new emerging approach which can be the best option to handle challenges related with groundwater potential mapping,

especially if it is coupled with other conventional methodologies(Ahmed & Shabana et al., 2020, Biswas et al., 2020, Rahaman et al., 2015).

Hence, by applying a comprehensive study including geological, hydrogeological, hydro meteorological, hydrochemical, and isotopic principles, in conjunction with an integrated GIS and RS approach, this research aims to fill the gaps mentioned above in the southern sections of the western Afar rift margin and associated rift floor. Besides, a simple steady-state groundwater flow modeling will be conducted for the selected catchment which can be used as a calibrating tool for the hydraulic system analysis

1.4 Objectives

1.4.1 General objective

This research aims to assess recharge source and groundwater dynamics in the Southern Sections of the Western Afar Rift margin and associated Rift floor.

1.4.2 Specific Objectives

The most important issues to be addressed in the course of the research work are the following:

- Identifying the source and mechanisms of groundwater recharge to the aquifer systems of the area
- Estimation of groundwater recharge to the aquifer system of the sub-basin using various methods
- Evaluating the groundwater potential of the area using GIS, and RS overlay analysis principles
- Groundwater resource evaluation using steady-state numerical modeling on selected catchment

1.5 Expected results and applications

After completing the research, there could be a lot of significance and applications for the detailed understanding of the groundwater dynamics along the boundary between the Middle Awash and the adjacent northwestern plateau of the Blue Nile basins. This will lead to proper identification of the source and mechanisms of groundwater recharge for the western Afar rift margin as well as associated rift floor aquifers. From the integrated GIS and RS output, a spatially distributed groundwater potential map will be prepared which will have vivacious significance for further groundwater development access in the area. In line with this, the major significant and controlling factors that are determinants for the occurrence of groundwater both in the rift margin and rift floor will be clearly understood and known, which reveals the upcoming groundwater development will focus on these parameters, and will be adopted to similar areas. Besides, the result will have a massive contribution to further groundwater evaluation, development, and management, particularly for the deep aquifers in the rift floor.

Furthermore, the output from the integrated approach utilizing geological, hydrogeological, hydro meteorological, hydrochemical, and isotope analysis and integrated GIS and RS approach will be used

as a good practice to conduct similar studies in arid to semi-arid and tectonically active areas. Last but not least, the new data generated in the course of the research will also enable further research at a larger scale in the area and the surroundings.

1.6 Methodology

Since the study area encompasses the Western Afar Rift margin and the associated Rift floor which is tectonically active, various methodologies and approaches, as well as materials, were used and deployed for the successful accomplishment of the research. To properly evaluate the source and mechanisms of groundwater recharge as well as the estimation of its rate, the research will be conducted in an integrated and converging approach. As a result, the following methodologies and procedures were followed and used.

1.6.1 Geological and Hydrogeological characterization

Although the Geological Survey of Ethiopia (GSE-2012) produced the geological map of the study area using six map sheets (Debre Birhan, Wereilu, Dessie, Dire Dawa, Sedro, and Ayelu Terara), subsequent integration and harmonization of these sheets revealed unmapped discontinuities along their adjoining boundaries. In addition, there are gaps in the identification and naming of the major geological units on some of the geological map sheets. To fill these gaps, a geological field survey was conducted by having a field traverse of NW-SE, W-E, and SW-NE directions and along the major tributaries of Awash River. The investigation also helped in constructing the lithological contacts among the different geological formations along the traverse. Faults and lineaments that have been extracted from satellite images with the aid of GIS and Remote Sensing software and previous works were confirmed through the geological study. Besides, strikes and dips of beds, joints, fractures, and faults were measured. The orientations of faults and lineaments were processed using QGIS. Finally, geological maps and cross-sections of hydrogeological significance, and structures were constructed using Arc GIS 10.3 and AUTOCAD22.

The Hydrogeological study was also conducted by giving more attention to differentiating the sediments and rock units of groundwater significance such as the bedding direction of the rock units, the degree of fracturing of the rock, space between fractures, and opening space of fractures, the extent and degree of effect of weathering in the rocks. Using the representative lithological log, the type and degree of precipitations of secondary materials in the fractures of the rocks, the thickness of the formations, the grain size, and sorting, shape, and the clay proportion in the sediments or deposits were clearly understood. Besides, the orientation of lineaments and faults with respective groundwater flow directions were analyzed. In addition, depth to the groundwater level was measured for selected, and representative boreholes in the plateau, rift margin, and rift floor using a deep meter. Furthermore, the discharge of

springs were also estimated wherever possible. Lithostratigraphy correlations for the selected flow directions from the plateau to the rift floor were prepared using Arc GIS 10.8, AUTOCAD22, and Starter software. Finally, a hydrogeological map containing groundwater head contours, flow directions, hydrogeological units and aquifer productivity were developed using Arc GIS 10.8.

1.6.2 Hydrochemical and Environmental Isotopes analysis and interpretations

For the hydrochemical and isotope study, representative water samples were collected from the adjacent Plateau (Blue Nile basin), Western Afar rift margin, and associated rift floor along N-S, SW-NE, NW-SE, and W-E directions (Figure 1). For the interpretation purpose, all the water samples from springs, rivers, and lakes belonged to surface waters, while hand-dug wells and boreholes with depths ≤150m belonged to shallow systems. Wells with a depth greater than 150m were considered as deep wells. For primary groundwater sampling in hand-pump-fitted wells, stagnant water was pumped away for ten to fifteen minutes. Groundwater samples for the borehole were taken from functional sources, at the point of emission for spring, and from the upper few millimeters of the surface, about five to ten meters from the beaches for the lake sources.

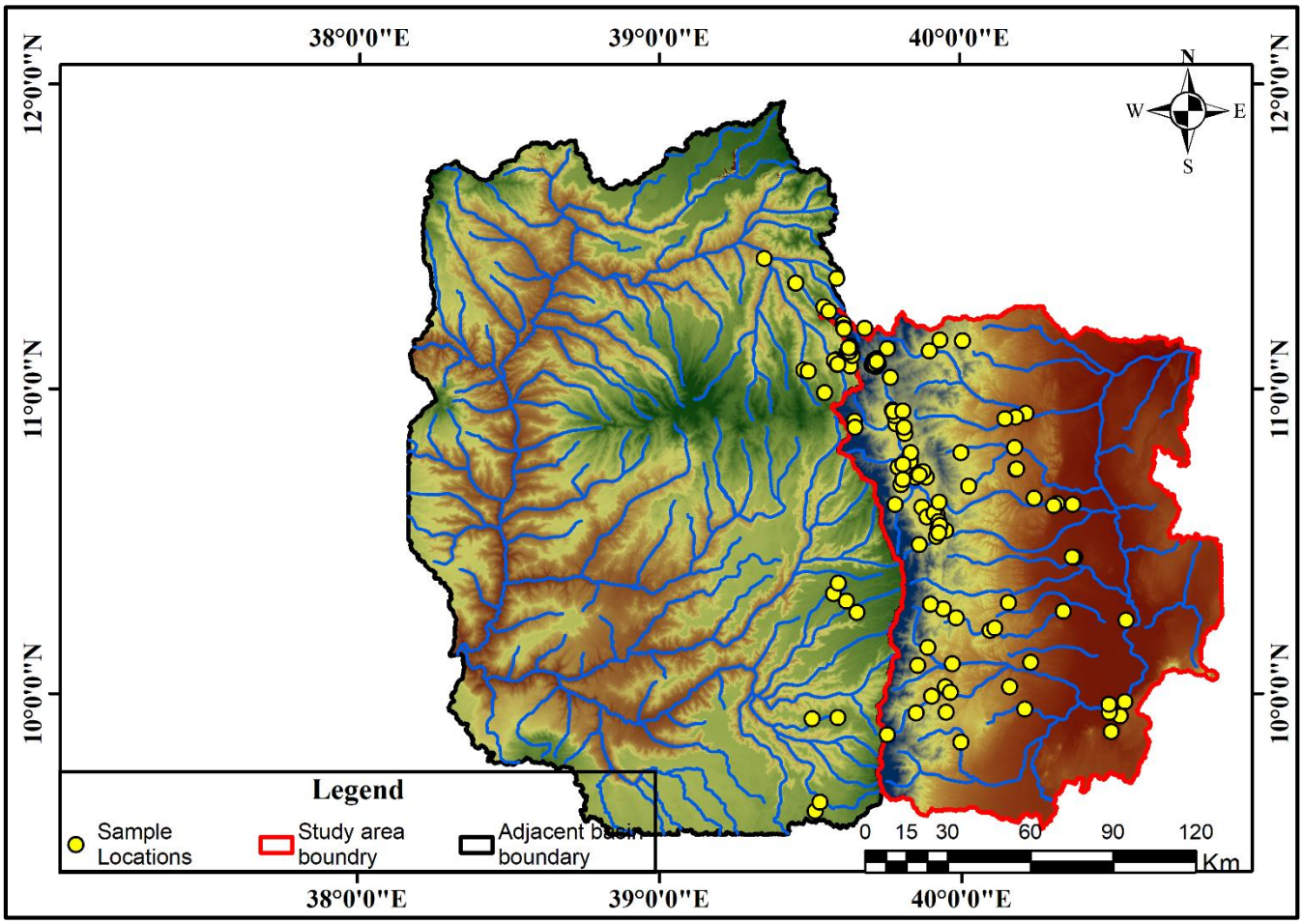


Figure 1: Sampling distributions along the plateau, rift margin, and associated rift floor

The samples were collected with strict sampling protocols into three separate plastic sample containers having a size of 15ml for cations, anions, and isotopes. During sampling, to separate suspended and fine particles, membrane filters having a size of 0.45µm for anions and isotopes, and 0.2µm for cation samples were used. At the end of sampling, the cations samples were acidified with drops of nitric acids for preservation purposes. In the case of isotope samples, the sampling bottles were filled, firmly capped, and plastered around the mouth to prevent isotopic exchange with the atmosphere. After collecting the samples, properly labeled, and stored them in a standard cool box kept at or below 5°C. Along with the sampling activities, in-situ water quality measurements including Electrical Conductivity (EC), Total Dissolved Solids (TDS), Temperature, and pH were conducted using multi-parameter portable and calibrated water quality measurement kits (HANNA hand-held instruments (Figure 2).



Figure 2: Insitu water quality measurement (A) and Sampling from hand-fitted pump wells (B)

The water samples were sent to the IHE-UNESCO water laboratory in the Netherlands for analysis. Cations, anions, and isotopes were analyzed using the Inductively Coupled Plasma Optical Emission Spectroscopy (ICP-OES1000) technique, using PerkinElmer Avio200, ICS 1000, and Laser Spectroscopy instruments respectively. The results were presented in mg/l and per mil (‰) for hydrochemical and isotope results respectively. The bicarbonate and total alkalinity (TA) levels were determined using titration methods.

Hydrochemical results have been interpreted using AquaChem version 14 and Golden Grapher software to determine the water type and understand groundwater flow dynamics along the flow directions. Besides, various ionic ratio relationships were developed to identify and understand the different weathering and geochemical processes. The analyzed results were also correlated with the in situ water

quality measurements including PH, TDS, and EC. Besides, the Total Alkalinity (TA) for each physiography were determined and correlated with other parameters.

Results for the stable isotopes of water (^{18}O and ^{2}H) were plotted using SPSS and Excel and interpreted by comparing the results with the Local Meteoric Water Line (LMWL) and Global Meteoric Water Line (GMWL). Besides, the minimum, maximum, mean, slope, and D-Excess values were also calculated for each physiography, and correlated. Moreover, isotopic ratio for each physiography were determined and compared.

Furthermore, to better understand the interaction between groundwater and surface water, which leads to knowledge of the degree of permeability of the underlying rock and groundwater structures, as well as for the qualitative identification of source of groundwater recharge, Radon measurements (^{222}Rn) were carried out using DURRIGE-RAD7 portable electronic ^{222}Rn meter equipped with a RAD aqua module. The measurement was conducted at the selected sites, mainly at the outlets of the marginal grabens specifically at Borkena, Ataye, Jara, Jewuha, and Robit rivers of the Awash tributaries, between the rift margin and the rift floor like Telalak river and finally within the rift floor and at the outlets of the study are such as the Yardi lake and the main river (Awash Adaitu) respectively (Figure 3). Besides to the surface water sources, Radon measurements were also conducted at the selected deep and shallow boreholes both in the rift margin and rift floor, for understanding recharge and discharge zones.

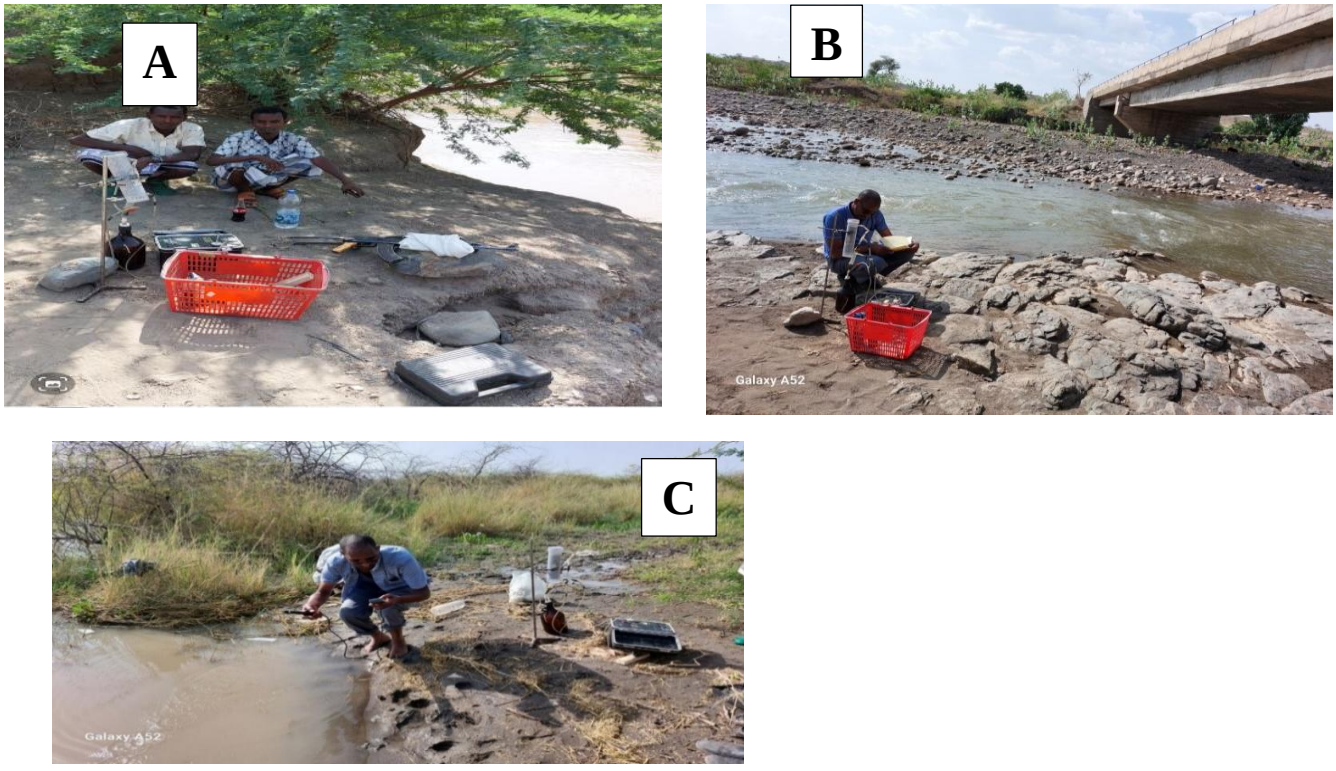


Figure 3: Radon measurement: (A) Awash Adaitu (Rift floor), (B) Telalak River (Rift margin), and (C) Lake Yardi (Rift floor)

1.6.3 Multivariate statistical analysis of hydrochemical data

This comprises the use of statistical methods to interpret and realize the relationships, patterns, and trends in hydrochemical data, which includes the chemical composition of water samples. Some of the statistical analysis includes Hierarchical Cluster Analysis (HCA), where the water samples were grouped into objective groups with comparable physical and chemical properties. The use of Hierarchical Cluster Analysis (HCA) for the statistical classification of geochemical data in Q-mode has demonstrated that it is a useful framework for classifying water composition into hydrochemical facies(Raiber et al., 2012, Farnham et al., 2003, Kebede et al., 2005, Baye, 2009). In addition, a Correlation Matrix and Principal Component Analysis (PCA) for a certain physical and hydrochemical parameter would also be conducted. In this study, SPSS version 27.0 statistical data analysis software was used for HCA, descriptive statistics, PCA, and linear correlations.

1.6.4 Different Recharge Estimation tools

There are numerous approaches to estimating groundwater recharge, including baseflow separation, tracer techniques, empirical relationships, direct measurements of water level changes, water balance methods, and numerical modeling(de Vries & Simmers, 2002, Jie et al., 2011, King et al., 2017). However, before the selection of the method in a given geo-hydrologic and climatic situation, a thorough understanding and assessment of the approaches, their limitations in terms of application, geological and tectonic situations, and the understanding of governing factors controlling recharge are necessary(Schilling et al., 2021, Ifediegwu et al., 2019, Kaewdum & Chotpantarat, 2002). Given these considerations and the study's objective to estimate groundwater recharge rates both spatial and temporal, the methods to be employed in this study include Water balance, the WetSpass M-model, the Chloride Mass Balance (CMB), and the Base flow separation method complemented by Radon measurement analysis.

1.6.5 Integrated Remote Sensing and GIS overlay analysis

To evaluate the spatially distributed groundwater potential map of the study area, Integrated Geographic Information System (GIS) and Remote Sensing (RS) overlay analysis techniques will be applied. The overlay analysis was used to consider eight thematic layers including geology, lineament density, soil, land use/land cover (LULC), recharge, drainage density, slope, and topographic wetness index, all of which are essential for groundwater occurrence, distribution, and movement in this specific area. With a spatial resolution of 100 meters by 100 meters, each of these thematic layers was generated as a raster file using the GIS working environment in zone 37 of the UTM projection with ADINDAN as the reference datum. Then, using a multi-criteria decision-making (MCDM) technique, namely the analytic hierarchical process (AHP) developed by Saaty and Modified Saaty called Fuzzy analytic hierarchical

process (FAHP), suitable weightage was given to each layer based on their relative influence on groundwater occurrence, supported by local geological and hydrogeological knowledge. Finally, a spatially distributed groundwater potential map is created in a GIS environment utilizing weighted overlay analysis.

1.6.6 Development of Numerical groundwater flow model for selected catchment

An attempt was made to develop a simplified 1-layer steady-state numerical groundwater flow model for the selected catchment as a preliminary modeling work, as the study area represents a large groundwater system that incorporates many small catchments, with complex groundwater flow dynamics. The selection criteria is based on the result of the geological, hydrochemical, and isotope analysis and interpretations. A numerical groundwater flow model has been run using MODFLOW-2000. Results were presented in tables and maps and used for the calibration and controlling mechanisms for the hydrologic parameters determined by other methods.

1.7 Materials

The following materials were used during the entire research period

- GPS for taking coordinates of water points as well as any features gathered during the field stage
- Geological hammer
- Handheld EC-Temperature-PH meter kits to take in-situ measurements during field works
- Cool box for storing the collected water samples
- Capped plastic bottles having a size of 15ml to collect separate water samples for cation, anion, and isotope analysis
- Radon in situ measuring instrument(RAD7)
- Deep meter for measuring static water level
- Plastic sampler for hand-dug well sources
- Compass
- Solutions of known pH (4, 7, and 10) for Calibration of pH meter
- Distilled water for washing the electrodes of pH meters, and other equipment frequently used during sampling to prevent sample contamination
- Nitric acid which will be added to the cation sample for preservation
- Marker, and nastro
- Landsat8 images from USGS website ,DEM,
- Topographic maps, previously done geological maps, and hydrogeological maps of Ethiopia;
- Etc.

1. 8 Software

Primary as well as secondary data were processed/analyzed to generate and visualize the anticipated objective results using the following scientific software such as;

- Global Mapper v.18 and Google Earth to access a variety of spatial features
- Golden Software Surfer v.16 to observe the 3-dimensional view of geological as well as topographical settings.
- PCI Geomatica17 to extract lineament features
- Aquitest version 3.5 for pumping test data analysis
- AquaChem v14, and Golden Grapher for hydro-chemical data analysis
- Q GIS, ArcGIS 10.8, and AutoCAD 2022 to make different maps and cross-sections
- Groundwater modeling programs like MODFLOW
- WetSpass M-model
- Rock works version 17
- River Analysis Package(RAP) for the separation of river data into base flow and runoff
- Starter for preparing litho stratigraphic cross-section along the selected flow direction
- SPSS version 27.0
- Etc.

Chapter Two: Description of the study area

2.1 Location and accessibility

Afar Depression is a broad area of subdued topography where the Red Sea from the north and extends to the SE through several offset rift basins, the Gulf of Aden from the east, and the East African Rift System from the south the third branch of the current converge at a triple junction (Rooney et al., 2020, Zwaan, Corti, Sani, et al., 2020) (Figure 4).

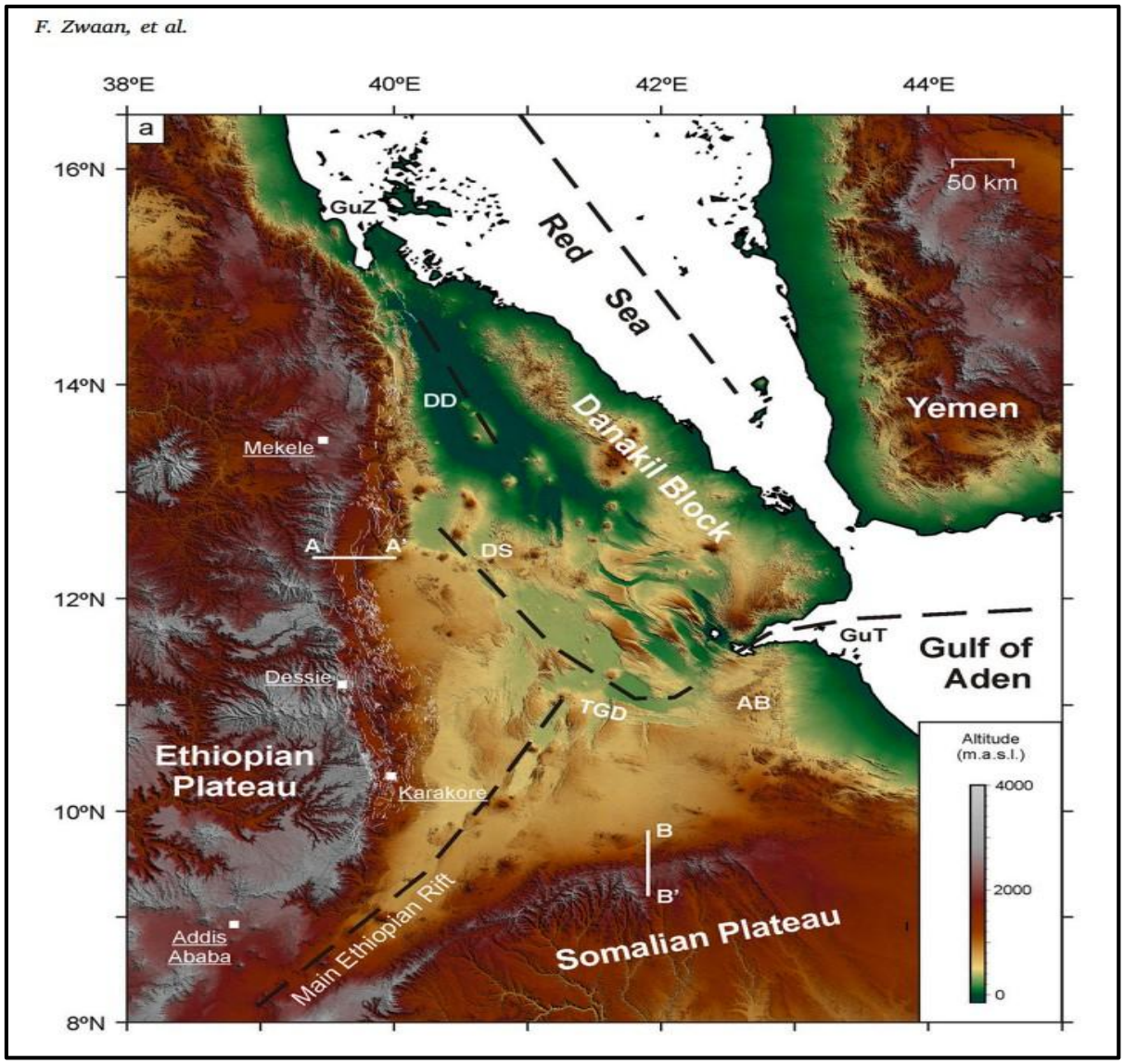


Figure 4: Afar Depression modified from Zwaan, Corti, Sani, et al., 2020 and Reference therein

The study area is located in the Southern Sections of the Western Afar Rift Margin and associated rift floor (Figure 5), dominantly in the Middle and partly in the Lower Awash River basin, the Eastern part of the Blue Nile basin. It encompasses part of North Shewa, Oromo Special, and South Wollo Zones of the Amhara region and Zone 3(three), and Zone 5(five) of the Afar region. The area is bounded within

9º40'11" to 11º42'22" N latitude and 39º31'25" to 40º 10'46" E longitudes and has area coverage of 19132 Sq. Km. It is found nearly 150km from Addis Ababa in the southwest and extends horizontally until Dessie town in the northwest and extends downward to the east and northeast until Gewane and other towns of the Afar region. The study area is accessed by the main asphalt road from Addis Ababa-Debre Birhan-Dessie, Kombolcha-Bati-Kasagita asphalt roads, and other gravel roads from Kasagita-Dewe-Telalak- Dalifagea, Shewa Robit – Semurobi-Gewane, Senbete-Hadeleala, Addis Ababa-Awash-Gewane-Mile main asphalt road and each sub-basin in the study area is accessible by dry weather roads. Generally, the study area has no significant accessibility problem.

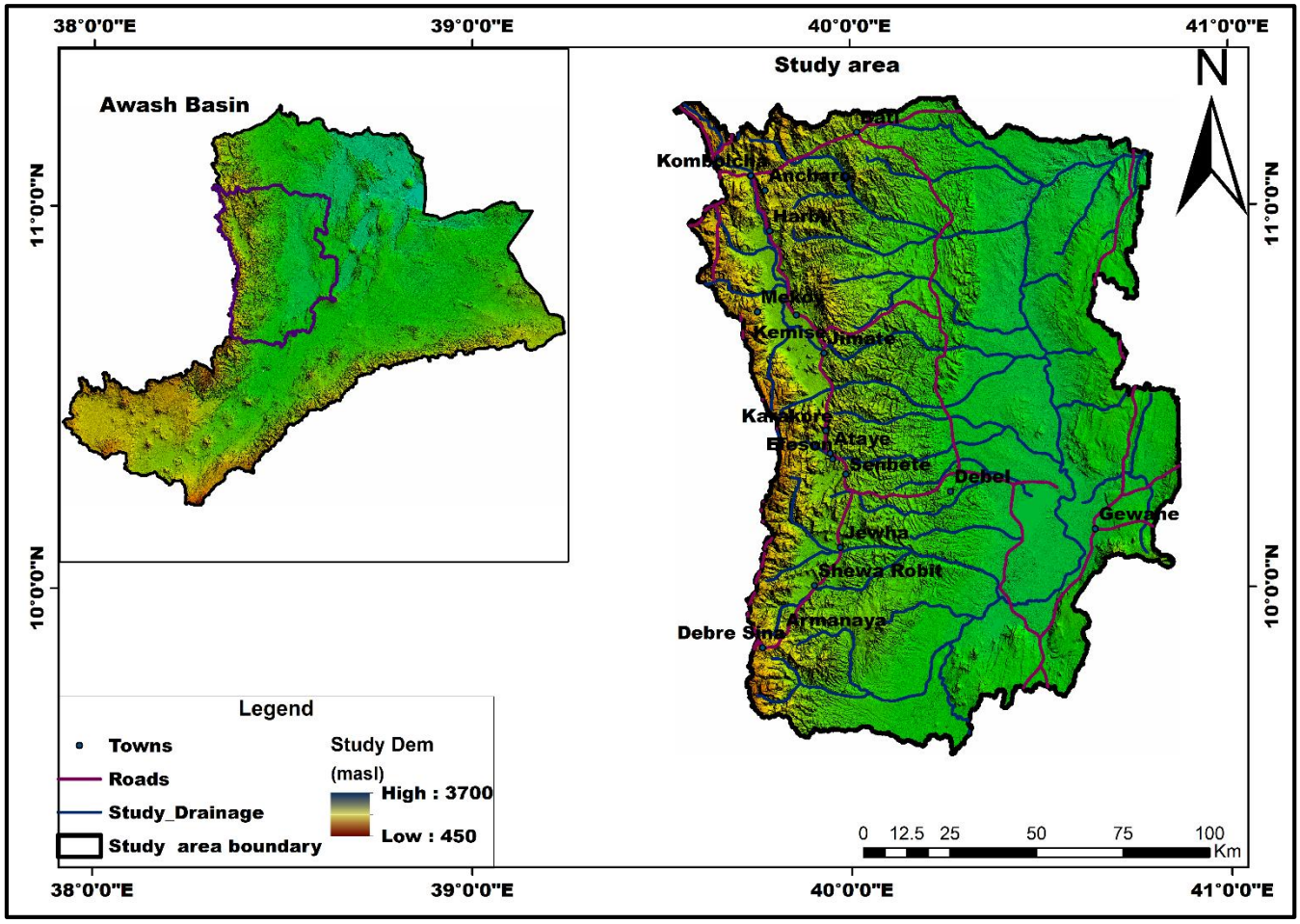


Figure 5: Location map of the study area

2.2 Climate

The spatial and temporal variation of rainfall in Ethiopia is strongly controlled by the inter-annual movement of the position of the Intertropical Convergent Zone (ITCZ) (Tenalem Ayenew and Tamiru Alemayehu,2001). During its movement to the north and south of the equator, the ITCZ passes over Ethiopia twice a year and this migration causes the onset and withdrawal of winds from the north and south. Hence, the spatial and temporal variation of rain fall in the study area is also influenced by ITCZ.

Based on these moisture distribution patterns, three rainfall (moisture) regimes can be identified in Ethiopia.

- The south-western and western areas of the country are characterized by mono-modal rainfall patterns,
- The central, eastern, and northeastern areas of the country experience a nearly bimodal rainfall distribution. These are the Belg rains (February to May) and the Kiremit rains (June to September). The study area is grouped under this regime and has a maximum and minimum rainfall of 1900mm/year and 320mm/year respectively from the available data.
- The southern and southeastern areas of the country are dominated by a distinctly bimodal rainfall pattern.

Furthermore, the climate of the study area ranges from warm and temperate to cool when it is classified based on altitude. As figure 5 above shows, the altitude ranges from 450 to 3700 meters above mean sea level. Therefore; cool (Kur), cool temperate (Dega), temperate (Weina Dega), and warm temperate (kola) are the climatic classification. The eastern portion of the study area is dominated by lowland i.e. warm temperate. While, the western and southwestern part is dominated by highlands and the climate is from cool to cool temperate. The maximum, minimum, and mean daily temperatures in the research area are 30.64°c, 11.2°c, and 20.59°c respectively.

2.3 Physiography and Drainage

2.3.1 Physiography

Physiographically, Ethiopia has three physiographic regions—the North Western Plateau (NWP) and related lowlands, the South East Plateau (SEP) and related lowlands, and the Main Ethiopian Rift (MER)—by the enormous East African and Afar rifts. It is flanked by the Ethiopian Plateau in the west, the Somalian Plateau to the south, and the Aisha and Danakil Blocks to the east and NE, respectively(Figure 16)(Zwaan, Corti, Keir, et al., 2020b). To the south, the Ethiopian and Somalian Plateaus are separated by the northeastern portion of the Main Ethiopian Rift(Beyene & Abdelsalam, 2005). Physiographically it ranges from the mountains having an altitude of more than 3,700 m above sea level to the Danakil Depression, which is 120 m below sea level(Godfrey & Hailemichael et al., 2016, Zwaan, Corti, Sani, et al., 2020b). The study area can be divided into mountainous, valley-filled, and low-lying areas (Figure 6). The western highlands generally consist of elevated plateaus, but the eastern highlands are rugged. The low-lying areas have flat to undulating topography with some volcanic ridges that separate the sub-basins, especially in the rift margin. The slope in the valley fills and low-lying areas have a range of 0-4.8 and the maximum slope is 77.14° found in the surrounding mountains. The minimum elevation in the study area is 450m and the maximum elevation is 3700m (Figure 5).

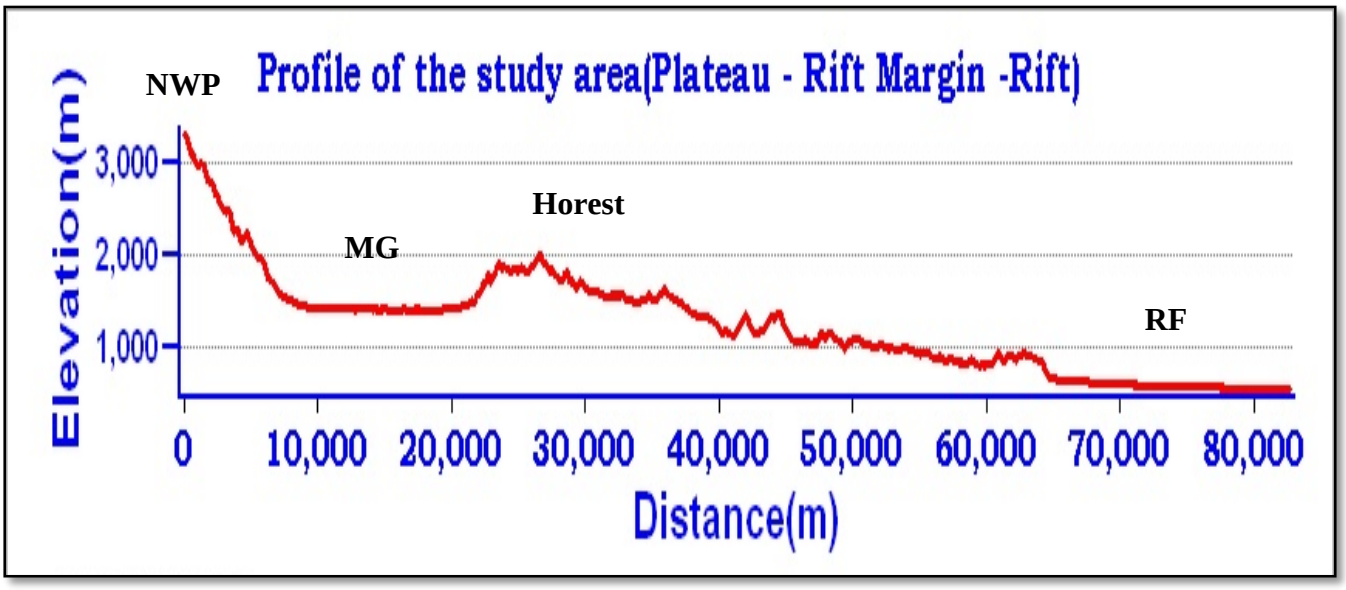


Figure 6: Profile of the study area (Plateau -Rift Margin-Rift floor)

2.3.2 Drainage System

The drainage system is mainly controlled by topography and geological structures. Each river in the study area has numerous small tributaries joining at right angles to the higher order streams that can be characterized as a dendritic drainage system and few streams have a character Trellis pattern. All the perennial rivers and streams in the study area are flowing toward the East and finally in North -East direction (Figure 7).

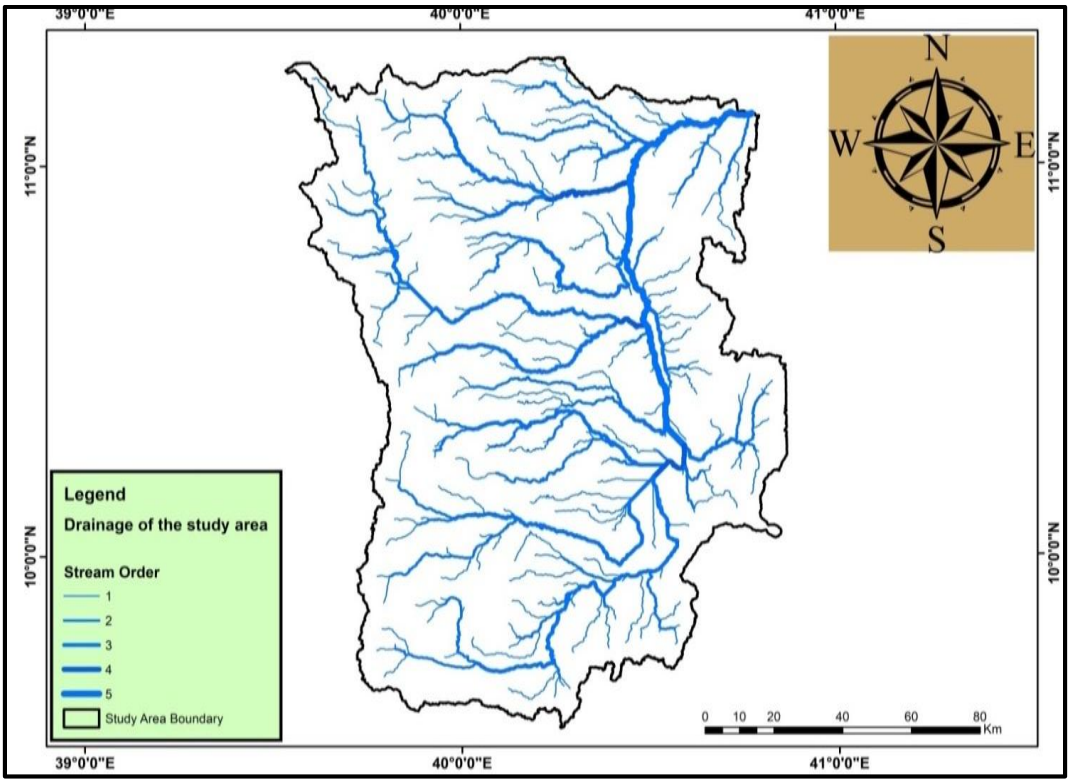


Figure 7: Drainage map of the study area

2.4 Geology

2.4.1 Regional Geology

Ethiopia's geology is greatly influenced by faulting and tectonics, making it a geologically unique place in the globe. The Precambrian geology, for instance, shows two major regional belts: the Arabian Nubian Shield and the Mozambique Belt, which converge in Ethiopia's northern region (Beyene & Abdelsalam, 2005, Zwaan, Corti, Sani, et al., 2020a). Both belts have undergone varying degrees of metamorphosis, foliation, fracture, and deformation. Based on the geological classifications done by Zwaan, Corti, Sani, et al., 2020 and Rooney, et al., 2017, 2020, the regional geology of the Western Afar Rift margin and rift floor can be divided into six primary units. Accordingly from the older to younger exposures, it can be classified as Precambrian (Neoproterozoic) metamorphic basement, Paleozoic rocks namely called Enticho sandstones and glacial deposits, Triassic Adigrat sandstones and Jurassic limestone, the Cretaceous deposits and finally extensive Miocene-present sedimentary and volcanic infill. The other geological classifications were also made by various scholars as described in detail by Varet & et al., 2018. Accordingly, the regional geology of the Afar depression can be divided into four broad groups including (1) Neoproterozoic basement, Mesozoic sedimentary rocks, and Eocene–Miocene basalts; (2) Miocene igneous rocks; (3) Pliocene volcanic rocks; and (4) Quaternary volcanic and sedimentary rocks (Figure 8).

The Neoproterozoic basement, which is part of the Arabian-Nubian Shield, is found on the borders of the Afar Depression. In eastern Eritrea and northern Ethiopia, the Arabian-Nubian Shield encompasses a large area to the north and northwest of the Afar Depression, respectively(Beyene & Abdelsalam, 2005, Justin-Visentin & Zanettin, 1974). Mesozoic sedimentary rocks, which are younger, cover the Neoproterozoic basement rocks of the Ethiopian Plateau to the south, and the Somalian Plateau to the southwest. The Mesozoic sedimentary rocks, which are mostly exposed on the northwestern Ethiopian plateau, include Early Jurassic Adigrat Sandstone, Middle Jurassic Abay Limestone, Late Jurassic Antalo Limestone, and Cretaceous Debre Libanos Sandstone(Beyene & Abdelsalam, 2005, Justin-Visentin & Zanettin, 1974). Early Jurassic Adigrat Sandstone, Early Jurassic Hamanilei fossiliferous Dolomite and Limestone, Late Jurassic Urandab gypsiferous Limestone, and Early Cretaceous Antalo Sandstones are among the Mesozoic sedimentary rocks found on the Somalian Plateau(Almond, 1986, Abbate et al., 2015, Hagos et al., 2016). In the Afar Depression, the pre-rift group (Neoproterozoic basement/Mesozoic sedimentary rocks) is either absent or covered beneath Pliocene and Quaternary volcanic and sediments(Beyene & Abdelsalam, 2005, Bonini et al., 2005).

The Mesozoic sedimentary rocks on both the Ethiopian and the Somalian plateau are covered by Eocene–Miocene flood basalts. These volcanic groups are also found in some parts of the marginal areas.

However, the Afar depression occurs in limited areas around the Gulf of Tajura and on the Ali-Sabieh Block(Varet & et al., 2018) and most of the flood basalts of 25–15 Ma are deeply weathered and intensely faulted. Thirty million years of tectonic and volcanic processes have sculpted the floor of Afar, resulting in the buildup of voluminous volcanic rocks and severe normal faulting(Ebinger & Belachew, 2010, Hagos et al., 2016, Hammond et al., 2011, Hayward & Ebinger, 1996). Although Oligocene to Early Miocene basalts belonging to the trap series are preserved in limited areas at the margins of the depression(Beyene & Abdelsalam, 2005), the majority of volcanic rocks are Upper Miocene– Recent in age, which includes intrusive rocks like granites, and younger volcanic rocks mainly Dalha basalt and Mabla rhyolites, and formed after the young rift subsided between the marginal faults(Koptev et al., 2018, Hofmann et al., 1997, Justin-Visentin & Zanettin, 1974). Compositionally the granite formation has Alkaline to per-alkaline nature and is mainly exposed along the western and eastern Afar margins and the northern part of Afar (Figure 8). As has been well discussed in Varet & et al., 2018, the granites display clear intrusive contact with the Neoproterozoic basement, Jurassic Limestones, and old Trap Series basalts. Based on the Sr isotope analysis, the lower value is found which indicates that the source of these intrusive rocks is possibly from a mantle source and might be associated with an early phase of continental break up(Barberi et al., 1972, 1974). The Mabla Series consists of rhyolites and ignimbrites with minor intercalation of basalts(Barberi et al., 1972, 1974). These were erupted along N–S trending vents(Varet & et al., 2018). The Dalha Series is a basaltic sequence up to 800 m thick found inter-bedded with rare detrital sedimentary rocks and ignimbrites(Varet & et al., 2018).

The Afar Depression is mostly covered by Pliocene–Pleistocene volcanic (Figure 8). Regarding the coverage and preservation of igneous features and tectonic activity, they are by far the most significant geological units. The most important of them is the Afar Stratoid Series, which is distinguished from the Dalha Series by a nonconformity that points to diminished magmatic activity and a longer period of erosion. Volcanism is dominated by basaltic activity, whose most important manifestation is the Afar Stratoid Series, a >55,000 km^2 -wide and >1,500 m-thick sequence consisting of basaltic lava flows varying from 1 to 6 m (Varet, 1978; Tefera et al., 1996) and minor rhyolitic ignimbrites erupted in the Pliocene–Pleistocene (4–0.5 Ma) mainly from volcanic fissures(Acocella et al.,2004, Barberi et al.,1974, LeGall et al.,2011, Kazmin,1991).

Quaternary volcanic rocks in the Afar Depression are composed of basaltic flows, scoria cones, and silicic rocks (Beyene & Abdelsalam, et al., 2005, Tefera et al., 1996). In most places basaltic fissure eruptions were followed by central eruptions that produced differentiates of basalt comprising alkaline and per-alkaline silicic rocks. However, the rift-parallel axial ranges (within the SE-propagating Manda Hararo–

Gobaad and the NW-propagating Asal–Manda Inakir rifts) in the northern and east-central Afar are dominated by basalts which are 1 Ma old. The Quaternary volcanic rocks, especially in the northern Afar are characterized by shield volcanoes. E–NE trending volcanic centers transverse the NW– SE rifts found along the eastern and western Afar margins (Figure 8). These transverse volcanic centers are associated with fracture zones equivalent to oceanic fractures and composed of alkali basalts with inclusions of peridotite nodules indicating a deeper mantle source (Barberi and Varet, 1975, 1977).

Quaternary sedimentary rocks in the Afar Depression are dominated by lacustrine deposits. The lacustrine sedimentary rocks were deposited in the central Afar along the Manda Hararo–Gobaad rift zones and Awsa plain of east central Afar and have a thickness of 180–200 m thickness cover the Awsa plain in the east-central Afar (Varet, 1978).

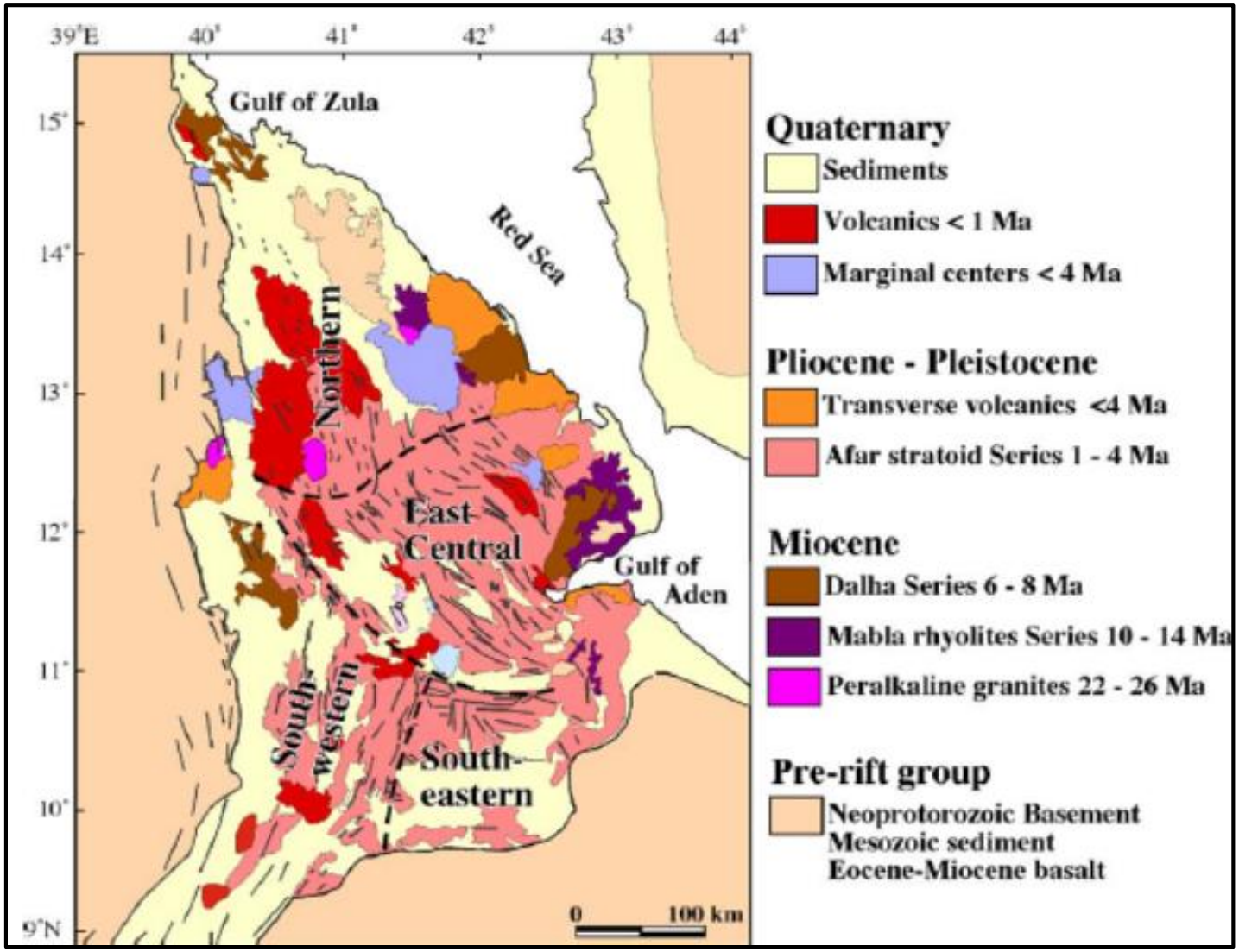


Figure 8: Geological map of the Afar Depression (a) (Beyene & Abdelsalam, et al., 2005, Tefera et al., 1996)

2.4.2 Local Geology

The local geology of the study area has been modified from the geological map of Ethiopia prepared by the Geological Survey of Ethiopia(GSE, 2010) having a scale of 1:250000 by correlating with land sat 8 images from USGS satellites, drilling logs, and other local sources and finally verified with field study. Accordingly, the following major geological classifications have been obtained, and described.

2.4.2.1 Columnar Jointed (Aiba) basalt

The columnar jointed lower basalt covers 1189 km^2 (6.21%) and outcrops mainly in the NNW and SSW of the study area part (Figure 19). The basalt is black in color, jointed, and mainly forms columnar. In the NNW of the study area, at the GPS locations of 1238298 N, 599182E, 1966m, and 1243850N, 609715 E, 1706m, the basalt is overlain by thin layers of Alaji ignimbrites with both units dipping ~40^0 eastwards towards the rift floor. The basalt outcrops are also observed in the western margin along the main road Shewa Robit – Kombolcha that form the lower elevation areas. Besides, the lower beds of the main tributaries of Awash River that flow from the marginal grabens towards the rift floor which includes Robit, Jewuha, Ataye, Jara, and Borkena at GPS location of 599031E, 1105354N, and 1260m, 606972E, 1116123N, and 1116m, 606735E, 1142965N, and 1438m, 6043954E, 1162 591N, and 1422m and 601644E, 1175548N and 1406m is covered by the columnar jointed basalt. The GPS location of 1222214 N, 500276 E, altitude 1843 meters, shows the boundary between the Aiba basalt to the East (rift side) and Alaji Rhyolite to the margin side along a North-South running fault line. In addition, near the rift floor at a GPS location of 613518E and 1087296N which is along the road from Shewa Robit to Semurobi woreda of the Afar region, highly weathered columnar jointed basalt is exposed with its typical properties (Figure 9).

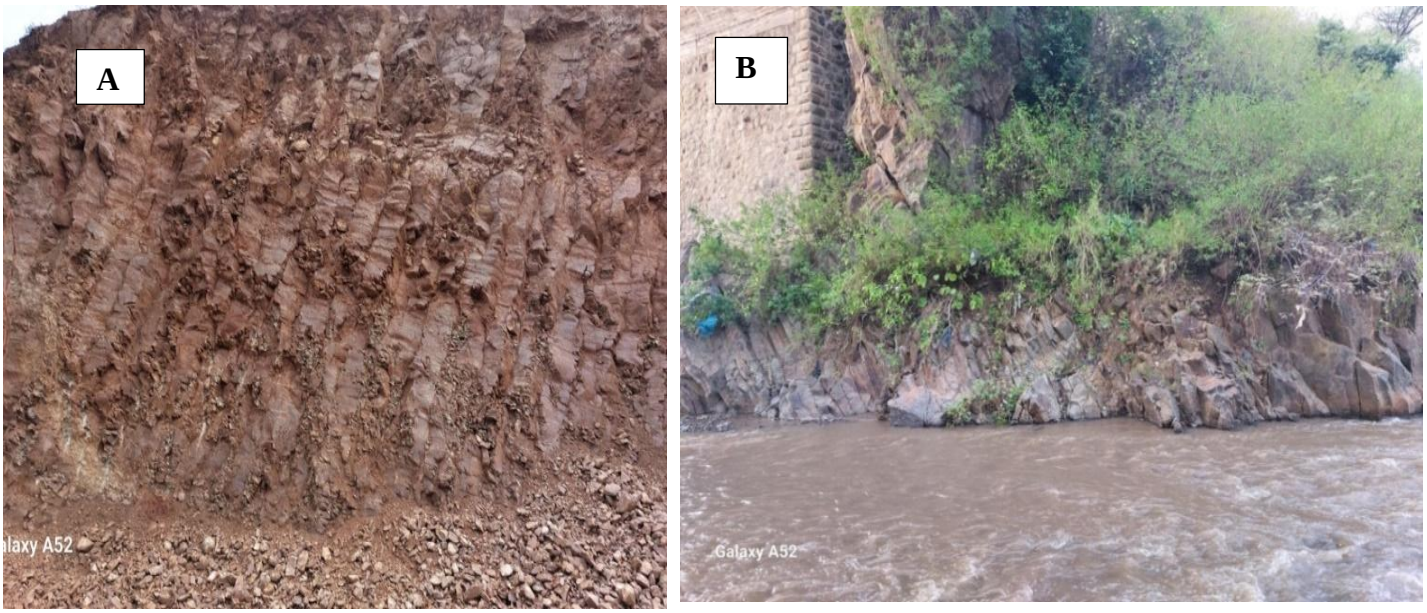


Figure 9: Columnar jointed basalt exposed towards the rift floor (A) & at the beds of the tributaries (B)

2.4.2.2 Alaji formations (Rhyolites and Ignimbrites)

Towards the upper limit of the lower columnar jointed Aiba basalt, the Alaji formation is defined by the conformable silicic (rhyolitic/trachytic) and ignimbrite horizon. They are light brown to brown colored rhyolites and ignimbrites, have moderate to high weathering and fracturing tendencies in most of the exposed areas, and cover 3788 km^2 (19.8%) of the study area. These formations are exposed in large parts of the study area bounding the marginal graben along the east and showing typical rift ward tilting (Figure 19). These acidic rock outcrops continue to the Margin/rift border and most of them show tilts of 30 º - 35 º towards the East while moving further towards the rift floor, ignimbrites that are highly fractured and tilted about 10º towards the east are exposed. At the GPS location of 1239875N, 560800E, 2894m, Alaji rhyolites, and ignimbrites are found on top of a sequence of thick lower(columnar jointed basalts) and are overlain by upper (Termaber basalt), the contact between the two is estimated at ~2900 m elevation(Figure 12). At the GPS coordinates 1051002N, 550049E, and elevation 2623m, poorly welded, grey to light yellow, and very hard acidic/rhyolitic rocks are observed and cut by a distinctive vertical basaltic dyke of nearly 140 cm width(Figure 10-B). It has crystals of quartz and feldspar identifiable to the naked eye. Besides, at GPS coordinates 1061005N, 559121E, and 1301 meters, and 1114214N, E561290E, and 1307 meters, rhyolitic breccia, and greenish-grey highly welded rhyolitic ignimbrites respectively were observed with intense faulting (Figure 11). Besides, at GPS coordinates 1152906N, 564004E, and 1879m elevation, highly fractured rhyolitic ignimbrite with at least two systematic joint sets and many other non-systematic joints are observed.



Figure 10: Fractured ignimbrite bounding the graben (A), poorly welded rhyolite cut by basaltic dyke (B)

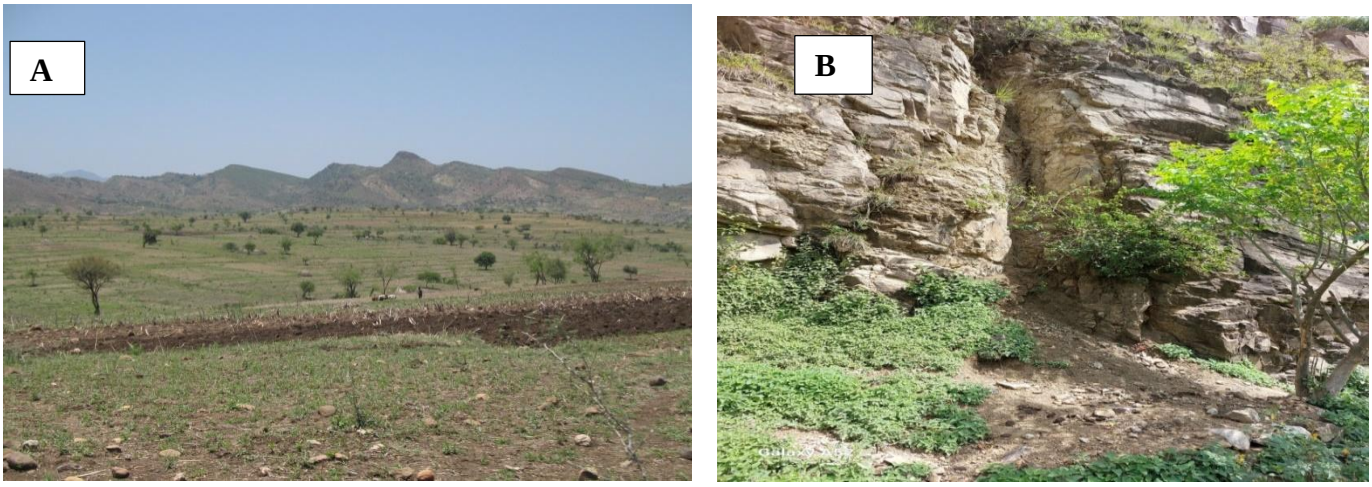


Figure 11: Tilted rhyolite beds in the margin/rift border (A), Rhyolite breccia with intense faulting (B)

2.4.2.3 Tarmaber (Upper) basalt

These formations cover 1127 km2 (5.89%) of the study area. Their exposures are mainly found in high-land areas but also occur on down-faulted blocks on the western escarpment (Figure 19). In the Northwestern and northern parts of the study area, at the GPS coordinates of 1239875N, 560800E, and 2894m, Termaber basalts are exposed overlying Alaji rhyolites, the contact estimated at ~2900 m elevation (Figure 12). At GPS coordinates 1243732E, 561837 E, and 2704m, Termaber basalt is exposed (down faulted) along the northern extension of Tosa Ridge. Besides, in the southwestern part of the study area, vesicular type Tarmaber basalt is also exposed. Several NNW-SSE trending normal faults with variable displacements affect the volcanic sequences thus changing the position of the contact between the basalt and the underlying acidic rocks. From the available drilling logs and surface stratigraphy, the upper basalt is underlain by fractured and weathered Alaji formations like ignimbrite and rhyolites. In most of the study areas, the formation is slight to moderately weathered and moderately to highly fractured.

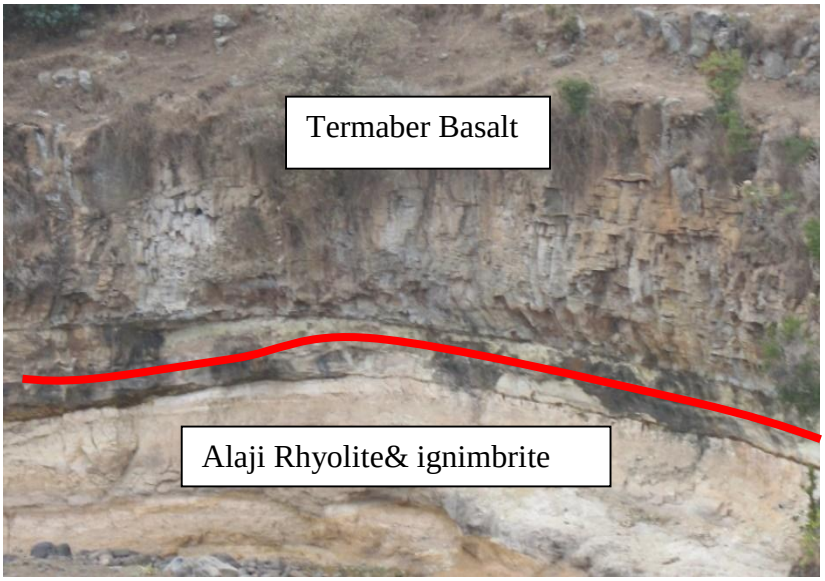


Figure 12: Contact between the Alaji rhyolite and Termaber basalt

2.4.2.4 Balchi Rhyolite and Ignimbrite

These are acidic rocks found in the southwestern part of the rift margin underlain in the west by the columnar jointed Aiba basalt and in the east overlain by the Dalha basalt. These geological units cover 300 Km2 (1.56%) of the study area (Figure 19). This formation comprises the silicic rocks of the rhyolites and ignimbrites of the northern surrounds of the Ethiopian rift valleys(Kazmin, 1991, Chorowicz, 1990). The color and degree of welding of these rocks are variable. Mostly these rocks are green, pink, and even reddish-colored pyroclastic flow with abundant plagioclase crystals.

2.4.2.5 Dalha Basalt

These formations cover 4593 km^2 (24.01%) of the study area and are mainly exposed in the boundary between the rift margin and the rift floor (Figure 19). In the northern part of the study area at the GPS locations of 632296E, 1223345N, and altitude 936.1m, this fresh-looking young basalt that forms block stone on the top of the ridges unconfomably overlays the highly weathered Ashangie basalt(Figure 13). This unit consists of a series of basaltic flows with rare intercalations of ignimbrite. It is slightly tilted ($7\text{-}10^0$) towards the east, i.e. towards the rift floor. The basalt is vesicular, columnar block forming, with typical black color rock, and shows no visible crystals at all(Rooney, 2017, Rooney, 2020).

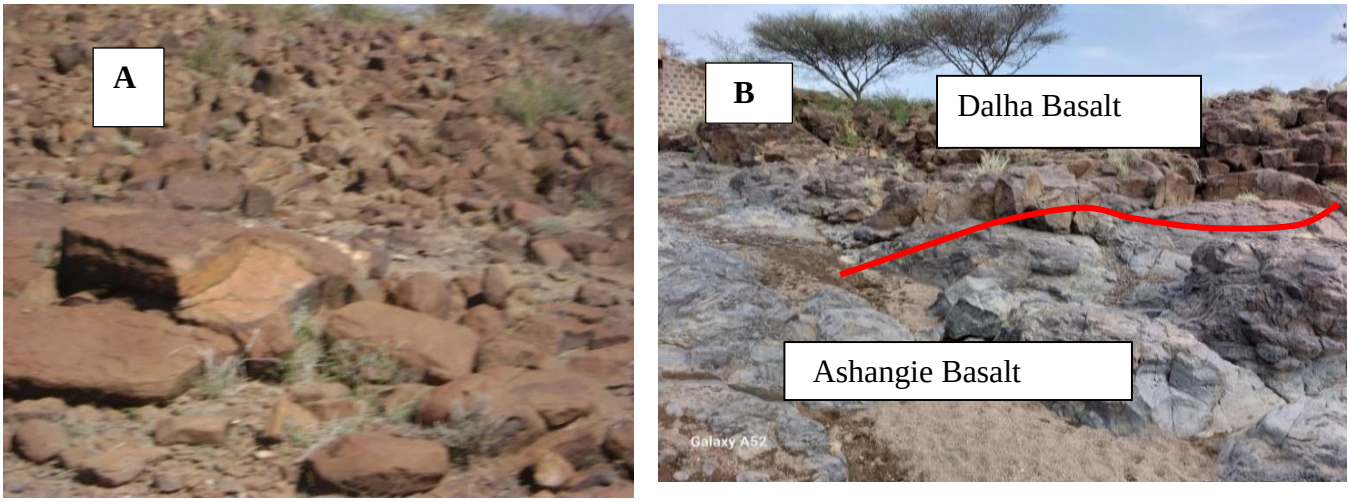


Figure 13: Blocks of Dalha basalt between RM and RF (A), Overlying weathered Ashangie basalt (B)

2.4.2.6 Afar Startoid Series

The Startoid series is the main formation outcropping in the northeastern, southeastern, and eastern parts of the study area (Figure 19). Besides, on the rift floor near the outlet of the study area; at Awash Adaitu, the river bed, the left and right banks are covered by the stratoid basalt (Figure 15-B). The basalt is mainly dominated by flood basalt magmatism with minor felsic activity(Barberi et al., 1972, Bonini et al., 2005, Doubre et al., 201). As a result, in the study area, the stratoid basalt is found with some intercalated rhyolitic flows ignimbrites, and sediments. The Startoid series is affected by normal N-S and NE-SW faults. It covers 3408 km^2 (17.81%) of the study area.

2.4.2.7 Lacustrine Deposit

The rift floor is mainly filled by the sediments consisting of layers of slightly compacted gravel, sand, silt, and clay with calcite concretions attesting to secondary processes after deposition as it is observed around the Meteka area of the rift floor. The formation ranges from light gray color lacustrine clay to light colored strongly compacted evaporate material (Figure 14). The deposition process appears to be strongly controlled by extensional faults and grabens (Mohr, 1983, Pagli et al., 2019). The lacustrine deposit covers 3039 Km^2 (15.88%) of the study area. The western and eastern side of this deposit is surrounded by the dark brown Dalha basalt and Afar stratoid series respectively (Figure 19). The thickness of the lacustrine deposits is unknown. However, from the recently drilled borehole around the Gewane area (rift floor), a 420 m thick lacustrine deposit dominantly clay was found, and it has been expected to be more.

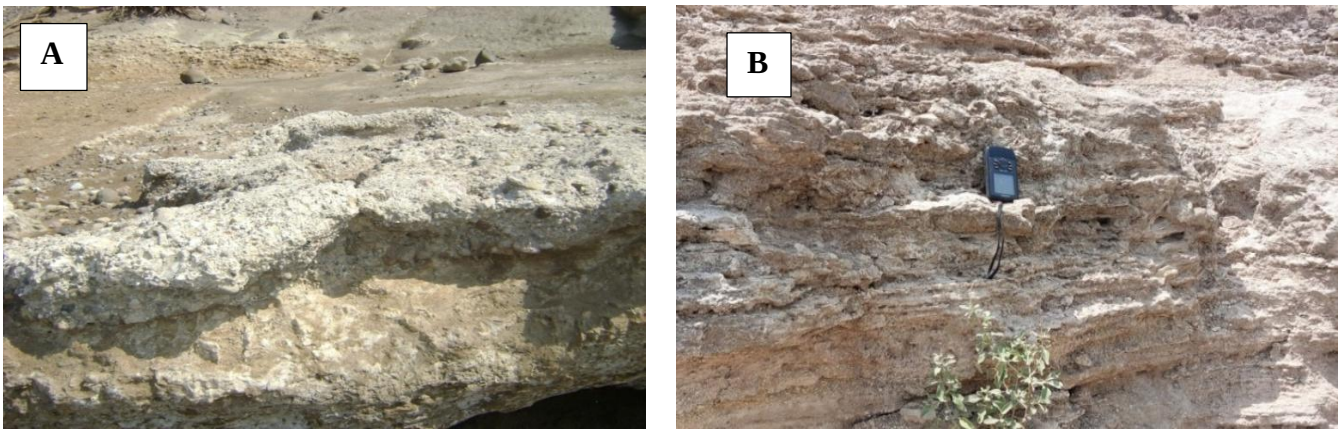


Figure 14: Welded lacustrine deposit (A), Layered lacustrine deposit around Meteka area (rift floor) (B)

2.4.2.8 Sub Recent to Recent Basalt

The Rift axis passes through the study area and along this axis, recent basaltic flows are exposed. This group of basalts covers 509 Km^2 (2.66%) of the study area. This recent basalt was exposed in the rift floor and eastern rift margin, particularly at the southeastern and southwestern of Gewane town. The basalt is found by overlying the lacustrine deposit and the stratoid series. The basalt looks fresh, brown-black, and block-forming and mainly follows the North East- South West- trending Wonji fault belt (Figure 15-A).

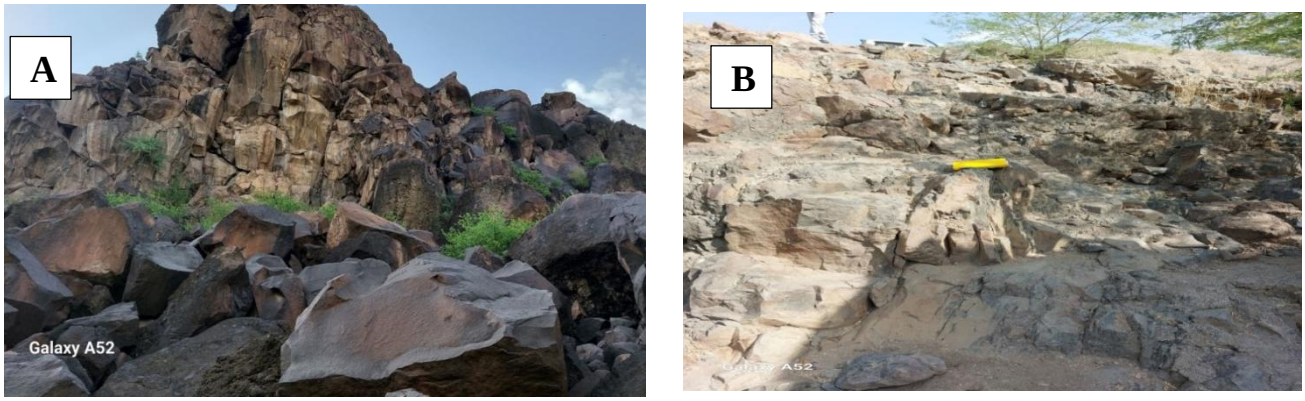


Figure 15: Sub-recent to recent basalt (A), Stratoid basalt (B)

2.4.2.9 Alluvial Deposits

The alluvial deposit is mainly exposed along the northwestern, western, and southwestern parts of the study area, particularly in the grabens, and covers a total area of 1179 km^2 (6.16 %) (Figure 19). It is comprised of gravel, sand with minor silt, and clay, and has an average thickness of 250m, as observed from the drilling logs. In the western rift margin, Stratigraphically the alluvial deposit is underlain by highly fractured and weathered upper basalt(Tarmaber basalt) followed by Alaji formation comprising of Ignimbrites and rhyolites and highly jointed and columnar forming Aiba basalts (lower basalt).

Table 1: Summary of identified geological formation and their coverage

Lithological Classifications	**Area coverage(Km^2)**	**Coverage (%)**
Termaber Basalt	1127	5.89
Aiba Basalt	1189	6.21
Alaji Formation	3788	19.80
Alluvium	1179	6.16
Dalha Basalt	4593	24.01
Lacustrine deposit	3039	15.88
Sub recent to Recent Basalt	509	2.66
Stratoid Basalt	3408	17.81
Balchi ignimbrite & rhyolite	300	1.57
Total	**19132**	**100**

2.5 Structures

The northwestern plateau (NWP) of Ethiopia is situated at the western margin of the Afar Rift. Most of the faults and fractures along this area are often aligned with the trends of the Afar Rift, indicating a structural continuity(Beutel et al., 2010), implying that the stress fields causing the rifting in Afar have an impact on the plateau as well. This demonstrates the structural and genetic connections between the northwest plateau and the Afar Rift. Hence, the rifting process has propagated westward from the Afar depression, influencing the structural development of the plateau(Zwaan, Corti, Sani, et al., 2020b). Accordingly, there are parallel to sub-parallel major and inferred faults, fractures, and lineaments with an alignment of N-S, NNW-SSE, NW-SE, NNE-SSW, and NE-SW, related with the main Ethiopian rift and the Red Sea rift systems respectively(Corti et al., 2015). Some of the prominent faults that connect the plateau to the rift margin include the Debresina fault and Dessie –Kombolcha- Bati fault systems.

The Afar depression is bounded to the west by the Ethiopian-Eritrean Plateau (African Plate), to the south by the southeastern plateau (Somali Plate), and to the northeast by the Danakil Horst (Barbot et al., 2008,

C. J. Ebinger, 1989, Hagos et al., 2016). It merges into the Ethiopian Main Rift Valley in the south, the Red Sea Rift Valley in the northwest, and the Gulf of Aden in the east, and it is a zone of active continental rifting and volcanism(Muirhead et al., 2019, Barberi et al., 1972, Beutel et al., 2010, Zwaan, Corti, Sani, et al., 2020, Manighetti et al., 1998, Bastow et al., 2011)(Figure 16).

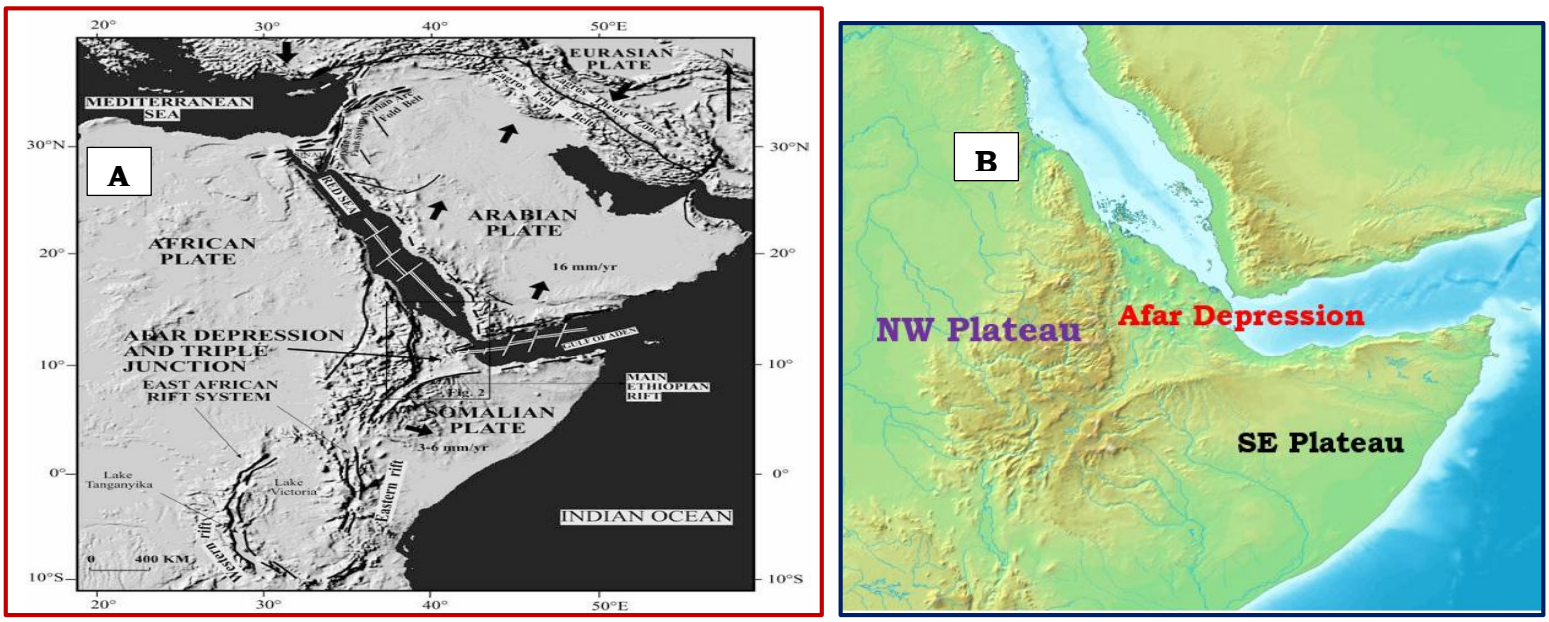


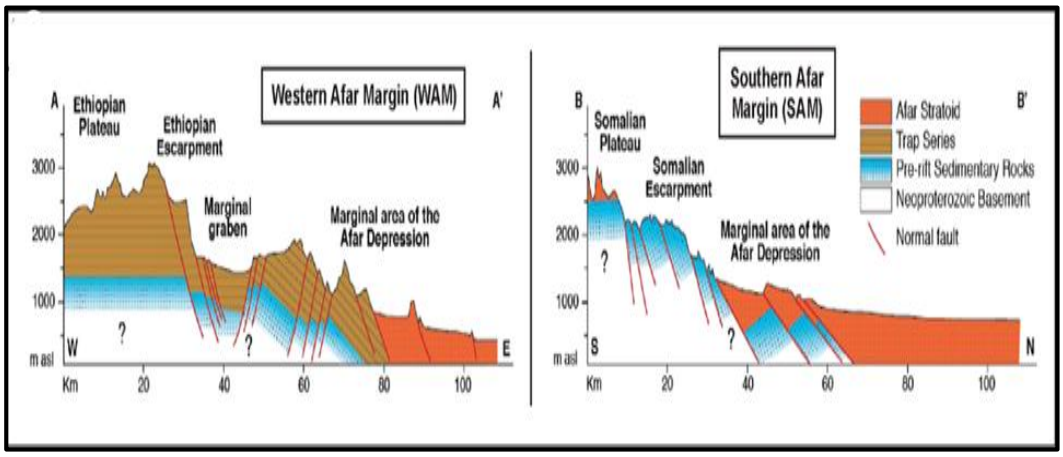
Figure 16: Digital elevation model of eastern Africa and Arabia showing the location of the MER, Red Sea, Afar Rift, and Gulf of Aden Rift modified from Tesfaye et al,2003(A), and Ethiopian physiography including NW Plateau, Afar Depression and SE Plateau(B).

The western margin was formed by the down-warping of the Afar Depression and subsequent faulting and rift-ward tilting of faulted blocks(Younes & McClay, 2002). It exhibits several normal faults with a significant NNW-SSE strike, although its southernmost part has a distinct NNE-SSW fault orientation acting on the main Ethiopian rift(Zwaan, Corti, Sani, et al., 2020a, Barbot et al., 2008)(Figure 17).



Figure 17: Major normal fault bounding a marginal graben along the escarpment dipping towards the rift

Besides, it exhibits several segmented, seismically active, and rightward steeping marginal grabens arranged in NNE and NNW trends (Corti et al., 2015, Beyene & Abdelsalam, 2005, P. Mohr, 1983)(**Figure 18**-C). These grabens are associated with the predominant antithetic fault which dips westward from the Afar rift (Justin-Visentin & Zanettin, 1974, Abbate et al., 2015, Chorowicz, 1990, Wolfenden et al., 2005, Almond, 1986, Beyene & Abdelsalam, 2005) (sections A-A′ of Figure 18), causes a dip of the fault blocks towards the Afar, as evidenced by increasing dips in the trap basalt layers (Wolde, 1989, Sacchi et al., 2006). In the southern part of the western Afar rift margin, however, they are only weakly developed. They are the continuation of the Wonji fault belt with an average width of 12 km (P. Mohr, 1987), the axial rift zone of the main Ethiopian rift. In contrast, the faults on the margins of Yemen and southern Afar are thought to be predominantly synthetic(sections B-B′ of Figure 18)(i.e. dipping towards the basin) (Corti et al., 2015, Morley, C.K., Ngenoh, D.K., Ego, 1999, Beyene & Abdelsalam, 2005).



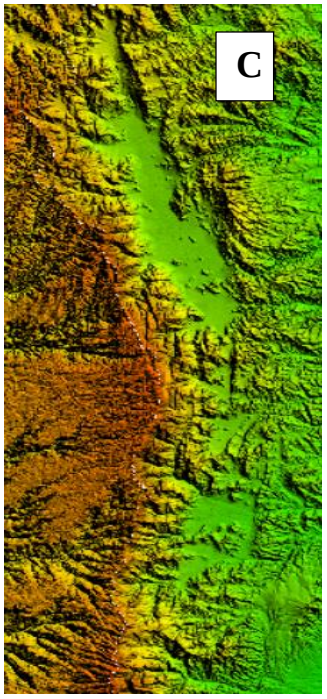


Figure 18: Schematic geological cross sections across the western (A) And southern Afar margins (B) (Beyene & Abdelsalam, 2005), NE-SW & NW-SE Trending marginal Grabens along the rift margin©

The connection zone between the adjacent marginal grabens sometimes called Linking zones exhibits N-S trend is an overlapping areas for at least two sets of fracture/fault systems, from the Main Ethiopian Rift and Red sea rift trending NE-SW and NW-SE respectively. So, transverse structures cut through this area obliquely in NE-SW , NW-SE trend and sometimes orthogonally in an E-W direction (Stab et al., 2016, Zwaan, Corti, Sani, et al., 2020a). These structures connect the marginal grabens to the rift floor and can sometimes be referred to as connection zones or accommodation zones (Fentaw et al., 2024, Kehali et al., 2021). In addition, the NW-SE trending western Afar Rift(Southern Red Sea Rift Trend) changes its direction to NE -SW(Main Ethiopian Rift Trend) (Asfaw, 2000, Tiercelin, 1986). A weakly

defined graben at the border between the plateau and escarpment and north-trending normal faults are features of the transition zone between the two rift arms(P. A. Mohr & Potter, 1976). Furthermore, the synthetic faulting of the major Ethiopian Rift margin is progressively replacing the antithetic faulting common to the western Afar margin(Makris & Ginzburg, 1987). This area is known as the Arcuate Accommodation Zone (AAZ) because it connects the Main Ethiopian Rift to the Southern Red Sea Rift in western Afar. It is concave, opens eastward, and is quite curved (P. A. Mohr, 1971, Tesfaye et al., 2003). The topography of it is higher in the middle and gets lower in the north and south(Beyene & Abdelsalam, 2005). Rather than being "in line" or "en echelon," the interacting rift segments are obliquely oriented, forming two arms of a triple junction(Wolfenden et al., 2005). Transverse structures in W-E, NE-SW, and NW-SE directions were found across the Arcuate Accommodation Zone (AAZ), connecting the marginal grabens to the rift floor. Most of the transverse structures include faults, lineaments, volcanic centers, and dykes and extend mainly from the marginal grabens to the rift floor (Figure 46).

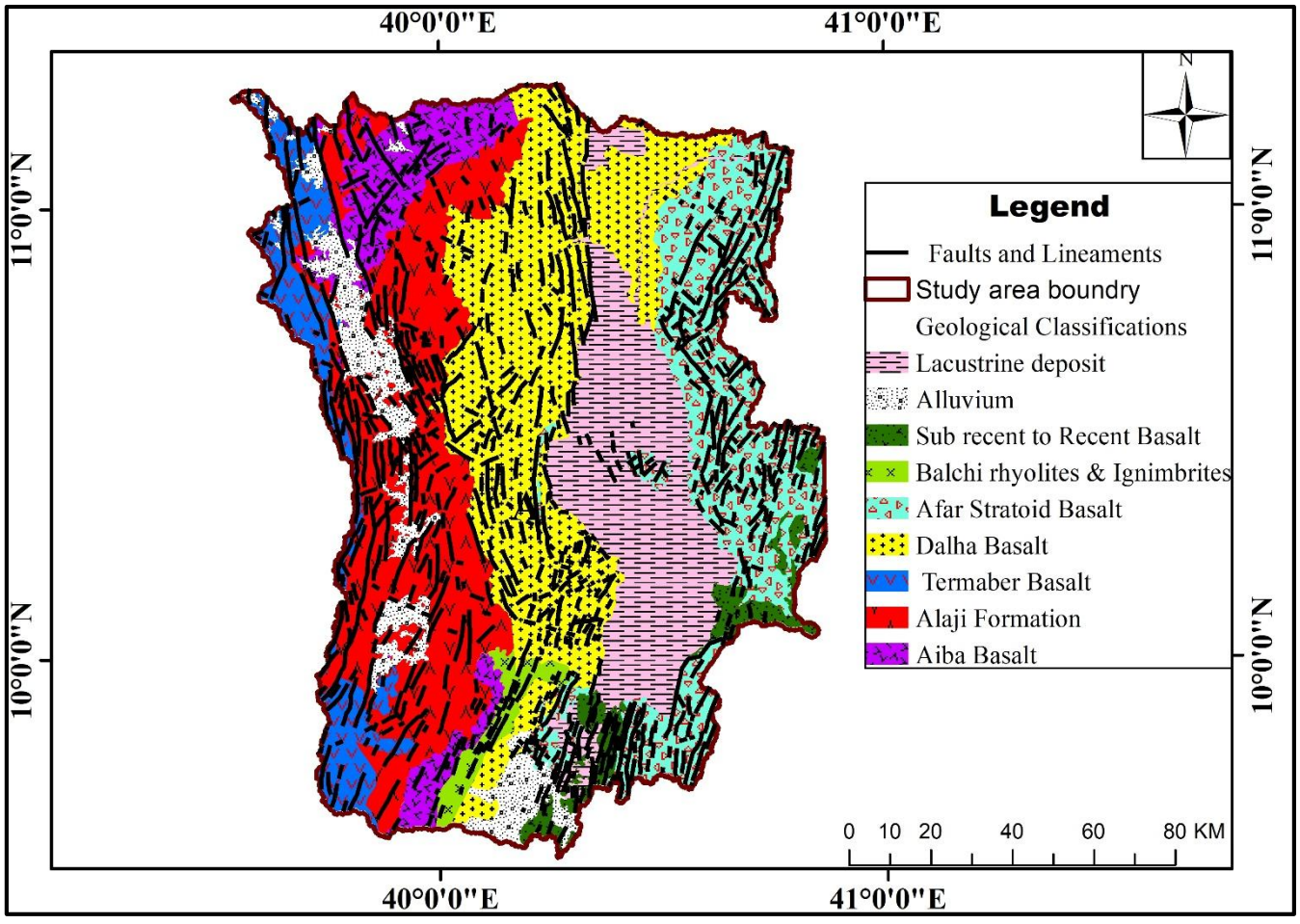


Figure 19: Geological map of the study area

Chapter Three: Evaluation of the source and mechanisms of Groundwater Recharge

3.1General

Evaluation of the source and mechanisms of groundwater recharge is thought to be an essential component for modeling and protecting groundwater systems from overexploitation and contamination (Galliari et al., 2021, Scanlon et al., 2002), especially in arid and semi-arid regions (Huang & Wang, 2017, Cook al., 2017, Galliari et al., 2021). It's critical to do this to accurately describe the aquifer system, flow circumstances, and groundwater resource management(Glynn & Plummer, 2005, Berhanu et al., 2017, Fetter 2001, Scanlon, Healy, and Cook 2002, Kresic, n.d.,2009, Le Mesnil et al. 2020). Based on the previous studies conducted by Ayenew, et al., 2008; Bretzler et al., 2011; Kebede et al., 2005, 2008, Azagegn, 2014; Baye, 2009 in the upper Awash basin of Ethiopia, the source of groundwater recharge for the rift aquifer is groundwater inflow from the adjacent Blue Nile basin. The main controlling mechanisms are due to the presence of the extended lower basalt connecting the two basins and the favorable geological architecture of the transition zone resulting from the intersection of the NE-SW trending Ethiopian Main rift and the E-W trending structure called the Yerer Tulu Volcanic Lineament (YTVL), which can be referred to as a "hydrogeological window". However, there have been no detailed scientific studies to identify the source and mechanisms of groundwater recharge for the deep aquifers in the southern section of the Western Afar rift margin, as well as the associated rift floor, which is located on the eastern side of the Blue Nile basin. Hence, to identify the source and mechanisms of groundwater recharge both for the western Afar rift margin and associated rift floor aquifers, hydrochemical and isotopes analysis were conducted by collecting water samples from the plateau, rift margin and rift floor. Besides, radon measurements were also conducted at the selected sites both in the rift floor and rift margin, for the proper understanding of surface and groundwater interactions. Furthermore, the preferential orientations and yield of high land springs distributed along the escarpments have been hydrogeologically interpreted, lithostratigraphic correlations from the plateau to the rift floor at the selected sections were constructed.

3.2 Results and Discussions

3.2.1 Preferential orientation of highland springs and Source of recharge

Numerous hydrogeological circumstances can lead to the occurrence of springs, which are typically caused by geologic features like faults that produce permeable paths or flow barriers (Curewitz & Karson, 1997, Glen et al., 2013). In the study area, mainly along the escarpments preferentially oriented highland springs nearly in NE-SW, and NW-SE orientations originate at the base of the upper basalt, and the

underlain ignimbrites(Figure 20). Local records and field observations indicate that the discharge of the springs varies from 30-70 lit/sec and flows constantly throughout the year from a very small recharge area. The presence of high discharge springs from small watersheds in a given area indicates that the permeable rocks are continuous and the underlying geometric architecture is conducive(Fetter, 2001, Glynn & Plummer, 2005, Springer et al., 2008, Bense et al., 2013, Caine, and Jonathan et al., 1996, Keegan-Treloar et al., 2022). Hence, considering their preferential orientation along the escarpments, constant flow, and significant yield from the small recharging catchment area, the influx of groundwater from the adjacent plateau area through the transverse structures running NW-SE and NE-SW serves as the primary source of recharge, in addition to local precipitation.

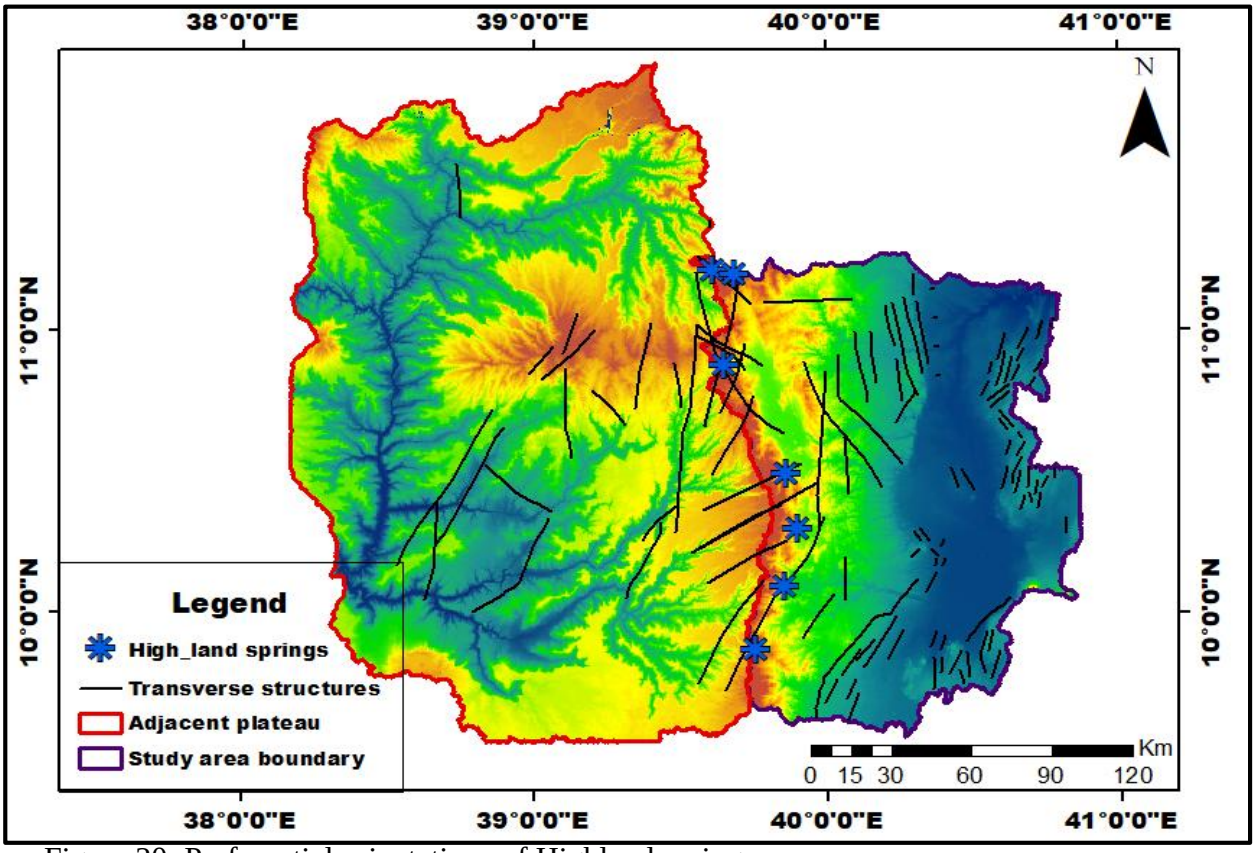


Figure 20: Preferential orientations of Highland springs

3.2.2 Lithostratigraphic Correlations, Source and Mechanisms of Recharge

Lithostratigraphic correlations from the plateau to the rift floor were performed using the drilling logs of the existing wells along the selected groundwater flow directions. Such analysis and interpretation is vital to constructing and conceptualizing the groundwater flow dynamics along the aforementioned areas and finally to establishing a correlation between the water chemistry and the lithology encountered. Prior to conducting lithostratigraphic correlation along the selected groundwater flow directions, a hydrogeologic map of the study area was developed using lithologic logs, well discharge data, aquifer parameters mainly

transmissivity, and structural considerations (Figure 21). Accordingly, the area was reclassified into five aquifer productivity categories: very low to low, low, low to moderate, moderate to high, and high.

Regions with very low to low aquifer productivity are primarily situated within the rift floor, where thick lacustrine deposits (approximately 420 meters) dominate. These areas exhibit transmissivity values between 0.15 and 45.1 m^2/day, indicating limited groundwater potential. Similarly, zones with low aquifer productivity are largely covered by acidic volcanic rocks including Alaji rhyolites, ignimbrites, and tuffs bounding the marginal grabens. Recent rift volcanics, such as the Balchi rhyolites and ignimbrites near the rift floor, further influence the hydrogeology, with transmissivity ranging from 42.64 to 87.44 m^2/day. Areas of low to moderate productivity aquifers are predominantly includes moderately fractured upper basalt and Afar Stratoid Series, exhibiting transmissivity values of 87.43–164.43 m^2/day. In contrast, moderate to high productivity zones are associated with columnar jointed lower basalt and moderately to highly fractured Dalha basalt, where transmissivity ranges from 164.43 to 331.475 m^2/day, and mainly distributed between the rift margin and rift floor of the study area. Moderately productive aquifers are also found on the rift floor, where thin lacustrine deposits overlie the regionally interconnected Dalha Basalt or Afar Stratoid Series. The productivity of these aquifers is highly dependent on the availability of transverse structures that connects to the rift margin and plays a vital role in transferring groundwater from the marginal grabens to the rift floor. The high productive aquifer is found in marginal grabens, characterized by alluvial deposits (sand and gravel) underlain by highly fractured and weathered volcanic rocks like upper basalt, moderately to highly fractured ignimbrites and columnar jointed lower basalt. These areas demonstrate transmissivity values of 331.5–613.4 m^2/day and more, reflecting high productive aquifer.

Lithostratigraphic correlations were established along the inferred groundwater flow directions (SW-NE, W-E, and NW-SE), corresponding to cross-sections A-A′, B-B′, and C-C′ on the hydrogeological map, respectively, as detailed below.

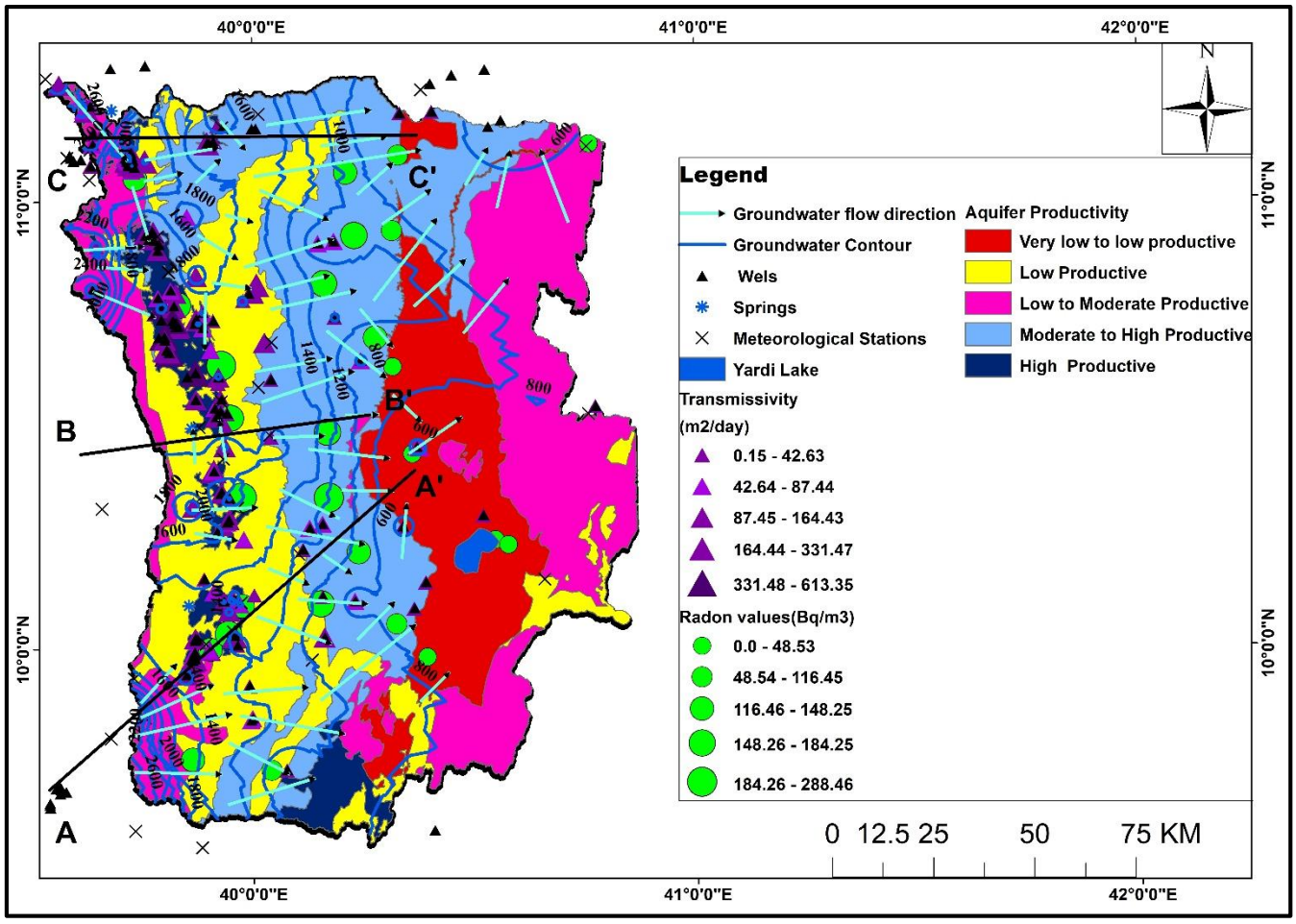
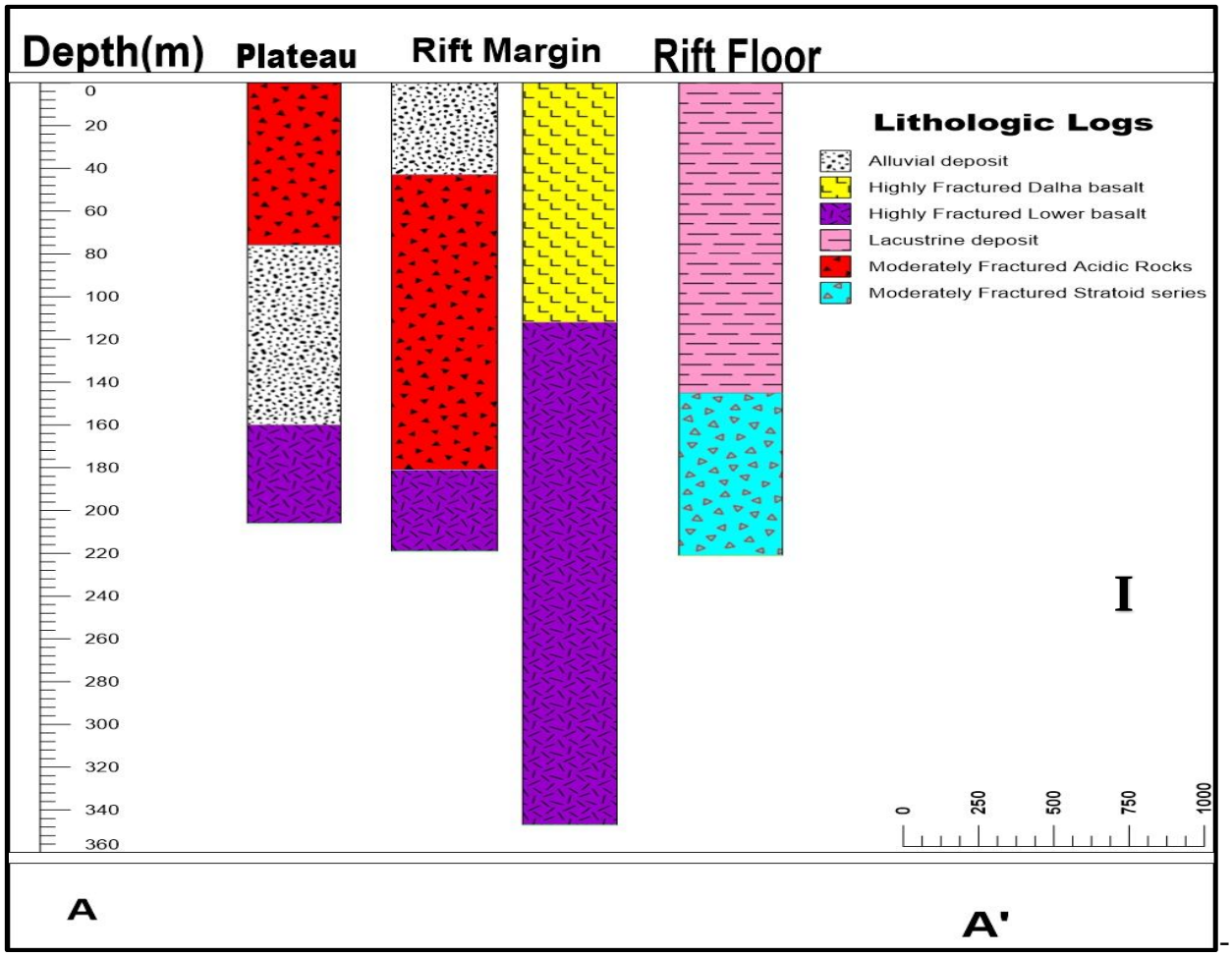


Figure 21: Hydrogeological map of the study area

3.2.2.1 A-A′ Correlation

The lithologic units from top to bottom in the plateau around the Deberebirhan areas are fractured and weathered ignimbrites, Sediments of sand and gravel, and columnar jointed lower basalt, ranging in thickness from 76 m to 206 m, 80m-100m, and 100 m, respectively (Figure 22). Although the annual rainfall in the plateau is very high, the availability of groundwater is highly controlled by NE-SW trending structures. Accordingly, most of the wells drilled along the structures have a yield of 30 l/s or more. The wells on the western Afar rift margin, especially in the marginal grabens, from top to bottom consist of alluvial deposits (50-100 m), fractured and weathered ignimbrites and rhyolites, and columnar jointed basalt respectively, and most of the boreholes have a yield of 30 to 40 l/s. The main source and mechanism for groundwater recharge is the inflow of groundwater from the adjacent plateau to the rift margin, due to the presence of the continuous and highly fractured columnar jointed lower basalt and the transverse faults with NE-SW orientation like Debresina fault connecting the two adjacent basins. Besides, the infiltration of precipitation through the overlying alluvial deposits and the local groundwater inflow from the surrounding volcanic mountains are also other sources of groundwater recharge. Between the Rift margin and Rift floor along the way from Shewa Robit to Semurobi wereda of Afar region,

mainly at the Rasa area the main lithologic units from top to bottom consisting of fractured Dalha basalt underlain by columnar-jointed lower basalt (Figure 22), with intercalations of intervolcanic sediments deposited during the eruptive and depositional gaps. Most of the drilled wells in this area such as BH#25 have a yield of 20 to 25 liters per second with insignificant drawdowns. The source and mechanisms of groundwater recharge here are due to the presence of extended columnar-jointed lower basalts and transverse structures (NE-SW, and W-E) connecting the plateau and rift margin and the marginal grabens to the rift floor respectively. In the rift floor, the main lithologic units are lacustrine deposits of varying thickness underlain by stratoidal basalt. The productivity of the wells in the rift floor depends to a large extent on the thickness of the overlying lacustrine deposits and their relative position to the cross structures. Accordingly, the yield of the wells drilled in the middle of the rift floor, where the lacustrine deposit is thicker (408 m), is very low or dry. When the thickness of the lacustrine deposit is very low and underlain by regionally inter connected stratoid basalt through the transverse structures, the wells drilled to 220 m depth such as Amma BH #1 and BH#2 yield 20 l/s and more with very low areal annual precipitation. This shows that there is a preferential groundwater flow from the western margin to the rift floor through the transverse structures.



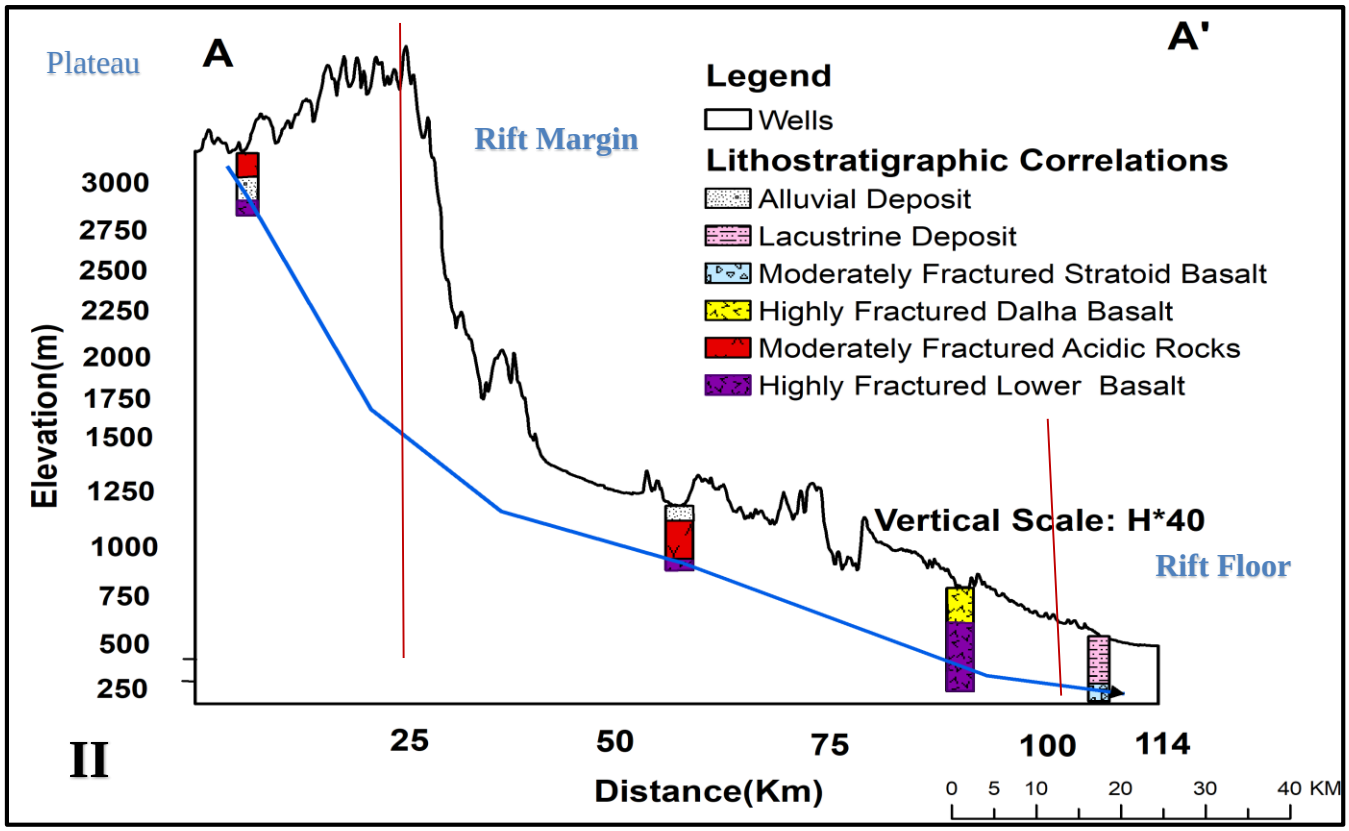


Figure 22: A-A′ (**I**: Lithostratigraphy, **II**: Correlation along the Plateau-Rift Margin-Rift floor)

3.2.2.2 B-B′ Correlation

In the plateau area, most of the boreholes along this section are shallow in depth (Figure 23). The main aquifer is the upper basalt with a very low discharge, ranging between 2-3 l/s, and the main source of groundwater recharge is local precipitation. In the marginal grabens of the rift margin around the Ataye area, well yields vary between 40-50 l/s, and the main lithologic units from top to bottom are alluvial deposits, fractured and weathered upper basalt, followed by ignimbrites and rhyolites. Here, the source and mechanism of groundwater recharge, in addition to local precipitation, is the subsurface groundwater inflow from the adjacent plateau to the rift margin. This is due to the presence of extensive and continuous trap series formations and NW-SE and NE-SW trending cross-structures connecting the two adjacent basins. At the rift margin near the rift floor around the Dalifage area, the main lithologic units consist of Dalha basalt underlain by columnar-jointed lower basalt. The wells yield 20-25 liters/second with insignificant draw down. Thus, the source and mechanism of groundwater recharge is the inflow of groundwater from the marginal grabens due to the presence of the extensive columnar jointed lower basalt and the NE-SW and W-E trending transverse structure. In the rift floor, the main lithologic units are the Dalha basalt, which is overlain by the lacustrine deposits as the trap series becomes discontinuous.

Thus, the predominant source and mechanism of recharge is groundwater inflow from the western margin due to the transverse faults and lineaments trending NE-SW and W-E.

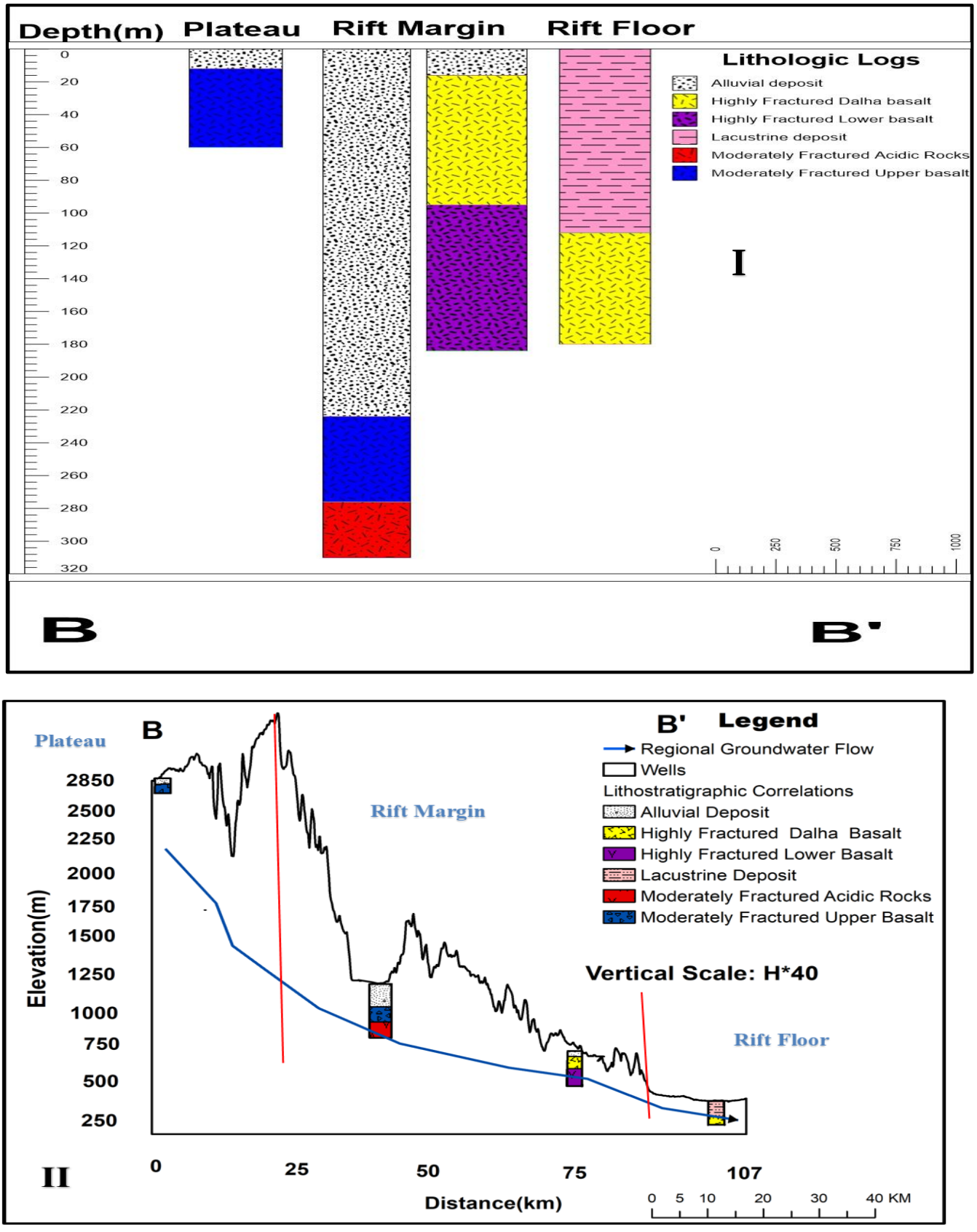
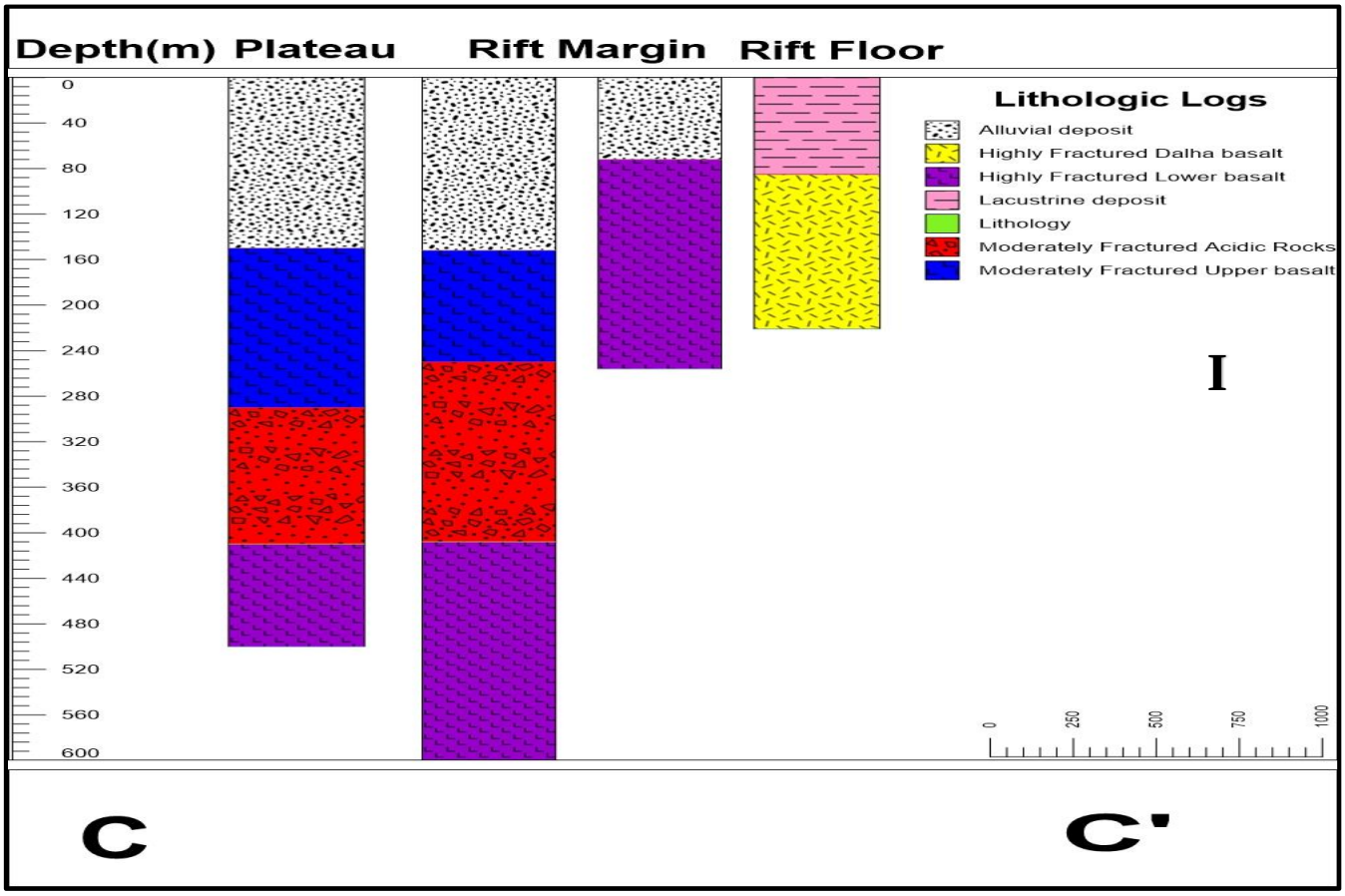


Figure 23: B-B′ (**I**: Lithostratigraphy, **II**: Correlation along the Plateau-Rift Margin-Rift floor)

3.2.2.3 C-C′ Correlation

The following litho-hydrostratigraphic correlations were established from the existing boreholes in the plateau, rift margin, and rift floor (Figure 24). In the center of the Gerado catchment(plateau area) which is found in the Blue Nile basin, the lithologic units from top to bottom (younger to older) are alluvial deposits consisting of gravel, sand, and silt (~150m), highly fractured and weathered upper basalt (~140m), ignimbrites and rhyolites (~120m), and highly jointed columnar basalt (~90). Most of the wells in this catchment have a yield greater than 50/sec and are artesian in nature. The source and mechanism of groundwater recharge at this location is due to infiltration and percolation of precipitation through the overlying alluvial deposits and inflow of groundwater from the surrounding volcanic mountains through fractures. Another likely source and mechanism for recharge is intermediate to the regional flow of groundwater through faults and lineaments trending N-S, NW-SE, and NE-SW. In the adjacent western rift margin, especially in the center of the Borkena graben, the lithological formations from top to bottom are alluvial deposits, fractured upper basalt, and acid rock underlain by columnar jointed basalt with a thickness of 150 m, 126 m, 192 m, and 134 m, respectively, and has a yield of more than 50 l/s with artesian nature. In the shallow wells (≤150m), however, the main lithological unit consists of alluvium and the yield of the well is no more than 30 l/s. Based on the yield of these two groundwater sources (i.e. shallow and deep wells), we can see that there are differences in the source and mechanism of groundwater recharge. In the case of shallow wells, the source of groundwater recharge is the infiltration and percolation of precipitation through the overlying alluvial deposits and the inflow of groundwater from the surrounding volcanic mountains through fractures. In the deep wells, on the other hand, in addition to the above-mentioned recharge sources and mechanisms, the regional groundwater flow from the adjacent plateau due to the presence of the continuous trap series, especially the columnar-jointed basalt from the plateau to the rift margin, and the transverse faults running in NW-SE and NE-SW directions like Dessie-Borkena –Bati fault connecting the two adjacent basins, are the decisive factors. East of the Borkena catchment, the upper basalt is getting diminished and the underlying acidic formation is exposed around elevated areas such as the Mitikolo Ridge (Figure 10A), which is also getting to very small exposure towards the east, i.e. towards Degan and Bati areas. In the Degan area the well drilled until 250m, the lithologic log is the columnar jointed lower basalt and have a maximum yield of 30 l/s. Nearby to the east of the town of Bati, highly fractured and eastward-dipping Dalha basalt was exposed, underlain by highly weathered Ashangie basalt (Figure 13). The wells tapping groundwater from these formations have a yield of not more than 15-20 l/s with very low annual rainfall. The source and mechanisms of groundwater recharge in these areas are therefore due to the flow of groundwater from the marginal grabens through the continuous and extensive traps series and cross-structures running NE-SW, NW-SE, and W-E connecting the rift floor to the rift margin. Along this groundwater flow direction,

the main lithologic units of wells drilled in the rift floor from top to bottom are lacustrine deposits and Dalha basalts respectively, having a maximum yield of 20 liters/sec. Thus, the predominant source and mechanism of recharge is groundwater inflow from the western margin due to the transverse faults and lineaments trending NE-SW, NW-SE, and W-E directions.



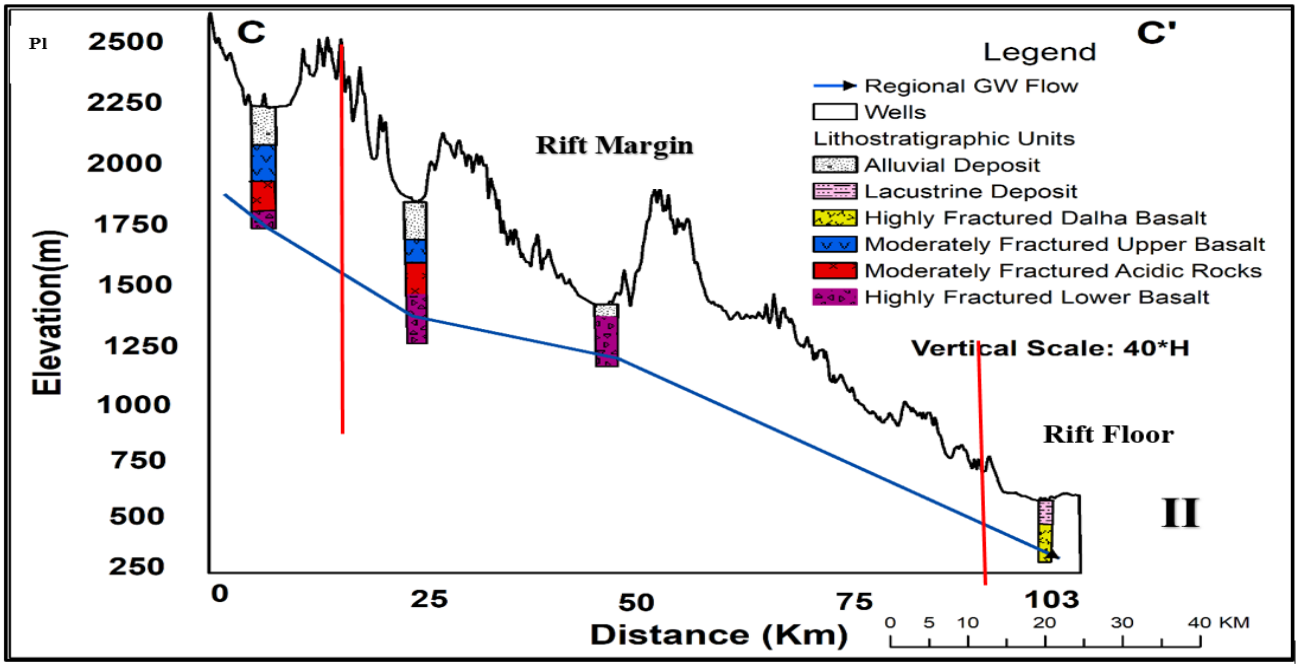


Figure 24: C-C′ (**I**: Lithostratigraphy, **II**: Correlation along the Plateau-Rift Margin-Rift floor)

3.2.3 Hydrochemical and Environmental Isotope analysis

3.2.3.1 Hydrochemical Interpretations

3.2.3.1.1 Data Quality Control

The chemical behavior of groundwater would continue to change over time from the source of precipitation. This modification aids in describing the dynamics of groundwater in the aquifer system(Ravikumar et al., 2015, Ganvir, 2023). Hydrochemical analysis can be used to understand the key processes that have occurred during the movement of water through aquifers. Besides, to obtain information about the source and rate of recharge, the direction of groundwater movement, the nature of the aquifer through which it has circulated, and anthropogenic activities influencing it, hydrochemical analysis is an important parameter(Clark & Fritz, 2013, Glynn & Plummer, 2005). Generally, it is vital for examining and comprehending the chemical interactions and geochemical evolution of groundwater in various physiographies(Ahmed et al., 2019, Vázquez-Suñé et al., 2010). However, before conducting any hydrochemical interpretations using a certain hydrochemical date, quality control should be carried out first. For this purpose, an integrated approach called Ionic balancing which is determined by Equation 1 was appied (Ako et al., 2012, Pradhan et al., 2022). The principle is that the major cations and anions in any given water sample should have about equal sums in mill equivalents (Volcker et al., 2005, Fritz et al.,1994). A positive CBE indicates that the water sample has a higher concentration of cations than anions, and a negative CBE indicates that anions are more abundant(McCleskey et al., 2012, Mueller, 2012). Acceptable water analyses should have a CBE value of ≤5 %(Kopáček et al., 2000, Huizenga, 2011)**.** Accordingly, based on the following water quality data suitability analysis methods, all the analyzed primary water samples of this study have a CBE value of <5 %(Figure 25). Together with the primary data, secondary data having a CBE value of ≤5% were used for hydrochemical analysis and interpretations (Appendices 2).

Equation 1:$$\mathbf{CBE} = \left(\frac{(\sum \boldsymbol{Cations} - \sum \boldsymbol{Anions})}{(\sum \boldsymbol{Cations} + \sum \boldsymbol{Anions})}\right) * \mathbf{100}\%$$

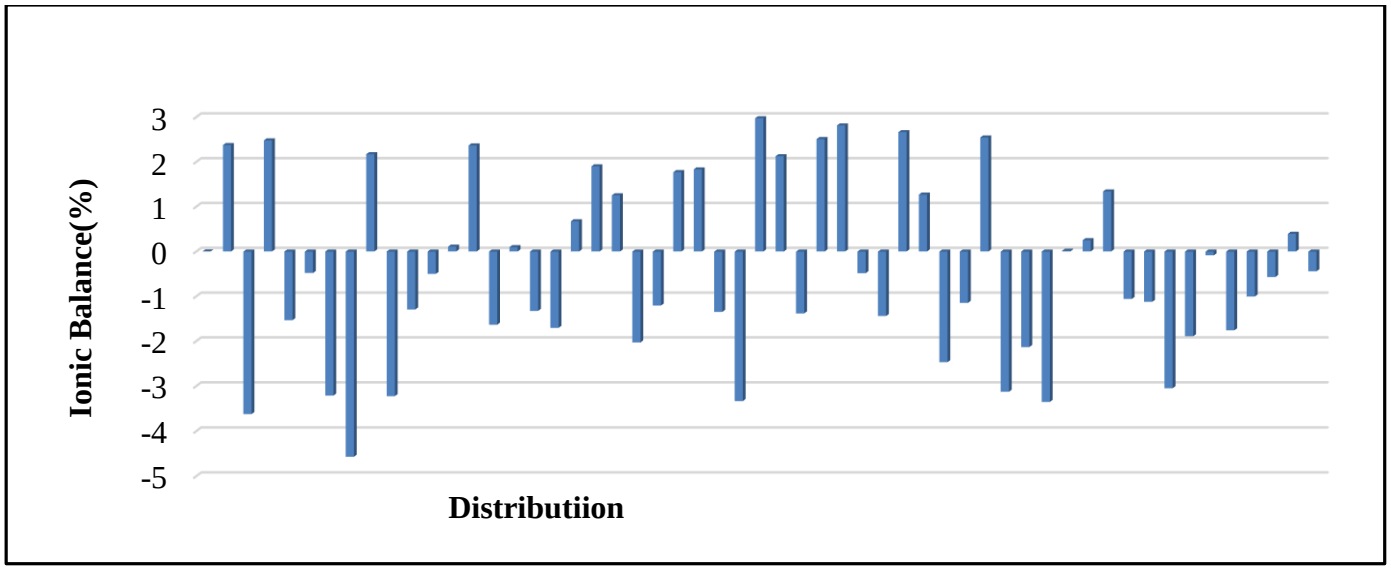


Figure 25: Ionic balance error distribution in the hydrochemical data

3.2.3.1.2 Distribution of Water Types

An important task in groundwater research is the compilation and presentation of chemical data in a convenient manner for visual inspection. For this purpose several commonly used graphical methods are available((Fisher & Mullican, 1997). In this study to identify the primary ion composition, trends of the water systems and to identify the water type that each sample belongs to along the particular physiography (plateau, rift margin, and rift floor), the results of the chemical analysis data were plotted using AquaChem 14 and Grapher Golden software utilizing Piper and Durov diagrams. Finally, the interpreted hydrochemical result has been correlated with the Insitu water quality parameters including Ph, TDS, and EC, Isotope result, and the lithostratigraphy correlations to get a comprehensive idea of the overall recharge condition and lead to knowing the groundwater flow dynamics of the western rift margin and associated rift floor aquifers. Based on the hydrochemical analysis and interpretations of the primary and secondary water samples from all the physiographies, the water types can be categorized into 4(four) major groups as presented in the Piper diagram (Table 2 and Figure 26).

Table 2: Major water type distribution along the plateau –Rift Margin (RM) –Rift floor (RF)

Major Water types	**Physiography**			**Water type category**
	Plateau	**RM**	**RF**	
Ca-HCO_3 and Ca-(Mg)-HCO_3	*	*	*	I
Ca-Na-HCO_3 and Ca-(Mg)-Na-HCO_3	*	*		Mixed water type (V and VI)
Na-Ca-HCO_3 and Na-HCO_3	*	*	*	III
Na-HCO_3-SO_4 and Na-HCO_3-Cl		*	*	IV

3.2.3.1.2.1 Ca-(Mg)-HCO3

These water types were found in most of the plateau samples, and in the boreholes having a depth of ≤ 150 m, primarily at the start of the Borkena river of the Awash basin in the northern part of the study area. The main water bearing unit both in the plateau and rift margin is highly fractured and weathered basalt, grouped under upper(Tarmaber basalt) with minor intercalation of paleo soils. These water types also found in the highland springs that emerge from the bottom of the upper basalt along the escarpments. Besides, in the rift floor mainly from shallow well sources similar water types were also available. The TDS and EC values in the plateau area are between 80 and 170mg/l and between 175µs/cm and 341µs/cm respectively. At the rift margin, the TDS and EC values at the highland springs vary from 71 to 172mg/l and the EC value from 140µs/cm and 345µs/cm respectively, and the boreholes have TDS and EC values from 150 to 196mg/l and from 300µs/cm to 395µs/cm respectively. Based on the groundwater chemical evolution models developed by Chebotarev, 1955, these water groups reflect recently recharged groundwater and/or water in the early phases of geochemical evolution that haven't undergone substantial interactions with rocks(Ako et al., 2012). When water type, lithostratigraphy, TDS, and EC values are combined, the main source of groundwater recharge on the plateau and at the rift margin is precipitation and local to intermediate groundwater inflow from the surrounding volcanic mountains. However, the shallow sources in the rift floor have a TDS value of much higher and can reach 1000mg/l, due to the high evaporation rate. Hence, local sources mainly rivers, flash floods, and streams are the main sources of groundwater recharge.

3.2.3.1.2.2 Ca-Na-HCO3 and Ca-(Mg)-Na-HCO3

These water groups are mixed water types dominantly found in the rift margin, especially in the marginal grabens and partly on the plateau near the watershed divide between the two adjacent basins. The available boreholes indicate that the lithologic units from top to bottom, both on the plateau and in the rift margin area are alluvial deposits underlain by fractured and weathered upper basalt. Sometimes the columnar jointed basalt, which is overlain by alluvial deposits at the rift margin, shows a similar water type. In the plateau area, the TDS value is between 121 and 250, and the EC value is between 256µs/cm and 427µs/cm. At the rift margin, the TDS value is between 243mg/l and 262mg/l and the EC value is between 438µs/cm and 524 µs/cm, depending on the thickness of the overlying deposit and the location relative to the plateau and the rift margin, i.e. the boreholes with a thin alluvial deposit near the rift escarpment have relatively lower TDS and EC values (example: BH#22, i.e. Asfachew kebele well) than the boreholes with a thick alluvial deposit (150-200m) in the middle of the rift margin. When water type, TDS and EC values, and lithology are correlated, the main source of groundwater recharge in the plateau area is precipitation and local to intermediate groundwater inflow. Infiltration of precipitation through the coarser alluvial deposits, the inflow of groundwater from the surrounding fractured volcanic rocks,

and the adjacent basin are the dominant sources of recharge for the rift margin, which leads to mixed types of water.

3.2.3.1.2.3 Na-Ca-HCO3 and Na-HCO3

These water types are dominantly found in the rift margin and rift floor and partly in the plateau area. In the plateau area, these water types are associated with deep wells (500 m) where alluvium, fractured ignimbrite, and the columnar jointed lower basalt are the main lithologic units. The TDS and EC values range from 185mg/l to 252mg/l and 370 µs/cm to 420µs/cm respectively. At the rift margin, particularly in the marginal grabens, a similar lithostratigraphy was found as on the plateau, but the TDS and EC values show an incremental order, ranging from 286mg/l to 355mg/l /l and EC from 572 µs/cm to 708µs/cm. In the rift floor, the lithologic units are lacustrine deposits underlain by fractured and weathered stratoid series. TDS and EC values range from 342mg/l to 580mg/l and from 680µs/cm to 1180µs/cm. The Na^+ dominance throughout the entire physiography is due to the presence of clay zones in most borehole logs which leads to the replacement of Ca^{2+} by Na^+ (Wilopo et al., 2019), and also the weathering of acidic rocks mainly ignimbrite and rhyolite with increasing depth and along the groundwater flow direction. Such processes could also have a bigger impact in increasing the TDS and EC values from the plateau to the rift floor. Correlating lithology, water type, TDS, and EC values, the main source of groundwater recharge is the regional groundwater flow.

3.2.3.1.2.4 Na-HCO3-SO4 and Na-HCO3-Cl

These water types are found in the rift margin near the rift floor, and rift floor areas. In the case of the rift margin, the lithological units are lacustrine deposits underlain by fractured and weathered Dalha basalt and acidic rocks like Mabla rhyolites. In the rift floor, the sources are thermal waters having a maximum temperature of 55^{o}c and located along the NE-SW trending Wenji fault belt and the lithology is lacustrine deposit underlained by Afar stratoid series. The probable reason for the subordination of the sulfate and chloride to the bicarbonate ion is due to the presence of the NE-SW trending Wonji fault belt along the rift floor which might increase their concentration from the lower mantle in addition to irrigation activities. TDS values in the rift margin ranged from 376 to 404 and in the rift floor from 618 mg/l to 895 mg/l. A probable cause for the observed increase in TDS is the interaction between water and rock along the flow path from the plateau to the rift floor. In addition, the groundwater temperature in the deep aquifers of the rift floor such as BH#15 and S#2 differs from the local air temperature by more than 10°C, indicating that these waters are connected to the deep regional groundwater circulation. Thus, correlating lithology, water type, TDS, EC, and temperature values, and the main source of groundwater recharge in the rift floor is the deep regional groundwater flow.

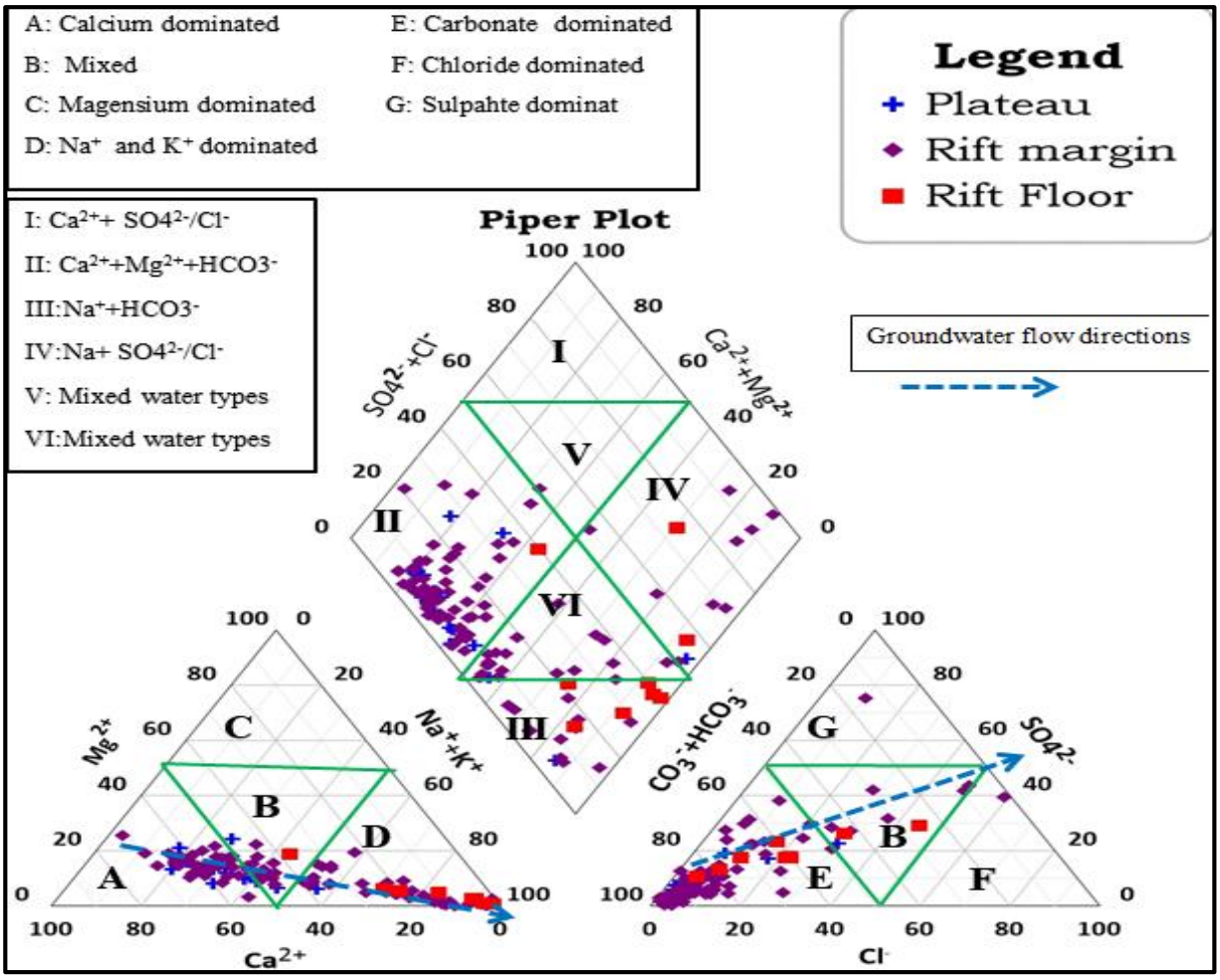


Figure 26: Piper plot of water samples

In addition to the piper diagram, the samples were also plotted using Durov diagrams. This is because, Durov diagrams can show ion exchange, reverse ion exchange, and mixing of various types of water as well as other hydrochemical processes that take place in groundwater systems(Sayyed et al., 2013, Ahmad & Mazhar, 2020). It also characterizes the hydrochemistry of groundwater based on pH and TDS values (Hegeu & Kshetrimayum, 2019, Panigrahi & Das, 2022). As can be seen in Figure 27, most of the samples from the plateau and rift escarpments, especially the highland springs and the boreholes drilled at the beginning of the Borkena river of the Awash basin, and shallow rift floor samples are distributed in field A, in which Ca^{2+} is the dominant cation, and the water type is Ca-(Mg)-HCO3, which is shown in field 2. The samples from the plateau and the rift margin fall on field B, where calcium is the predominant cation, followed by sodium, and the water type is Ca-(Mg)-Na-HCO3 which can be considered as mixed water type and is shown in field 3. The samples from the deep wells of the plateau, rift margin and rift floor are Na^{+} dominated and are distributed in the field C. From the Piper diagram, the water type is Na-Ca-HCO3 and Na- HCO3 and is plotted in region 4. The Durov diagram generally shows that Ca^{2+} is the predominant cation in the plateau aquifers, but gradually decreases towards the rift

floor, while the concentration of Na^+ increases along the depth and groundwater flow direction(field 2 to 4) (Plateau-Rift margin-Rift floor) with increasing TDS values . This is due to the existence of a normal cation exchange between Na^+ from the aquifer material and Mg^{2+} or Ca^{2+} in the groundwater (region 2 to region 4)(Figure 27)) as well as the weathering of acidic rocks at depth and along the groundwater flow direction. The observed HCO_3^- concentrations indicate an increasing trend from the plateau towards the rift floor with respect to the anions, which is consistent with the rise in Na^+ and K^+. In addition, like TDS, pH shows a positive trend with depth and along the groundwater flow direction (i.e. towards the rift floor), from acidic (pH 6.88) in the plateau and rift margin to strongly alkaline (pH 9) in the deep groundwater of the rift floor, because the water has had more time to interact with minerals and buffer the acidity. Longer residence times in the aquifer generally allow more extensive mineral-water interactions, which increases pH and bicarbonate levels along the groundwater flow direction (Plateau-Rift margin-Rift floor).

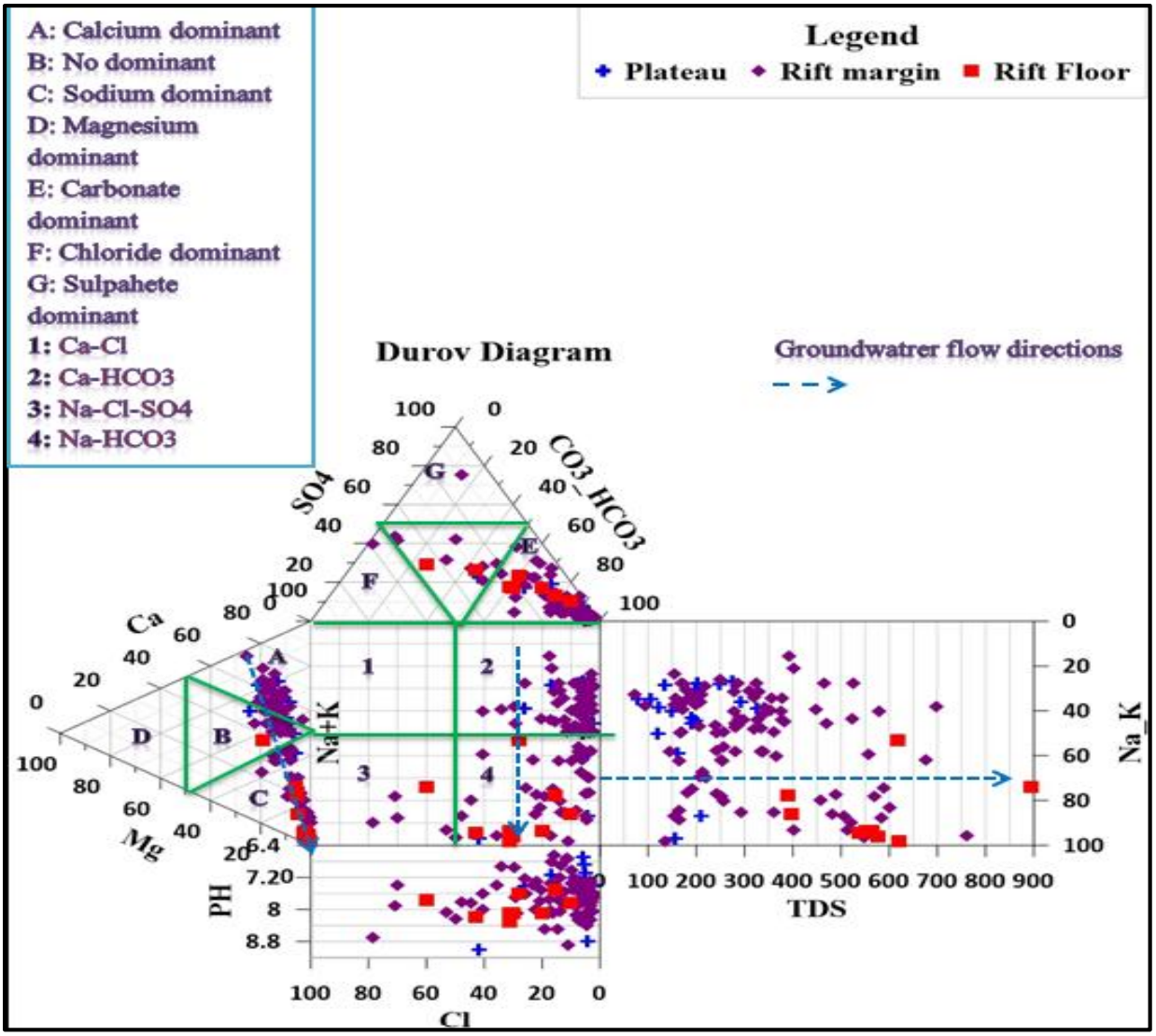


Figure 27: Durov diagram of water samples

Table 3: Summary of the relation between water type, TDS, & Lithology along all physiography

Water type	Physiography	TDS (mg/l)	Lithology/Remark
Ca-HCO3 &Ca-Mg-HCO3	Plateau	80 to 170	Highly weathered and fractured basalt intercalated with unconsolidated formations mainly sand at varying depths.
	Rift margin	71 to172, 150 to 196	A lower TDS value is found with highland springs emanating from the foot of the upper basalt. While, in the case of the boreholes, the main lithological unit is highly fractured & weathered upper basalt with minor intercalations of palaeosols dominantly clay and mainly found at the beginning of the Borkena river of the Awash river basin in the northern part.
	Rift floor	285 to 326	Shallow wells getting recharged from local sources.
Ca-Na-HCO3 & Ca-Mg-Na-HCO3	Plateau	121 to 250	Alluvial deposits, and fractured and weathered upper basalt
	Rift margin	243 to 262	Alluvial deposits are underlain by fractured and weathered upper basalt.
Na-Ca-HCO3 & Na-HCO3	Plateau	185 to 252	Alluvial deposit, underlain by highly fractured and weathered ignimbrite and rhyolite and the lower columnar basalt
	Rift margin	286 to 355	Alluvial deposit underlain by highly fractured and weathered ignimbrite followed by the lower columnar basalt
	Rift floor	342 to 580	Lacustrine deposits are underlain by fractured and weathered Stratoid basalt.
Na-HCO3-SO4 & Na-HCO3-Cl	Rift margin	376 to 404	Lacustrine deposit is underlain by fractured and weathered Dalha basalt and Mabla rhyolites.
	Rift floor	618 to 895	Lacustrine deposit is underlain by the Afar stratoid series.

3.2.3.1.3 Geochemical Process

To identify the geochemical processes that control and affect the chemistry of groundwater in a certain area, the Gibbs plot is a commonly used method(Marandi & Shand, 2018, Kumar et al., 2022). GIBBS suggested a graphical diagram to illustrate the three major mechanisms called evaporation, precipitation, and rock weathering displayed in the upper right corner, the lower right corner, and the middle area of the Gibbs diagram respectively that regulated the chemistry of groundwater(Varade et al., 2018, Nagaraju et al., 2016). To identify these controlling mechanisms in a certain water sample, GIBBS proposed the determination of **GIBBS Ratio I** for cations and **GIBBS Ratio II** for anions computed using Equation 2 and Equation 3, respectively(Marandi & Shand, 2018b, Nandimandalam, 2012). Finally, the computed results were plotted against TDS (in mg/ l) values. Accordingly, as shown in Figure 28 and Figure 29, all the groundwater samples from the rift floor are far away from the region indicated by the precipitation zone (TDS<100mg/l), proving that the influence of precipitation on the concentration of groundwater

ions is not the main controlling factor, which is highly consistent with the Afar rift floor having low annual rainfall. Hence, the rift floor's groundwater chemistry mainly the deep groundwater sources is resulted from water rock interactions (100≤TDS≤1000mg/l) (Figure 28 and Figure29) which leads to have highly evolved water type(Na-HCO3), supporting the idea that the groundwater is a regional rather than a precipitation source. However, as displayed in GIBBS diagrams both in the plateau and rift margin areas, precipitation (TDS≤100) as well as rock water interaction (100≤TDS≤1000mg/l) influences the chemistry of the groundwater. As a result, the majority of the plateau water samples, and rift margin samples from highland springs and boreholes found near the rift escarpment are Ca-(Mg)-HCO3, resulting from precipitation influence and didn't undergo much water-rock interactions. There are also mixed water types (Ca-Na-HCO3) in the plateau and rift margin, where precipitation and rock water interaction are the major controlling factors for groundwater chemistry. Besides, Na-dominated groundwater is found in the deep wells in both physiographies, reveals acidic rock water interactions is the prominent process. Hence, correlating with the piper diagram, the deep wells from the plateau, rift margin, and rift floor areas, the dominant water type is Na-dominated, which results from rock water interaction influence, leads the conclusion that the source of recharge is regional. Generally, the groundwater chemistry in the area is highly controlled by rock weathering dominance mainly for deep wells in all the physiography, and the influence of precipitation is found in the plateau and rift margin for shallow wells and highland springs.

Equation 2:**GIBBS Ratio I** $= (\frac{Na+}{Na+ + Ca2+})$

Equation 3: **GIBBS Ratio II** $= (\frac{(Cl-)}{(Cl- + HCO3-)})$

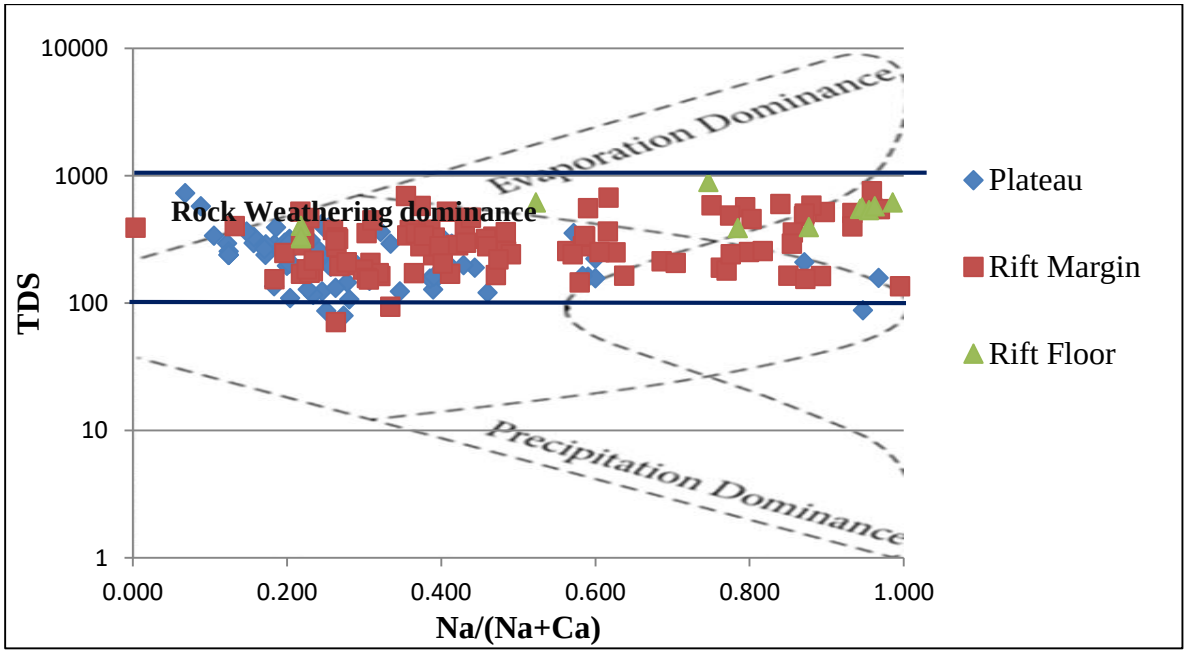


Figure 28: Gibbs Ratio I: (Na+/Na+Ca2+) VS TDS

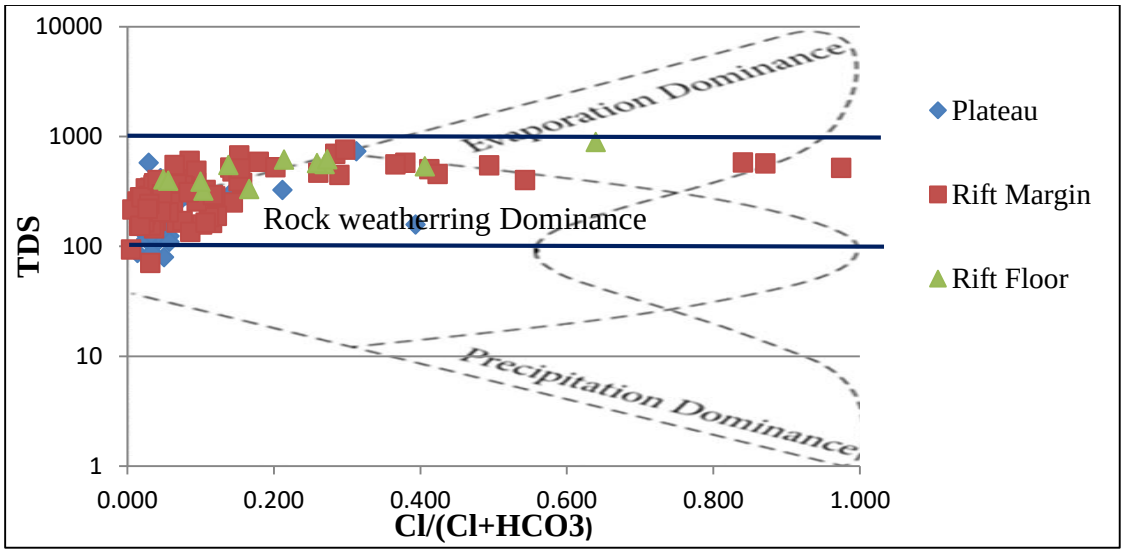


Figure 29: Gibbs Ratio II: ($Cl^-/Cl^-+HCO_3^-$) VS TDS

3.2.3.1.4 Weathering Process

As can be seen from the GIBBS diagram, the main process which controls the concentration of chemicals in the groundwater mainly for the deep aquifers is rock water interactions due to prolonged residence time. So, to identify the type of rock weathering that affects the major ion concentration during groundwater flow is determined by examining the relationship between major cations and anions(Cloutier et al., 2008, Okiongbo & Douglas, 2015, Adeyeye et al., 2021). For this purpose, an end member diagram (Gaillardet et al., 1999) was used with a bivariate plot containing the ratio of ($HCO3^-/Na^+$) versus (Ca^{2+}/Na^+) and (Ca^{2+}/Na^+) versus (Mg^{2+}/Na^+) (all data in meq/l). The result shows that the most important weathering process that affects groundwater chemistry throughout the physiography is silicate mineral weathering (Figure 30 and Figure 31). As a result due to the weathering of silicate minerals like feldspar, pyroxene, plagioclase and olivine there will be an increase of cations including Ca^{2+}, Mg^{2+}, Na^+, K^+, and silica (H_4SiO_4) to be released into the groundwater. For example in the plateau (recharge) area, since the main lithological units is basalt, dominantly composed of Ca rich feldspars $CaAl_2Si_2O_8$, pyroxene, and olivine(Kieffer et al., 2004). Hence, the weathering of these minerals release Ca^{2+}, Mg^{2+} and silica to the groundwater according to the following reactions, which leads the groundwater to be Ca dominated. Besides, there will be a formation of secondary minerals like clay, which can absorb or release ions, further influencing groundwater chemistry.

$CaAl_2Si_2O_8$(feldspar) $+2CO_2+3H_2O \rightarrow Ca^{2+}+2HCO_3^-+Al_2Si_2O_5(OH)_4$(clay) $+H_4SiO_4$(Silica).

However, with increasing depth and along groundwater flow directions due to the presence of acidic rocks including ignimbrite and rhyolite, the weathering of silicate minerals like Albite ($NaAlSi_3O_8$) from the felsic rocks will increase of Na^+ and silica to the groundwater.

$2NaAlSi_3O_8+2H_2O+2H^+ \rightarrow 2Na^++Al_2Si_2O_5(OH)_4+4SiO_2$

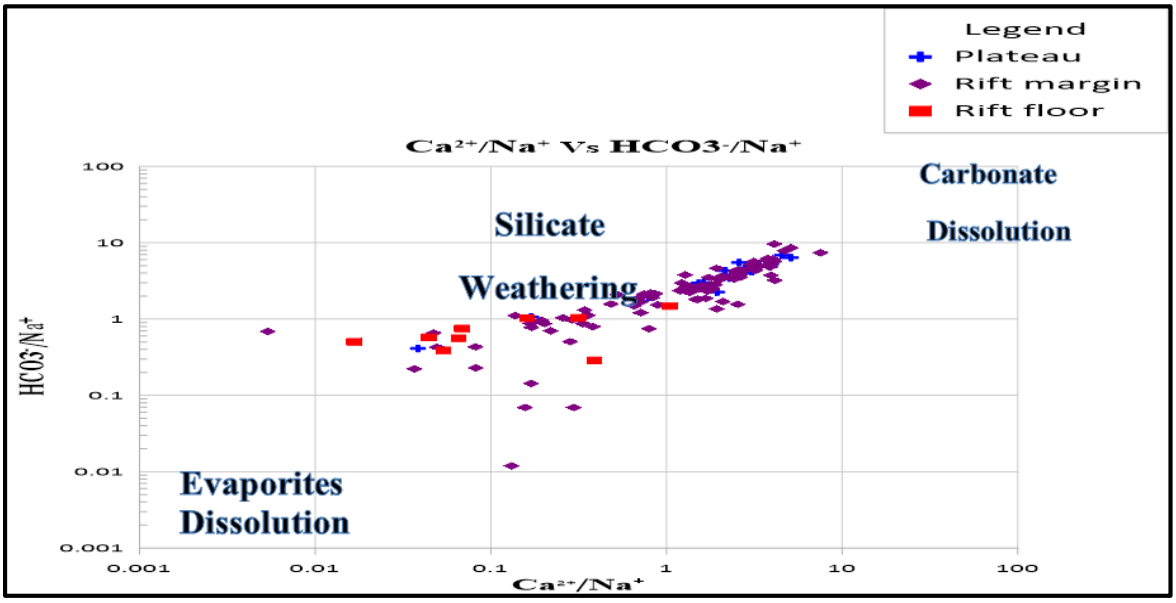


Figure 30: Plot of Ca^{2+}/Na^{+} vs HCO_3^{-}/Na^{+}

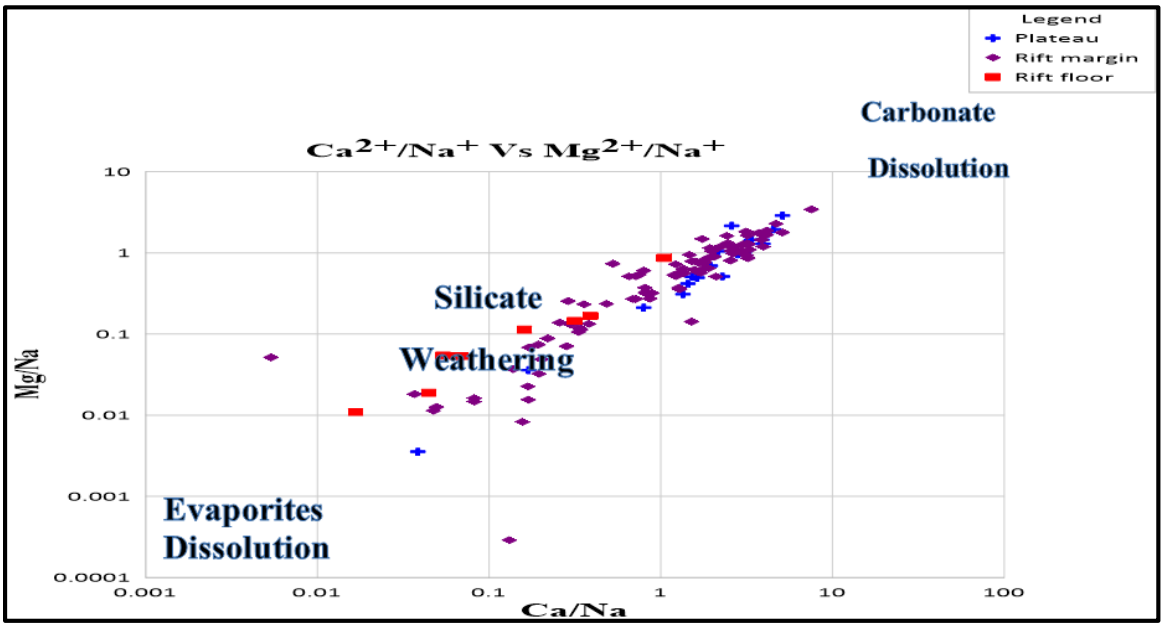


Figure 31: Ca^{2+}/Na^{+} vs Mg^{2+}/Na^{+}

3.2.3.1.5 Ion Exchange Process

In addition to the rock weathering process, ion exchange is also an important process that can control the ion concentration in groundwater, and has a big impact on the chemistry of groundwater(Onyekuru, 2010, Martínez & Bocanegra, 2002). The process of cation exchange occurs when positively charged ions or cations in groundwater are replaced with cations on the surface of organic or mineral particles in the aquifer matrix(Onyekuru, 2010, Martínez & Bocanegra, 2002). For this purpose, Schoeller has proposed the Chloro-Alkali Index (CAI) (meq/l), which is calculated using Equation 4 and indicates the exchange

of Na^+ and/or K^+ ions with Ca^{2+} and/or Mg^{2+} ions between the groundwater and its host rock(Kaur et al., 2019, Ishaku et al., 2011). **Equation 4: CAI 1** $= \boldsymbol{Cl} - (\frac{\boldsymbol{Na+K}}{\boldsymbol{Cl}})$

Accordingly, when there is a reverse ion exchange between the groundwater and aquifer material, the Chloro-alkali indices (CAI) are positive. As a result, the concentration of Mg^{2+} and Ca^{2+} will increase in the groundwater ($2Na^+ + Ca_{clay} \rightarrow Ca^{2+} + 2Na_{clay}$). On the other hand, if there is a normal ion exchange between the groundwater and aquifer material, the indices are negative. In this instance, the groundwater solution's concentrations of Na^+ or K^+ will rise ($Ca^{2+} + 2Na_{clay} \rightarrow 2Na^+ + Ca_{clay}$) (D. Parkhurst and C.Appelo, 2002). In this study, in all physiographies the values of CAI I are negative with an increasing trend from the plateau to the rift floor indicating normal ion exchange of Na^+ and K^+ from the host rock with Mg^{2+} and Ca^{2+} of the groundwater(Table 4), and is highly consistent with the interpretation using Durov diagrams(Figure 27).. Under these conditions, the concentrations of Na^+ or K^+ in the groundwater increase ($Ca^{2+} + 2Na_{clay} \rightarrow 2Na^+ + Ca_{clay}$), which leads the Na^+ concentration along the groundwater flow direction (plateau -rift margin -rift floor) increases with increasing TDS), resulting in the water type being Na-dominated. This is related to the presence of clay minerals in most of the drilling logs with depth and along groundwater flow directions. Besides, due to the increase of water rock interaction with depth and along groundwater flow directions, the weathering of silicate minerals will increase. This process contributes a secondary product called clay-like kaolinite ($Al_2Si_2O_5(OH)_4$). So, the presence of this clay mineral will favor the replacement of Ca^{2+} by Na^+, eventually leading the groundwater to be Na-dominated. The increased cation exchange is supported by the increase of temperature and pH with depth and along groundwater flow directions (Figure 27).

Table 4: Mean Chloro-Alkaline Indices (CAI)

Physiography	**Mean Chloro-Alkaline Indices (CAI-1)**	**Remark**
Plateau area	-4.495	Recharge area
Rift Margin	-4.256	Transition zone
Rift Floor	-1.914	Discharge area

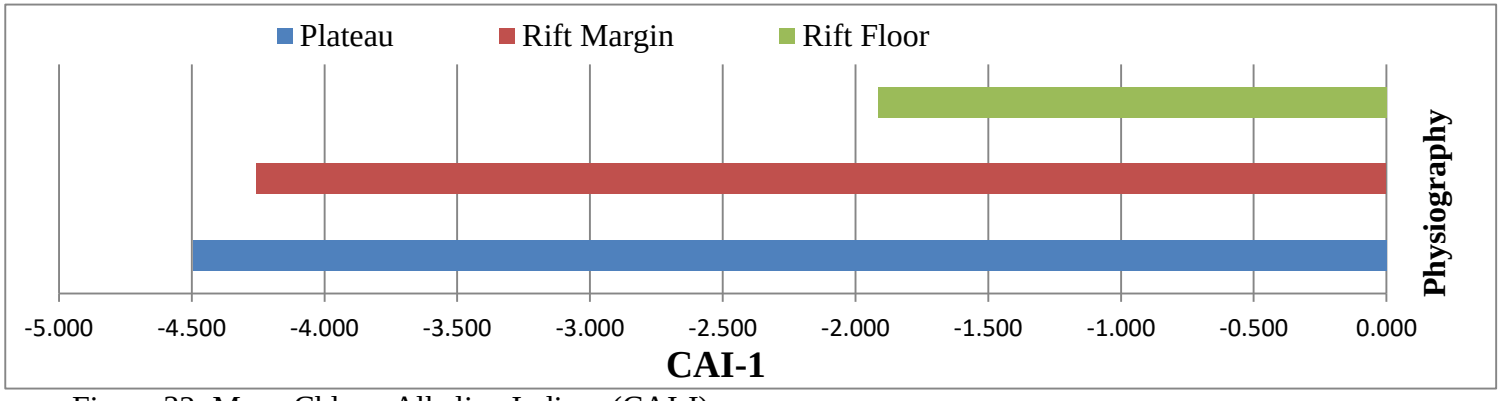


Figure 32: Mean Chloro-Alkaline Indices (CAI-I)

3.2.3.1.6 Total Alkalinity (TA) Analysis

Alkalinity in groundwater refers to the capacity of water to neutralize acids, typically due to the presence of dissolved bicarbonate (HCO_3^-), carbonate (CO_3^{2-}), and occasionally hydroxide (OH^-) ions(Dragon & Gorski, 2015). In groundwater it is often used as an indicator of geochemical processes occurring in the water, which can be influenced by various factors such as mineral dissolution, soil interactions, and water-rock interactions. It is also a useful parameter for identifying the recharge and discharge zones in a groundwater system(Aghazadeh & Mogaddam, 2011). In the recharge zones, the interaction between groundwater and geological formations is minimal, leads a low dissolved mineral content, and thus the alkalinity in the groundwater is usually lower. In other words, the lower alkalinity reveals that the groundwater hasn't yet interacted significantly with the surrounding rock. However, groundwater in the discharge zones is typically older and has undergone more residence time with the surrounding geological formations, which leads to higher alkalinity in contrast to the recharge zones. So, higher alkalinity content signals the groundwater is found at the discharge zone(Manta et al., 2022). In this study, the alkalinity for the plateau, rift margin, and rift floor samples have been measured using the titration method. Finally, the mean Total Alkalinity (TA) in mg/l for the plateau, rift margin, and rift floor samples is estimated to be 127.68, 251.25, and 283.75 respectively and presented in Table 5. So, from these results, the total alkalinity value is showing increasing trends and is consistent with the pH values from the plateau towards the rift floor (i.e. along the groundwater directions). Hence, correlating the Total Alkalinity with other hydrochemical and isotope parameters, the plateau is the main recharge area for the rift aquifers, the rift floor is the discharge area, and the rift margin can be taken as the transition zone.

Table 5: Mean Total Alkalinity (TA) along the physiography

Physiography	Total Alkalinity(TA) (mg/l)	Mean pH	Remark
Plateau	127.68	7.14	Recharge zone
Rift margin	251.25	7.68	Transition
Rift floor	283.75	8.06	Discharge zone

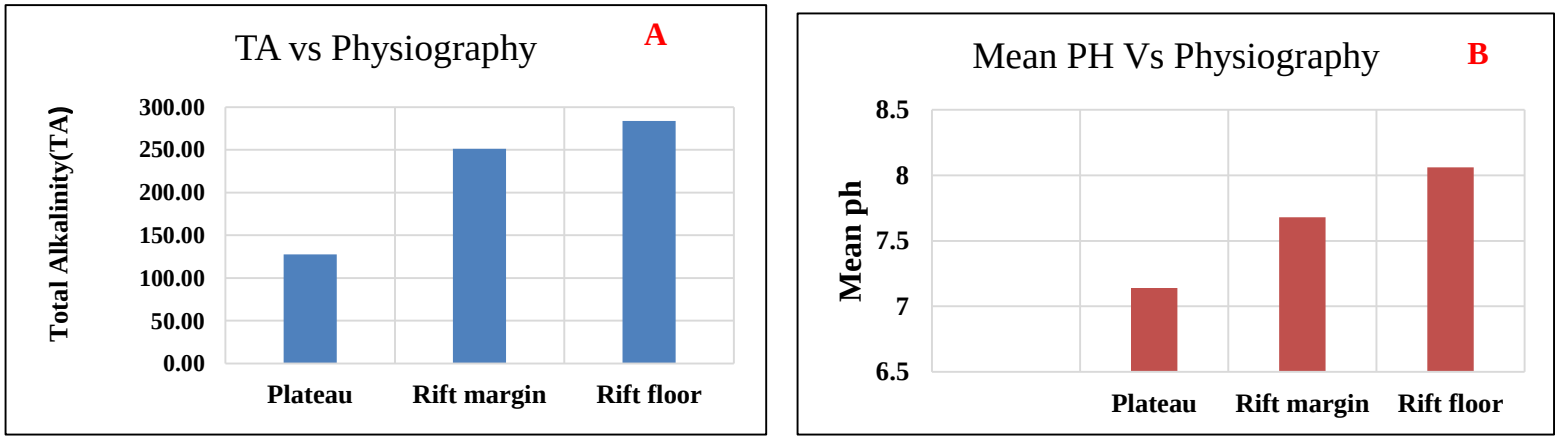


Figure 33: Total Alkalinity (A) and PH (B) along Plateau-Rift margin –Rift floor

3.2.3.1.7 Summary of the Hydrochemical analysis and Interpretations

Correlating the water types from the Piper and Durov diagrams with the Insitu measured parameters like TDS and PH, the dominant weathering and cation exchange processes, and Total Alkalinity(TA) interpretations, the groundwater has evolved from Ca dominance in the plateau, the recharge area, to Na dominance in the rift floor, the discharge area of this study. Thus, in the order Ca-(Mg)-HCO3, Ca-(Mg)-Na-HCO3, Na–Ca–HCO3, Na–HCO3–SO4, and Na–HCO3–Cl. This shows that the groundwater exhibits a regular change in hydrochemical facies along its flow direction (Plateau-Rift margin-Rift floor) from weakly mineralized to moderately and eventually strongly mineralized. These groundwater facies from the plateau to the rift floor can be well explained by considering the major geochemical processes mainly silicate weathering and cation exchange that affect the hydrochemical nature of the groundwater and show two distinct hydrochemical systems:

- The majority of the borehole samples found on the plateau and rift margin mainly in the northern part of Borkena river of the Awash basin, and the highland springs along the escarpment are calcium-dominated due to lower cation exchange and shorter residence time, indicating that the groundwater is in an early stage of recharge and has a source from precipitation and a local to intermediate groundwater inflow, and
- Due to high residence times, which increase normal cation exchange and acidic rock-water interaction with increasing depth and along the groundwater flow direction, the deep aquifers in the plateau, rift margin, and rift floor are Na-dominated. This indicates that the deep circulating groundwater in the upper catchment area (plateau and escarpment) is recharged and chemically altered with depth and along its flow path into the rift floor.

3.2.3.2 Isotopic Signatures

Isotopes are forms of a given chemical element that have a different number of neutrons and therefore has a different atomic mass, but the same number of protons and so have the same atomic number. To understand groundwater origin and its age, spatial variation, evolution, and the interaction of surface water to groundwater, & define groundwater flow direction, isotope techniques are effective tools for fulfilling such critical hydrological and hydrogeological information(Bretzler et al., 2011, Ayenew, Kebede, et al., 2008). In this study, for the identification of the source of groundwater recharge, as well as for understanding groundwater and surface water interactions, the stable isotopes of water ($\delta^{18}O$, and $\delta^{2}H$) and unstable isotope (Radon) were used and the results have been interpreted in the following ways.

3.2.3.2.1 Stable Isotopes

The stable isotopes of water molecules ($\delta^{18}O$, and $\delta^{2}H$) have been commonly used as natural tracers to identify the source of groundwater recharge in a certain catchment(Mechal et al., 2017, Mahamat et al., 2017, Bajjali, 2006, 2008). In this study, samples were taken from surface water and groundwater sources

to compare and evaluate the influence of evaporation on the isotopic signatures among the resources. However, for the identification of the source of groundwater recharge, both for the rift margin and rift floor aquifers, samples from surface water bodies were excluded, while shallow and deep wells, as well as spring sources from the plateau, rift margin, and rift floor were utilized.

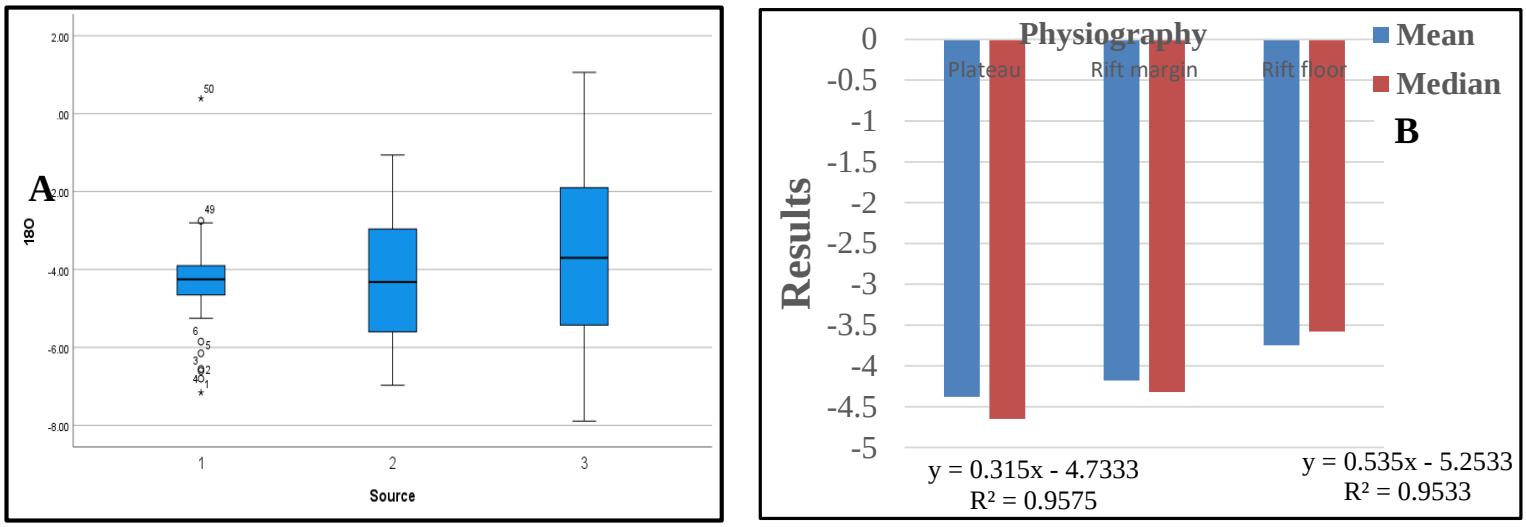
The isotopic results were interpreted using graphical presentation including box plots, and scatter presentations comprising both the LMWL and GMWL (i.e. $\delta^{18}O$ versus $\delta\ ^{2}H$ concentrations). This is because, for identifying the source of groundwater recharge, and knowing the effect of evaporation on the source of recharge of a certain catchment, the isotopic results need to be compared with the Local Meteoric Water Line (LMWL) and the Global Meteoric Water Line (GMWL)(Aghazadeh & Mogaddam, 2011, Yitbarek et al., 2012, Ahmed et al., 2019). For this specific study, the average Local Meteoric Water Line (LMWL) is derived from the mean isotopic composition of rainfall data monitored by IAEA at Addis Ababa station represented by $\delta^{2}H=7.2\delta^{18}O+11.9$ has been used. While, the GMWL data containing both ^{18}O and ^{2}H was downloaded from the Global Network of Isotope in Precipitation (IAEA/WMO/GNIP) database(http://isohis.iaea.org) represented by: $\delta^{2}H=8^{18}O+10$(Aghazadeh & Mogaddam, 2011,Putman et al., 2019, Margareth, 2017), where $\delta^{2}H$ is isotopic composition of hydrogen and $\delta^{18}O$ is isotopic composition of Oxygen-18 expressed in per mill (‰). Besides, Slope, D-Excess, and Isotopic Ratio for the plateau, rift margin and rift floor samples were determined and correlated with each other and has been used as an additional way of interpretations for the proper identifications of the source of groundwater recharge of the western Afar rift margin and the associated rift floor aquifers. Finally, the various isotope interpretations were integrated and correlated with the geological, lithostratigraphic correlations constructed from the lithological logs, and hydrochemical interpretations for the better evaluation of the source of groundwater recharge.

3.2.3.2.1.1 Graphical Presentations

I. Box Plot

The box plots of statistical analysis were conducted using SPSS version 27.1 software and can be used for the interpretation of isotopic results by comparing them with the known location and altitude(P. Cook, 2017). In this study, the results containing ^{18}O from the plateau, rift margin, and rift floor were plotted as displayed in Figure 34. Accordingly, as we can see from the statistical summary table (Table 6), the mean of the isotopic signature along the plateau, rift margin, and rift floor is -4.38. -4.18‰ and -3.75‰ with a correlation (R^2=0.96). In addition the median of the isotopic signatures along the plateau, rift margin, and rift floor is -4.65‰, -4.32‰ and -3.58‰, with a correlation (R^2=0.95) (Table 6).The mean and median along the plateau-rift margin and rift floor looks very comparable (R^2=0.96 and R^2=0.95 respectively), revealing that they have a common source of groundwater recharge. This is due to the presence of

columnar jointed basalt and transverse structures that allow for the flow of groundwater from the plateau to the rift margin and finally to the rift floor. However, the top (1.06‰) and bottom whiskers (-7.89‰) which represent the highly enriched and depleted groundwater sources have been found in the rift floor (Figure 34). The former is found in shallow wells that have local recharge source but have been affected by evaporation. The latter is found in deep wells, where, in contrast to shallow wells, the primary source of recharge is unrelated to local sources, but it is deep circulating groundwater recharge from the plateau area due to the presence of preferential pathways. In the plateau areas, the depleted outlier(-7.16‰) is related to the deep well (500m) in the Blue Nile basin, and the enriched outliers(0.39‰) is hand dug well, where the top cover is open to the surface, as a result the lighter isotopes are removed from the well and leaves the heavier ones. In the case of the rift margin, the minimum value (-6.97‰) is found in deep wells having a deep circulating groundwater recharge source, and the maximum value (-1.05‰) is found in hot springs around the outlets of the Borkena river. Hence, the plateau area is the main source of groundwater recharge for the rift margin and rift floor deep aquifers.



NB: 1: Plateau, 2 Rift margin, 3: Rift floor

Figure 34: Box plot of ^{18}O isotopic signatures along the plateau, Rift margin, and Rift floor (A), Mean and Median Correlations (B)

Table 6: Statistical summary of ^{18}O Isotope results

Physiography	Minimum	Maximum	Mean	Median
Plateau	-7.16	0.39	-4.38	-4.65
Rift margin	-6.97	-1.05	-4.18	-4.32
Rift floor	-7.89	1.06	-3.75	-3.58

II. Scatter Plots

In addition to the box plot presentation above, the scatter plots for the isotope results including ^{18}O and ^{2}H with respective of the sampled physiography have been conducted, which will help to see the deviation of the sampled data relative to the LMWL and GMWL. This interpretation has a vital significance in the identification of the source of groundwater recharge for a certain aquifer and is described as follows.

Plateau

In the plateau area, the minimum, maximum and mean for ^{18}O and ^{2}H were determined to be -7.16‰, 0.39‰ and -4.38‰, and -35.94‰, 11.41‰ and -14.5‰ respectively. At this physiography, the slope and d-excess values are 5.31 and 5.39, with a good correlation (R^2=0.78) (Figure 35). However, the isotopic signature varies in groundwater samples collected from deep wells, shallow wells, hand-dug wells, and spring sources. For hand-dug wells such as HDW-36, the isotopic signature is highly enriched(0.39) because the opening of the dug well is exposed to the atmosphere, which leads to the evaporation of lighter isotopes and leaves heavy isotopes behind, resulting in the well-being enriched. Cold spring samples such as CSP-8, CSP-11, and CSP-53 as well as shallow wells were plotted close to and along the LMWL. From the drilling logs, the water-bearing formation of the shallow wells is mainly fractured and weathered upper basalt with a discharge rate of 2-3 l/s. The hydrochemical analysis, and interpretations shows that the main water type for the cold springs and shallow wells is Ca-(Mg)–HCO3 and the TDS value is not more than 100 mg/l. Combining the hydrochemical analysis, TDS value, and isotopic signatures of these sources, the groundwater is at an early stage of recharge that does not undergo much development and is mainly -derived from local precipitation. Deep wells with a depth of more than 150m such as BH#4, BH#19, BH#21, etc. are isotopically depleted and lie to the left of LMWL and GMWL. Drilling logs of these samples indicate that the main water-bearing formation is fractured upper basalt underlain by ignimbrite and rhyolite. Hydrochemical analysis shows that the main water type is Na-dominated with medium mineralization. The combination of the hydrochemical analysis and the isotope signature shows that the main groundwater recharge for the deep wells in the plateau area is a medium to regional groundwater flow.

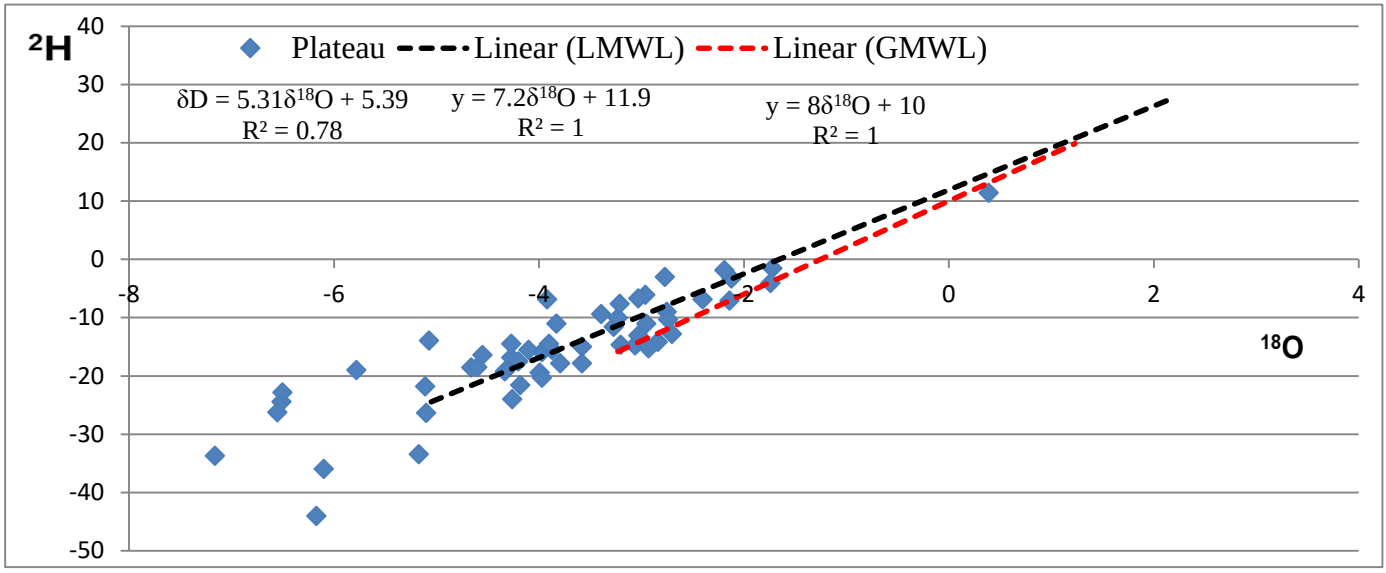


Figure 35: Plateau samples Vs LMWL and GMWL

Rift Margin

In the rift margin area, the minimum, maximum, and mean for ^{18}O and ^{2}H were determined to be -6.97‰, -1.05‰, and -4.18‰ and -29.4 ‰, 3.86‰ and -12.507‰ respectively. At this physiography, the slope and d-excess values are 4.2 and 5.08 respectively, with a correlation (R^2=0.76) (Figure 36). However, the isotopic signature of deep wells, shallow wells, springs, and river sources varies. As a result, most deep wells tapping groundwater from ignimbrites and the lower columnar jointed basalt in addition to overlying alluvial deposits, and upper basalts are depleted in isotopic signature and plotted on the left side of both the LMWL and GMWL (Figure 36). From the hydrochemical analysis, and interpretations, the main water type in the deep groundwater samples is Na-dominated, followed by Ca cations with moderate mineralization. Thus, combining the hydrochemical and isotopic analysis, it can be possible to conclude that the main groundwater recharge occurs in colder climatic conditions and is a regional groundwater flow. The boreholes that were found near the escarpments mainly in the northern part of the Borkena River of the Awash basin are plotted close to and along the LMWL, suggesting that the water has undergone minimal evaporation. From the hydrochemical analysis, these water groups show Ca-(Mg)-HCO3 water type, with low TDS values. Combining the isotope result with the hydrochemical analysis, these water groups have local recharge mainly from precipitation, and local groundwater inflow from the surrounding mountains. Shallow borehole samples such as BH#36, BH#41, and BH#42 that tap groundwater primarily from the uppermost porous alluvial deposit (100-150 m depth) are plotted to the enriched side of LMWL due to the evaporation effect. The hydrochemical analysis shows that most of the shallow well samples have mixed water types. Thus, correlating the hydrochemical and isotopic analysis, these water samples have local to medium groundwater recharge, mainly from precipitation and

the surrounding volcanic mountains. However, the highland springs that have originated from the bottom of the upper basalt along the uplands of the rift escarpments are relatively depleted and are distributed on the depleted side of the diagram, which contains both the LMWL and the GMWL. From the hydrochemical analysis, the spring samples show a Ca-(Mg)-HCO3 water type with low mineralization, indicating that the groundwater source is in an early stage of recharge. Combining the hydrochemical analysis, the isotopic signatures, their preferential orientation along the rift escarpments, and their significant yield with the constant flow (30-70l/sec) from a very small recharge catchment; the main source of groundwater recharge comes from the adjacent plateau area but has not experienced much groundwater development with the modification from the local precipitation.

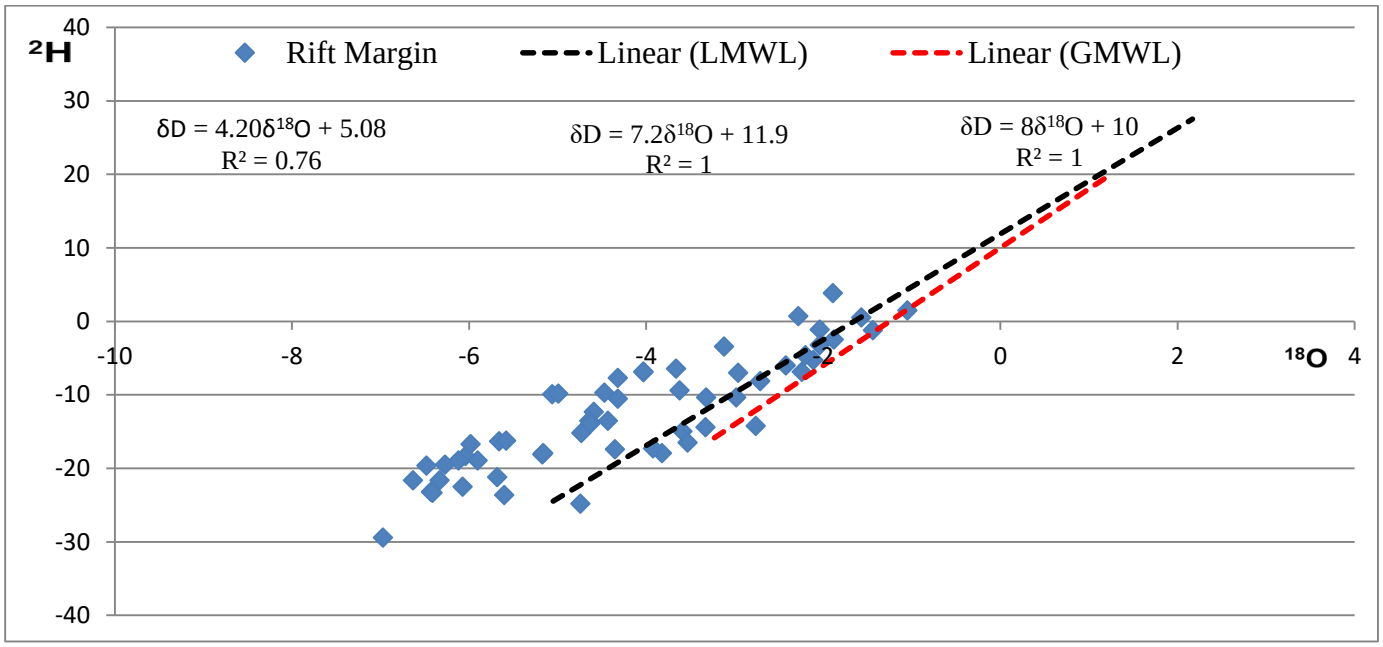


Figure 36: Rift margin samples Vs LMWL and GMWL

Rift floor

The samples along this physiography have minimum, maximum, and mean values of -7.89 ‰, 1.06‰ and -3.75 ‰ for ^{18}O and -26.4 ‰, 9.87‰ and -11.3‰ for ^{2}H, respectively. At this physiography, the slope and d-excess values are 3.37 and 3.46 respectively, with a correlation (R^2=0.79) (Figure 37). However, the isotopic signature varies in the water samples, which originate from deep thermal wells, springs, and shallow wells sources. In the rift floor, all samples from deep thermal wells are isotopically depleted and are plotted to the left side of the graph containing LMWL and GMWL (Figure 37). The hydrochemical analysis shows that these water samples have a Na-dominated water type and are highly mineralized with higher TDS values. The integration of these parameters indicates that the main groundwater recharge originates from the regional aquifer, mainly from the north-western plateau. However, the enriched water samples plotted on the right of the LMWL are shallow wells that receive recharge from enriched sources such as rivers, rainwater, flash floods, and streams due to the evaporation

effect (Ayenew et al., 2008, Kebede et al., 2005, Ayenew, Kebede, et al., 2008, Bretzler et al., 2011). In addition, spring sample like **S2** is also plotted towards the enriched side, which is due to the effect of evaporation as it preferentially removes lighter isotopes, leaving behind a more enriched isotopic signature. In addition, since the resource is found along the NE-SW trending Wenji fault belt which facilitates the addition of large amounts of CO_2 from the mantle plume joining the groundwater, and leads to a relatively enriched isotopic signature(Tesfaye et al., 2003, Corti et al., 2015).

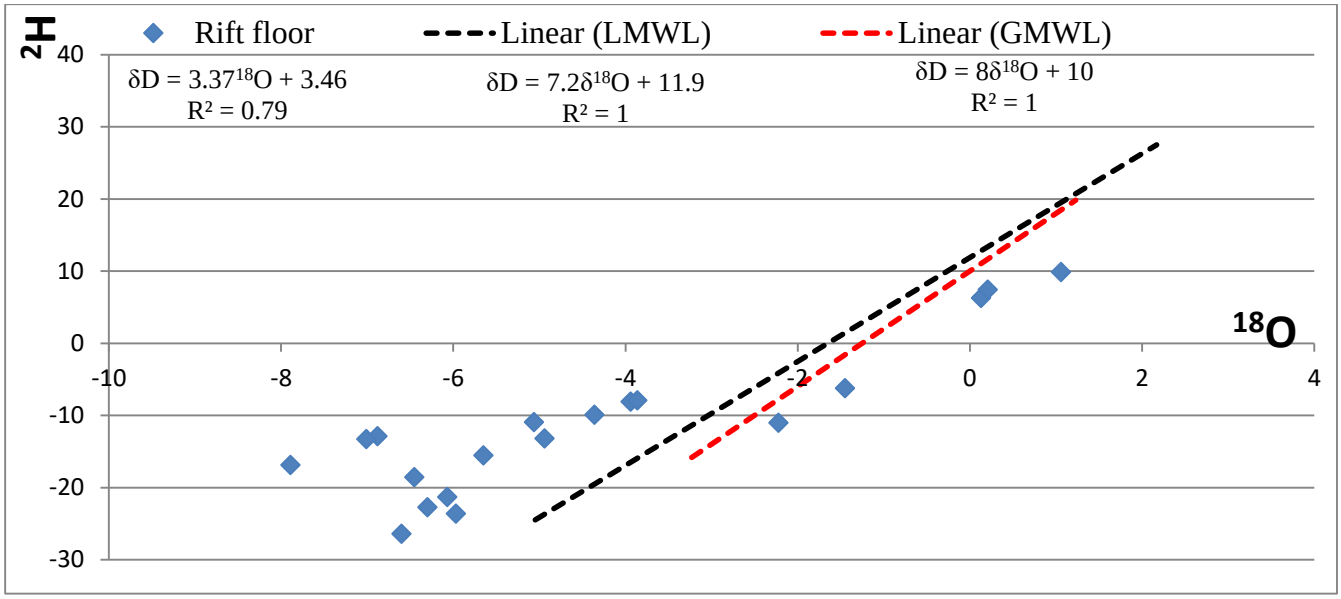


Figure 37: Rift floor samples vs LMWL and GMWL

3.2.3.2.1.2 Determination of Isotopic Ratios

Isotopic ratios are useful tools for comprehending hydrological processes, such as groundwater recharge under various climatic conditions(Thomas & Rose, 2003). This is especially true for stable isotopes like oxygen-18 (^{18}O) and deuterium (^{2}H) (Manta et al., 2022). It offers important insights into groundwater recharge processes and is essential in locating the sources of groundwater recharge. A common way to express isotopic ratios is with delta notation (δ), which shows how the sample's isotopic ratio deviates from the standard given by:

Equation 5: $\boldsymbol{\delta = \frac{(Rsample - Rstandard) * 1000}{Rstandard}}$, Where R_{Sample} is the ratio of the heavy to light isotope (e.g., $^{18}O/^{16}O$, $^{2}H/^{1}H$) of the sample, and $R_{Standard}$ is Vienna Standard Mean Ocean Water (VSMOW), with the following isotopic ratio values(Clark & Fritz, 2013):

- R_{VSMOW}, $H=(^{2}H/^{1}H)_{VSMOW}=0.00015576$
- R_{VSMOW}, $O=(^{18}O/^{16}O)_{VSMOW}=0.0020052$

For the determination of the isotopic ratio of oxygen and hydrogen in the study area, rearranging Equation 5 will be given by Equation 6 and Equation 7.

Equation 6: $$\delta^{18}O(^{o}/_{oo}) = \frac{\left(\frac{^{18}O}{^{16}O}\right)_{sample} - \left(\frac{^{18}O}{^{16}O}\right)_{stan\,dard}}{\left(\frac{^{18}O}{^{16}O}\right)_{stan\,dard}} x\,1000$$

Equation 7: $$\delta^{2}H(^{o}/_{oo}) = \frac{\left(\frac{^{2}H}{^{1}H}\right)_{sample} - \left(\frac{^{2}H}{^{1}H}\right)_{stan\,dard}}{\left(\frac{^{2}H}{^{1}H}\right)_{stan\,dard}} x\,1000$$

Accordingly, based on the following mean isotopic results from each physiography, the isotopic ratio can be determined for the Plateau, Rift margin, and Rift floor and finally a comparison will be made.

1. Plateau

$\delta^{18}O$: -4.38 ‰

$R_{Sample}=0.0020052\times(\frac{-4.38}{1000}+1)=0.0020052\times0.99562=\underline{0.001996}$

- **$\delta^{2}H$**: -14.50 ‰

  $R_{Sample}=0.00015576\times(\frac{-14.71}{1000}+1)=0.00015576\times0.98529=\underline{0.000153}$

2. Rift Margin

- **$\delta^{18}O$**: -4.18 ‰

  $R_{Sample}=0.0020052\times(\frac{-4.18}{1000}+1)=0.0020052\times0.995819=\underline{0.001997}$
- **$\delta^{2}H$**: -12.507 ‰

  $R_{Sample}=0.00015576\times(\frac{-12.507}{1000}+1)=0.00015576\times0.987493=\underline{0.000154}$

3. Rift floor

- **$\delta^{18}O$**: -3.75 ‰

  $R_{Sample}=0.0020052\times(\frac{-3.76}{1000}+1)=0.0020052\times0.99624=\underline{0.001998}$
- **$\delta^{2}H$**: -11.3 ‰

  $R_{Sample}=0.00015576\times(\frac{-11.3}{1000}+1)=0.00015576\times0.9887=\underline{0.000154}$

Table 7: Summary of Isotopic Ratios

Source	Mean $\delta^{18}O$ (‰)	Mean $\delta^{2}H$ (‰)	Isotopic Ratio ($\delta^{18}O$)	Isotopic Ratio ($\delta^{2}H$)
Plateau	-4.38	-14.5	0.001996	0.000153
Rift Margin	-4.18	-12.507	0.001997	0.000154
Rift Floor	-3.76	-11.3	0.001998	0.000154

Based on table 7, the isotopic ratio of ^{18}O and $\delta^{2}H$ of the Rift Margin is comparable to that of the rift floor area but slightly depleted with respective of oxygen. In addition, the rift floor has an isotopic ratio that is less depleted than the plateau. The slight increment of oxygen along the plateau to the rift margin and finally to the rift floor is due to the effect of evaporation which is more pronounced in the rift floor area. While, the isotopic ratios of oxygen and hydrogen along the Plateau, Rift margin, and Rift floor have strong correlation (R^2~1) (Figure 38), reveals that they share a common source of recharge, as a result of preferential pathways, leads deep circulating groundwater flow from the former to the latter. Hence, the rift margin often acts as a transition zone between the Plateau and the Rift floor, as its source of recharge is influenced by mixing with local recharge mainly from the surrounding volcanic mountains as a result of the overlying porous alluvial deposit, especially in the marginal grabens.

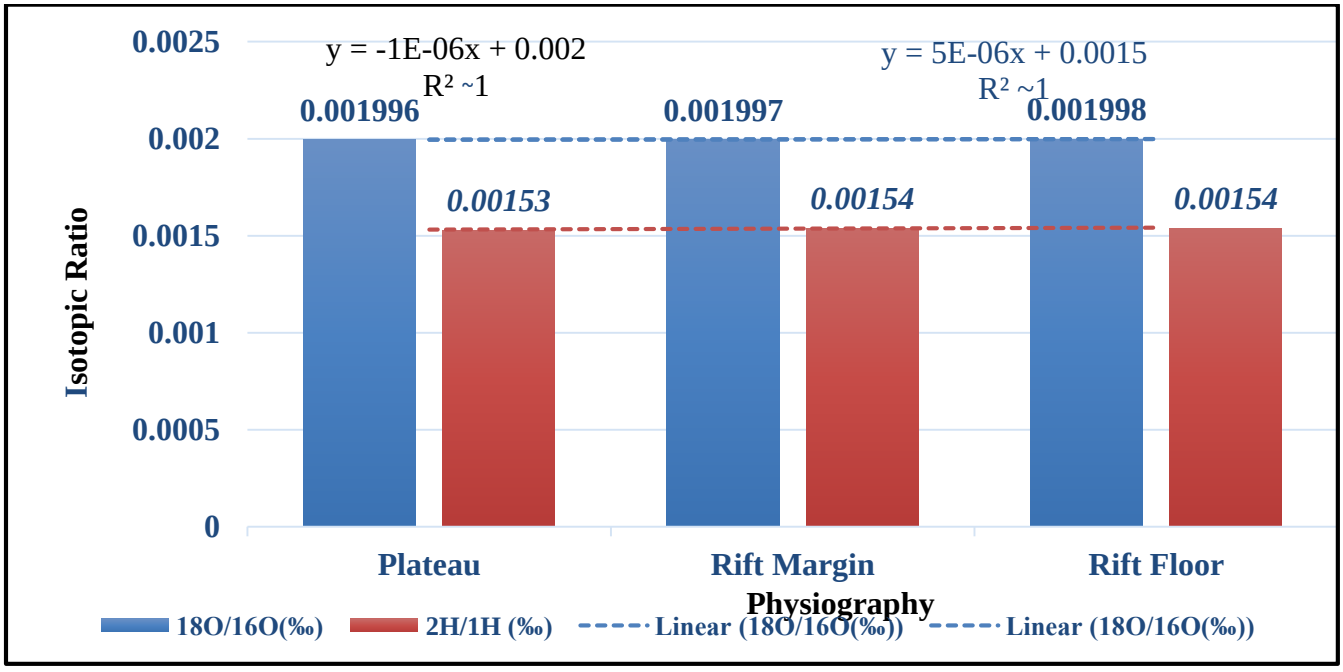


Figure 38: Isotopic Ratio (Plateau-Rift margin -Rift floor)

3.2.3.2.1.3 Correlation of Slope and D-Excess along the Plateau, Rift margin and Rift floor

In groundwater recharge studies the slope and D-excess of isotopes are of great value in understanding the dynamics, sources and processes of groundwater recharge (Mohamed et al., 2021).By comparing the Slope and D-excess of groundwater data from different source types, we can understand the impact of evaporation, the recharge source and overall recharge dynamics in a particular area (P. Cook, 2017). For this purpose the Slope and D-excess of isotopic data from the Plateau, Rift margin and Rift floor of the study area were correlated. This study shows that the slope value decreasing from the plateau to the rift floor shows high evaporation effects (Table 8), but generally it exhibits strong correlations (R^2=0. 99) (Figure 39), so that a strong relationship exists in the isotopic composition of the water sources in these regions. As well as discussed in Clark, I. D., & Fritz, P. (1997), the correlation value of high R^2 suggest that the water sources in the two respective physiographic regions have possibly a common source or similar recharge mechanism, due to the hydraulic connectivity of the two adjacent physiographies (where groundwater flow systems are interconnected) which leads to similar isotopic signatures in recharge areas. Hence in this study, the groundwater sources (i. e. the deep boreholes along the plateau, rift margin and rift floor areas) share a common source of recharge; that is deep circulating groundwater recharge, which is highly consistent with the hydrochemical analysis and interpretations made earlier. Likewise, the high correlation of D-excess (Deuterium excess) isotopic results across different physiographies suggests that the source of recharge or the processes leading to the changes of the isotopic composition of the water might be common or highly similar (González-Trinidad et al., 2017). In this study, the D-excess values of the isotopic signatures along the plateau, rift margin and rift floor are high (R^2=0. 87) (Table 8 and Figure 39). The high correlation of D-excess values across the plateau, rift margin and rift floor definitely indicates a common (or very similar) source of recharge; that is deep circulating groundwater recharge from the plateau along the preferential pathways and less local modifications; but the values is decreasing in order toward the rift floor probably due to the increasing evaporation effect of the plateau towards the rift floor.

Table 8: D-Excess and Slope along Plateau-Rift margin and Rift floor

Physiography	**D-Excess**	**Slope**
Plateau	5.39	5.31
Rift margin	5.08	4.2
Rift floor	3.46	3.37
R^2	**0.87**	**0.99**

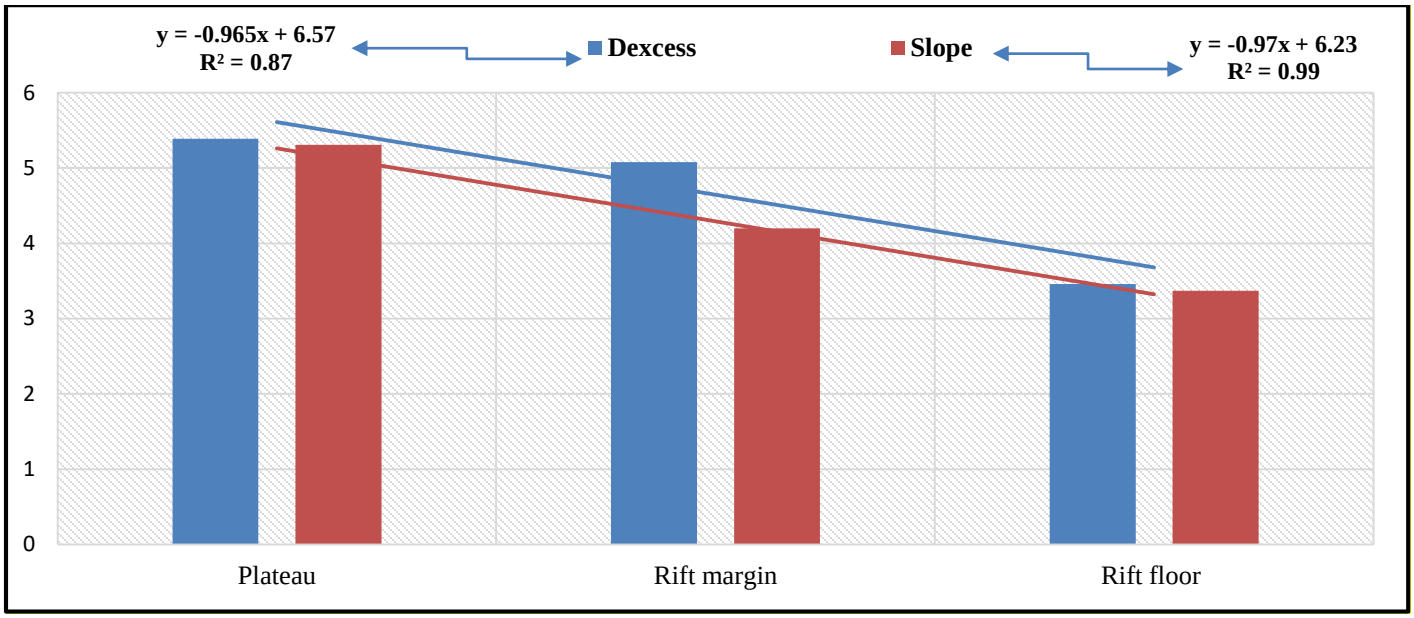


Figure 39: D-Excess and Slope along plateau-rift margin and Rift floor

3.2.3.2.1.4 Correlation of Isotopic Results with Recharge Elevation

Groundwater recharge elevation and its isotopic data are related, which is a basic aspect of isotope hydrology and provides an extra hint as to where recharge originates in a particular groundwater basin(Azevedo da Silva et al., 2020, Souza et al., 2015, Thomas & Rose, 2003). This helps to identify the source of groundwater recharge area for a certain aquifer in that particular basin or catchment(Jasechko, 2019, Liu & Yamanaka, 2012, Cooper, 2010). In this study, for the determination of the groundwater recharge elevation particularly for the deep rift aquifers, the altitude- gradient or the relationship between the $\delta^{18}O$ values and elevation determined by Kebede et al., 2011 in the Afar depression and the western Ethiopian plateau(−0.10 ‰/100 m) was used. Accordingly, the average recharge elevation for the $\delta^{18}O$-depleted deep groundwater sources of the rift floor aquifers is estimated to be 3105 m a.s.l. This altitude belongs to the physiographic region of the north western plateau, which is approximately between 2,680 and 3,380 meters above sea level. Therefore, the $\delta^{18}O$-depleted groundwater in the rift floor is deep circulating groundwater originating from the northwestern plateau and the highland parts of the escarpment. In other words, the deep aquifers of the rift floor are hydraulically connected to the deep aquifers of the rift margin and the plateau.

3.2.3.2.1.5 Summary of Isotopic interpretations

Integrating the various isotopic interpretations conducted above, the deep groundwater systems in the western Afar rift margin and associated Afar rift floor aquifers is dominated by deep circulating groundwater from the plateau with little to moderate addition from local sources. However, in the rift margin, in addition to the intermediate to regional groundwater flow from the plateau, local precipitation as well as groundwater inflow from the surrounding volcanic mountains also has a major impact on the

source of groundwater recharge. The shallow groundwater sources in the rift floor are recharged by local sources mainly Awash River, tributary, rainwater, flash floods, and streams, which are highly affected by evaporation before recharging.

3.2.3.2.2 Radon Isotopes

3.2.3.2.2.1 General

The radioactive noble gas radon (^{222}Rn), which has a half-life of 3.8 days and is the daughter of radium (^{226}Ra), is found in groundwater in much higher concentrations than in surface water(Hamada, 1999, Yang et al., 2020). Because radon outgasses into surface water upon release, low radon levels in rivers suggest that the water in the river is not the product of base flow from nearby or adjacent areas(Baskaran et al., 2009). On the other hand, surface water with elevated radon levels often indicate groundwater feeding the river, as groundwater usually has much higher radon concentrations due to its prolonged contact with radon-producing minerals(P. G. Cook et al., 2003). This characteristic of radon (^{222}Rn) is a qualitative indicator of the interaction between surface water and groundwater, and makes radon an excellent natural tracer for identifying groundwater inputs into surface water systems(Texier et al., 2024). Besides, it is also a good option for the identification of recharge and discharge zones, as discharge zones tends to have higher radon amount than recharge zones due to the prolonged contact between the groundwater and the host rocks(Grolander et.al, 2009).

3.2.3.3.2.2 Data Interpretations

A total of 27 (twenty-seven) ^{222}Rn measurement points were taken. At each site, the ^{222}Rn count was taken 4 to 5 times per 15 minutes, depending on the stabilization of the readings. The initial measurement was usually excluded, and the mean ^{222}Rn composition of the particular location was determined by averaging the last three or four readings. The Radon results were presented in maps with graduated point plots using Arc GIS 10.8, and integrated with the underground geology, hydrochemical and stable isotope analysis. Based on the recorded data on the river, the radon measurements taken at the exit of marginal grabens and the surrounding margins have a higher value than the rift floor (Figure 21 and Figure 40), as a result of the flow of groundwater into the river due to the presence of highly fractured columnar jointed basalt in the river bed and NE-SW and NW-SE trending transverse faults and lineaments. Besides, between the rift floor and rift margin like at Telalak River, due to the presence of subsurface weak zones/transverse structures, oriented predominantly NE-SW and sometimes orthogonally E-W, extending from the marginal grabens to the rift floor across the accommodation zones leads the groundwater to flow to the river, as a result, higher radon values were also obtained. Therefore, the river at the rift margin zonation is called the "gaining river". However, there are potentially two possibilities for the groundwater flowing from the rift margin towards the rift floor. The first scenario is that since the area between the rift margin and the rift floor is in the Arcuate Accommodation Zones (AAZ), the Dalha Basalt tends to

be highly fractured and faulted. This circumstance favors that the groundwater flows downwards following the weak zones and is at a greater depth. In this condition, the river is feeding the groundwater and can be called a losing river. As a result, the surface water sources in the rift floor are depleted in the radon values. The radon measurements conducted within the rift floor, such as at Lake Yardi and the Awash River around the Gewane area (Rad#9 and Rad#11), confirm this notion. The second but less probable scenario is that the groundwater leaking from the marginal area can flow as surface water over long distances with high surface temperature, which leads to a gradual decrease in radon value as the lifetime of radon is very short (3.8 days) (Tadesse et al., 2023), resulting in lower values in the surface waters. However, at some gauging stations in the rift floor such as the outlet of the study area (Awash Adaitu), where the river bed is covered by the Afar stratoid series, which is regionally connected by the cross structures with other volcanic rocks such as Dalha and columnar jointed basalt, the radon value in the river is relatively higher. Hence, the river at this particular location is labeled as a gaining river. Therefore, in the rift floor the river can lose or gain depending on the local geology of the river bed and the availability of transverse structures.

For the identification of recharge and discharge zones, Radon measurements were also conducted at the deep and shallow wells both at the rift margin and rift floor and the result was correlated with the geological, hydrochemical, and stable isotope result and analysis. Accordingly, the deep wells in the marginal grabens like BH#33, and between the rift margin and the rift floor such as BH#13 contain high radon values. The hydrochemical and isotope analysis of these sources shows that the groundwater is Na-dominated and isotopically depleted. Integrating these parameters with the Radon values, the groundwater has undergone prolonged residence time and recharged under colder climatic conditions and is mainly from the plateau area due to the presence of preferential pathways. In the rift floor area shallow wells like HDW#1, hydrochemical and isotopic analysis shows that the groundwater is Ca-dominated and isotopically enriched with low Radon values. Integrating these parameters, the source of recharge is local having minimum rock-water interactions, and is mainly rivers, streams, and flash floods. While, in the deep well sources like Amma#1 and #2, from the lithologic logs, the thickness of the lacustrine deposit is minimal and encounters the underlying volcanic rocks. In these wells, the yield is good (≥20lit/sec), hydrochemically Na-dominated, and isotopically depleted, with high radon values. Correlating the geology, yield, hydrochemical, and isotope analysis with the Radon values, the groundwater in the deep wells has undergone high residence time and recharged under high altitude and is mainly from the plateau area due to the presence of preferential pathways. However, the wells drilled in the area covered by thick lacustrine deposits (~420m) become dry, reveals the productivity of the wells in the rift floor is highly controlled by geology and the presence of transverse structures. So, the interpretation made using the

radon measurement is highly consistent and correlated with the hydrochemical and stable isotope results and interpretations made above.

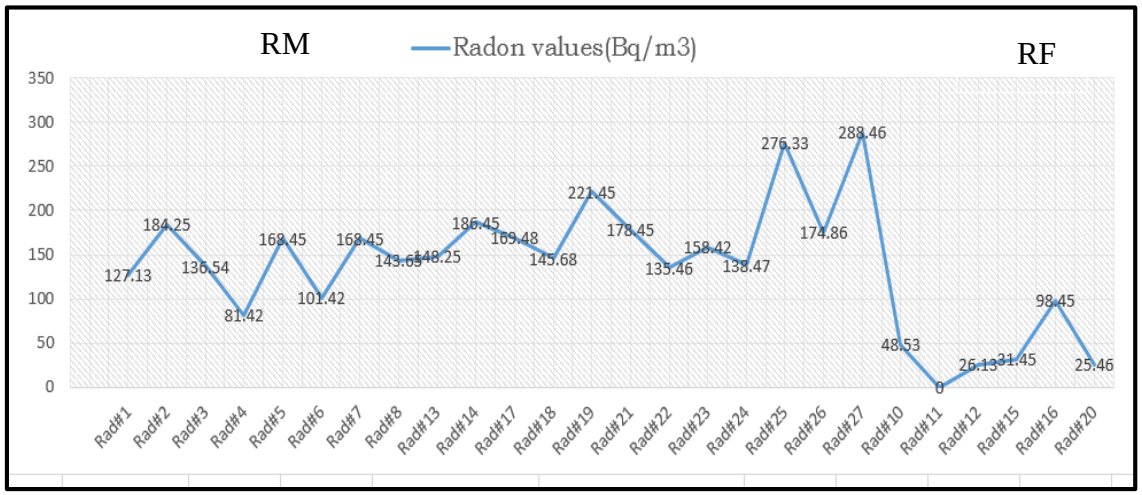


Figure 40: Measured Radon values and distribution

3.2.4 Multivariate Statistical Analysis

3.2.4.1 General

The use of graphical techniques for large data sets is more effective than multivariate methods(Raiber et al., 2012, Farnham et al., 2003, Kebede et al., 2005, Baye, 2009). Furthermore, the chemistry of statistical groupings cannot be determined by statistical methods(Kebede et al., 2005, Baye, 2009). Consequently, the combination of graphical and statistical techniques provides a consistent and objective method of classifying a large number of samples while preserving the ease of use of classical graphical representation(Adimalla et al., 2018, Monjerezi et al., 2011). However, before performing statistical analysis, the raw data should be checked using statistical measures such as the Kaiser–Meyer–Olkin (KMO) test and Bartlett's test to decide whether the data are suitable for factor analysis or not (Napitupulu et al., 2017, Ul Hadia et al., 2016). A statistical tool called the KMO test is used to assess if the data are suitable for factor analysis and to look at how strongly the factors partially explain each other's variations(Shrestha, 2021, Napitupulu et al., 2017). Furthermore, the test assesses the suitability of sampling for every variable in the model as well as the overall model. As mentioned in Ul Hadia et al., 2016, and Shkeer & Awang, 2019, the higher the KMO values (closer to 1.0), the better the data fit for factor analysis, while values below 0.5 are not acceptable. In this study, the KMO value is 0.677(Table 9), making it plausible to perform a factor analysis. The Bartlett's test for sphericity is also used to check whether the data are suitable for further factor analysis(Dziuban & Shirkey, 1974, Tobias & Carlson, 1969). The correlation matrix is demonstrated to be not an identity matrix by a statistical test, which is often less than 0.05 (rejection of the null hypothesis). In this study, the value is 0(Table 9) and is found to be good for factor analysis.

Table 9: KMO and Bartlett's Test

KMO and Bartlett's Test		
Kaiser-Meyer-Olkin Measure of Sampling Adequacy.		0.677
Bartlett's Test of Sphericity	Approx. Chi-Square	1385.194
	Df	55
	Sig.	0.000

3.2.4.2 Hierarchal Cluster Analysis (HCA)

A common statistical technique that groups observed data into relevant clusters in their hierarchy based on similarities between observations within the same cluster is called Hierarchical Cluster Analysis (HCA)(Raiber et al., 2012, Farnham et al., 2003). The use of Hierarchical Cluster Analysis (HCA) for the statistical classification of geochemical data in Q-mode has demonstrated that it is a useful framework for classifying water composition into hydrochemical facies(Raiber et al., 2012, Farnham et al., 2003, Kebede et al., 2005, Baye, 2009). Therefore, the water samples were grouped into objective groups with comparable physical and chemical properties using Hierarchical Cluster Analysis (HCA). However, before applying HCA, the raw chemical data should be logarithmically transformed and standardized to lessen bias and get the variables closer to normally distributed data(Tiouiouine et al., 2020). Without standardization, the Euclidean distances would be most influenced by the variable with the largest magnitude (Rezende et al., 2019). The standardization process in this study scales the logarithmically processed data to a range of -3 to +3 standard deviations around a zero mean (Figure 41). This ensures that each variable is weighted equally in the statistical analyses. In this study, samples were compared based on several parameters and grouped according to their "similarity" in the Q-mode classification. Hence, eleven (11) parameters including pH, Ca^{2+}, Mg^{2+}, K^{+}, Na^{+}, HCO_3^{-}, NO_3^{2-}, Cl^{-}, SO_4^{2-}, EC, and TDS were used to generate the HCA, and the result was presented in a dendrogram diagram (Figure 42). Accordingly, 2 (two) major groups and 4 clusters (subgroups) were identified**.** The two major groups were distinguished by their TDS values, with Group #1having $71 \leq TDS \leq 298.5$ and Group#2 having $324 \leq TDS \leq 895$ values. Group #1 water samples were mainly distributed in the plateau area and at the rift margin, but close to the rift escarpments, but also in the marginal grabens where the main lithological unit is alluvial deposit underlain by the upper basalt or the lower columnar jointed basalt. Group #2 water samples were found in the deep wells of the plateau, rift margin mainly in the marginal grabens and rift floor areas. The 4 (four) subgroups or clusters were classified based on lithostratigraphy and water type. The minimum, maximum, and mean of the physicochemical parameters, the average physicochemical compositions of each subgroups/cluster and the interpretation of each subgroup or cluster are presented in the following ways.

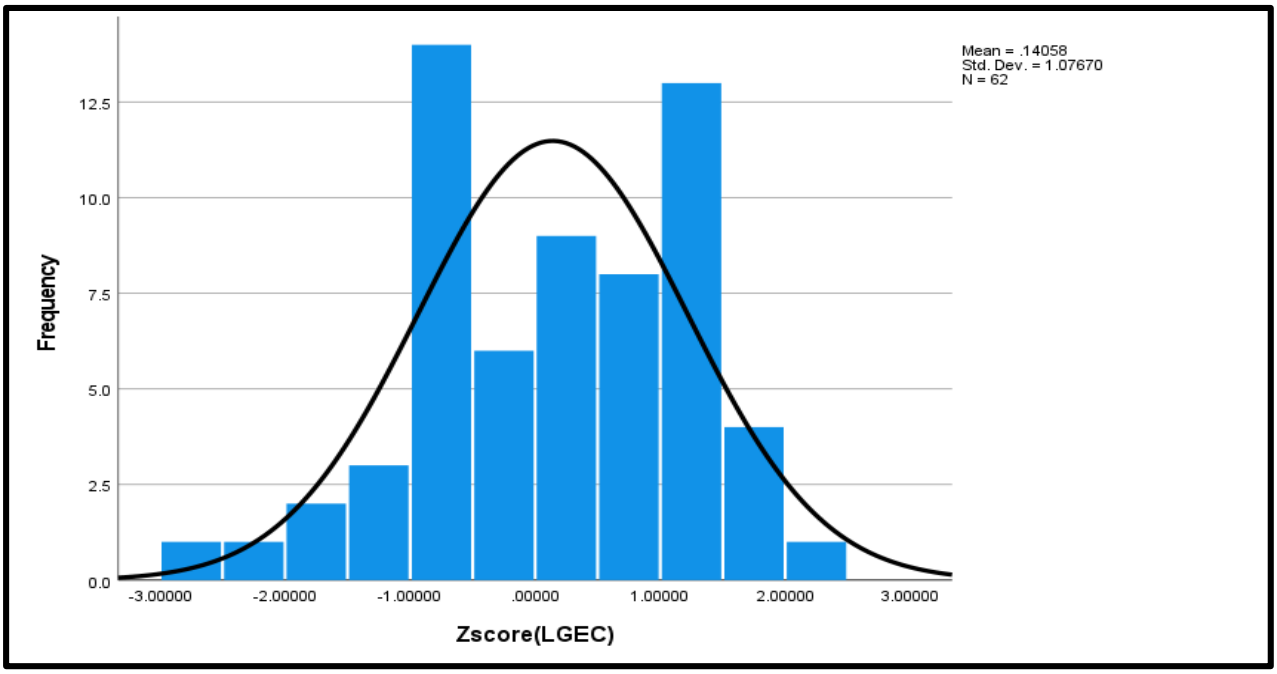


Figure 41: Histogram plots of water samples

Table 10: Physical and chemical composition of water samples

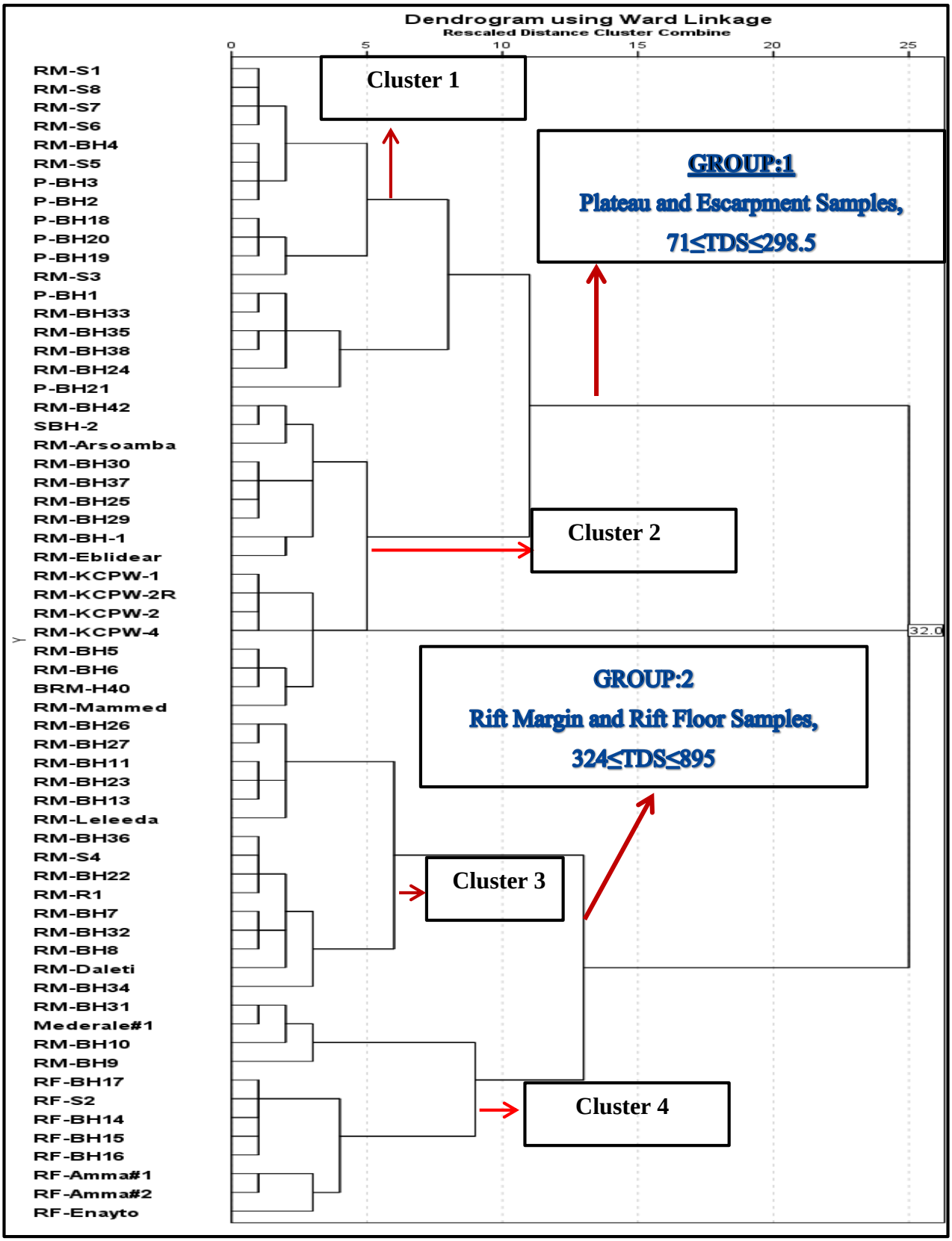
Parameters	N	Minimum	Maximum	Mean	Std. Deviation
PH	129	6.64	9.00	7.70	0.45
EC(µs/cm)	129	151.00	1790.00	655.88	327.42
TDS	129	71.00	895.00	319.03	160.47
Cl^-(mg/l)	129	0.57	394.60	38.53	59.31
$NO3^-$(mg/l)	129	0.00	87.39	11.46	15.61
$SO4^{2-}$(mg/l)	129	0.00	265.00	44.18	60.88
$HCO3^-$(mg/l)	129	10.35	521.11	258.04	109.29
K^+(mg/l)	129	0.24	47.30	3.88	5.14
Na^+(mg/l)	129	0.20	375.02	68.05	72.36
Ca^{2+}(mg/l)	129	0.30	167.20	46.00	30.44
Mg^{2+}(mg/l)	129	0.05	41.50	12.01	8.89

Table 11: Summary of the mean hydrochemical composition of sub-groups (Clusters) (EC in µS/cm), all others in mg/l)

Group	Subgroup/ Cluster	PH	EC	TDS	Cl^-	$SO4^{2-}$	HCO_3^-	K^+	Na^+	Ca^{2+}	Mg^{2+}
Group -1	1(n=37)	7.82	348.5	164.61	7.94	8.37	146.8	1.85	27.89	76.3	22.48
	2(n=35)	7.45	570.8	276.53	14.9	11.75	289.7	6.7	49.94	47.39	11.06
Group-2	3(n=32)	7.58	667.5	332	57.05	77.15	325.4	3.12	70.45	25.49	6.03
	4(n=25)	7.98	951	473	141.5	133.9	211.9	6.64	191.3	23.37	5.53

Table 12: Summary of interpretation for the HCA major groups and Subgroups/clusters.

Group-I Cluster-1 (n=37)	The majority of the plateau samples, where the main lithological unit is highly fractured and weathered upper basalt, and the rift margin samples including highland springs (S#1, S#3, S#5, S#6, S#7, and S#8) which have been emanating from the foot of the upper basalt, and boreholes found at the beginning of the Borkena catchment in the northern part of the study area where the main lithological unit is highly fractured and weathered upper basalt with minor intercalations of palaeosols (like BH#4, BH#22, and BH #39), etc., were grouped in cluster1 and the dominant water type is **Ca-(Mg)-HCO3.** The mean TDS and EC values of this cluster are 164.61mg/l and 348.5µs/cm respectively. These groups of samples were plotted along the LMWL. Combining the above interpretations, the source of recharge is recently recharged in which the groundwater is not undergoing much interaction.
Group-I Cluster-2 (n=35)	The dominant water type in this cluster is **Ca-Na-HCO3 and Ca-(Mg)-Na-HCO3** and is mainly found in the rift margin, particularly in the marginal grabens, and plateau samples near the water divide between the two adjacent basins. From the available boreholes, the main lithological units from top to bottom both in the plateau and rift margin areas are, alluvial deposits, and fractured and weathered upper basalt. Sometimes, this water type was also found in the lower basalt aquifer. The mean TDS and EC values of this cluster are 276.53mg/l and 570.8µs/cm respectively, and can be taken as mixed water type, having recharge source from precipitation and local to intermediate groundwater flow.
Group-II Cluster3 (n=32)	The dominant water types in this cluster are **Na-Ca-HCO3 and Na-HCO3** which are found in the plateau, rift margins, and rift floor of the study area. In the plateau part of the study area, these water types are associated with deep wells (500m) having similar lithological log with the rift margin where the alluvial deposit, fractured acidic rocks mainly ignimbrite, and the lower columnar basalt are the main lithological units. In the case of the rift floor, the main lithological units are lacustrine deposits underlain by fractured and weathered Stratoid basalt. This cluster has a mean TDS and EC values of 332mg/l and 667.5 µs/cm respectively. These groups of samples are depleted in their isotopic signatures and plotted to the depleted side containing LMWL and GMWL. Combining these interpretations, they have similar sources of groundwater recharge, mainly from the adjacent plateau.
Group-II Cluster4 (n=25)	The dominant water type in this cluster is **Na-HCO3-SO4 and Na-HCO3-Cl** and is mainly distributed in the rift margin, and rift floor areas. In the rift margin, the lithological units are lacustrine deposits underlain by fractured and weathered Dalha basalt and acidic rocks like Mabla rhyolites. In the rift floor, the sources are thermal waters having a maximum temperature of 51^{o}c and located along the NE-SW trending Wenji fault belt and the lithology is lacustrine deposit underlained by Afar stratoid series. This cluster has mean TDS and EC values of 473 mg/l and 951µs/cm respectively, and depleted in their isotopic signature. Integrating the above analysis and interpretation, the recharge source is regional.



NB: RM: Rift margin, RF: Rift floor, P: Plateau

Figure 42: Dendrogram diagram of water samples

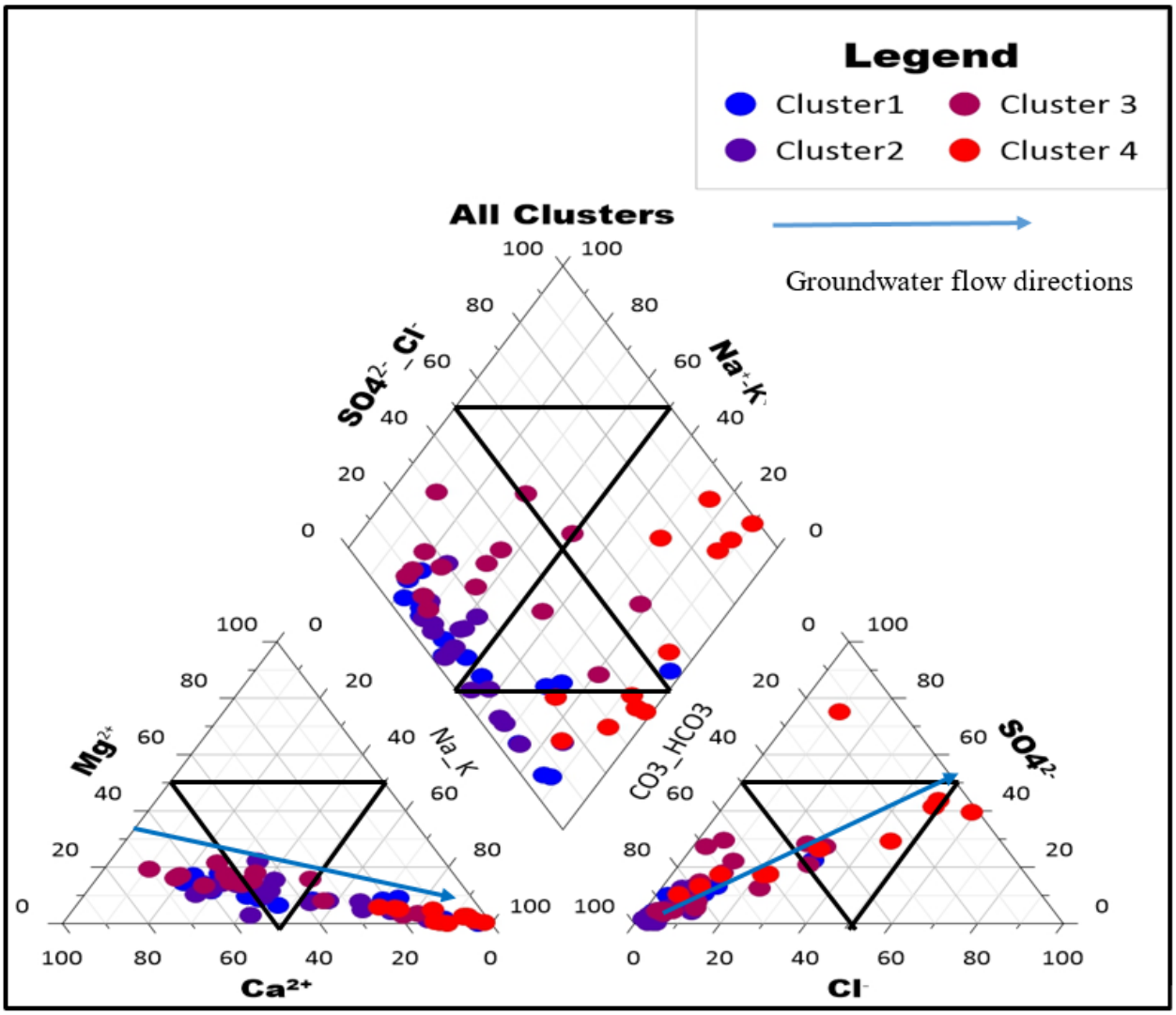


Figure 43: Piper plots of all clusters

3.2.4.3 Statistical Correlation and Principal Component Analysis (PCA)

Statistical correlation matrix and Principal Component Analysis (PCA) were used to examine the water samples' physiochemical characteristics to comprehend hydrochemical evolution and geochemical reactions(Sayadi et al., 2014, Tanasković et al., 2012). The physical components and geochemical processes influencing water chemistry have been identified through the application of Principal Component Analysis (PCA)(Abdi et al, 2010; Ravikumar & Somashekar, 2017).

Based on the correlation matrix displayed in Table 13, the elements Na^+, K^+, Cl^-, SO_4^{2-}, EC, and TDS have positive correlations with one another but negative correlations with elevation, suggesting that they progressively increase along the groundwater flow direction (the rift floor). On the other hand, Ca^{2+} and Mg^{2+} are positively correlated with elevation and HCO_3^-, but negatively correlated with Na^+, K^+, Cl^-, SO_4^{2-}, TDS, and EC. This shows that Ca^{2+} and Mg^{2+} are the dominant hydrochemical parameters of

groundwater in high-elevation areas(plateau) where groundwater is in an early stage of recharge and their concentrations decrease along the groundwater flow direction (rift floor). The negative correlation of Ca^{2+} and Mg^{2+} to Na^{+} and K^{+} indicates a geochemical reaction that removes the divalent cations and the addition of Na^{+} and K^{+} along the flow direction due to cation exchange and silicate weathering of acidic rocks (Figure 44). As a result, the water type has evolved from Ca-HCO_3 to Na–HCO_3 from the plateau towards the rift floor.

Table 13: Correlation matrix of variables

Parameters	*Alt*	*PH*	*EC*	*TDS*	*Cl*	*NO3*	*SO4*	*HCO3*	*K*	*Na*	*Ca*	*Mg*
Alt	1											
PH	-0.099	1										
EC	-0.68	0.01	1									
TDS	-0.668	-0.017	0.978	1								
Cl^-	-0.53	0.126	0.732	0.742	1							
$NO3^-$	-0.141	-0.258	0.316	0.272	0.223	1						
$SO4^{2-}$	-0.576	0.092	0.79	0.799	0.756	0.169	1					
$HCO3^-$	-0.271	-0.152	0.382	0.362	-0.087	0.134	0.03	1				
K^+	-0.3	-0.179	0.252	0.269	0.183	0.072	0.174	0.175	1			
Na^+	-0.623	0.264	0.727	0.75	0.723	-0.077	0.836	0.177	0.19	1		
Ca^{2+}	0.661	-0.41	0.34	0.304	0.141	**0.587**	0.017	**0.529**	0.104	-0.198	1	
Mg^{2+}	**0.525**	-0.278	0.306	0.244	0.056	**0.575**	-0.017	**0.538**	0.048	-0.238	0.838	1

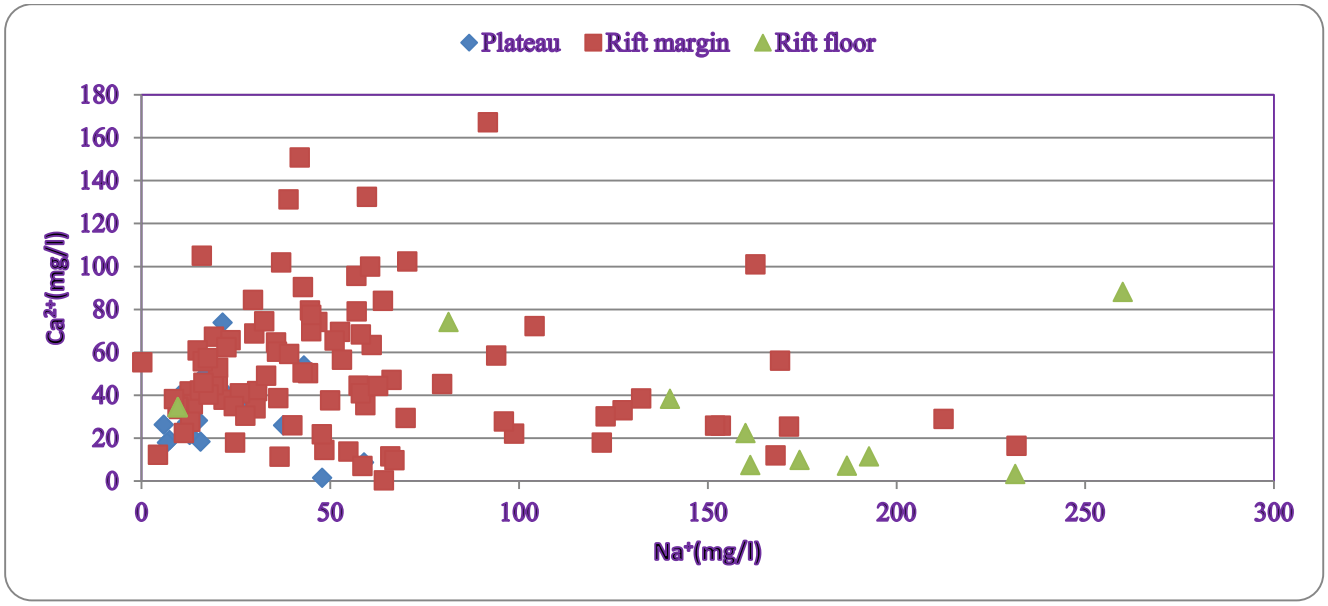


Figure 44: Na^{+} vs Ca^{2+} correlation along the plateau, Rift margin, and Rift floor

Using the Principal Component Analysis (PCA), a total of four (4) PCs, explaining 85.12 % of the total variance was extracted (Table 14). The loading of the variables for the PCs is represented by the numbers, and the degree of similarity between the variables and the PCs describes how well the variance of the variable is explained.

Principal component No. 1: Of the overall variation, 40.36% was explained by this PC. It has significant positive loading for EC, TDS, Na^+, $SO4^{2-,}$ and Cl^- and a negative loading for Ca^{2+} and $Mg^{2+.}$ This PC corresponds to clusters 3 and 4 of group II of the HCA classification, which represents the Na-dominated waters of the plateau, rift margin and rift floor with the Na-HCO3-($SO4^{2-}$/Cl^-) water type. The high positive loading of Na^+ and the negative loading of Ca^{2+} at this factor level are explained by the natural hydrogeochemical evolution of groundwater through the interaction between groundwater and geologic medium which leads to a cation exchange between Na^+ and Ca^{2+} along the flow direction, besides to the weathering of acidic rocks along the groundwater flow directions, i.e. towards the rift floor. The high positive charges of PC1 for Cl^- and SO_4^{2-} and the less positive charges for $HCO3^-$ mark a geochemical reaction that causes the evolution of Cl^- and $SO4^{2-}$ along the flow direction.

Principal component No. 2: This PC accounts for 25.92% of the variance overall and shows significant positive loading for Ca^{2+} and Mg^{2+} and negative loading for Na^+, EC, TDS, $SO4^{2-}$ and Cl^-. This PC corresponds to cluster 1 of group I of the HCA classification, which represents the Ca^{2+} and Mg^{2+} dominated waters of the Plateau areas and the uplands of the rift margin in the northern part and is thought to be in an early stage of groundwater recharge. In addition, this principal component contains a moderate positive load of HCO_3^- and NO_3^-, with the NO_3^- being associated with anthropogenic contamination in the shallow wells (SBH) on the Rift margin.

Principal component No. 3: This PC contributes 9.67% of the total variance and shows a moderately positive loading of HCO_3^- and a less positive loading of Ca^{2+} and Mg^{2+}, but a relatively higher than Na^+ and K^+. This principal component corresponds to cluster 2 of group I of the HCA classification, which is mainly found in the transition between the plateau and rift margin, having mixed water type.

Principal component No. 4*:* This PC contributes 9.15 % to the total variance and shows a moderately positive loading of pH and HCO_3^- and a less positive loading of Mg^{2+}, $Ca^{2+,}$ and Na^+. This principal component corresponds to cluster 2 of the HCA classification, which represents a mixed water type where there are no dominant cations in the water chemistry.

The plot of PC coordinates on the trapezoid along the X, Y, and Z axis (Figure 45) further makes clear how well the factors explain the variance. This figure provides the extent to which each variable is represented by the current set of PCs; that means, the closer the variable plotted along a certain axis, the

better the PC explains the variance and vice versa. As shown in the figure Cl^{-}, and $SO4^{2-}$, TDS, EC, and Na^{+} are plotted closer to unity on the PC#1 coordinate plane(X axis). The concentrations of these variables are increasing in groundwater along the flow direction and with greater depth and represent **clusters 3 and 4** of the HCA. On the other hand Ca^{2+} and Mg^{2+} are plotted closer to unity on the PC2 coordinate plane(Y axis), and their concentrations are decreasing along the groundwater flow directions and with depth due to the geochemical reaction which involves the dissolution of Na-silicate minerals and the cation exchange along the flow direction and represents mainly plateau waters and the uplands of rift margin of **Cluster 1**of the HCA**.**

Table 14: Principal Component classifications

Component Matrix				
	Principal Components			
	1	**2**	**3**	**4**
PH	-.028	-.555	-.212	**.541**
EC(µs/cm)	**.962**	-.026	.016	.091
TDS	**.957**	-.069	.052	.057
Cl(mg/l)	**.806**	-.297	-.260	-.181
NO3(mg/l)	.388	**.581**	-.455	-.267
SO4(mg/l)	**.842**	-.368	-.110	-.098
HCO3(mg/l)	.372	**.504**	**.495**	**.551**
K(mg/l)	.319	.063	.013	.492
Na(mg/l)	**.762**	-.551	.192	.106
Ca(mg/l)	-.392	**.846**	**.385**	.045
Mg(mg/l)	-.335	**.837**	.215	.173
Extraction Method: Principal Component Analysis.				
a. 4 components extracted.				

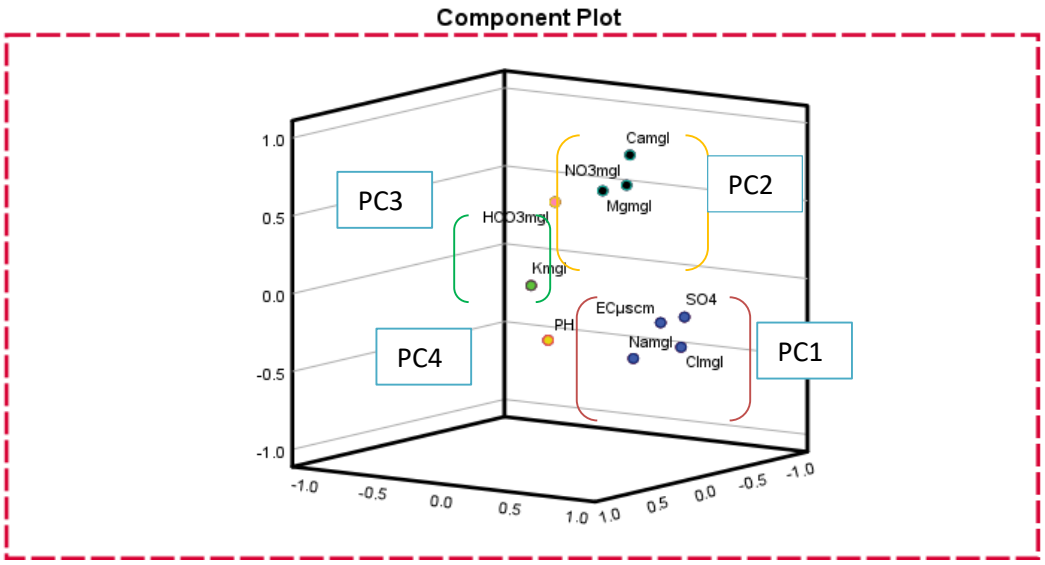


Figure 45: Principal component plots

3.2.5 Structural analysis and their role in transferring groundwater

From the recorded earthquake history, seismic activity in the Afar depression has caused several large seismic events along the western Afar rift margin, like a landslide that demolished Ankober; and a swarm of earthquakes that destroyed Majete and Karakore(Alemayehu & Asefa, 2023, Gouin, 1970). The region still exhibits active deformation as evidenced by the concentration of seismic activity along the marginal graben's eastern boundary fault (Zwaan, Corti, Sani, et al., 2020b and reference therein, Illsley-Kemp et al., 2018). This propagation of seismic activity from the rift floor to the western rift margin, and finally to the northwestern plateau suggests that the plateau and rift margin are in direct contact with the rift floor via transverse structures mainly faults and lineaments. Besides, the alignment of major dykes, elliptically elongated cinder cones, rhyolitic domes, and open fractures could trigger the transfer of seismic activity from the Afar rift floor to the western rift margin, and finally to the plateau area(Kehali et al., 2021, Robson et al., 2018, Hagag & Obermeyer, 2017, Uemura, 1994, Acocella et al., 2004).

From the structural interpretations, the western Afar Rift margin and the northwest plateau are connected by regional transverse structures that run in both NW-SE (Red Sea rift trend) and NE-SW (MER trend) directions, like the Debresina Fault, Dese-Kombolcha –Bati Fault, and the Wonji Fault Belt systems. Besides, the western rift margin and rift floor are connected through younger transverse structures which could be faults or lineaments, dykes, elliptically elongated cinder cones, rhyolitic domes, and open fractures. They generally exist across the intensively faulted accommodation zones mainly between the adjacent marginal grabens and the two rift arms of the main Ethiopian Rift(NE-SW), and the southern Red Sea Rift of the western Afar Rift margin(NW-SE)(Acocella et al., 2004, Tesfaye et al., 2003, Zwaan, Corti, Sani, et al., 2020). These structures cut the NW-SE oriented boundary faults obliquely in the NE-SW trend and sometimes orthogonally in an E-W direction (Stab et al., 2016, Zwaan, Corti, Sani, et al., 2020a) and propagate from the rift floor towards the rift margin. They are Quaternary in age and younger than the rift-bounding fault (Barberi et al., 1972), and sometimes can be called connectors. These structures facilitate the transmission of seismic activity from the rift floor to the rift margin and finally to the plateau. Accordingly, these structures likely supports the flow of deep groundwater from the plateau to the western marginal grabens, and finally delayed deep flow into the Afar Rift floor aquifer and serves as a preferential pathway (Faulds & Varga, 1998, Younes & McClay, 2002, Mozafari, 2022). Hence, the conveyance of groundwater from the plateau to the rift margin, and finally to the rift floor is thus greatly dependent upon the existence of these transverse structures (Figure 46). This shows that there is no overall barrier effect of the marginal grabens on the regional groundwater flow to the rift floor.

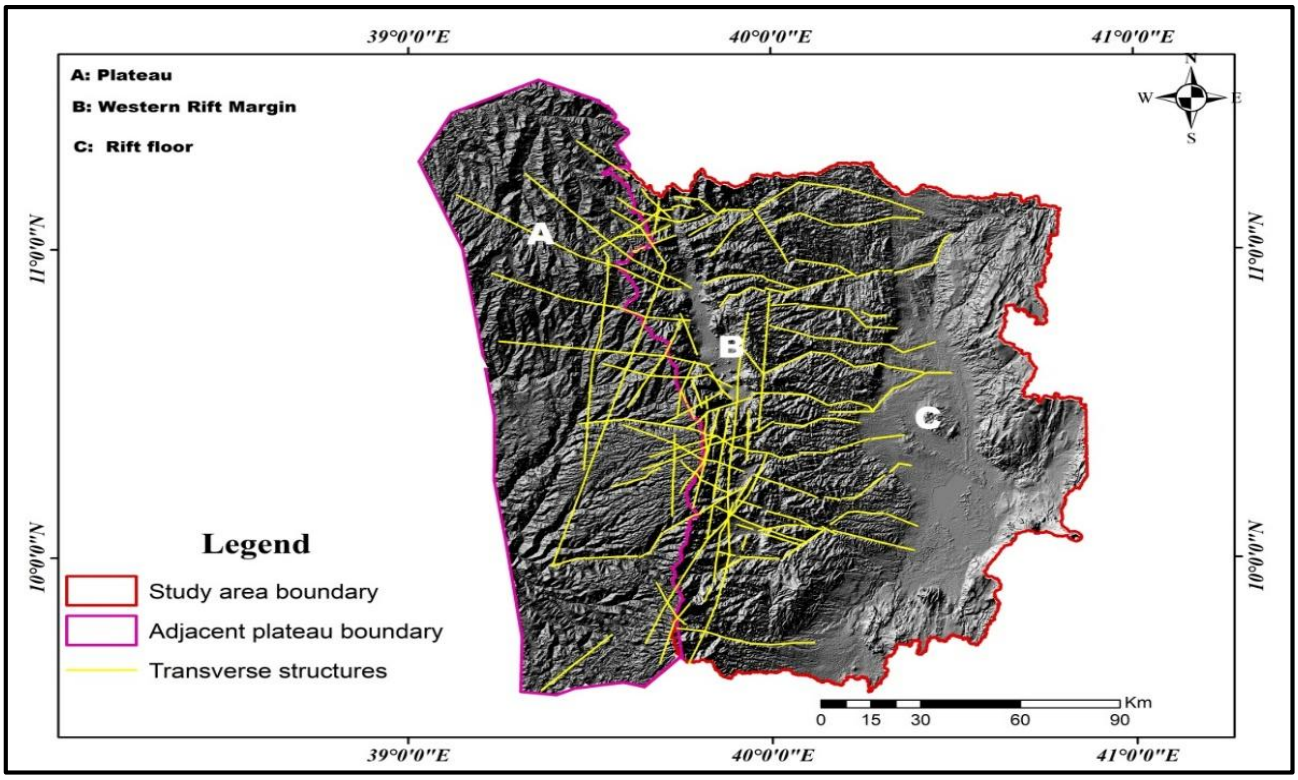


Figure 46: Transverse structures from plateau to Rift margin, Rift margin to the Rift floor

3.3 Summary of the Source and Mechanisms of Groundwater Recharge

Based on the geological study and the lithostratigraphic correlations of the boreholes both on the plateau and on the rift margin, the trap series mainly the columnar jointed lower basalt extended continuously from the northwestern plateau to the rift margin without any discontinuities. In addition, regional transverse structures running NW-SE and NE-SW connect the northwestern plateau with the western Afar rift margin. The presence of these features plays a significant role in the transfer of deep groundwater from the northwestern plateau (Blue Nile) to the western Afar Rift margin (Awash Basin). In the case of the rift floor, younger transverse structures have extended from the rift floor to the marginal grabens along the accommodation zones, likely supporting the delayed and preferential deep groundwater flow from the western marginal grabens to the Afar rift floor aquifer.

The majority of the plateau samples, where the main lithological unit is highly fractured and weathered upper basalt and boreholes found at the beginning of the Borkena catchment of the Awash basin in the northern part of the study area with a similar lithological unit with minor intercalations of palaeosols are related to the Ca-(Mg)-HCO3 water type, with low TDS values. According to models of groundwater chemical evolution developed by Chebotarev, 1955, these water groups correspond to freshly recharged groundwater and/or water in the early geochemical evolution stages that have not yet seen major water-rock interactions. Furthermore, data from analyses of stable isotopes of the boreholes were plotted close to and along the LMWL, which reveals that the source of recharge is local precipitation.

The preferential orientation of the highland springs distributed along the rift escarpments, their considerable yield (30-70 l/s) from a small recharging catchment area, Ca-(Mg)-HCO3 water type, the very low TDS values, and the relatively depleted isotopic signature suggest that the groundwater is at an early recharge stage, not undergoing major groundwater development. Hence precipitation, and regional groundwater flowing from the adjacent plateau is the main source of recharge, through the NW-SE and NE-SW trending transverse structures, and the extended trap series to the western rift margin. The deep groundwater in the rift margin is associated with moderately mineralized, Na-Ca-HCO3 and Na-HCO3 water type and depleted isotope content similar to the deep groundwater of the plateau area. This indicates that deep circulating groundwater is present from the Northwest Plateau (NWP) in the Blue Nile Basin to the western rift margin of the Awash Basin. This is due to the presence of continual columnar jointed lower basalt connecting the two basins and transverse structures trending NE-SW and NW-SE. In addition, the increase in TDS and EC values from the plateau to the rift margin and high Radon values in some of the boreholes in the marginal grabens is due to the fact that the groundwater has undergone prolonged residence time along the flow directions. Mixed water types are also present along the rift margin, suggesting that there is the mixing of groundwater from different sources, mainly from precipitation, and local to intermediate flow from the surrounding volcanic mountains, besides the regional flow. This is due to the presence of the overlying porous alluvial deposits and highly fractured volcanic rocks that surround the marginal grabens and facilitate infiltration of groundwater as well as circulation of deep groundwater from the plateau area.

The shallow aquifers in the rift floor exhibit high mineralization (due to the high evaporation effect), a Ca-HCO3 water type, enriched isotopic signatures, and low radon values. Integrating the hydrochemical and isotopic signatures the main source of recharge is local sources mainly from Awash River, tributaries, rainfall, flash floods, and stream channel loss, but are highly affected by evaporation as a result of high local temperature before recharging the aquifer. Such kind of recharge source is also identified by Ayenew, Kebede, et al., 2008, Bretzler et al., 2011, and Kebede et al., 2008. In contrast, the deep thermal groundwater boreholes in the rift floor are predominantly Na-HCO3/SO_4/Cl^- water type, isotopically depleted and highly mineralized, high Radon values which distinguishes them from the shallow systems, suggesting different recharge sources and mechanisms, mainly from the western Afar rift margin through the transverse structures.

The hydrochemical parameters along with the isotopic signatures of the deep aquifers in all the physiography and radon measurements conducted at the rift floor and rift margin in conjunction with geological and lithostratigraphic correlations demonstrate that deep circulating groundwater from the plateau area across the rift margin with little addition of local sources is the main source of recharge for

the deep groundwater systems of the Western Afar rift margin and associated rift floor due to the presence of preferential path ways. Based on this assumption, the main source of recharge along the groundwater flow direction (SW-NE) from the North Western plateau to the Rift floor has been summarized and a conceptual groundwater flow model was developed and presented in Figure 47.

A: North Western Plateau (NWP)

- Direct recharge from precipitation infiltration and percolation to the shallow volcanic aquifers
- Recharge from intermediate to regional groundwater source and flow to the deep aquifer system.

B: Marginal Grabens (Western Afar Rift Margin)

- Direct recharge from precipitation and local to intermediate groundwater flow from the surrounding volcanic mountains along the overlying deposit and structures
- Deep groundwater recharge from the North Western plateau through the transverse structures and extended columnar jointed lower basalt from the former to the latter

C: Rift floor

- Recharge from rainfall, rivers, flash floods, and streams for shallow aquifer system
- Preferential deep groundwater flows from the marginal grabens to the deep volcanic aquifers of the rift floor through the transverse structures and is mainly along the accommodation zones.

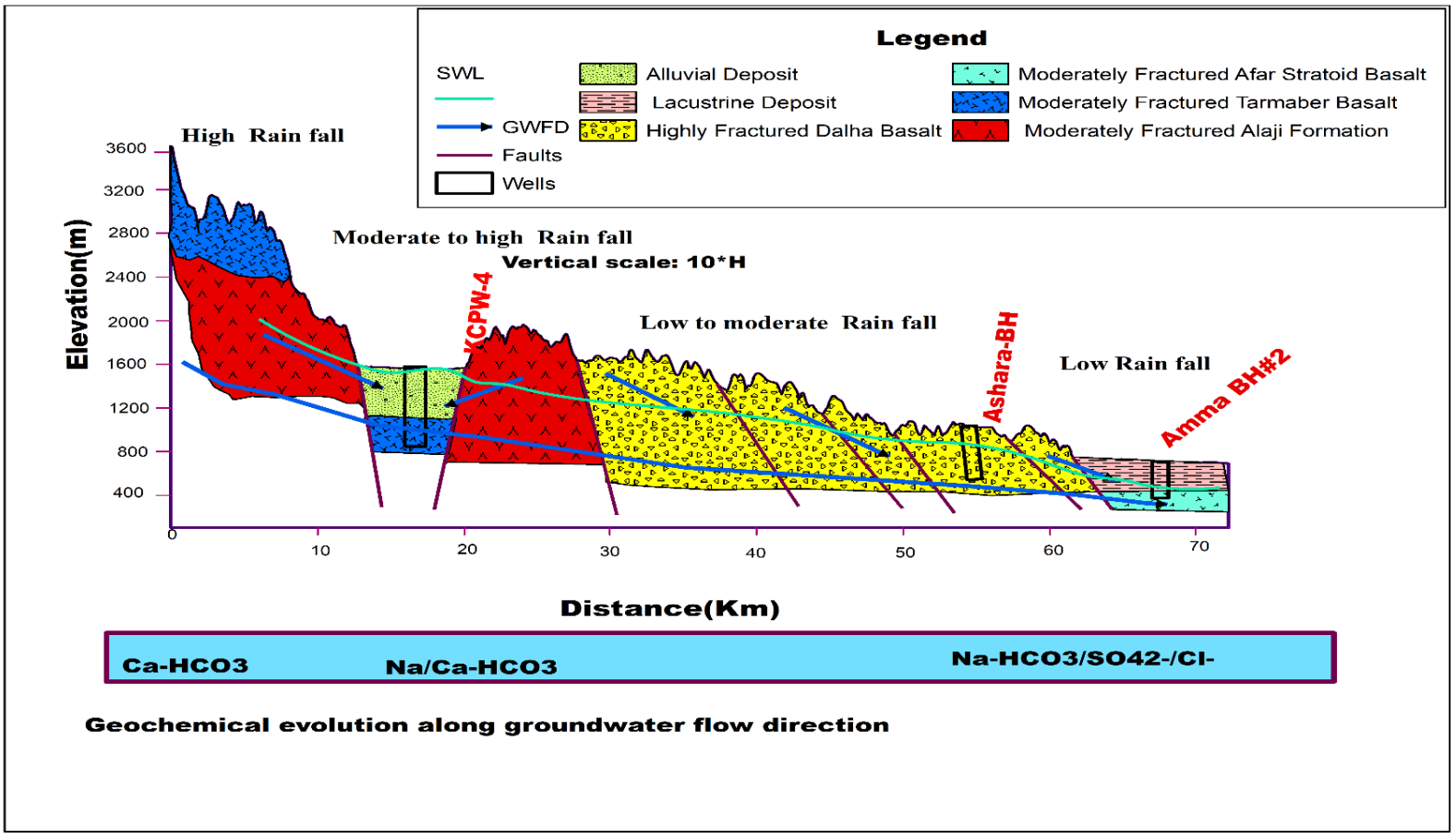


Figure 47: Conceptual groundwater flow model

Chapter Four: Groundwater Recharge Estimations

4.1 General

Groundwater recharge can occur naturally or artificially when water percolates into the ground, reaches the water table, and is added to the aquifer (Diouf et al., 2016, Huang et al., 2023). This process is highly influenced by the amount and duration of rainfall, type of land use and land cover, slope, geology, tectonics, depth of the water table, and soil type (Penner et al., 2023, Sibanda et al., 2009). Although the parameter is the least known in hydrogeology (Atawneh et al., 2021, Scanlon et al., 2002), it emphasizes the need to quantitatively assess the spatial and temporal distribution of groundwater recharge for sustainable resource use and management(de Vries & Simmers, 2002, Kumar et al., 1997). However, one of the most difficult tasks is the estimation of realistic recharge rates, especially for arid and semi-arid regions (Di Lena et al., 2023, Glendon et al., 1988) due to differences in soil properties, topography, climate, geology, tectonics and land use (Fetter, 2001, Karlović et al., 2022). In addition, it is often very difficult to estimate recharge directly and must instead be done using indirect methods(Obuobie et al., 2012, Kaewdum & Chotpantarat, 2021, King et al., 2017, Mohan et al., 2018). Furthermore, when estimating recharge using various methods, obtaining high-quality and sufficient data is challenging, which is more pronounced in tectonically active regions like the Afar depression. In the Afar depression the mechanisms and estimations of the rate of groundwater recharge are highly complex, as the groundwater flow is highly controlled by geology and structures. Hence, considering these constraints, it is advisable to estimate the temporal and spatial distribution of the groundwater recharge of the area using various methods(Achraf et al., 2017, Afrifa et al., 2017). The importance of this approach is that the recharge estimates from all methods are compared and their applicability under different hydrological, hydrogeological, and climatic conditions is evaluated and recommended. In addition, the influence of geology and structure on recharge, especially in rift aquifers, is adequately assessed and examined.

4.2 Data Processing

4.2.1 Determination of areal depth of precipitation

Rainfall measurement is a point observation and may not be used as a representative value for the area under consideration. Therefore, it is necessary to obtain an effective uniform depth of rainfall of the catchment to get more reliable and representative results(Al-hallaq et al., 2008). Accordingly, the mean annual rainfall of the study area is estimated by Arithmetic, Thiessen Polygon, and Isohyetal methods.

Arithmetic Mean Method: This method implies summing up all the rainfall values from all the rain gauging stations and then dividing it by the number of stations in that basin using the following formula(Taesombat & Sriwongsitanon, 2009): Equation 8: $P= (P_1+P_2+P_3+-----+Pn)/n$,

Where P is the average depth of precipitation of the area, P_1, P_2, P_3, and P_n are the rainfall records at stations 1, 2, 3, etc. and n is the number of meteorological stations. Accordingly, the mean areal depth of rainfall of the study area is estimated to be 1009.59 mm, where the minimum and maximum mean annual rainfall is 324.6 mm/year and 1900mm/year respectively (Appendices 5).

Thiessen polygon Method: This method provides for non-uniform distribution of rain gauge by determining a weighted factor for each gauge and it is generally more accurate than the arithmetic mean method(Gidafie et al., 2016). The Thiessen Polygon method of determining the areal depth of precipitation assumes that at any point in the area under consideration, the rainfall is the same as that as the nearest gauge so the depth recorded at a given gauge is applied out to a distance halfway to the next station in any direction. The relative weights for each gauge are determined from the corresponding areas created in a Thiessen polygon network; the boundaries of the Polygons are formed by the perpendicular bisectors of the lines joining adjacent gauges(Fiedler, 2003). The Thiessen polygon has been prepared using Arc GIS 10.3(Figure 48), and the average depth of rainfall is determined using Equation 9. Accordingly, the areal depth rainfall of the study area is determined to be 843mm/year (Appendices 6).

Equation 9: $P = \frac{P_1A_1+P_2A_2+P_3A_3+\text{--------}+P_nA_n}{A_t}$

Where P is areal average precipitation, P1, P_2 … P_n are mean annual rainfall recorded at each rainfall station and A1, A2...A_n are polygonal areas around each gauging station enclosed in the catchment and A_t is the total area of the catchment.

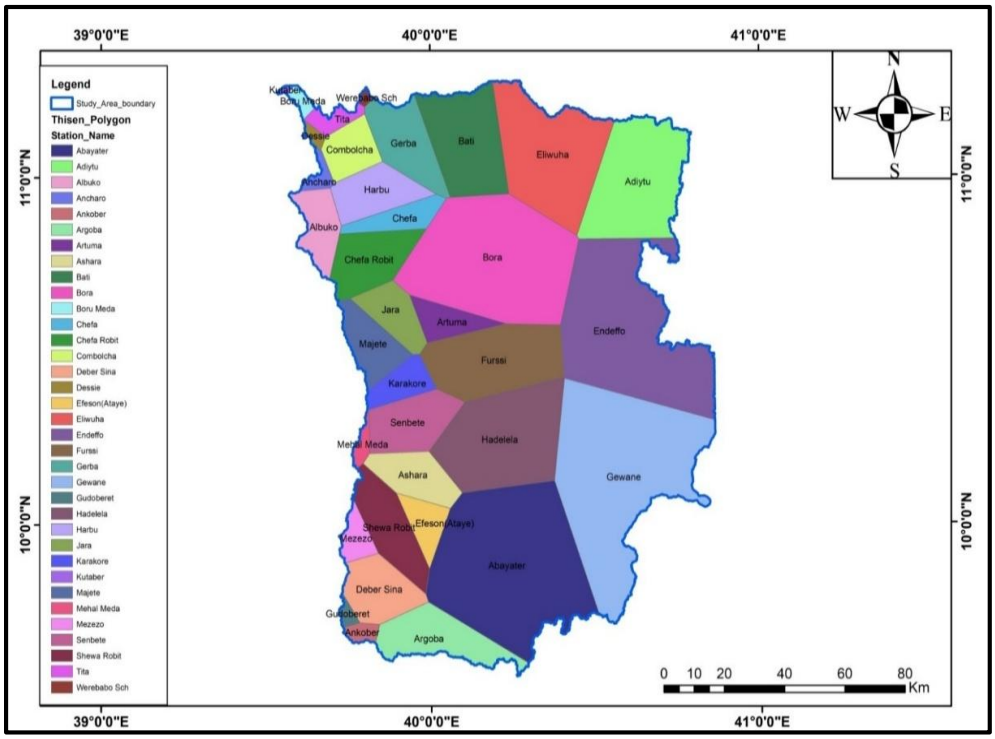


Figure 48: Thiessen Polygon Map

Isohyetal method: the Isohyetal method is used to estimate the areal depth of rainfall of the study area as it takes into account the effects of physiographic factors such as elevation, slope, distance from the coast, and exposure to rain-bearing winds (Fiedler et al., 2003, Penkova & Shiklomanov, 2007). It is employed by drawing contours of equal areal depth of precipitation and then measuring their inter-Isohyetal area (Figure 49), and determined by the following equation.

Equation 10**:** $P = \frac{P_1A_1+P_2A_2+P_3A_3+--------+P_nA_n}{A_t}$

Where P is areal average precipitation, P_1, P_2 … P_n are mean annual rainfall calculated between consecutive isohyets and A_1, A_2...A_n is the enclosed area found between Isohyets and A_t is the total area of the catchment. Using Equation 10, the mean annual rainfall of the study area computed is 834.2 mm (Appendices 7). This method is possibly the best of the three and has the advantage that the isohyets may be drawn to take account of local effects like prevailing wind and uneven topography (Al-Timimi et al., 2020). Accordingly, the mean annual rainfall of the study is taken to be 834.2mm/year and this value is used for further interpretation and analysis.

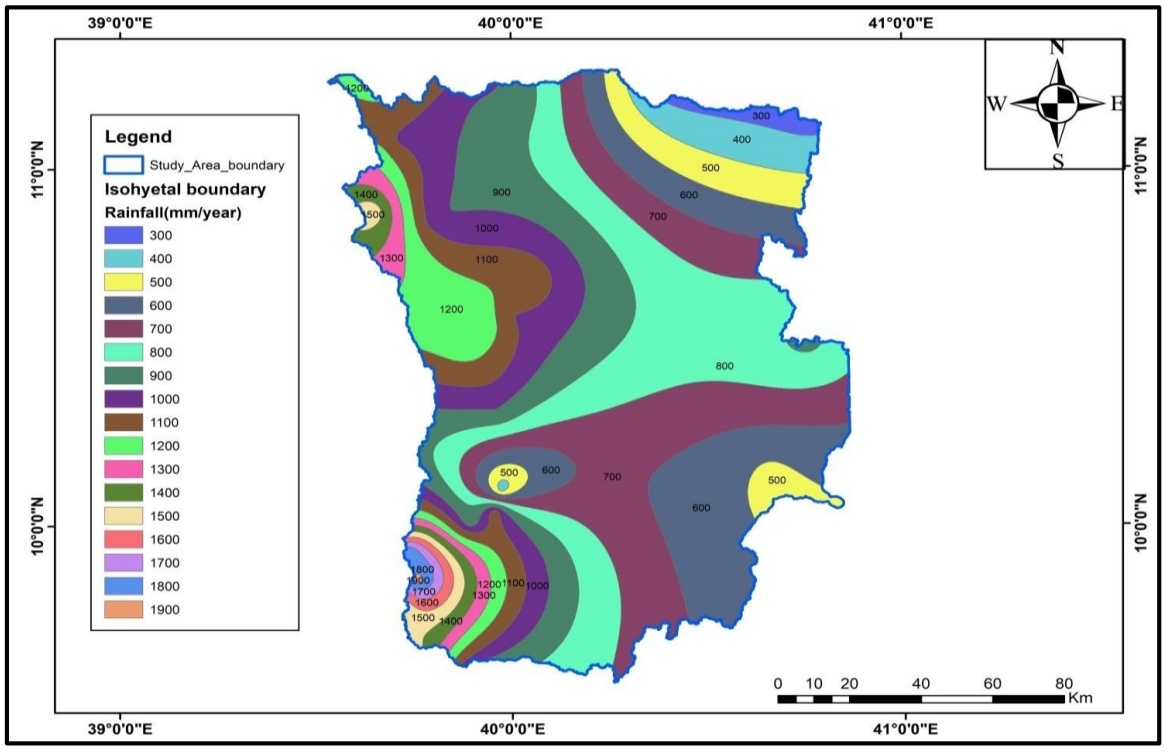


Figure 49: Isohyetal Map

Rainfall characteristics: To know the monthly distribution of rainfall and then to distinguish between rainy and dry seasons, the rainfall coefficient method developed by Gamachu, 1977 was used. This method involves the calculation of the "rainfall coefficient" for each month at the station, the coefficient being the ratio between the mean monthly rainfall and one-twelve of the annual mean.

$$R.C = \frac{(12Pm)}{Pa}$$ Equation 11

Where R.C is the Rainfall coefficient (unit less), P_m is the mean monthly rainfall (mm) and P_a is annual areal rainfall (mm).

Table 15: Classification scheme of monthly rainfall values (Source: Daniel Gemechu, 1977).

Designation	Rainfall Coefficient
Dry Month	Less than 0.6
Rainy Month	0.6 and above
Small Rains	0.6 to 0.9
Big Rains	1.0 and above
Moderate Concentration	1.0 to 1.9
High Concentration	2.0 to 2.9
Very High Concentration	3.0 and above

Based on this classification (**Table 15**), the study area has two rainfall regimes (bimodal rainfall characteristics) (**Table 16**). Hence, during March, April, and May the area has got small rain (Belg season) while in July, August, and September the area has heavy rain (Kiremit Season) and the other months are dry seasons with intermittent rainfall. Accordingly, dry months in this specific study area include January, February, June, October, November, and December. These months have a mean annual rainfall of 139.93mm/year, which is 16.77% of the mean annual rainfall. On the other hand, the mean annual rainfall during the rainy months is 694.3mm/year (83.22%) of the mean annual rainfall, where 186.64mm/year (22.37%) of the rainfall is contributed during the small rainy months (Belg) and 507.63mm/year (60.85%) of the rainfall is contributing during the big rainy months (Kiremit).

Table 16: Rainfall characteristics

	Dry months	**Rainy months (0.6 and above)**			
		Small rain	**Big Rain**		
			Moderate C	**High C**	**Very high C**
Months	Rc < 0.6	0.6<Rc<0.9	1<Rc<1.9	2<Rc<2.9	Rc≥3
	October	March	September		July
	November	April			August
	December	May			
	January				
	February				
	June				

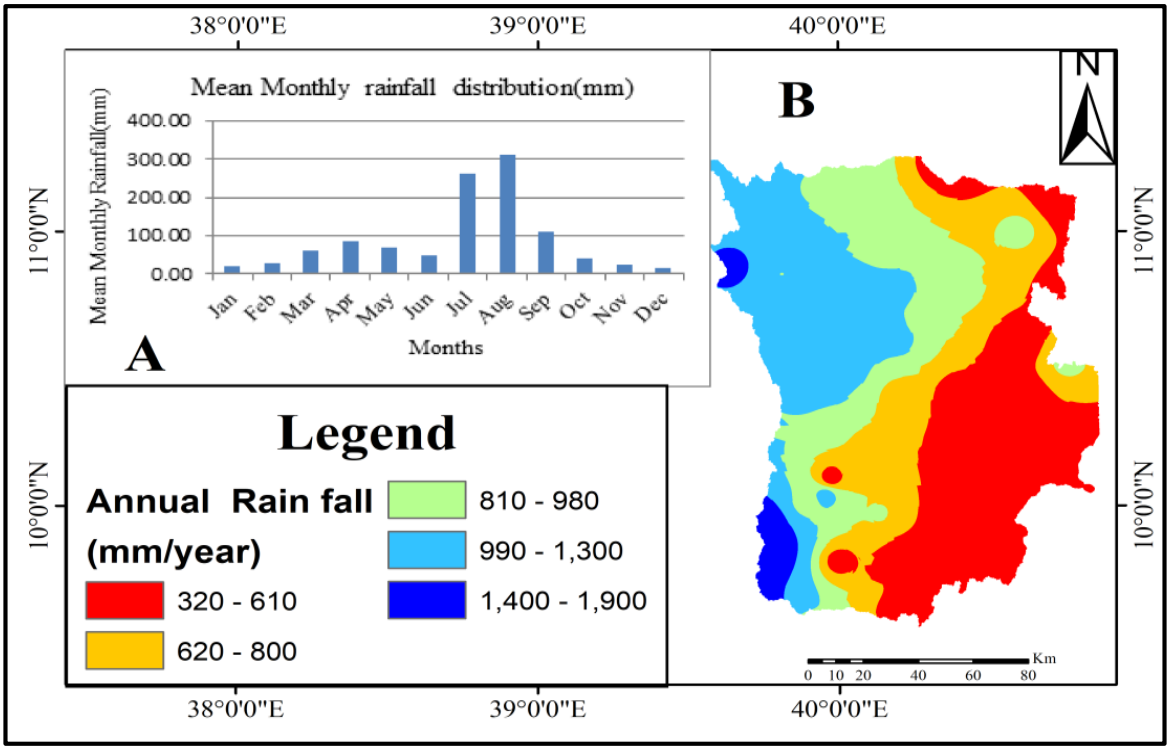


Figure 50: Mean monthly rainfall distribution (A): Spatial rainfall distribution (B)

4.2.2 Temperature

Air and water temperatures are dependent on solar radiation and have a direct influence on evaporation. It governs the rate at which water molecules leave the surface and enter the overlying air(Aliran et al., 2013). From the available 33 meteorological stations, the mean maximum and mean minimum as well as the mean monthly temperature of the study area is 27.88°c, 13.29°c, and 20.59°c respectively (Appendices 8).

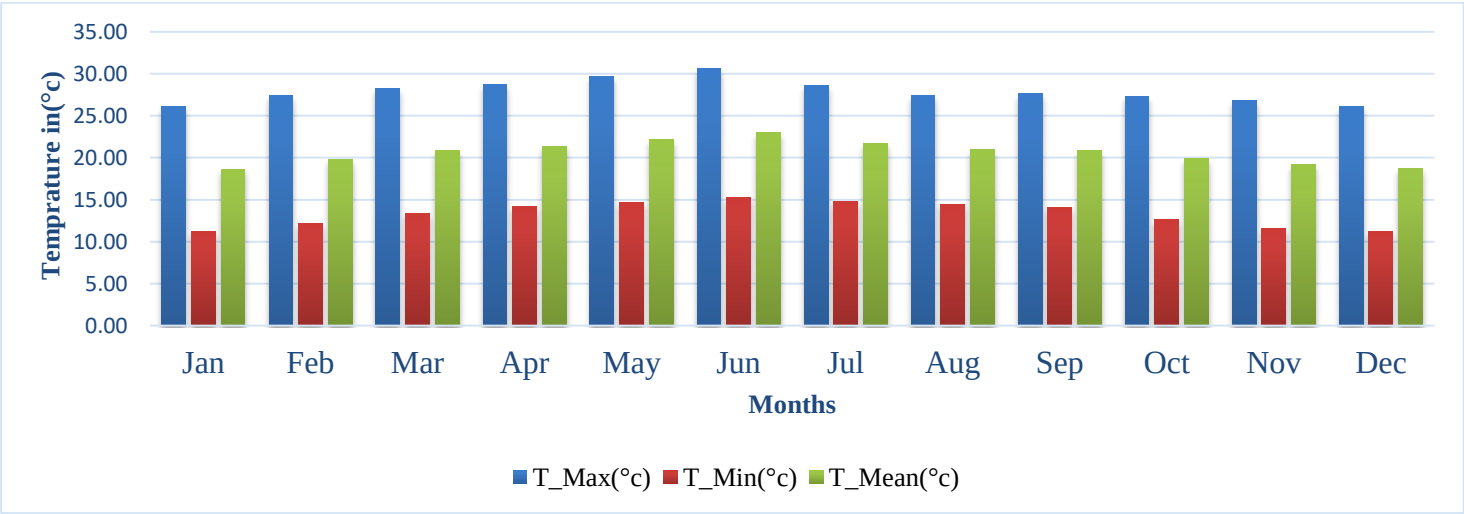


Figure 51: Mean Monthly max, min, and Mean temperature of the study area vs. Months

4.2.3 Sunshine hours

Although evaporation takes place almost without interruption during the daylight and the night, the process is most active under direct radiation from the sun. Therefore variation in sunshine hour is an important factor for evapotranspiration. In the study area, 13 stations have the daily sunshine hour data. From the available data the mean minimum, mean maximum, and mean sunshine hour of the study area is found to be 6.58, 8.79, and 7.49 respectively(Appendices 9).

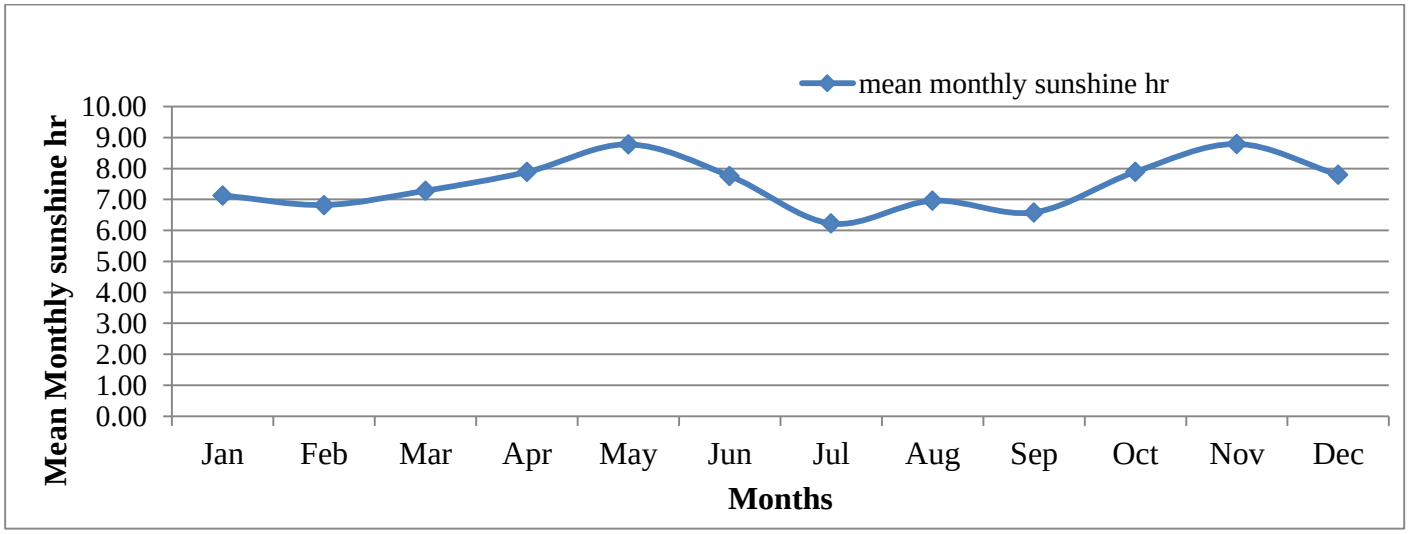


Figure 52: Mean monthly sunshine hour

4.2.4 Wind Speed

The rate of evaporation and evapotranspiration has a direct relation to and is strongly affected by wind speed. As water vaporizes into the atmosphere, the boundary layer between earth and air becomes increasingly more saturated so the water vapor has to be removed and replaced with drier air continuously. This movement of the air and moisture transfer is directly proportional to wind speed and turbulence (Shaw, 2005). In the study area, 11 stations have daily wind speed data. From the available data the mean minimum, mean maximum, and mean wind speed of the study area is found to be 1.22, 1.77, and 1.51m/sec respectively (Appendices 10).

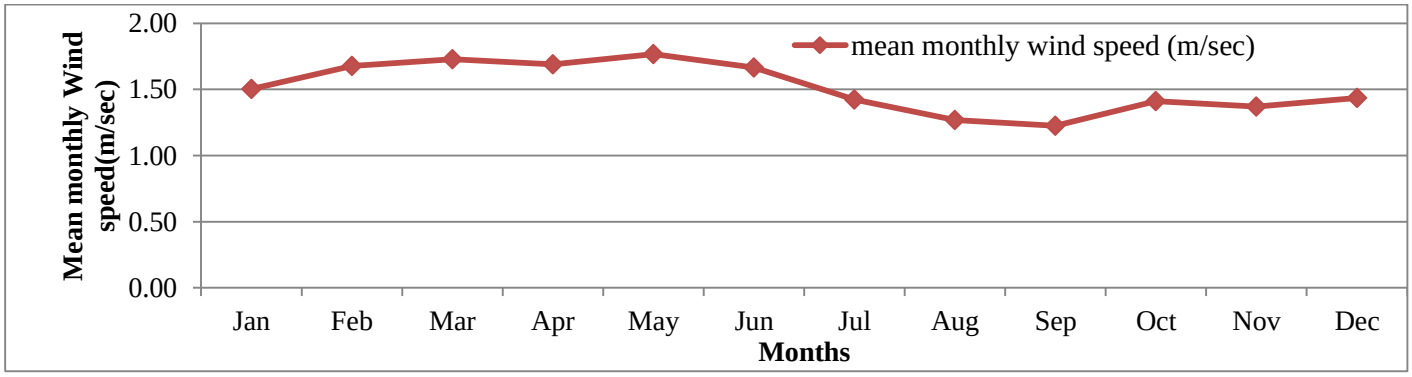


Figure 53: Mean monthly wind speed (m/sec)

4.2.5 Relative Humidity

Relative humidity is the ratio between the amount of water the ambient air holds and the amount it can hold at the same temperature (Shaw, 1995). The relative humidity expresses the degree of saturation of the air. It is a dimensionless quantity and is commonly given as a percentage. Monthly and annual means of humidity in the sub-basins were taken from available point data. In the study area, 12 stations have relative humidity, and the mean maximum, mean minimum and mean annual relative humidity of the study area is determined to be 71.81, 51.05, and 741.98 respectively(Appendices 11).

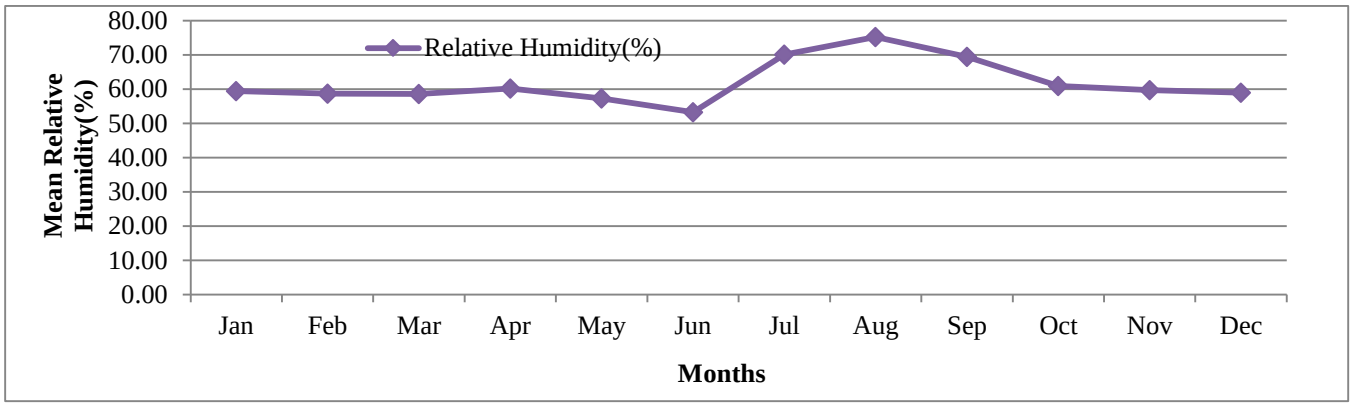


Figure 54: Mean monthly and annual Relative Humidity (%)

4.2.6 Land use and land cover

Land use and land cover influence groundwater recharge and potential by affecting evapotranspiration, soil erosion, and runoff(Abijith et al., 2020). Recharge under different land use areas, i.e., forest, grassland, cropland, urban land with concrete pavements, etc., also varies considerably. By integrating and modifying the data from different organizations and websites, the land used and land cover map of the study area has been developed using the Arc GIs 10.3 tool and the following classifications have been obtained (Table 17).

Table 17: Land use land cover and their area coverage

S.No	Land use land cover	Area coverage (km^2)	Coverage (%)	Remark
1	Dispersed Shrub	3379	17.66	
2	Bare Land	3380	17.66	
3	Rocky Bare Land	2105	11	
4	Agricultural Land	3750	19.6	
5	Dispersed Acacia	1150	6.01	
6	Acacia	484	2.53	
7	Shrub Land	3924	20.5	
8	Grass Land	102	0.53	
9	Eucalyptus	272	1.42	
10	Water Body	106	0.55	
11	Settlement	60	0.313	
12	Forest	420	2.19	
	Total	19132	100	

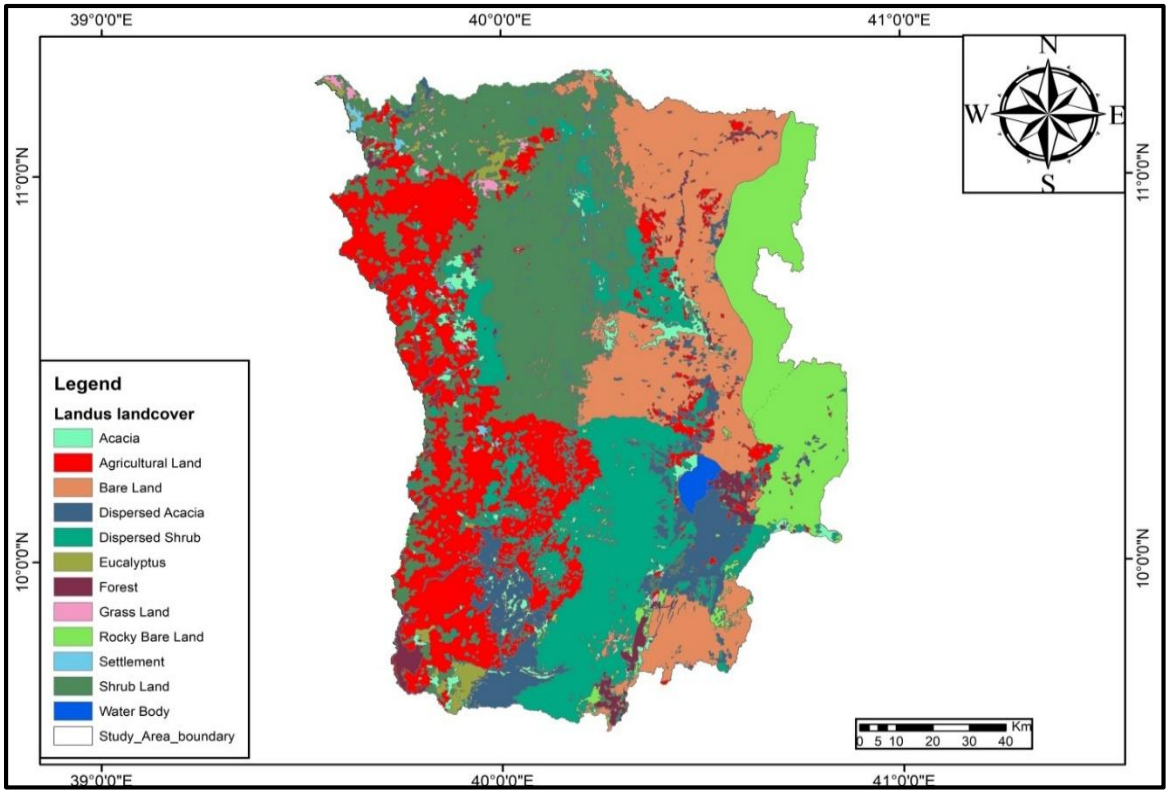


Figure 55: Land Use and Land Cover map of the study area

4.2.7 Soil

Soil is another factor that determines the infiltration capacity of a region which plays a vital role in groundwater recharge. By integrating and modifying the data from different organizations and websites, the soil map of the study area has been developed using the Arc GIs 10.3 tool (Figure 56) and the following classifications have been obtained.

Eutric Cambisols: These soil groups are mainly found at the western rift escarpments, especially at the northwestern, and southwestern of the research area. It covers 733 sq.km (3.8%) of the study area. According to the FAO textural classification, the top soil texture is medium-grained, the drainage class is moderately well and it's grouped under loam soil.

Vertic Cambisols: These soil groups are exposed along the southern and southeastern parts and cover 1664Sq.Km^2 (8.7%) of the study area. According to the FAO textural classification, the soil has less drainage property. As a result, it is grouped under clay silt which is near the escarpment, and clay away from the escarpment and towards the rift.

Eutric Fluvi Sols: These groups of soils are found in the Southern and Eastern parts and cover 3388 Sq. Km (17.7%) of the study area. Based on the FAO textural classification, the top soil texture is medium to fine-grained; their drainage class is moderate to less. Accordingly, the soil is grouped as Silty clay.

Eutric Leptosols: Cover 3328 covers Sq. Km (17.4%) of the area, and are mainly exposed near the western escarpment of the rift of the study area. According to the FAO textural classification, the top soil texture is imperfectly grained. The soil is grouped as sandy clay which is near the escarpment &gets finer towards the rift.

Lithic Leptosols: Cover 5873 sq. km (30.7%) of the area. These soil groups are entirely exposed along the western escarpment of the main rift of the study area. According to the FAO textural classification, the top soil texture is medium-grained, and sand, silt, and clay fractions are 50%, 30%, and 20% respectively. As a result, the soil is grouped as the sand which is found at the plateau and escarpments, and gets sandy loam away from the escarpment.

Haplic Solon Chaks: These soil groups are found at the lowland of the research area, especially at the center of the rift, which is along the flow direction, eastern and western course of the Awash River. The solo Chaks include soils that have a high concentration of ‘soluble salts’ at some time in the year. Common international names are 'saline soils' and 'salt-affected soils'(Schilling et al., 2021). According to FAO textural classification, topsoil texture is fine, drainage class low, and the composition of sand, silt, and clay is 50%, 28%, and 22% respectively. It covers 4152Sq.Km (21.7 %) of the study area including the water body called Yardi Lake. From the drilling of boreholes in the area, texturally it gets finer towards the center and is mainly composed of clay and silt.

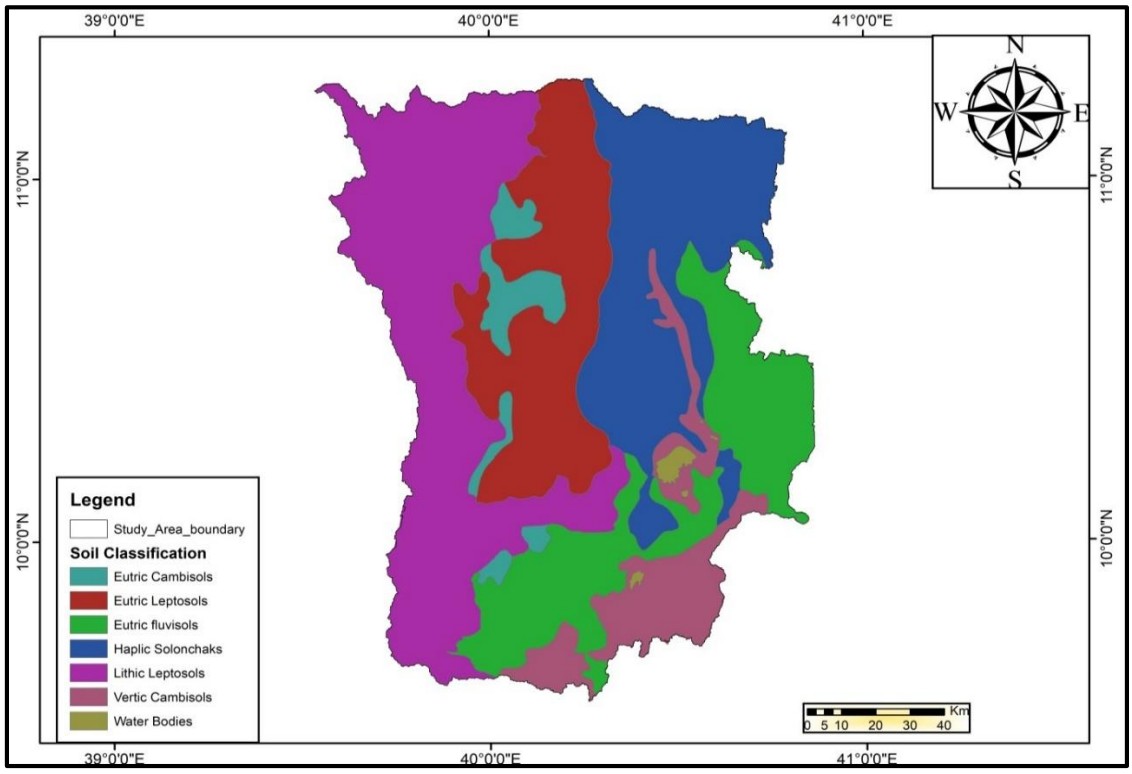


Figure 56: Soil map of the study area

4.2.8 Slope

The slope dominantly influences the infiltration, surface runoff, and groundwater recharge of a certain area. The steeper slope causes less recharge due to increased runoff, hence insufficient time for infiltration (Bhattacharya et al., 2021). In the study area, a Digital Elevation Model (DEM) with 30 m resolution was used to derive the slope using the ArcGIS 10.3 tool. Accordingly, the following classifications have been obtained (Figure 57).

Table 18: Slope and its area coverage

S.No	Slope Classes(Degree)	Description
1	0-4.9	Flat
2	5-11	Flat to Gentle
3	12-20	Gentle to Steep
4	21-29	Steep to very steep
5	30-88	Very steep

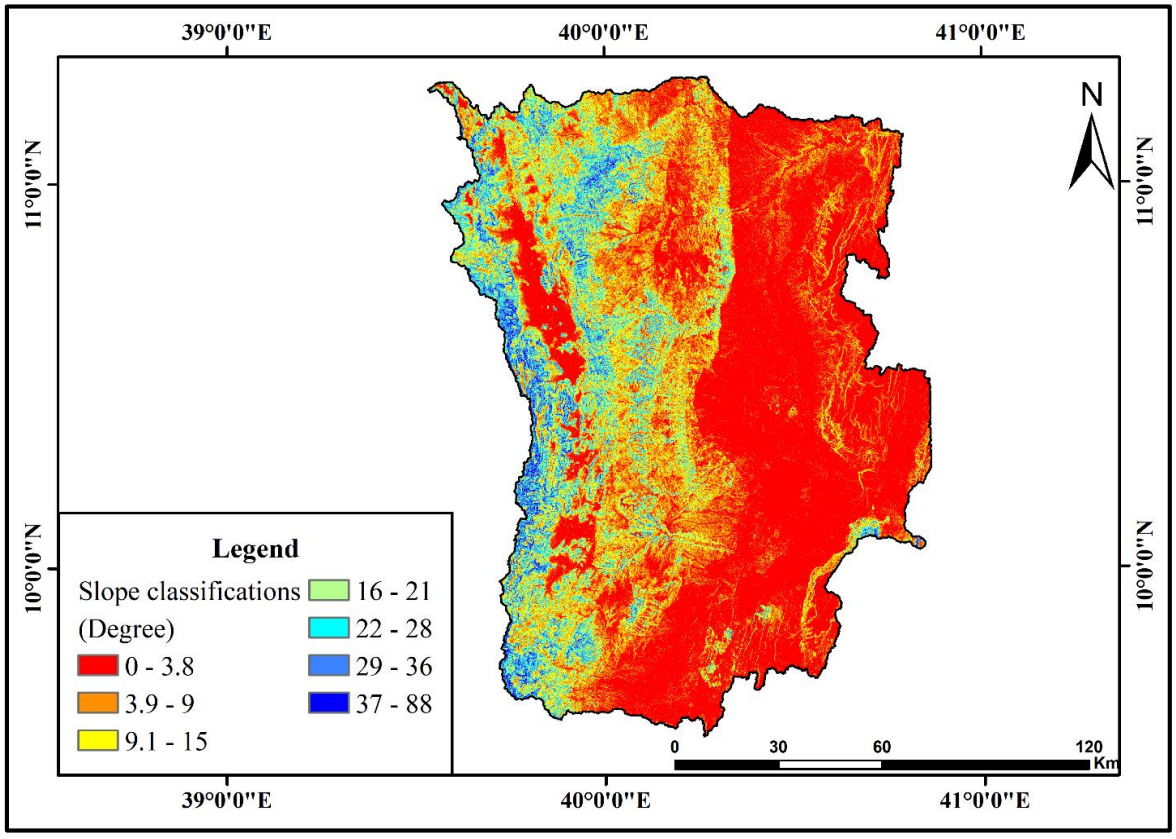


Figure 57: Slope map of the study area

4.3 Estimation of Hydro meteorological Variables

4.3.1 Potential Evapotranspiration (PET)

Potential evapotranspiration is evapotranspiration from vegetation cover if sufficient water is supplied to obtain optimum growth or the maximum amount of vapor that might be transferred under existing metrological conditions, water is not the limiting factor(D. Huang et al., 2021). Potential evapotranspiration can be calculated with various methods based on the available metrological data(Carter & Liang, 2019, Filgueiras et al., 2020). In this study, for the determination of potential evapotranspiration, Thornthwaite (Thornthwaite and Mather, 1957) and Penman combination methods were used.

Thornthwaite method uses air temperature as an index of the energy available for evapotranspiration, assuming that air temperature is correlated with the integrated effects of net radiation and other controls of evapotranspiration and that the available energy is shared in fixed proportion between heating the atmosphere and evapotranspiration(Santos, 2022, Bhaskar R. Nikam,2014).

Equation 12 : $PET = 16 (10T_m/I)^{a}$ mm

Where **T** is the mean monthly air temperature (ºC), **I** is the heat index of the region, which is calculated using the following equation: Equation 13: $I = \Sigma im = \Sigma(T_m/5)^{1.514}$ for m=1... 12**,** and a is, given by:

Equation 14: $a=6.7x10^{-7} I^3 – 7.7 x10^{-5} I^2 + 1.8x10^{-2}I+0.49$**.** To account for variable hours of daylight and month lengths, PET must be adjusted to:

Equation 15: $PET_m = 16 Nm (10Tm/I)^{a}$

Where PET is Potential evapotranspiration in mm/month, m is the months 1, 2, 3……12, and N_m is the monthly adjustment factor related to hours of daylight. It is found from the standard table by dividing possible sunshine hours for the appropriate latitude (10^0 N) of the study area by twelve.

Using

Equation 15, the Potential Evapotranspiration (PET) has been computed and the result is displayed in Table 19. Accordingly, the mean annual potential evapotranspiration of the area is 935.85mm/year**.**

Table 19: Determination of Potential Evapotranspiration using Thornthwaite method

Thornthwaite Method of PET Calculation													
Month	**Jan**	**Feb**	**Mar**	**Apr**	**May**	**June**	**July**	**Aug**	**Sep**	**Oct**	**Nov**	**Dec**	**Annual**
N(Hrs)	7.13	6.82	7.28	7.89	8.78	7.76	6.22	6.96	6.58	7.89	8.79	7.80	
N_m	0.97	0.98	1.00	1.02	1.05	1.05	1.05	1.03	1.03	0.98	0.96	0.95	
T_m(0c)	18.65	19.79	-20.81	21.40	22.16	22.97	21.68	20.93	20.88	19.96	19.14	18.67	247.02
i_m	7.34	8.03	8.66	9.04	9.53	10.06	9.21	8.74	8.71	8.13	7.63	7.35	102.41
I=102.41													
a = 2.25													
PET	**59.59**	**68.80**	**78.58**	**85.41**	**95.08**	**103.05**	**90.46**	**82.04**	**81.59**	**70.15**	**62.53**	**58.55**	**935.85**

The original Penman model is a combination method in which the total evaporation rate is calculated by weighing the evaporation rate due to net radiation and the evaporation rate due to mass transfer, as follows (Ponce, 1989): Penman combined method used to allow for the condition under which evaporation and transpiration take place from a vegetated surface:

Equation 16: $\Delta E = (\Delta E_n + \gamma * E_a)/ (\Delta + \gamma)$, in which E = total evaporation rate; E_n = evaporation rate due to net radiation; E_a = evaporation rate due to mass transfer; Δ = saturation vapor pressure gradient, a function of air temperature; and γ = psychrometric constant, which may be shown to vary slightly with temperature. The mass-transfer evaporation rate E_a is calculated with an empirical mass-transfer formula. Using Equation 17, the mean annual potential evapotranspiration of the study area is 986.90mm/year (Table 20). Taking the average of the two methods, the PET of the study area is determined to be 961.36mm/year (Table 21).

Table 20: PET calculation using the Penman method

Month	Temp (Oc)	Ea (mm/d)	RH (%)	Ed (mm/d)	U2 (mile/d)	T (kelvin)	n (hr/d)	N (hr/d)	n/N	Ra (mm/d)	fa(n/N)	RI (1r) (mm/d)	σT4 (mm/d)	Ro (mm/d)	HT	Eat (mm/d)	Δ/γ	PET (mm/d)	PET
Jan	18.65	15.97	59.43	9.49	109.23	66	8.5	11.6	0.7	12.8	0.61	5.90	14.50	2.70	1.73	4.74	2.1	2.71	84.01
Feb	19.79	8.91	58.66	5.23	106.81	68	8.4	11.8	0.7	13.9	0.60	6.27	14.70	3.34	1.36	2.67	2.2	1.77	49.56
Mar	20.81	18.68	58.57	10.94	103.86	69	7.5	12	0.6	14.8	0.55	6.08	15.00	2.29	2.27	5.52	2.2	3.27	101.48
Apr	21.40	18.68	60.24	11.25	101.75	71	6.5	12.3	0.5	15.2	0.49	5.56	15.00	1.99	2.18	5.24	2.2	3.13	93.77
May	22.16	18.68	57.27	10.70	108.08	72	6.9	12.6	0.5	15	0.50	5.62	15.00	2.10	2.11	5.81	2.2	3.26	100.95
Jun	22.97	18.68	53.31	9.96	88.28	73	5	12.7	0.4	14.8	0.40	4.49	15.00	1.74	1.63	5.75	2.2	2.90	87.05
Jul	21.68	18.68	70.15	13.10	67.10	71	2.9	12.6	0.2	14.9	0.30	3.38	15.00	1.07	1.46	3.26	2.2	2.02	62.59
Aug	20.93	18.68	75.27	14.06	72.77	70	3.4	12.4	0.3	15	0.33	3.71	15.00	1.13	1.66	2.79	2.2	2.01	60.30
Sep	20.88	18.68	69.45	12.97	87.41	70	5.1	12.1	0.4	14.8	0.42	4.68	15.00	1.56	1.95	3.74	2.2	2.50	77.64
Oct	19.96	17.53	60.93	10.68	108.13	68	8.2	11.8	0.7	14.2	0.59	6.29	14.70	2.47	2.25	4.99	2.2	3.11	96.30
Nov	19.14	16.47	59.69	9.83	113.62	66	9.2	11.6	0.8	13.1	0.65	6.40	14.70	2.86	1.94	4.96	2.1	2.91	87.43
Dec	18.67	16.22	59	9.57	107.34	66	9.4	11.5	0.8	12.5	0.67	6.25	14.50	2.93	1.76	4.83	2	2.77	85.84
Total PET(mm/month)																			**986.90**

Table 21: Average PET

Month	PET(mm/month) (Thornthwaite Method)	PET(mm/month) (Penman Method)	PET(mm/month) (Average)
Jan	59.59	84.006	71.798
Feb	68.8	49.564	59.182
Mar	78.58	101.475	90.028
Apr	85.41	93.765	89.588
May	95.08	100.947	98.014
Jun	103.05	87.052	95.051
Jul	90.46	62.586	76.523
Aug	82.04	60.297	71.169
Sep	81.59	77.641	79.615
Oct	70.15	96.299	83.225
Nov	62.53	87.430	74.980
Dec	58.55	85.836	72.193
Total(mm/year)	**935.83**	**986.90**	**961.36**

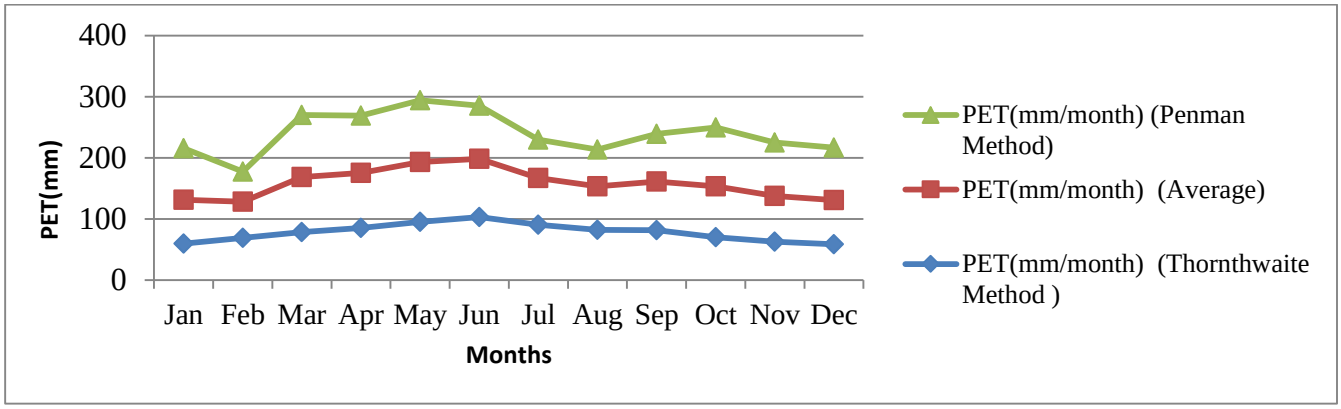


Figure 58: PET vs. Months

4.3.2 Actual Evapotranspiration (AET)

Actual evapotranspiration is evapotranspired under the existing soil moisture supply. It is dependent on the unsaturated moisture storage properties of the soil(Hsuen-chun, 2009, Liu, 2022). It is also affected by vegetated factors such as plant type and stage of growth. In this study, for the estimation of the actual evapotranspiration, the Thornthwaite soil water balance model (Dunne and Leopold, 1978), the Turc method, and the WetSpass Model were utilized.

The Thornthwaite soil water balance model requires the mean monthly precipitation, the mean monthly potential evapotranspiration, the water holding capacity of the predominant soil type, and the monthly soil moisture storage(Morton et al., 1983, Steenhuis et al., 2018). The area represented by each major soil type and associated land use was used to weight the actual evapotranspiration (AET), and the weighted AET was calculated as follows (Quej et al., 2019, Steenhuis et al., 2018):

$$\mathbf{AETW} = \frac{\sum(\boldsymbol{AETi})\boldsymbol{ai}}{\boldsymbol{At}}$$ Equation 17

Where AET_w is weighted actual evapotranspiration, AET_i is actual evapotranspiration of the dominant soil types, a_i is the area of each soil coverage: and, A_t is the total area of soil coverage.

Since the values of soil moisture deficit and AET vary with soil type and vegetation (Detto et al., 2006, Glenn et al., 2011, Williams et al., 2012), the study area has been reclassified into four land use/land cover units and vegetation with varying root depths and available water capacity and soils.

(i) Clay soil covered by cropland with shallow rooting cereals with an available water capacity of 50 mm,

(ii) Clay silt and Silty loam soil covered by cropland with shallow rooting cereals, with an available water capacity of 100 mm,

(iii) Clay soil covered with moderately deep-rooted cereals with an available water capacity of 150 mm,

(iv) Sandy loam covered with pasture and shrubs with an available water capacity of 250 mm,

(v) Sandy soil covered with mature forests (eucalyptus, acacia, and scattered acacia) was characterized by an available water capacity of 350 mm.

Therefore, a soil moisture budget was constructed for these land use/cover classes each month according to their root constants, using the average monthly precipitation and average monthly PET from Thornthwaite and Penman's average formula. The actual evapotranspiration, AET, for the predominant soil types and each land use in the area, was weighted according to the proportion of the area it represents, and the weighted AET was calculated using equation 18(Chanasyk et al., 2006). Accordingly, the Actual Evapotranspiration (AET) of the catchment is 509.04 mm/year (Table 27).

Table 22: Calculated AET using soil water balance method for clay soil covered with shallow deep rotted cereal crops &available water capacity of the root zone 50mm. All values in the table are in mm.

Parameters	Jan	Feb	Mar	Apr	May	Jun	Jul	Aug	Sep	Oct	Nov	Dec	Sum
PPT	18.2	25.5	54.3	74.1	58.2	25.5	200.5	228.3	78.9	32.8	21.3	16.7	834.20
PET_Ave	71.8	59.2	90.0	89.6	98.0	95.1	76.5	71.2	79.6	83.2	75.0	72.2	961.38
P-PET	-53.6	-33.7	-35.7	-15.5	-39.8	-69.6	123.9	157.1	-0.7	-50.5	-53.7	-55.5	-127.2
APWL	-162.7	-196.5	-232.1	-247.7	-287.4	-357				-50.5	-104.2	-109.2	-1747.3
Sm	1.9	1.0	0.5	0.4	0.2	0.0	50.0	50.0	50.0	18.2	6.2	5.6	184.0
AET	**14.5**	**24.5**	**53.8**	**73.9**	**58.0**	**25.3**	**76.5**	**71.2**	**79.6**	**83.2**	**9.3**	**16.1**	**586.2**
SMD	66.0	59.2	43.7	15.9	38.2	55.4	-20.0	-17.9	-9.7	6.7	74.3	63.7	375.6

Table 23: Calculated AET using soil water balance method for clay silt and Silty clay soil covered with shallow deep rotted cereal crops & available water capacity of the root zone 100mm. All values in the table are mm.

Parameters	Jan	Feb	Mar	Apr	May	Jun	Jul	Aug	Sep	Oct	Nov	Dec	Sum
PPT	18.2	25.5	54.3	74.1	58.2	25.5	200.5	228.3	78.9	32.8	21.3	16.7	834.20
PET_Ave	71.8	59.2	90.0	89.6	98.0	95.1	76.5	71.2	79.6	83.2	75.0	72.2	961.38
P-PET	-53.6	-33.7	-35.7	-15.5	-39.8	-69.6	123.9	157.1	-0.7	-50.5	-53.7	-55.5	-127.2
APWL	-162.7	-196.5	-232.1	-247.7	-287.4	-357				-50.5	-104.2	-109.2	-1747.3
Sm	19.6	14.0	9.8	8.4	5.6	2.8	100.0	100.0	100.0	60.4	35.3	33.6	489.6
AET	**4.3**	**19.8**	**50.1**	**72.6**	**55.5**	**22.6**	**76.5**	**71.2**	**79.6**	**83.2**	**-3.8**	**15.0**	**546.8**
SMD	76.2	63.9	47.4	17.2	40.8	58.2	-20.0	-17.9	-9.7	6.7	87.4	64.8	415.0

Table 24: Calculated AET using soil water balance method for Loam soil covered with shallow deep rotted cereal crops and available water capacity of the root zone 150mm. All values in the table are in mm.

Parameters	Jan	Feb	Mar	Apr	May	Jun	Jul	Aug	Sep	Oct	Nov	Dec	Sum
PPT	18.2	25.5	54.3	74.1	58.2	25.5	200.5	228.3	78.9	32.8	21.3	16.7	834.20
PET_Ave	71.8	59.2	90.0	89.6	98.0	95.1	76.5	71.2	79.6	83.2	75.0	72.2	961.36
P-PET	-52.5	-30.3	-28.4	-5.6	-29.7	-49.2	176.9	229.3	29.5	-43.1	-51.3	-56.4	961.4
APWL	-160.2	-190.5	-219.0	-224.6	-254.3	-303.5				-43.1	-94.4	-107.7	-1597.3
Sm	51.5	42.1	34.8	33.6	27.5	19.8	150.0	150.0	150.0	112.5	79.9	73.2	925.1
AET	**-3.4**	**16.0**	**47.1**	**72.8**	**52.2**	**17.8**	**76.5**	**71.2**	**79.6**	**83.2**	**-11.3**	**9.9**	**511.63**
SMD	75.2	43.1	43.0	16.8	45.8	77.3	0.0	0.0	0.0	0.0	86.3	62.3	449.7

Table 25: Calculated AET using soil water balance method for Sandy clay soil covered with pasture and shrub lands and available water capacity of the root zone 250mm. All values in the table are in mm.

Parameters	Jan	Feb	Mar	Apr	May	Jun	Jul	Aug	Sep	Oct	Nov	Dec	**Sum**
PPT	18.2	25.5	54.3	74.1	58.2	25.5	200.5	228.3	78.9	32.8	21.3	16.7	834.20
PET_Ave	71.8	59.2	90.0	89.6	98.0	95.1	76.5	71.2	79.6	83.2	75.0	72.2	961.36
P-PET	-52.5	-30.3	-28.4	-5.6	-29.7	-49.2	176.9	229.3	29.5	-43.1	-51.3	-56.4	114.7
APWL	-160.2	-190.5	-219.0	-224.6	-254.3	-303.5				-43.1	-94.4	-107.7	-1597.3
Sm	131.7	116.7	104.1	101.8	90.4	74.3	250.0	250.0	250.0	210.4	171.3	162.5	1913.2
AET	**-12.5**	**10.4**	**41.8**	**71.8**	**46.8**	**9.3**	**76.5**	**71.2**	**79.6**	**83.2**	**-17.8**	**7.8**	**468.19**
SMD	87.7	32.7	1.2	-55.0	-1.0	68.0	-76.5	-71.2	-79.6	-83.2	104.1	54.4	-18.4

Table 26: Calculated AET using soil water balance method for Sandy soil covered with Matured forest and available water capacity of the root zone 350mm. All values in the table are in mm.

Parameters	Jan	Feb	Mar	Apr	May	Jun	Jul	Aug	Sep	Oct	Nov	Dec	**Sum**
PPT	18.2	25.5	54.3	74.1	58.2	25.5	200.4	228.29	78.89	32.76	21.3	16.7	834.20
PET_Ave	71.8	59.2	90.0	89.6	98.0	95.1	76.5	71.2	79.6	83.2	75.0	72.2	961.36
P-PET	-52.51	-30.32	-28.43	-5.59	-29.72	-49.17	176.9	229.34	29.48	-43.09	-51.4	-56.3	114.73
APWL	-160.2	-190.5	-219.0	-224.6	-254.29	-303.5	0	0	0	-30.00	-81.45	-107.7	-1571.1
Sm	221.4	203.1	187.2	184.3	169.3	147.1	350.0	350.0	350.0	321.2	277.4	257.3	3018.3
AET	**-17.6**	**7.1**	**38.5**	**71.1**	**43.24**	**3.3**	**91.2**	**71.2**	**79.6**	**83.2**	**-22.54**	**-3.4**	**444.92**
SMD	5.1	3.3	3.3	0.7	3.59	6.0	-14.76	0.00	0.00	0.00	4.77	11.27	23.3

Table 27: Weighted Actual Evapotranspiration (Wtd AET)

Soil type	**Area (Km^2)**	**LULC**	**Wtd area**	**AWC (mm)**	**AET**	**Wtd. AET**
Clay	4146	Shallow rooted cereals	0.217	50	586.2	122.03
Clay silt and Silty clay	5052	Shallow rooted cereals	0.264	100	546.8	144.39
Loam	733	Moderately deep-rooted cereals	0.038	150	511.63	19.6
Sandy clay	3328	Pasture and shrubs	0.174	250	468.19	81.44
Sand	5873	Matured forest(Forest, Eucalyptus, and woodland)	0.307	350	442.92	136.58
Total	19132		**1**			**509.04**

Turc proposed the following empirical method to estimate the Actual Evapotranspiration from mean annual temperature and precipitation data: Equation 18: $E=\frac{P}{\left(0.9+\left(\frac{P}{L}\right)^2\right)^{1/2}}$, Where E: Annual Actual Evapotranspiration, P: is annual Areal Rainfall (mm), T: is the mean annual Temperature in ^{O}c, and L: is the Thermal indicator, defined by Equation 19: $L=300+25T+0.05*T^3$. Using the following values: P = 834.2mm and T = 20.59^{o}C, and by using Equation 18, the mean annual actual evapotranspiration (AET) rate is determined to be 719 mm/year. However, several authors have reported that the Turc equation,

which was originally developed for Mediterranean countries, tends to overestimate Evapotranspiration for humid locations(Diouf et al., 2016). In addition, comparing to other methods it takes temperature and precipitation as the only factors, and it does not account for other parameters like soil type, vegetation cover, or wind speed, which can influence AET. As a result, the value determined by this method is not used for the determination of annual Actual Evapotranspiration.

WetSpass's calculation of the annual actual evapotranspiration includes evaporation from bare ground, transpiration of the vegetated cover, interception loss by vegetation, and evaporations from open water bodies (Dereje & Nedaw, 2019).

$$ETraster = avETv + asEs + aoEo + aiEi \quad \text{(Eq. 20)}$$

The index raster refers to a raster cell, with $ET_{raster,}$ as the total evapotranspiration, in a raster cell and a_v, a_s, $a_{o,}$ and a_i respectively the vegetated, bare soil, open water, and impervious area fractions of a raster cell. The total actual evapotranspiration per pixel is calculated using a WetSpass-M model as the sum of evaporation from open water, impervious surface, bare soil, vegetation interception, and transpiration of vegetative cover (Salem, Ali et.al, 2019). Accordingly, evapotranspiration is responsible for a loss of 483.39 mm/year (57.95%) of the average annual precipitation of the study area. The minimum and maximum values of AET are 74.52 mm/year and 1125.48 mm/year, respectively (Figure 59). During the rainy season, 397.66 mm/year (82.26%) of the total annual evapotranspiration is lost, while during the dry season, the water lost through this process is 85.73 mm/year (17.73%). These fluctuations are due to the different amounts of precipitation during the rainy and dry seasons. Comparing the distribution of evapotranspiration with soil coverage; clay and sandy soils have the highest and lowest evapotranspiration, respectively (Table 28). In addition, the distribution of evapotranspiration with land use and land cover shows that water bodies and settlements experience the highest and lowest evapotranspiration respectively (Table 29).

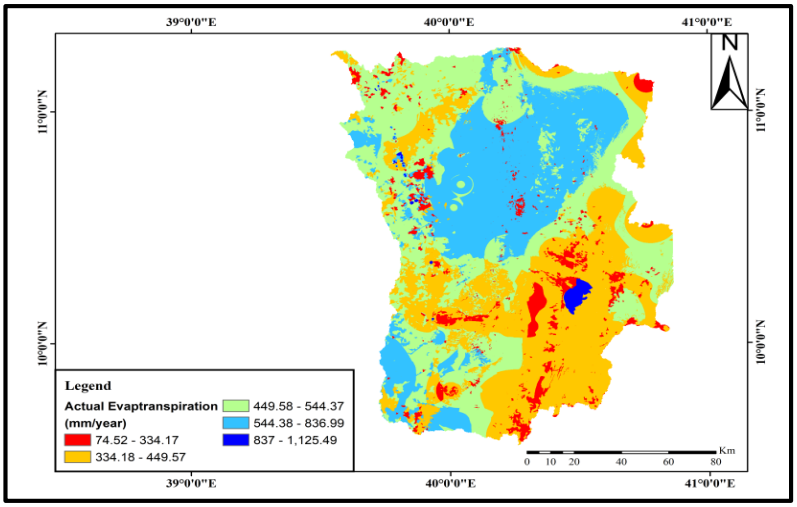


Figure 59: Spatial distribution of AET

Table 28: Distribution of Evapotranspiration with Soil Coverage

Soil Texture	Sand(Lithic Leptosols)	Sand clay(Eutric Leptosols)	Clay (Vertic Cambisols)	Clay (Haplic Solonchaks)	Silt clay(Eutric Fluvisols)	Loam(Eutric Cambisols)
AET(mm/year)	409.80	533.50	546.36	498.32	437.03	475.36
Area(km^2)	5873	3328	1664	4146	3388	733

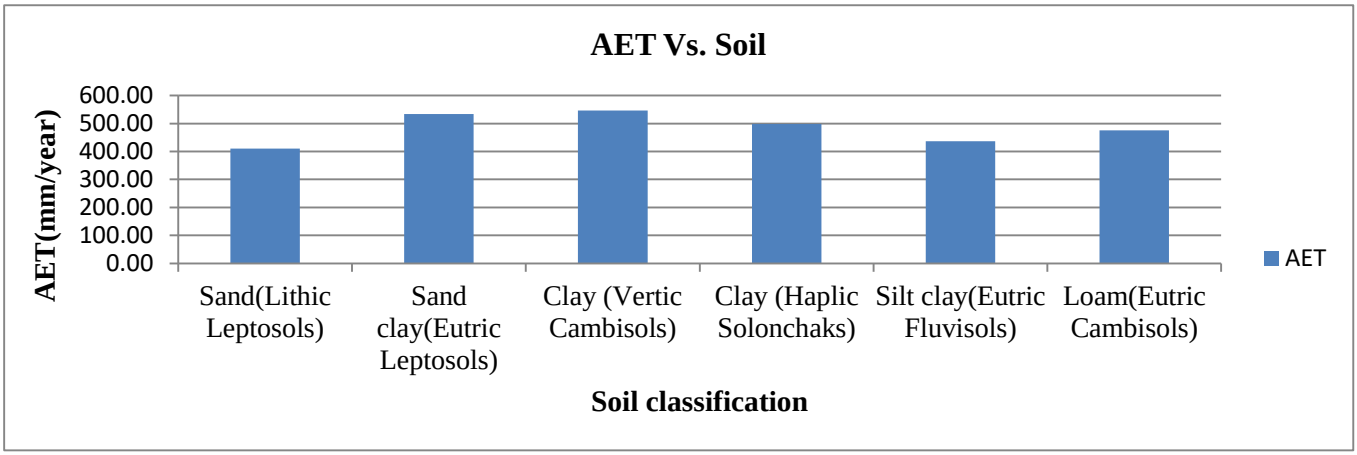


Figure 60: Distribution of AET with soil coverage

Table 29: Distribution of Evapotranspiration with land use and land cover

Land use	Forest	Settlement	Water Body	Eucalyptus	Grass Land	Shrub Land	Acacia	Dispersed Acacia	Agricultural Land	Rocky Bare Land	Bare Land	Dispersed Shrub
AET	389.2	226.39	1161.45	241.73	357.7	549.98	361.05	431.02	493.68	468.4	526.4	475.26
Area(Km^2)	420	60	106	272	102	3924	484	1150	3750	2105	3380	3379

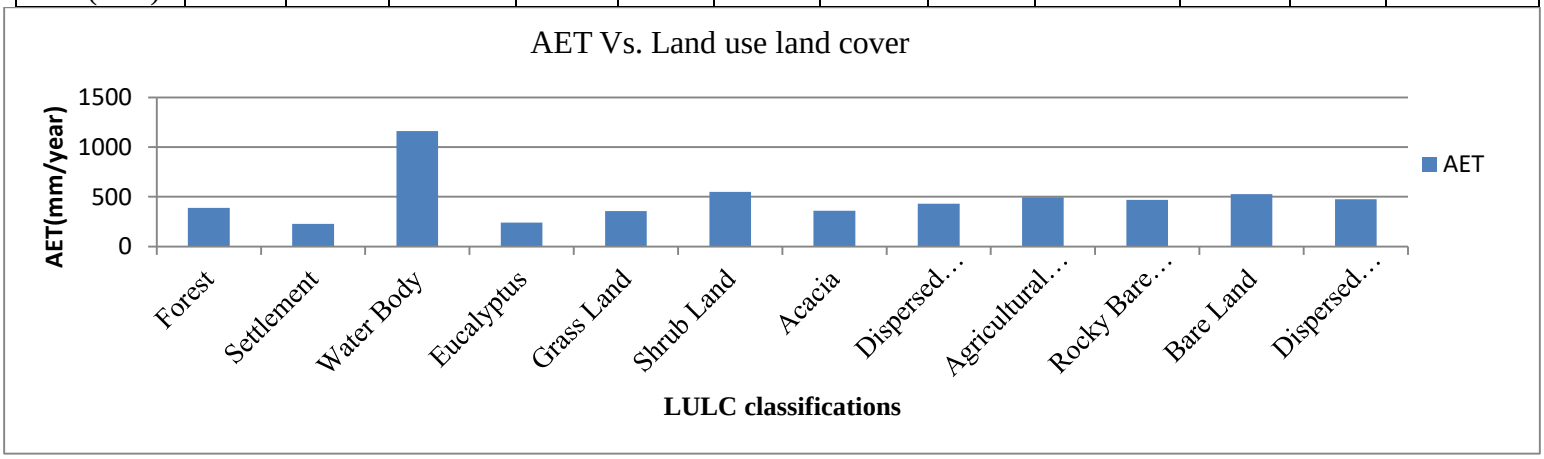


Figure 61: Distribution of AET with LULC

The average AET determined from Soil water balance and WetSpass model is 496.22mm/year(Table 30).

Table 30: AET summary

Parameter	**Methods of Estimations**		**Average**
	Thornthwaite	**WetSpass**	
AET(mm/year)	509.04	483.39	496.22

4.3.3 Surface Runoff:

Surface runoff is defined here as the excess precipitation that flows at the land surface immediately following a storm event(Weatherl et al., 2021). In this study, the water that is lost through surface runoff has been determined using the Runoff Coefficient Method and WetSpass model, ultimately using the average results of the two methods. The runoff volume of a given catchment is calculated using the runoff coefficient method established by Garg, 1987 as cited in Şen & Altunkaynak et al, 2006, Abijith et al., 2020, Scanlon et al., 2005**,** and given by: Equation 21: $Q = KPA$, Where Q is the runoff, m^3: K is a constant also known as the runoff coefficient, which depends on the impermeability of the drainage area: P is the precipitation (mm): and A is the area of the catchment (m^2). The land cover, land use, and slope of the study area should be organized to determine surface runoff using this method (Mattivi et al., 2019). Accordingly, the amount of water lost from the catchment as surface runoff using Equation 22 is 4,257,927,811.00 mm^3 (222.56 mm/year) (Table 31) which is 26.68% of the mean annual rainfall.

Table 31: Runoff calculation using the Runoff Coefficient method

S.No	Soil	LULC	Area (Km^2)	Slope	Areal Rainfall (km/year)	K	Runoff (Km^3)
1	Loam, Silty clay, clay, clay slit, sandy clay& sand	Dispersed Shrub	3,379	Gentle	0.000834	0.2	0.56
2	Loam, Silty clay, clay, clay slit, sandy clay& sand	Bare Land	3,380	Flat to Gentle	0.000834	0.6	1.69
3	Rocky/sand	Rocky Bare Land	2,105	Gentle to steep	0.000834	0.5	0.88
4	Loam and sand	Agricultural Land	937.5	Flat to Gentle	0.000834	0.11	0.09
5	Silty clay, clay silt, and sandy clay	Agricultural Land	2,812.5	Gentle to steep	0.000834	0.12	0.28
6	Loam, Silty clay, clay, clay slit, sandy clay& sand	Dispersed Acacia	1,150.0	Gentle to steep	0.000834	0.15	0.14
7	Loam, Silty clay, clay, clay slit, sandy clay& sand	Acacia	484	Flat to Gentle	0.000834	0.1	0.04
8	Loam, Silty clay, clay, clay slit, sandy clay& sand	Shrub Land	3,924.0	Gentle to steep	0.000834	0.12	0.39
9	Silty clay, clay, clay slit, sandy clay& sand	Grass Land	102	Gentle to steep	0.000834	0.25	0.02
10	Loam, Silty clay, clay slit, sandy clay& sand	Eucalyptus	272	Gentle to steep	0.000834	0.22	0.05
11	Clay	Water Body(Pond)	106	Flat	0.000834	0.11	0.01
12	Rocky/sand	Settlement	60	Flat to Gentle	0.000834	0.75	0.04
13	Loam, Silty clay, clay, clay slit, sandy clay& sand	Forest	420	Gentle to steep	0.000834	0.175	0.06
		Total	19,132	100			4.26
Surface runoff (mm/year)							**222.56**

To estimate the surface runoff of the catchment using the WetSpass model, the method uses a runoff coefficient whose value varies with vegetation, land use, soil type, and slope (Mohan et al., 2018, Yenehun et al., 2022).

$$\mathbf{Sraster = avSv + asSs + aoSo + aiSi}, \text{ Equation 22}$$

The index raster refers to a raster cell; with S_{raster} is a Surface runoff in a raster cell and a_v, a_s, $a_{o,}$ and a_i respectively the vegetated, bare soil, open water, and impervious area fractions of a raster cell. Using this model, surface runoff leads to an annual water loss of about 224.62 mm/year, which corresponds to 26.92% of the annual areal precipitation. The minimum and maximum Surface runoff calculated using this method is 8.87 mm/year and 745.96 mm/year respectively (Figure 62). The high amount of surface runoff in the study area is found in the northwestern and southwestern parts, which is due to the high amount of precipitation and the hillside topography, and it varies in the rainy and dry seasons. The mean total surface runoff during the dry season is 8.97 mm/year, which is nearly 4% of the annual surface runoff and 1.07% of the mean annual rainfall. During the rainy season, the mean annual surface runoff is 215.67 mm/year, which corresponds to 96% of the annual surface runoff and 25.85% of the annual precipitation. This deviation is due to the different amounts of precipitation in the rainy and dry seasons. This is because the amount of precipitation is higher in the rainy months than in the dry months, which exceeds the infiltration capacity of the soil and leads to high surface runoff. In the dry months, on the other hand, the incoming precipitation is less than the infiltration capacity of the catchment area's soils, resulting in less surface runoff. As with that of AET, runoff value has also shown a variation with respective of soil and land use land coverage. In the case of soil, the higher and lower runoff is obtained from clay and sand (Table 32). Besides distribution of surface runoff with respective land use and land cover shows that maximum and minimum runoff is found at settlement areas and dispersed acacia respectively (Table 33).

Table 32: Distribution of Surface runoff with respective Soil coverage

Soil Texture	**Area(Km2)**	**Runoff(mm/year)**
Sand(lithic Leptosols)	5873	88.754
Sand clay(Eutric Leptosols)	3328	110.372
Clay(Vertic Cambisols)	1510	377.039
Clay(Haplic Solonchaks)	4300	334.697
Silt clay(Eutric Fluvisols)	3388	92.285
Loam(Eutric Cambisols)	733	206.39

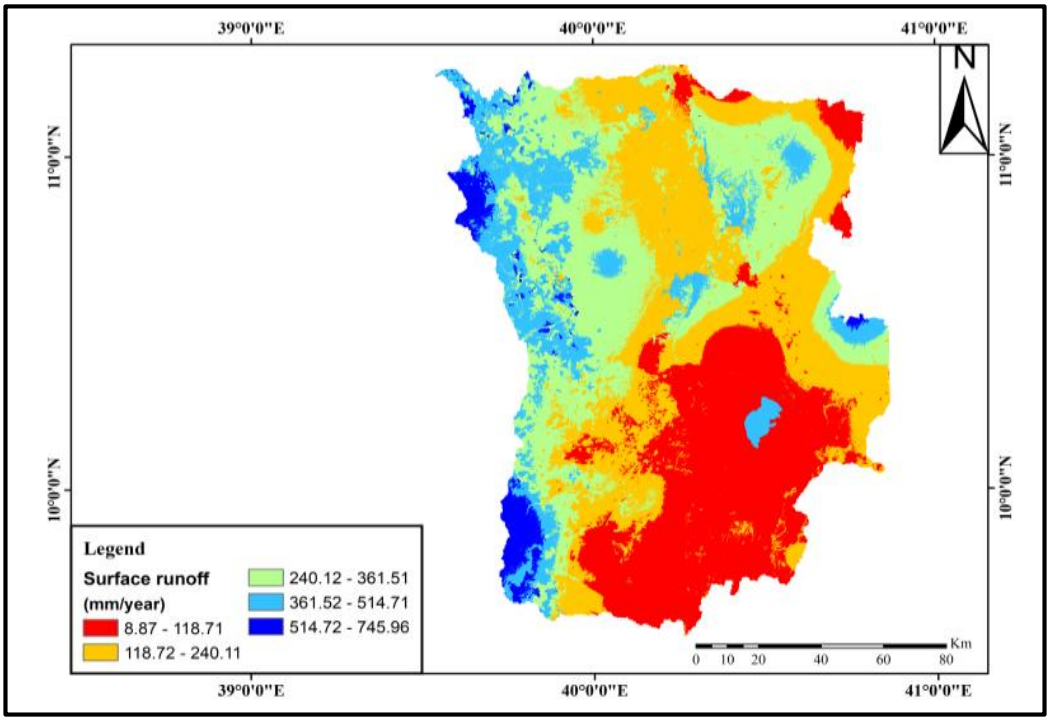


Figure 62: Spatial distribution of surface runoff

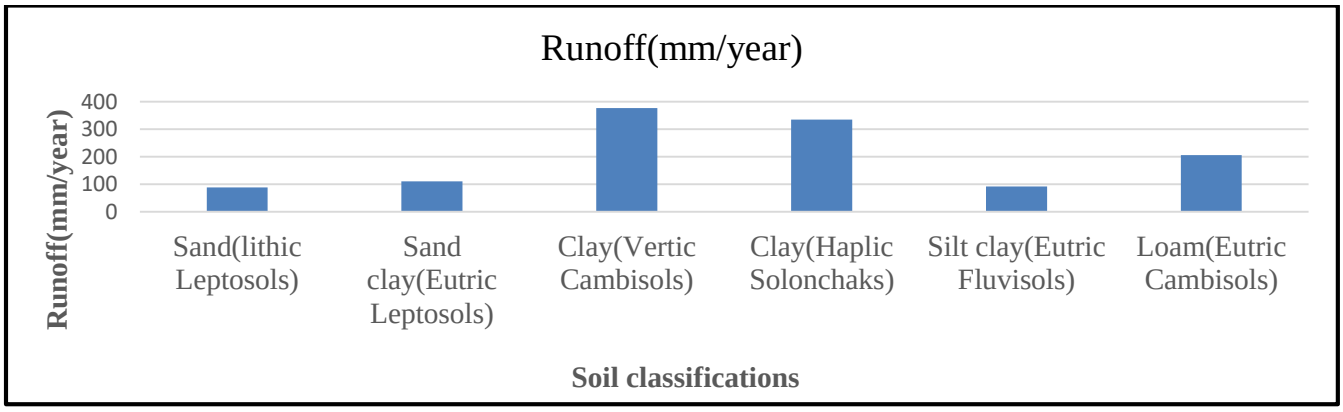


Figure 63: Distribution of runoff with soil coverage

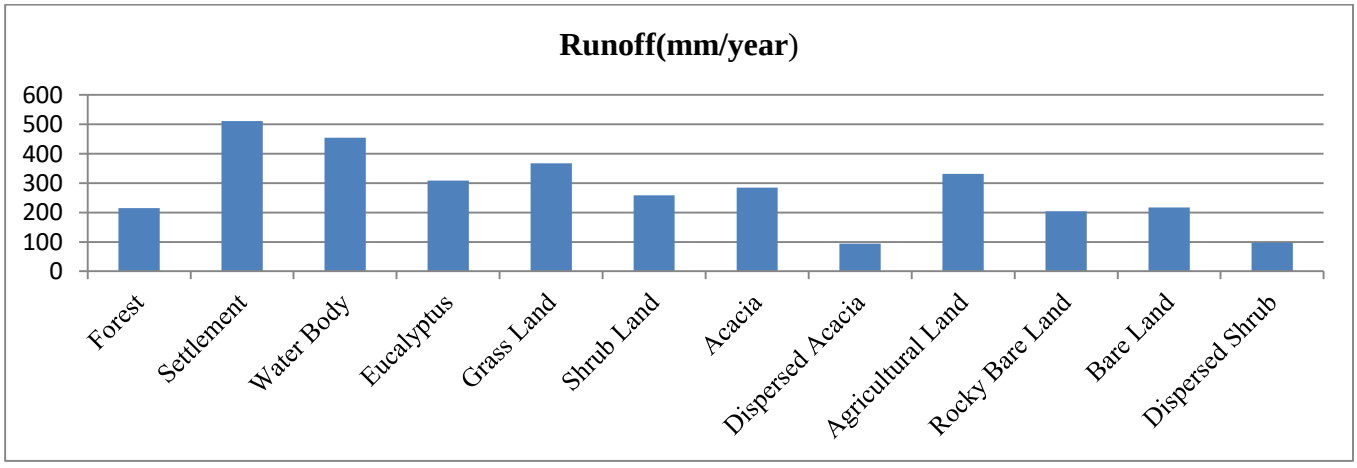


Figure 64: Distribution of runoff with land use land cover

Table 33: Distribution of Surface runoff with respective Land use land cover

Land use Land cover	**Area(km2)**	**Runoff(mm/year)**
Forest	420	215.45
Settlement	60	510.83
Water Body	106	454.33
Eucalyptus	272	308.65
Grass Land	102	367.44
Shrub Land	3924	258.82
Acacia	484	284.24
Dispersed Acacia	1150	94.18
Agricultural Land	3750	331.49
Rocky Bare Land	2105	203.74
Bare Land	3380	217.25
Dispersed Shrub	3379	97.49

Finally, taking the average results of the two methods, the Surface runoff of the study area is calculated to be 223.59mm/year (Table 34) which is 26.8 % of the mean annual rainfall.

Table 34: Average Surface Runoff

Parameter	Methods		Average
	Runoff coefficient	WetSpass	
Surface Runoff (mm/year)	222.56	224.62	223.59

4.3.4 Groundwater Recharge

4.3.4.1 Water Balance Method

Water balance models were developed in the 1940s by Thornthwaite (1948) and revised by Thornthwaite and Mather (1955) (Abdalla, 2012, Babu et al., 2020, Edet et al., 1998). Due to the large uncertainty in the input data, the results of this model have very little significance without calibration and validation (Nimmo et al., 2015, Penkova & Shiklomanov, 2007). Despite these limitations, the approach is fascinating because it can be applied wherever precipitation data is available (Dennis Risser et al., 2005, Surinaidu et al., 2021). The rule of conservation of energy over a period of time serves as the basis for the basic idea underlying the water balancing method and is stated as follows (Babu et al., 2020):

Equation 23: Inflow to the system-Outflow from the system=Δstorage

The inflow components include recharge from precipitation and groundwater inflow from other catchment areas. The outflow components include actual evapotranspiration (AET), runoff, groundwater discharge between catchments, and groundwater abstraction by pumping. Taking into account the inflow and outflow components, the general groundwater balance equation for estimating groundwater recharge in the area under consideration for a given period with the same unit is (Scanlon et al., 2005):

$R = (P + Gi) - (Et + Ro + Go + W)$ (Eq. 24)

Where R is recharge, P is mean precipitation, E_T is mean actual evapotranspiration, Ro is mean runoff, Gi is groundwater inflow, Go is groundwater outflow and W is the withdrawal of groundwater from the aquifer system. The following summarizes the various assumptions used in calculating the water balance equation for the study area:(1) no discharge from other watersheds is assumed (2) surface and subsurface water exchange with surrounding watersheds is assumed to be zero and (3) since the calculations are performed annually, the net change in soil moisture and groundwater storage is assumed to be zero. Based on these assumptions, the above formula is reduced to (Arnold & Allen, 1999):

$\mathbf{R = P - (AET + SRO)}$ Equation 25

Where P = Precipitation; AET = Evapotranspiration; SRO= River discharge from the catchment (Surface Runoff); and, R = Recharge. Hence, the water balance calculates Groundwater Recharge (GWR) as the residual of relevant terms including Precipitation (P), Evapotranspiration (ET), and Surface runoff (Runoff) (Weatherl et al., 2021). Accordingly, the amount of water that recharges the groundwater is 114.39mm/year which is 13.71% of the mean annual rainfall (Table 35).

Table 35: Recharge Estimation using the Water Balance Method

S.No	PPT(mm/year)	Surface Runoff(mm)	AET(mm/year)	R(mm/year)
1	834.2	223.59	496.22	114.39

4.3.4.2 WetSpass Model

Most models for estimating groundwater recharge have a flaw in that they assume uniform groundwater recharge over the model area, which is not the case in most cases(Xu & Beekman et al, 2003). The determination of spatially and temporally distributed recharge is therefore of crucial importance. For this purpose, WetSpass, a GIS-based model for estimating long-term average spatially varying surface runoff, evapotranspiration, and groundwater recharge is well suited (Amiri et al., 2022, Dereje & Nedaw, 2019). In this study, a WetSpass-M model is used to estimate the spatially distributed groundwater recharge on a seasonal and annual basis. The principle of the model is that the total water balance for a cell in a spatially distributed grid is split into independent water balances for vegetated, bare soil, open and impervious parts of the grid cell(Aish et al., 2010, Bhattacharya et al., 2021, Martín-Loeches et al., 2018). This makes it possible to take into account the non-uniformity of land use depending on the resolution of

the grid cell (Obuobie et al., 2012, Tilahun & Merkel, 2009). Accordingly, the total water balance per grid cell and the hydrological season are calculated as follows:

Equation 26:$\mathbf{Rraster = avRv + asRs + aoEo + aiEi}$, the index raster refers to a raster cell, where raster is the new formation in a raster cell and av, as, ao and ai are the proportions of vegetated, unvegetated soil, open water, and impermeable area of a raster cell, respectively.

The WetSpass–M model requires several basic input data, including spatially distributed mean monthly precipitation, temperature, wind speed, potential evapotranspiration, depth of groundwater, land use, soil types, elevation, and slope (Giovanni & Donnell et.al, 2001). In this study, all point data including precipitation, temperature, wind speed, PET, and depth to groundwater level were interpolated using Kriging and Inverse Distance Weighting (IDW) techniques, by comparing the percentage error of each interpolation technique for each input parameter in the Arc GIS 10.3 working environment. Besides, the spatially distributed data for soil, slope, elevation, and land use were also processed and converted to raster formats (Batelaan & De Smedt, 2007). Finally, all the input raster data were converted to ASCII and table formats. Soil, land use, and land cover as well as monthly rainfall and degree days are included in the table formats or files. The spatial resolution of all ASCII and table formats is 100 meters by 100 meters, with 1460 columns and 1899 rows. After the model was run, using the raster calculation algorithm in the Arc GIS working environment, the output ASCII files were summed up and converted to a raster format. These resulted in the final spatially distributed and mean annual groundwater recharge of the study area. Accordingly, the mean annual recharge is calculated as 100.88mm/year, which corresponds to 12.09% of the mean annual precipitation, where the minimum and maximum annual groundwater recharge is 40 mm/year and 396.6 mm/year respectively (Figure 67). The minimum, mean, and maximum annual recharge during the dry months is 0.42mm/year, 8.48mm/year, and 44.7mm/year respectively, and during the rainy season, is 75.43mm/year, 92.48mm/year, and 649.30mm/year respectively(Figure 67)). The mean contribution to groundwater recharge during the wet and dry seasons being 91.6% and 8.4% respectively.

The distribution of recharge shows variation with respective soil. Accordingly, the maximum and minimum recharge are obtained with sand and clay soil respectively (Table 36). Similar to soil coverage, the groundwater recharge also showing variation with land use and land cover. As a result, eucalyptus and bare and rocky land show maximum and minimum groundwater recharge respectively (Table 37).

Table 36: Distribution of Recharge, Evapotranspiration, and Surface runoff with soil distribution

Outputs (mm/year)	Sand (Lithic Leptosols)	Sand clay (Eutric Leptosols)	Clay	Clay (Vertic Cambisols)	Clay (Haplic Solonchaks)	Silt clay (Eutric Fluvisols)	Loam (Eutric Cambisols)
Recharge	160.47	106.19	52.54	64.68	52.82	64.25	125.88
Evapotranspiration	411.80	534.22	948.86	546.72	498.60	437.57	475.47
Surface Runoff	86.17	128.43	358.69		321.77	252.81	199.85

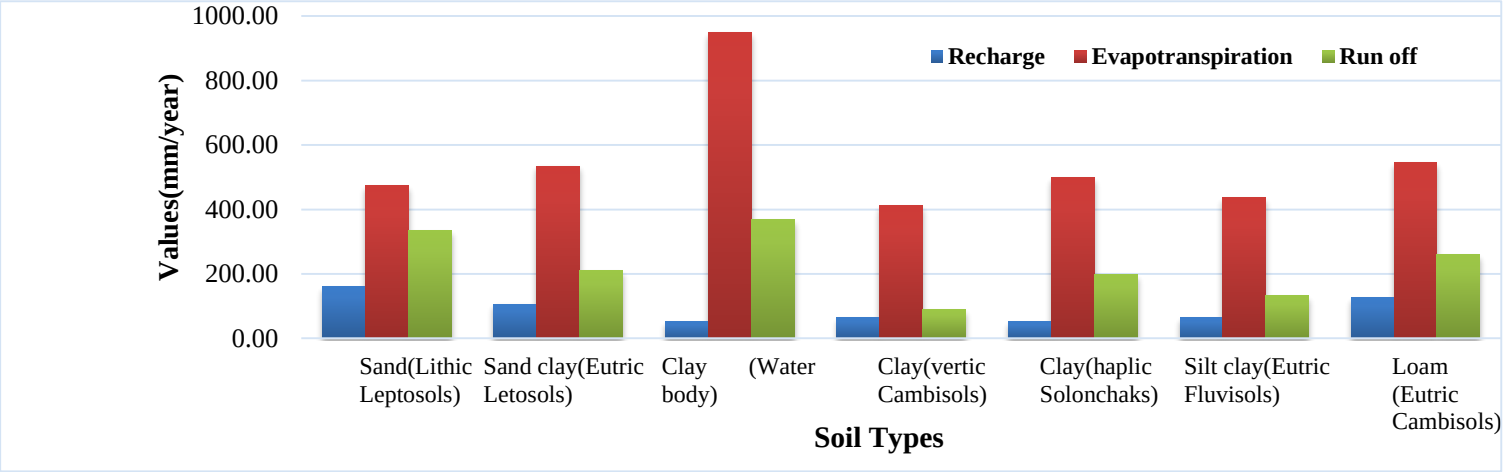


Figure 65: Distribution of Recharge, Evapotranspiration, and Surface runoff with Soil coverage

Table 37: Distribution of Recharge, Evapotranspiration, and Surface runoff with LULC

Outputs (mm/year)	Land use land cover											
	Forest	Settlement	Water Body	Eucalyptus	Grass Land	Shrub Land	Acacia	Dispersed Acacia	Agricultural Land	Rocky Bare Land	Bare Land	Dispersed Shrub
Recharge	196	58	41	224	175	133	114	95	133	41	41.84	97
AET	388	205	1121	242	358	550	359	431	463	457	508	460
Runoff	215	511	454	309	367	259	284	94	331	204	217	97

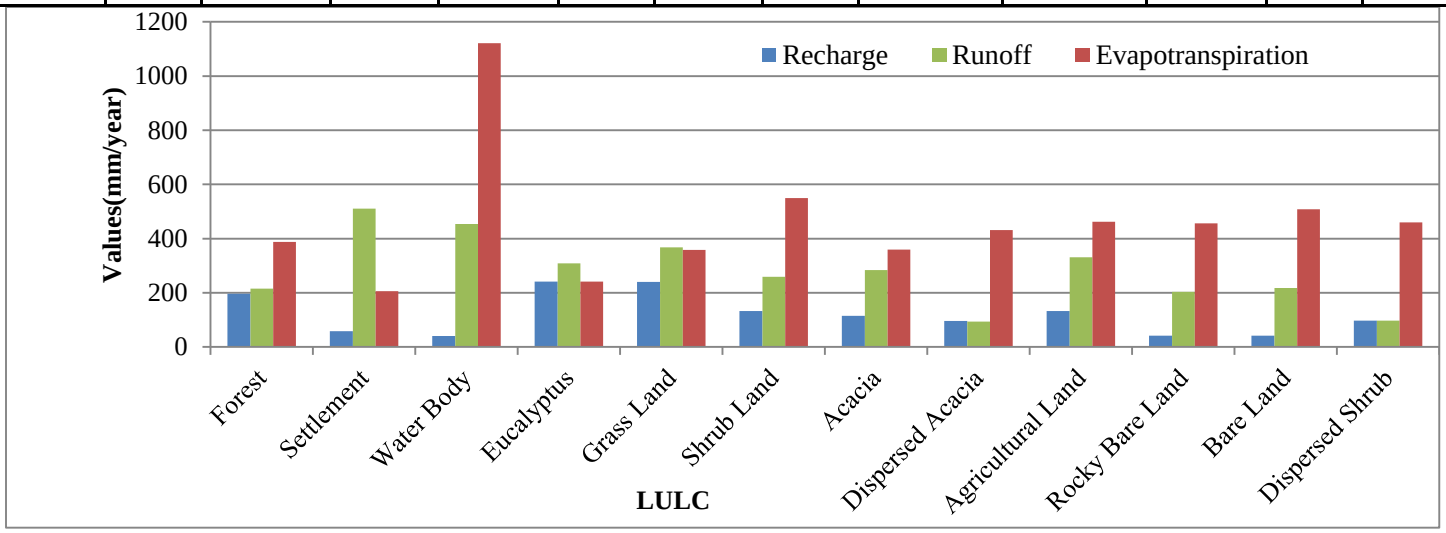


Figure 66: Distribution of Recharge, Evapotranspiration, and Surface Runoff with respective LULC

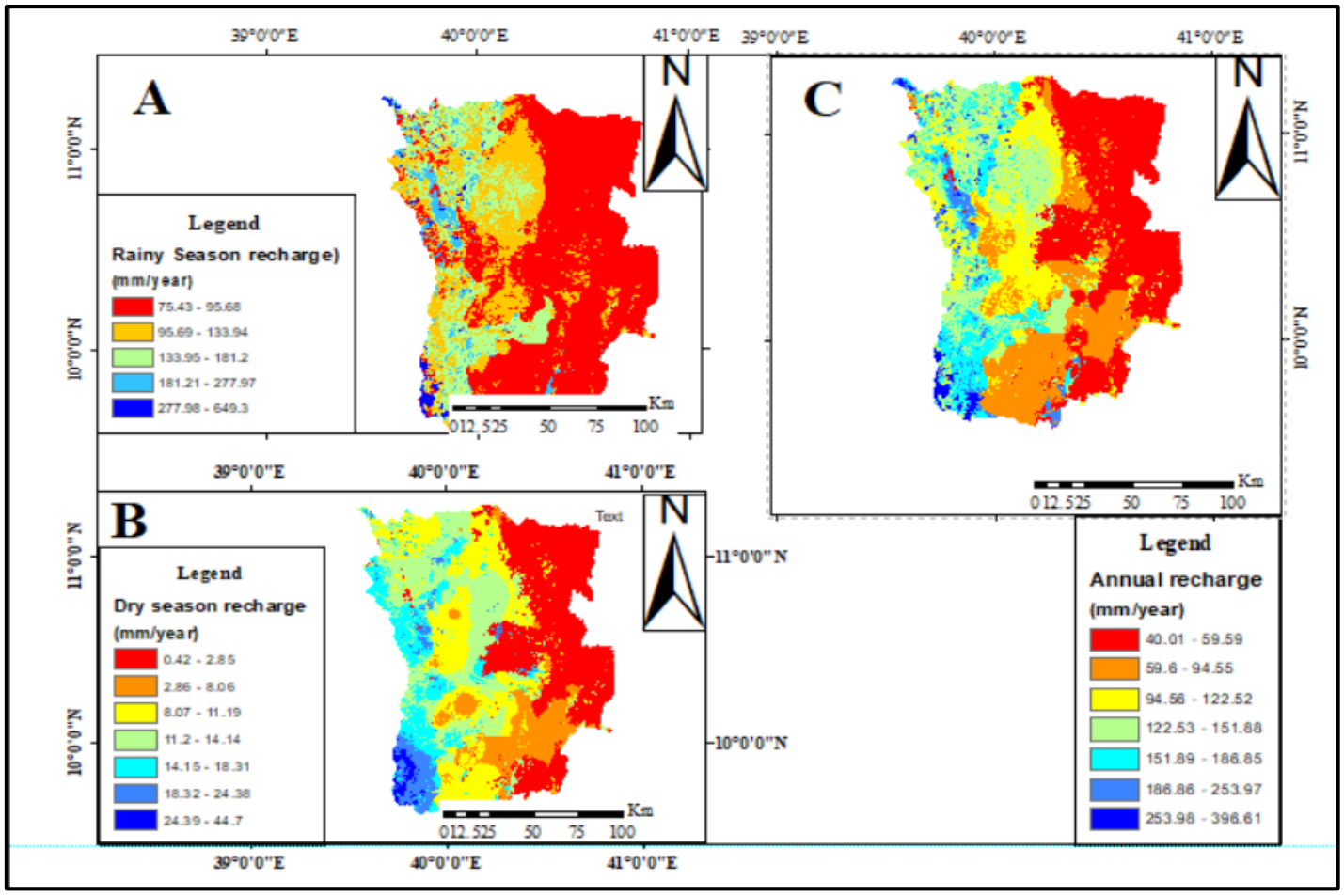


Figure 67: Rainy season recharges (A), Dry season recharge (B), Annual recharges(C)

4.3.4.3 Chloride Mass Balance (CMB) method

The CMB approach assumes that the tracer (Cl^-) input flux at the surface is identical to the tracer (Cl^-) input flux reaching the water table(Hem, 1985, Subyani & Sen, 2006). The method considers chloride as an inert element because, unlike other inorganic ions, it is not added or removed by the interaction of water and rock(Ferede et al., 2020, VANUM, 2012) and has the atmosphere as its source. It has the advantage that atmospheric inputs are preserved during recharge processes, which allows the application of a mass balance approach (Yin et al., 2011). The basic premise of the CMB method is that the water mass flux across the water table can be calculated if certain conditions are met (Tyner et al., 1999), including (i) the chloride in the groundwater originates only from precipitation directly in the aquifer; (ii) the chloride is conservative in the system; (iii) the chloride-mass flux has not changed over time; and (iv) there is no recycling or concentration of chloride within the aquifer. As described by Somaratne & Smettem, 2014, the basic equation for estimating recharge using the chloride mass balance method is:

Equation 27:$\boldsymbol{R = \frac{(PClp)}{Clg}}$ Where: R is the annual recharge (mm), P is the mean annual precipitation (mm), Clp is the chloride concentrations in the precipitation (mg/l), and Clg are chloride concentrations in the GW (mg/l). So, to determine groundwater recharge using the chloride mass balance (CMB) method, the

chloride concentration both in the precipitation and groundwater should be measured (Demlie, 2015). In the study area, the chloride concentration in the surface water sources (lake and river) varies between 33.2mg/l and 60.4mg/l. In the shallow wells, the minimum and maximum chloride concentrations are 23.8 and 394.6mg/l respectively. For the deep wells (≥150m) and the highland springs, the minimum and maximum chloride concentrations are 1.9mg/l and 20mg/l respectively, with an average value of 10.95mg/l. These results show that the chloride concentration of surface water, and shallow well sources is higher than that of deep wells and highland springs. The higher concentration in the surface water bodies and shallow sources is attributed to the high evapotranspiration and the addition of chloride from the Awash River and its tributaries, which is used for irrigation purposes in many places of the study area. In addition, the thermal springs and shallow wells found on the eastern side of the rift floor have higher chloride content, which is due to the addition of chloride through faulting effects. This reasoning is supported by the measured values of electrical conductivity, where the EC value is lower in deep wells in which the main aquifer consists of fractured and weathered basalt besides the alluvial deposit and other recent volcanic rocks indicate low chloride content, while the electrical conductivity is higher in shallow wells where the main aquifer units consist of alluvium, indicating high chloride content. As a result, for the estimation of groundwater recharge using the CMB method, shallow wells have been excluded and the result from deep wells is used for further interpretations. Since the sampling period was conducted during the dry seasons, the chloride concentration of precipitation was taken from the previous work conducted by Demlie et al., 2015 and Dawana et al.,2020 for the central and the whole of Ethiopia respectively. Accordingly, the minimum and maximum chloride concentration in precipitation determined by the above authors (all in mg/l) is shown in Table 38. Finally, the groundwater recharge rate determined using Equation 27 is 92.37 mm/year, which corresponds to 11.07 % of the mean annual precipitation amount.

Table 38: Annual recharge from the CMB method

Chloride concentration in ppt (mg/L)				**Chloride concentration in gw (mg/L)**			**Mean areal rainfall (mm/year)**	**Recharge (mm/y)**
Authors	***Minimum***	***Maximum***	***Average***	***Minimum***	***Maximum***	***Average***		
Demlie et al	0.15	2.2	1.175	1.9	20	10.95	834.2	92.37
Dawana et al	1.1	1.4	1.25					
Average	0.625	1.8	1.21					

4.3.4.4 Base flow separation method supported by Radon measurement analysis

The most important assumptions when using baseflow to predict recharge are that baseflow is equal to groundwater discharge and that groundwater discharge is approximately equal to recharge(Eckhart, Maxwell & Culligan et al, 2009). The underlying assumption is that groundwater losses from the measured catchment due to underflow, groundwater evaporation, and groundwater exports are negligible (Lott & Stewart, 2016). If these criteria are met, the base flow could provide a reliable long-term estimate of recharge (Dennis Risser et al., 2005, Penkova & Shiklomanov, 2007), which is determined by dividing the hydrograph into the components of baseflow and flood discharge(Arnold & Allen, 1999, Gonzales et al., 2009). In this study, to better understand and evaluate the groundwater contribution (Base flow) to the total river flow, Radon measurements were conducted using the RAD7 instrument at the selected river gauging stations installed at the outlets of the marginal grabens and outlets of the study area (Awash Adaitu). Besides, radon measurement was also conducted in the ungauged areas in the rift margin, and in the rift floor mainly at the tributaries, the main river route, and lake for the better evaluation of the groundwater contributions and also for conceptualizing the tectonic situations of the area (Figure 21). Accordingly, the main tributaries originating from the marginal grabens like Borkena, Ataye, Jara, Robit, and Jewuha have higher radon levels than the tributaries, lake, and Main River located within the rift floor. The most likely reasons for the higher radon levels at the outlets of the rift margin are the flow of groundwater to the river due to the presence of columnar jointed basalt in the river bed extending from the plateau to the rift margin and cross-structures with a NE-SW, NW-SE, and W-E trend. This is why the river is called a "gaining river" at the rift margin zonation. While, towards the rift floor, the surface water is depleted with radon values, and the base flow portion in the total river flow is decreased, hence the river is referred to as a losing river. This is because the groundwater emerging from the marginal grabens mainly follows the weak zones found in the highly faulted Dalha basalt, as it is found in the Arcuate Accommodation Zone (AAZ). The radon levels measured at the Awash River around the Gewane area and at Lake Yardi support this idea. The other but less probable scenario is that the groundwater that partially emerges from the marginal rift may migrate with the surface water over long distances with high surface temperature, which causes the radon value to gradually decrease as the lifetime of radon is very short (3.8 days) (Tadesse et al., 2023) resulting in a lower value in the rift floor. However, at some gauging stations in the rift floor, such as Awash Adaitu, the radon value is relatively high (Table 39) because the river bed is covered by stratoidal Afar basalt, which is regionally connected to the marginal grabens due to the cross-structures. Thus, in the rift floor the likelihood of groundwater contributing to the total river flow depends on the underlying geology and the presence of transverse structures. Accordingly, the river within the rift floor can be characterized as losing or gaining depending on the local geology of the riverbed and the availability of transverse structures. The above explanations

using the radon value analysis have given a clear indication that the contribution of groundwater to river flow is higher at the rift margin and tends to decrease to the rift floor (Table 39). These circumstances lead to the assumption that the contribution of groundwater to the total flux at the rift margin and the rift floor should be evaluated independently. The Time Series Analysis (TSA) module of the river analysis package (RAP version 3.03) (Aliran et al., 2013, Kang et al., 2022, Ladson et al., 2013, Molla & Tegaye, 2019) was used to separate the river discharge data into their respective components of baseflow and direct runoff, where the input data are daily time series. Although the selection of an appropriate alpha value in the program remains an open question, it is highly dependent on the aquifer's ability to store and transmit groundwater through it (Dennis Risser et al., 2005, Ladson et al., 2013). Hence, higher and lower alpha value is assigned to high and less permeable lithology respectively. Accordingly, as the main hydrogeological units on the rift margin includes alluvial deposit underlain by moderately to highly fractured and weathered volcanic rocks supposed to have high permeability nature, the alpha value is set at 0.94. While, the main geological formation near the rift floor is highly faulted and fractured Dalha basalt and found along the Arcuate Accommodation Zone(AAZ), which leads the groundwater to go downward, the alpha value is set at 0.96 rather than using the default value of 0.975. Accordingly, the contribution of groundwater to river flow at the rift margin and on the rift floor is 136.7 mm/year and 17.86 mm/year respectively. The baseflow result is highly consistent with the radon values conducted at both regions (Figure 69 and Table 39), where higher baseflow contribution has higher radon values and vice versa.

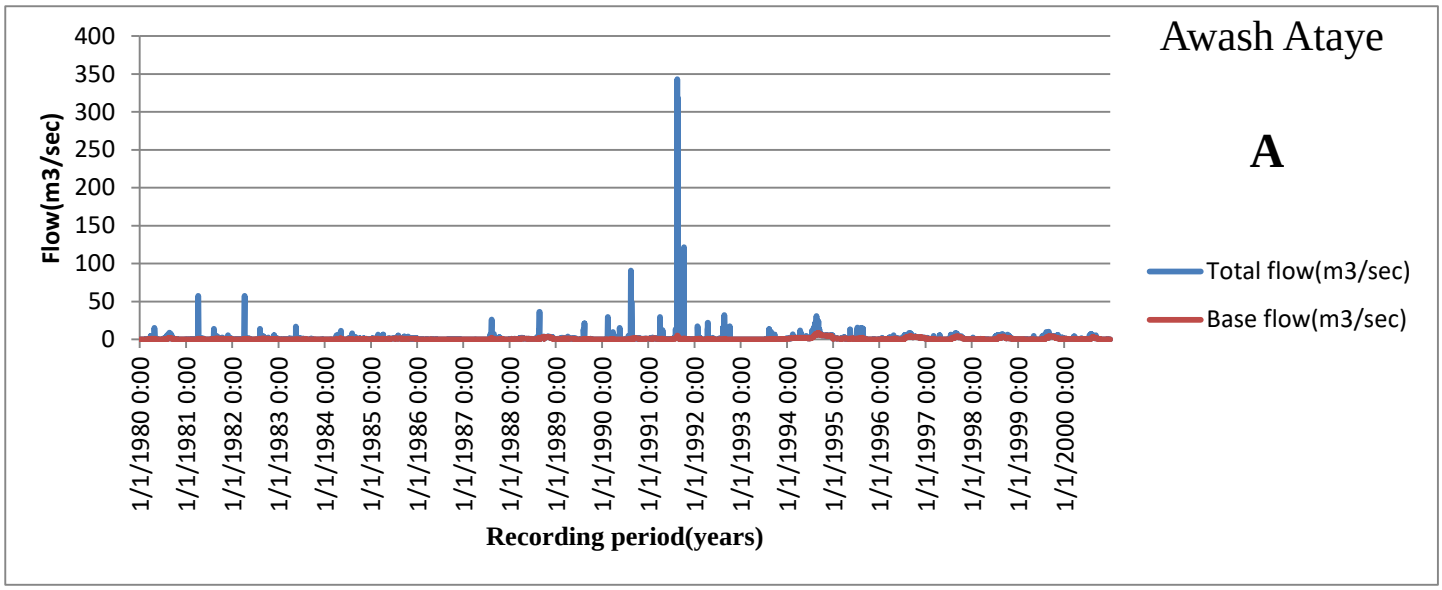
Table 39: Base flow estimation at the rift margin and rift floor

S.No	Station name	Area (km2)	Wtd-Area	Recording period (years)	Alpha value	MDBF	Base flow (mm/year	Wtd-Base flow	BFI	Radon (Bq/m3)	Physiography
1	Borkena	1735	0.60	20	0.94	5.70	103.61	62.16	0.41	288.46	Rift Margin
2	Jara	235.4	0.08	20	0.94	1.28	171.21	13.69	0.51	142.54	Rift Margin
3	Ataye	166.4	0.06	20	0.94	0.92	172.84	10.37	0.54	276.33	Rift Margin
4	Jewuha	514.4	0.18	20	0.94	2.67	163.57	29.44	0.45	138.47	Rift Margin
5	Robit	263	0.09	20	0.94	1.95	233.82	21.04	0.45	158.42	Rift Margin
	Total	2914.2	1					136.7			
7	Awash Adaitu	52836	1	20	0.96	29.918	17.86	17.86	0.35	48.53	Rift floor





Figure 68: River gauging station at Awash Adaitu, and Borkena outlet (Left to Right)



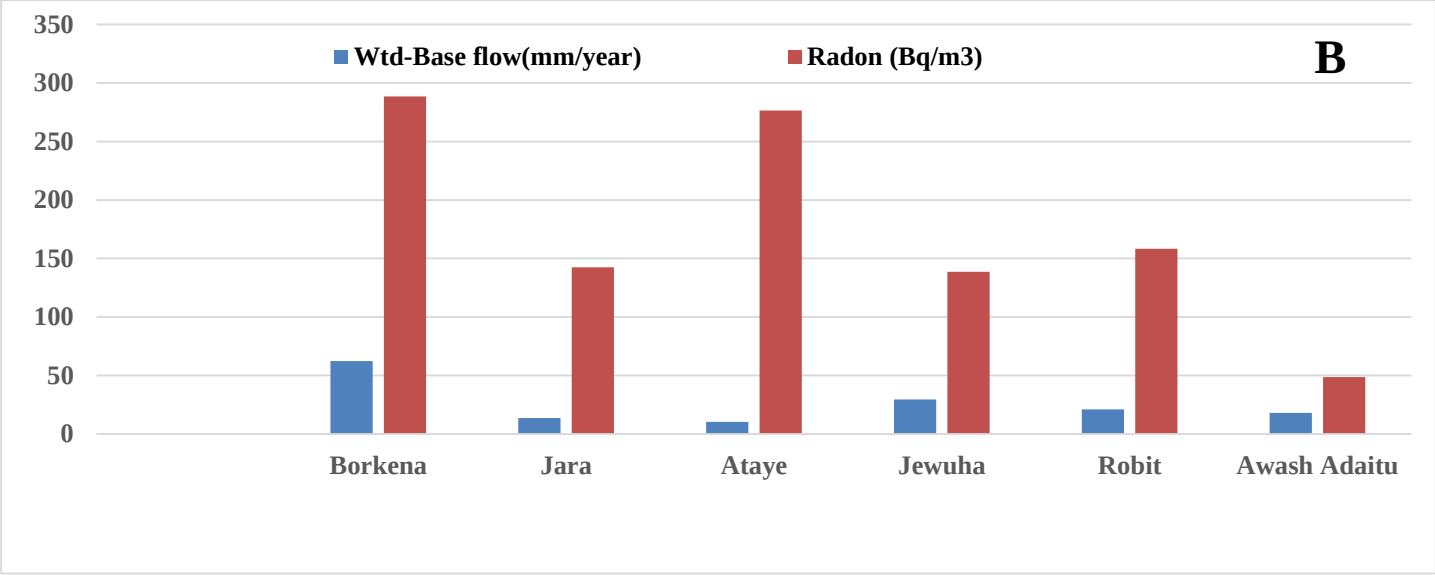


Figure 69: Base flow separation for Awash Ataye using RAP (Version 3.0.3) (A), Radon and Wtd Baseflow correlations along the gauging stations (B)

4.3.4.5 Comparison of Results and their limitations

From the multiple recharge estimation approaches, the smallest recharge rate was determined from the Chloride Mass Balance (CMB) method. In this study, additional chloride was found in the shallow wells, surface waters, and thermal spring sources than in deep wells and highland springs. This shows that the estimation of groundwater recharge using CMB at any depth and location has limited applicability, especially in arid to semi-arid climatic regions. Hence, the CMB method should be used with extreme caution if the assumptions are not fully met.

The Water balance method has limitations, especially on the rift floor, as there are few spatially distributed meteorological stations, so the result should be calibrated and compared with the other methods.

The spatially distributed groundwater recharge from the WetSpass model reveals that groundwater recharge in arid and semi-arid climatic regions is often heterogeneous. Accordingly, the rift margin shows a higher level of groundwater recharge than the rift floor due to different favorable conditions like moderate to high annual recharge, a valley filled by alluvial deposits surrounded by fractured volcanic mountains which favors high infiltration of the rainfall. However, from the geological, hydrochemical, stable isotope, and radon analysis, the rift floor receives groundwater recharge from the western rift margin through the transverse structures besides the local recharge. Hence, the rift floor cannot be classified as a low recharge area; rather, it could be considered low to moderate. This shows that the WetSpass model did not reveal groundwater recharge conditions in the intermountain valleys, and structural contributions and needs integrations with other approaches.

The Base flow separation method often yields higher results at the outlets of marginal grabens than the rift floor. Similarly, Radon measurements reveal that the tributaries originating from the marginal grabens in the rift margin have significantly higher radon levels compared to those on the rift floor. The increasing tendency of baseflow and Radon at the rift margin occurs because groundwater enters the river through columnar-jointed basalt and cross-structures, classifying it as a "gaining river." Conversely, as the groundwater is discharged from the marginal grabens, it flows along the weak zones in the highly faulted Dalha basalt found in the accommodation zones, leading the groundwater to seep down, resulting in the decrease of the Radon levels, and base flow contribution, leads the river in the rift floor and surrounding area is categorized as a "losing river." The baseflow at the outlets of the study area (Awash Adaitu) is estimated to be much lower (17.86mm/year), supporting the radon result and interpretations. These illustrations reveal how the local geological, structural and tectonic situations significantly influence the contributions of groundwater to river flow, leading to distinct behaviors along the rift margin in contrast

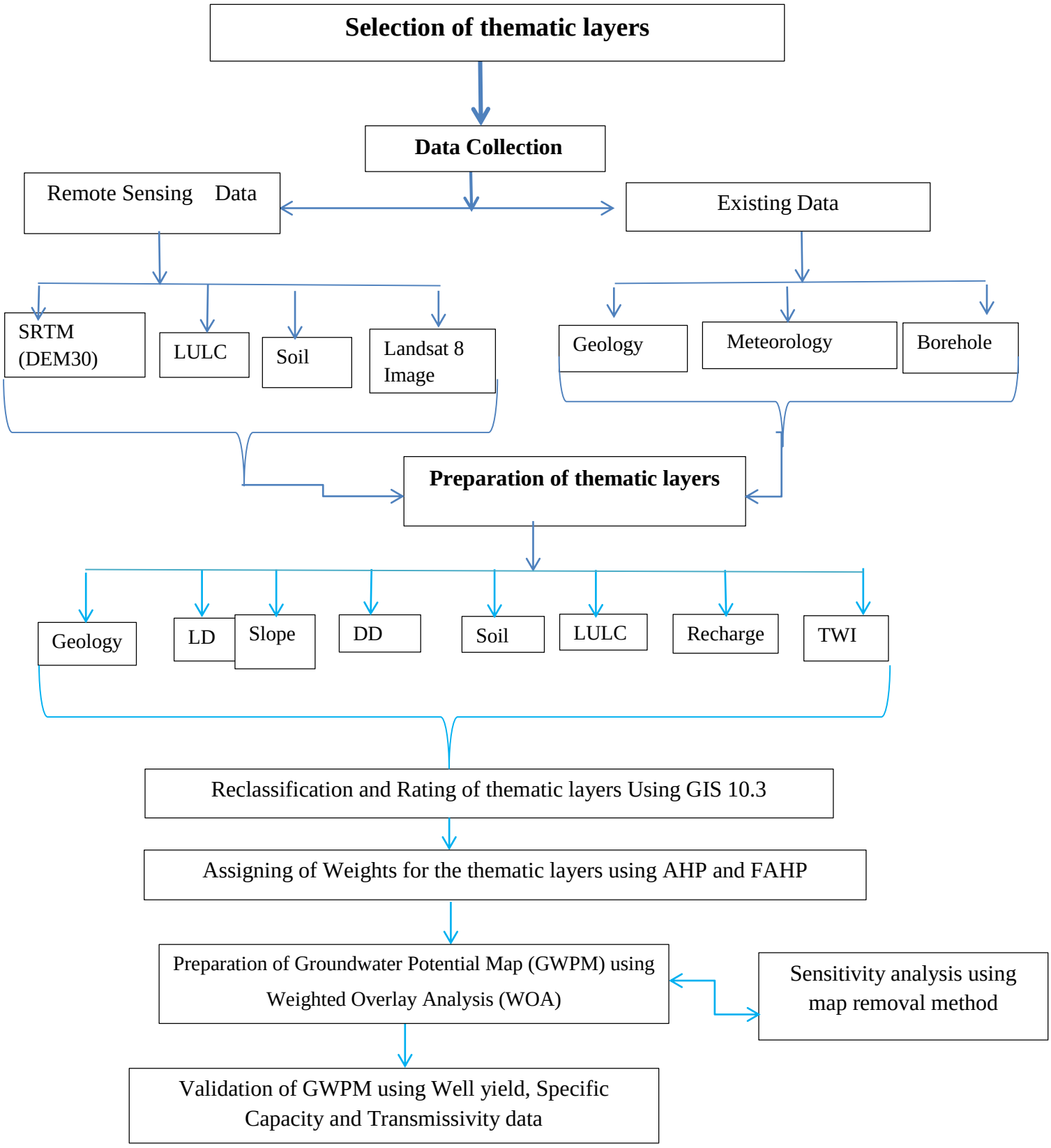
to the rift floor. Hence, in tectonically active regions like the Afar Triangle, the applications of the baseflow separation method can be challenging and limited due to complex geological and structural configurations and groundwater flow dynamics; therefore, the method should be supplemented by other techniques such as radon measurements to evaluate the accuracy. Besides, the absence of flow monitoring stations at the end of the rift margin or within the rift floor limits assessments of baseflow contributions along these areas. The variable baseflow output at the outlets of the marginal grabens and within the rift floor renders comparisons with the other three methods unfeasible, while the remaining three methods are found to behave a good correlations

Chapter Five: Integrated Remote Sensing (RS) and Geographic Information System (GIS) overlay analysis for groundwater potential evaluation

5.1 General

Remote sensing and geographic information system (GIS) overlay analysis techniques with the help of AHP and FAHP have been used to evaluate the groundwater potential zones of the southern sections of the Western Afar Rift margin and associated rift floor. The specific objectives are (i) to generate thematic layers that could regulate groundwater storage and flow using data from remote sensing, other sources, and field visits; (ii) to identify and delineate groundwater potential zones through the integration of these thematic maps with GIS techniques; and (iii) to determine the extent to which controlling factors for groundwater occurrence and distribution, as well as their interrelationships, play a part.

Hence, before defining the groundwater potential zones of a particular area using GIS overlay analysis approaches, the main regulating elements for groundwater circulation and storage should be investigated and defined(Danso & Ma, 2023, Haile et al., 2022). When choosing these parameters for groundwater potential zone mapping, it's crucial to take their impact on groundwater occurrence, data accessibility, and the basin's climatic circumstances into account (Adeyeye et al., 2019, S. Das, 2019b). Accordingly, in this specific study, the overlay analysis was conducted by considering eight input thematic layers including geology, lineament density, soil, land use/land cover (LULC), recharge, drainage density, slope, and topographic wetness index, all of which are essential for groundwater occurrence, distribution, and movement. With a spatial resolution of 100 meters by 100 meters, each of these thematic layers were generated as a raster file using the GIS working environment in zone 37 of the UTM projection with ADINDAN as the reference datum. Then, using a multi-criteria decision-making (MCDM) technique, namely the Analytic Hierarchical Process (AHP) developed by Saaty and Modified Saaty called FAHP, suitable weightage was given to each layer based on their relative influence on groundwater occurrence, supported by local geological and hydrogeological knowledge. Finally, a groundwater potential map is generated in a GIS environment utilizing weighted overlay analysis. The following flow chart has been utilized for the overall accomplishment of the work.



Flow chart 1: Summarized Methodology used for delineating groundwater potential zones

LD: Lineament Density, DD: Drainage Density, LULC: Land use Land cover, TWI: Topographic Wetness Index

5.2 Selection, Reclassification, and Ratings of Thematic Layers

To develop the spatially distributed Groundwater Potential zone in the study area, 8(eight) thematic layers including geology, lineament density, soil, land use/cover, slope, recharge, drainage density, and topographic wetness index (TWI) were selected and integrated. Once each thematic layer was selected and prepared, the Arc GIS 10.3 spatial analyst tool was used to reclassify the different classes of the -parameter. Rates were given to each class following the order in which the classes affected groundwater storage potential(Arulbalaji et al., 2019, Karlović et al., 2022). Ratings of 1 to 5 were therefore selected, with rates 1, 2, 3, 4, and 5 denoting, respectively, very low, low, moderate, high, and very high appropriate groundwater storage potential(Table 40).

Table 40: Assigned Rates and Groundwater occurrence suitability classification

Rates	Suitability for Ground Water occurrence
1	Very Low suitable for groundwater occurrence
2	Low suitability for groundwater occurrence
3	Moderately suitable for groundwater occurrence
4	High Suitable for groundwater occurrence
5	Very high suitable for groundwater occurrence

5.2.1 Geology

Geology has a significant influence on a region's potential for groundwater because it exerts strong control over the infiltration and flow processes, which depend on the formation porosity and permeability(Ahmad, Dar, Andualem, et al., 2020, Rajesh et al., 2021, Doke et al., 2021, Duah et al., 2021and Razandi et al., 2015). Lithological characteristics such as the weathering and fracturing of rock units, rock hardness, fracture spacing, grain size, and fracture infilling materials all have a significant impact on the occurrence, movement, quality, and quantity of groundwater in arid and semi-arid climate regions (Abdalla et al., 2012, Mart et al., 2019). As has been discussed in section 2.4.3, the main geological units in the study area are volcanic rocks comprising of Tarmaber basalt, Alaji formations, and Columnar jointed (Aiba) basalt which are highly exposed along the escarpments and marginal grabens. The marginal graben is filled by alluvial deposits and underlain by trap series. Between the rift margin and rift floor, highly fractured and weathered Dalha basal is exposed and serves as the main water-bearing formation along this area. The rift floor is mainly filled by lacustrine deposits with some stratoid basalt outcrops. Based on the available drilling logs, well yield, geological and hydrogeological conceptualization and experience (Bersi & Saibi, 2020, Edet et al., 1998), the aforementioned lithological units have been reclassified and rated with respective of groundwater storage and movement, in the

southern sections of Western Afar Rift margin and associated rift floor(Table 41and Figure 70). Accordingly, the alluvial deposit is rated and reclassified as very high suitable followed by fractured and weathered Aiba & Dalha basalt, Tarmaber basalt, Acidic rocks & Afar stratoid series and the lacustrine deposit is the least suitable respectively for groundwater occurrence.

Table 41: Reclassified geological formations for the occurrence of groundwater potentiality.

S.No	Geology	Hydrogeological Descriptions	Area (km^2)	Area (%)	Rate	Remark
1	Alluvial Deposit	Comprising of sand & gravel	1173	6.13	5	Very high suitable for groundwater occurrence
2	Aiba and Dalha Basalts	Highly fractured and weathered basalt	5831	30.48	4	High suitable for groundwater occurrence
3	Tarmaber Basalt	Moderately fractured and weathered basalt	1121	5.86	3	Moderately suitable for groundwater occurrence
4	Acidic rocks & Afar stratoid series	Slightly fractured & weathered rocks	7974	41.68	2	Low suitability for groundwater occurrence
5	Lacustrine Deposits	Dominantly clay and silt	3033	15.85	1	Very low suitable for groundwater occurrence
		Total	**19132**	**100**		

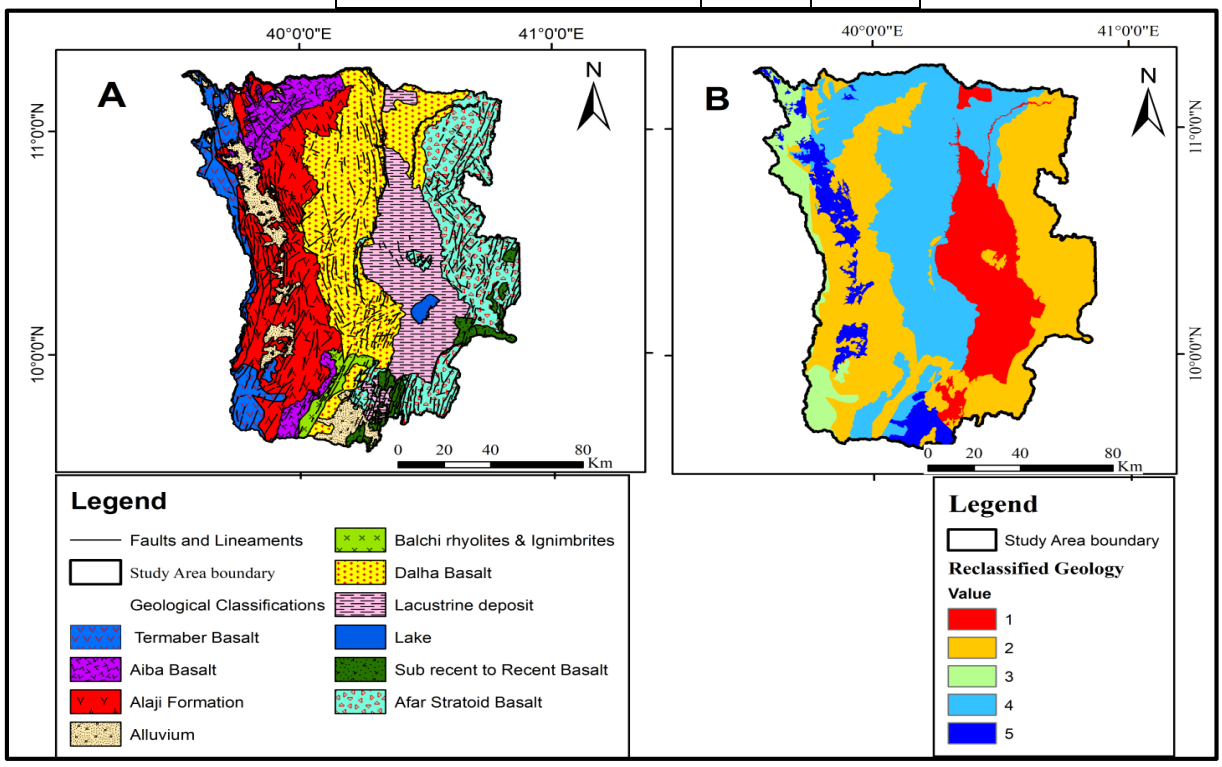


Figure 70: Geological map (A), Reclassified geological map (B)

5.2.2 Lineament Density

Lineaments, such as joints, fractures, and faults, provide essential details on the underlying fractures that may restrict the flow and storage of groundwater. They also play a key role in influencing the occurrence, movement, and distribution of groundwater, especially in hard-rock terrains(S. Das, 2018, Jaafarzadeh et al., 2021, Martín-Loeches et al., 2018). Since they serve as channels for groundwater flow and storage, lineaments can result in increased secondary porosity and serve as groundwater potential zones, which is why they are often used in groundwater studies to identify groundwater prospect sites(Ahmad et al., 2021, Bhattacharya et al., 2021). In the study area, along the escarpment, the lineament density is found to be higher, these are faults and lineaments having orientations of NW-SE, and NE-SW, NNE-SSW, connecting the plateau to the rift margin. Highly discharged springs can be seen at the foot of some of the fault scarps that bound the margin, indicating that these faults serve as conduits for the flow of groundwater from the plateau to the rift margin, mainly to the marginal grabens. Besides, some faults and lineaments trend NE-SW, and sometimes orthogonally to the rift-bounding fault, were also found connecting the rift margin to the rift floor. These structures that connect the plateau to the rift margin and the rift margin to the rift floor can be called connection zones (Figure 71), which are vital for the flow of groundwater from the former to the latter. The lineament density was calculated using a line density analysis tool and classed into five groups in Arc GIS 10.3 by dividing the total length of all recorded lineaments by the area under consideration(Arulbalaji et al., 2019; Kaur et al., 2020). According to Prabu & Rajagopal et al., 2013 ratings, the higher number (0.34-0.51km/Km^2) is given a rating of 5, indicating that it represents areas and zones with greater porosity and permeability, and the lower value (0-0.05 Km/Km^2) is given a rating of 1. Finally, Q GIS was used to create a rose diagram to show the major orientation of the lineaments (Bonetto et al., 2021, S. Das, 2018), and is mainly NNE-SSW and NE-SW (Figure 71).

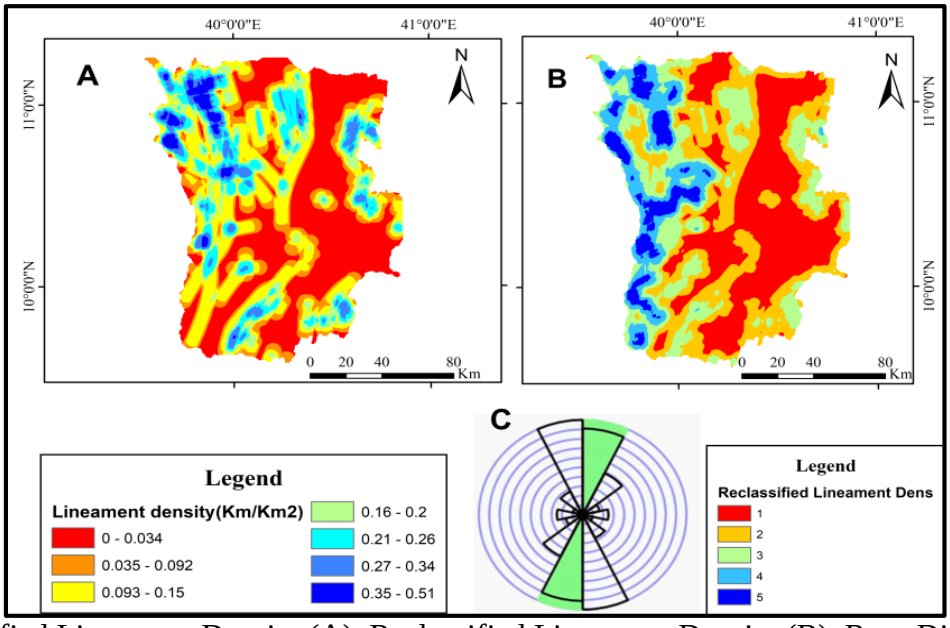


Figure 71: Classified Lineament Density (A), Reclassified Lineament Density (B), Rose Diagram (C)

5.2.3 Slope

The slope was used to identify sites for groundwater prospecting and can be thought of as a crucial factor in regulating runoff flows and infiltration, which will regulate the groundwater recharge (Khan et al., 2022). The digital elevation model (DEM) from the Shuttle Radar Topography Mission (SRTM) with a resolution of 30 m was used to create the slope map, which was then resampled into 100m using the slope function in the GIS 10.3 working environment. According to Ahmad et al., 2020, and Martín-Loeches et al., 2018, the lower slope value is given a higher rank because the surface runoff is frequently slow in locations of a gentle slope, allowing more time for precipitation percolation and promoting significant groundwater recharge. Conversely, areas with higher slope values promote rapid surface runoff, which allows rainwater less time to infiltrate and replenish groundwater aquifers, which are classified as lower rankings (Figure 72). Accordingly, the higher slope value (37-88) is scored as 1, since it is less suitable for groundwater occurrence, and the lower value (0-3.8^{O}C) is ranked as 5.

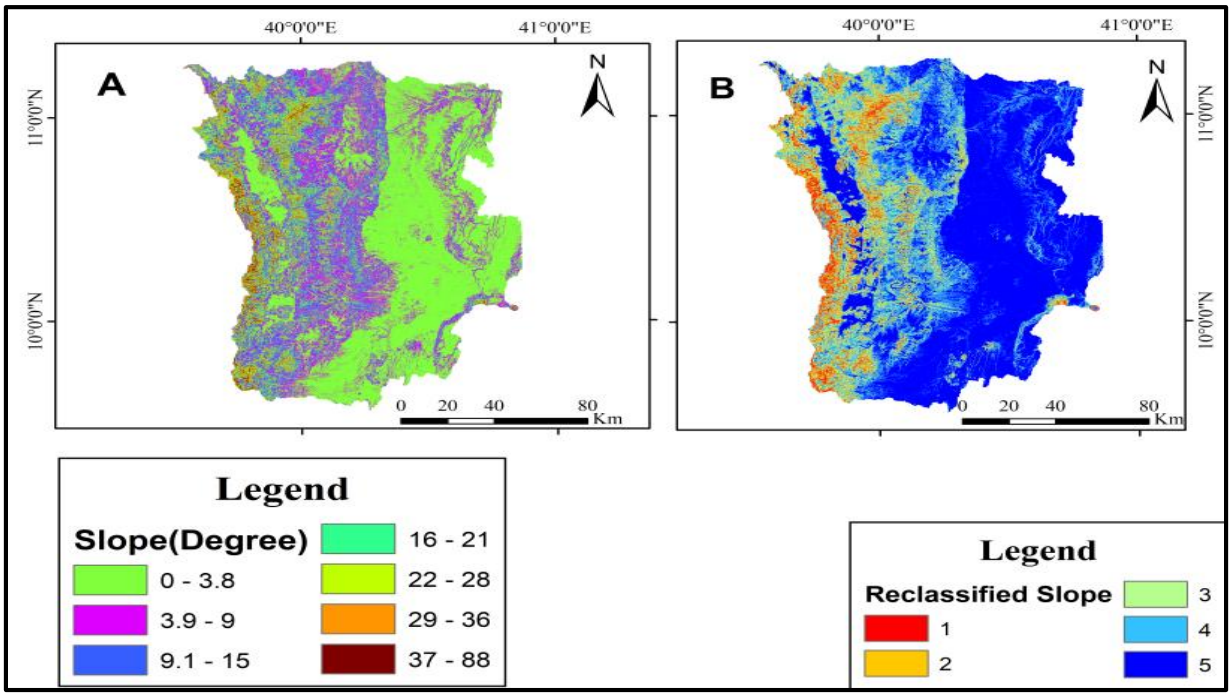


Figure 72: Classified Slope (A), Reclassified Slope (B)

5.2.4 Drainage Density

Drainage density reflects the proximity of channel spacing as well as the composition of the surface material (Prasad et al., 2008). Using the flow direction and flow accumulation commands in ArcGIS, a thorough drainage map has been generated to create a drainage density map (Danso & Ma, 2023, S. Das, 2019a). In Arc GIS, a line density tool was used to calculate the drainage density. According to Arulbalaji et al., 2019, from the perspective of groundwater potential, the higher the drainage density, the higher the surface runoff would be, so a low rank is assigned for a value of 0.4km/Km2; conversely, the lower the

drainage density, the higher the probability of recharge, so a high rate is assigned for a value of 0.000042Km/km^2(Figure 73).

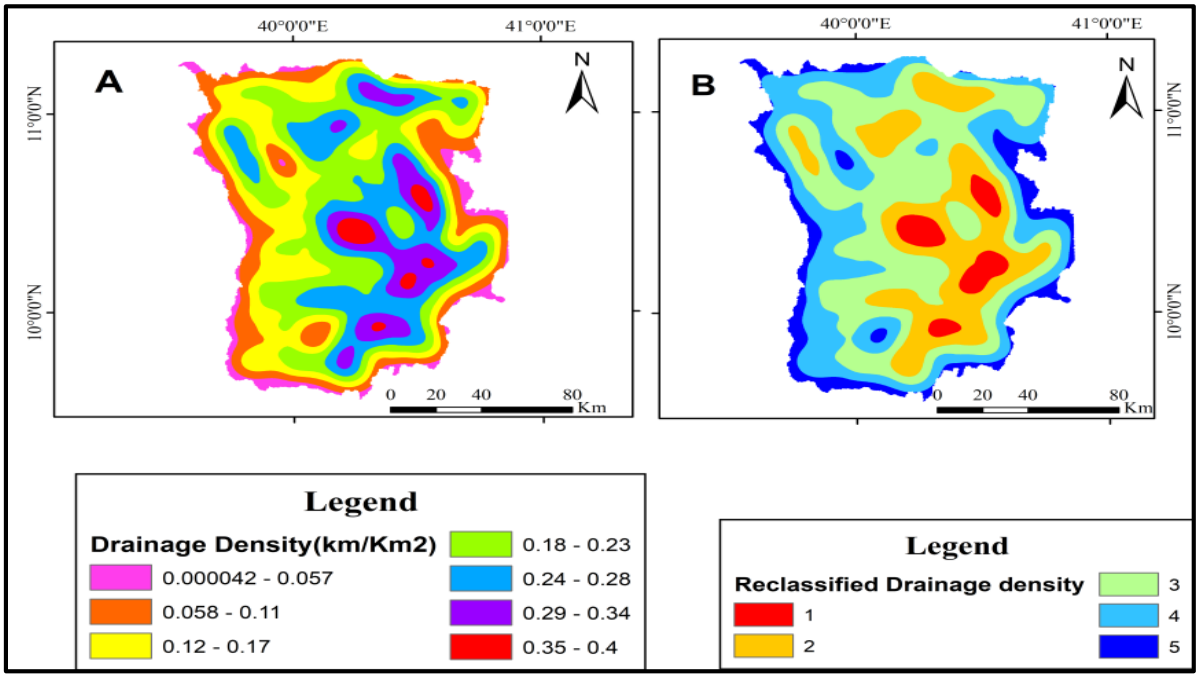


Figure 73: Classified Drainage Density (A), Reclassified Drainage Density (B)

5.2.5 Soil

Soil is a parameter that influences the percolation capacity of precipitation and reveals the groundwater potential of a certain area(Abdalla, 2012, Babu et al., 2020, Edet et al., 1998). Reclassification and rating of soils with respective groundwater storage and occurrence were conducted based on the grain size's ability for infiltration (Machiwal et al., 2011, S. Das & Pardeshi, 2018, Radulović et al., 2022). While groundwater infiltration is slower in fine-grained soils, it is higher in coarse-grained and porous textures(Ibrahim-Bathis & Ahmed et al., 2016). As a result, soil having coarser and finer grain sizes like sand and clay is assumed to be high and low suitable for the infiltration of precipitation and classified and rated as very high and low respectively (Table 42 and Figure 74).

Table 42: Soil coverage and Reclassified based on the Groundwater occurrence suitability

S.No	Soil type	Texture (Based on FAO)	Coverage (Km^2)	Coverage (%)	Rate	Suitability for GW occurrence
1	Lithic Leptosols	Sand	5873	30.67	5	Very high suitable
2	Eutric Cambisols	Loam soil	733	3.83	4	High suitable
3	Eutric Leptosols	Sandy Clay	3328	17.39	3	Moderate suitable
4	Eutric Fluvisols	Silty clay	3388	17.75	2	Very suitable
5	Haplic Solon Chaks & Vertic Cambisols	Clay	5810	30.36	1	Very low

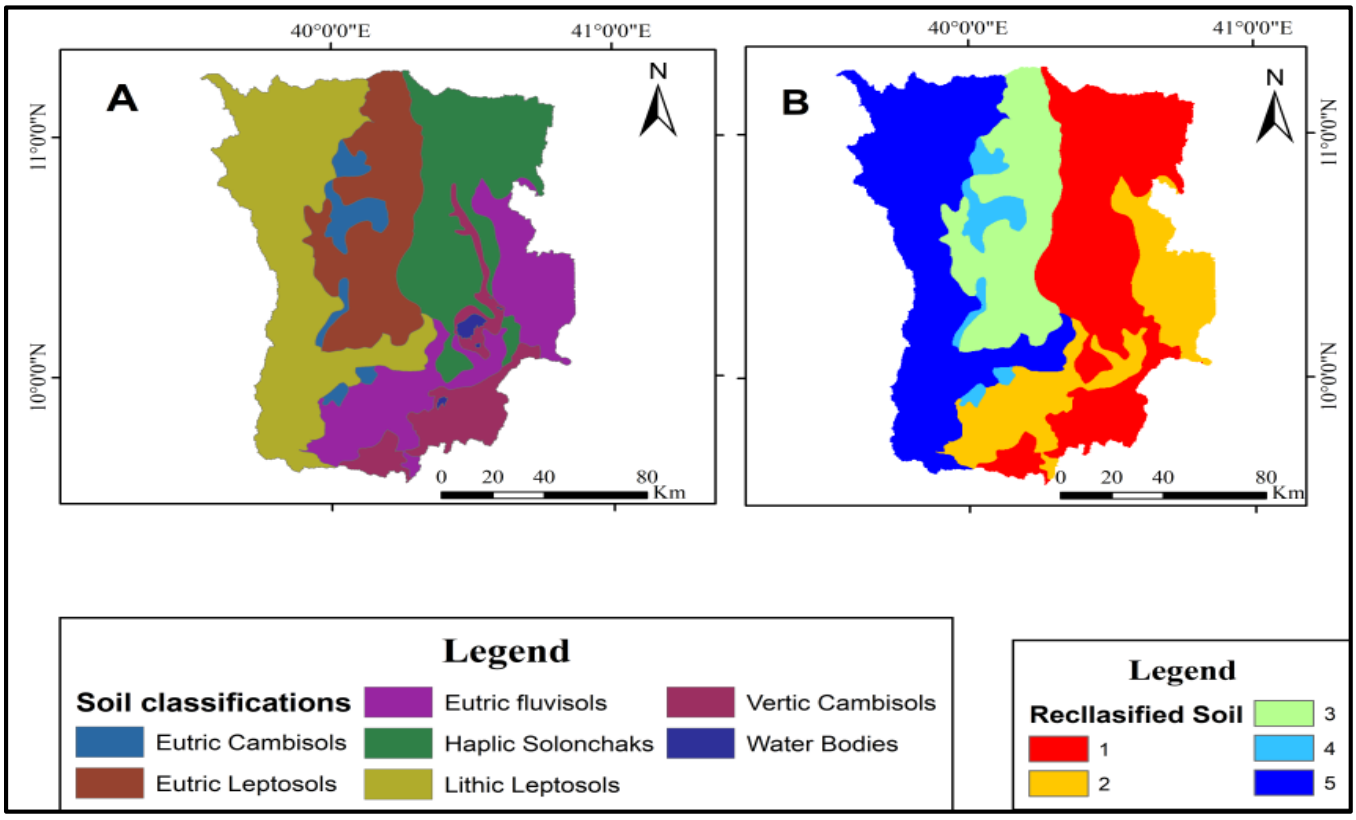


Figure 74: Classified soil (A), Reclassified soil (B)

5.2.6 Land use

Land use and cover will have a massive impact on the availability of groundwater in a certain area by affecting the hydrologic cycle components (Abijith et al., 2020, Allafta et al., 2021). According to N. Rane et al., 2023, land use is a key element that affects the soils' ability to retain water. The evaluation, utilization, and development of groundwater must therefore be done with a proper understanding of land use, and land cover(Regasa et al., 2021). Based on their ability to hold and permeate water into the ground, land use and cover were reclassified and rated for analysis(Ibrahim-Bathis & Ahmed, 2016, Williams et al., 2012). In other words, if the surface is covered with dense forest, the infiltration will be higher and the runoff will be lower, but concreted areas have less potential for recharge (Detto et al., 2006). Accordingly, eucalyptus and forest have been assumed to be more favorable for the existence of groundwater, while bare land and rocky land were assigned less suitable (Doke et al., 2021). Therefore bare land, rocky, and settlement areas are assigned a low and very low rank, while forest and eucalyptus areas are given a higher rank (Table 43).

Table 43: Reclassified LULC based on the suitability for Groundwater (GW) occurrence.

S.No	Land use land cover type	Area (Km^2)	Area (%)	Rate	Suitability for GW occurrence
1	Eucalyptus, forest, and water body	692	3.62	5	Very high suitable
2	Agriculture and grassland	3852	20.13	4	High suitable for
3	Shrub land, dispersed shrub land, acacia, & dispersed acacia	8937	46.71	3	Moderate suitable
4	Bare land & Rocky bare land	5485	0.86	2	Low suitable
5	Settlements	166	28.67	1	Very low

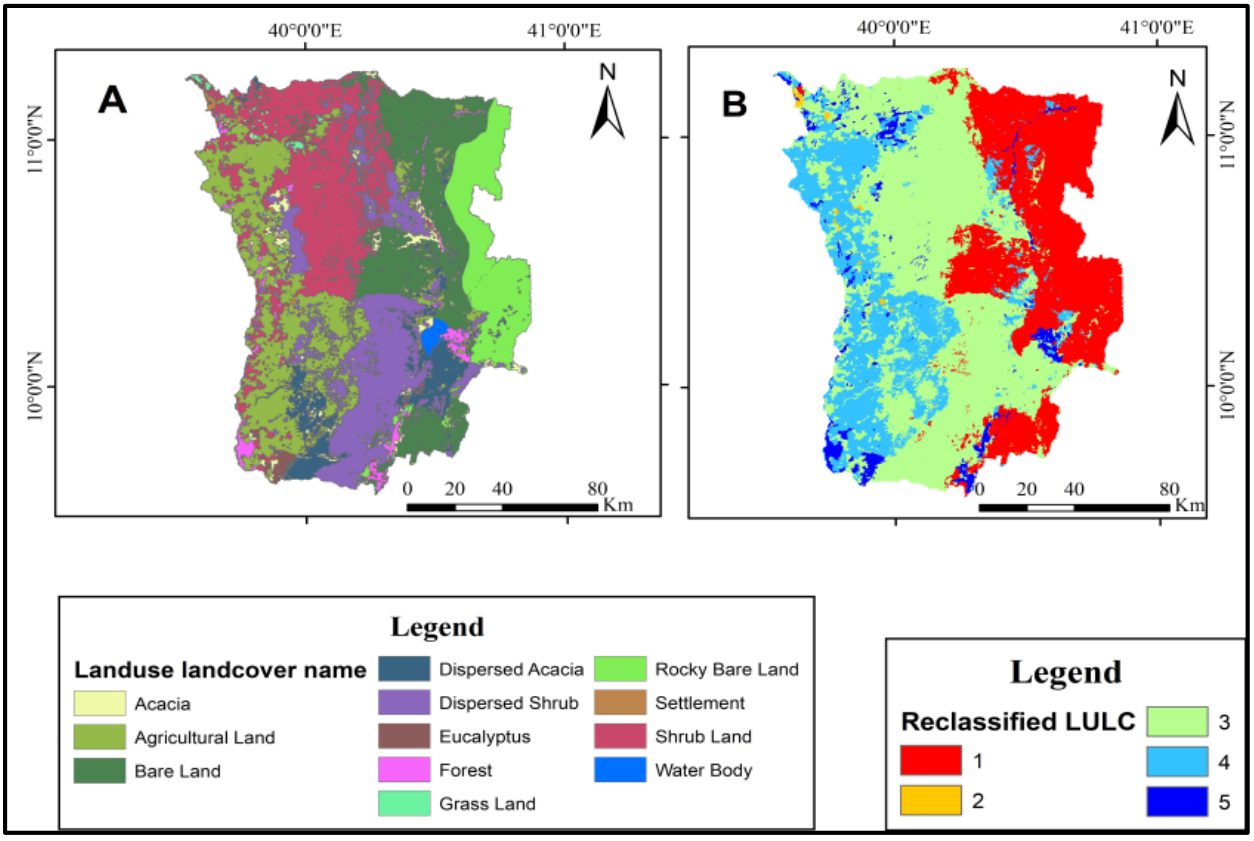


Figure 75: Classified LULC (A), Reclassified LULC (B)

5.2.7 Recharge

Recharge is the main controlling factor that impacts the groundwater potential of a certain area (Mekonen et al., 2020, Yenehun et al., 2022). As described in Jesiya & Gopinath, 2020, and Kaewdum & Chotpantarat, 2021, those with higher rates of groundwater recharge often have greater potential for groundwater than those with lower rates of groundwater recharge. Numerous approaches are frequently taken into consideration to determine recharge, although estimations are frequently fraught with difficulty because of the varied surface and subsurface conditions and environment(Ifediegwu et al., 2019,

Kaewdum & Chotpantarat, 2022, Schilling et al., 2021). Since the study area is found in the Afar depression; where there has been a high variation in climate, physiography, geology, tectonics, soil texture, and land use, the recharge will also vary both spatially and temporally. Therefore, using the traditional point recharge and water balance estimation methodologies to generalize the result is not a good idea (Ifediegwu, 2022, Obuobie et al., 2012, Tilahun & Merkel, 2009). As a result, to estimate the long-term average, spatially distributed, a physically based water balance model termed WetSpass –M model was used(Amiri et al., 2022, Dereje & Nedaw et al., 2019). Accordingly, the maximum, minimum, and mean recharge determined by the WetSpass-M mod is 396.61mm/year, 40.011mm/year, and 100.88mm/year respectively (Section 4.3.4 Groundwater Recharge). Based on the model's output, the study area's western, northwestern, and southwestern parts experience high levels of groundwater recharge because of the area's high annual precipitation, sandy soil, and eucalyptus and grassland cover. The low terrain particularly in the eastern, northeastern, and southeastern regions of the research area, on the other hand, has relatively low recharge levels because of little rainfall, barren ground, rocky surfaces, and silt to clay soil (Figure 76). Because high recharge values favor groundwater potential, the rate was assigned in ascending order of the amount of recharge noted on the recharge map (Jaafarzadeh et al., 2021).

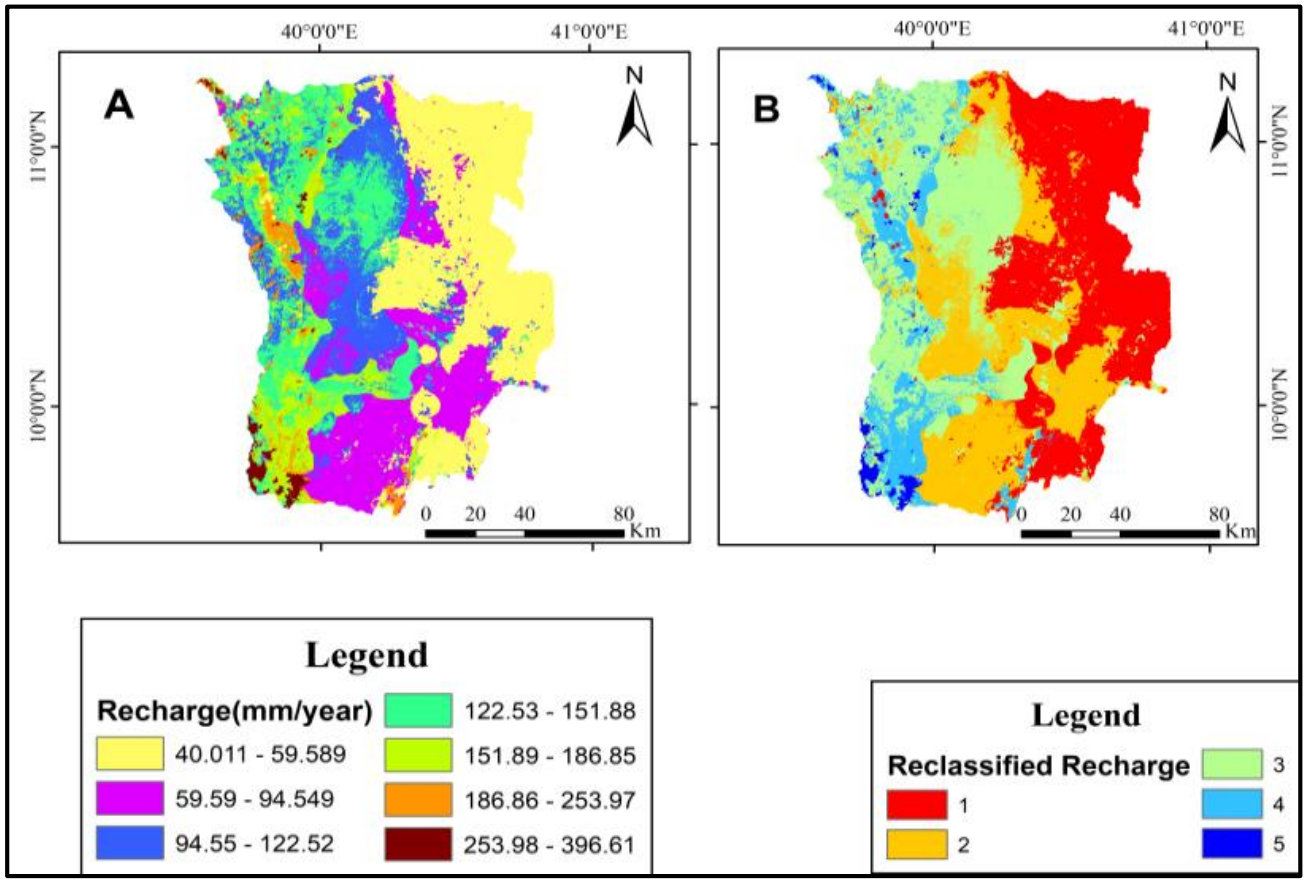


Figure 76: Classified Recharge (A), Reclassified Recharge (B)

5.2.8 Topographic Wetness Index (TWI)

The Topographic Wetness Index (TWI) is the other parameter that will affect the distribution of groundwater in a certain area. The model is used to understand groundwater accumulation areas with elevation variation(Hoffmann & Sander, 2007). It is a function of both the slope and the upstream contributing area per unit width orthogonal to the flow direction (Sorensen et al., 2006, Obuobie et al., 2005). Creating a Topographic Wetness Index (TWI) requires: Slope (in degree), flow direction, and flow accumulation which are generated from elevation maps (DEM) extracted from SRTM (30m resolution) as an input layer. To calculate the TWI, as it is well described in El Ayady et al., 2023, and Mattivi et al., 2019, the equation developed by Moore et al., 1991 was used and given by the following formula.

Equation 28: $TWI = \ln(\frac{As}{\tan\beta})$

Where, As is flow accumulation and tan β is tan of slope in degree

Based on the above formula, the maximum TWI value in this particular work is 31, and the lowest value is 6.5(Figure 77). According to Gebre et al., 2018, a greater number denotes a larger likelihood of water accumulating due to a low slope and vice versa. As a result, the greater value is given a rating of 5, and the lower value is given a rating of 1.

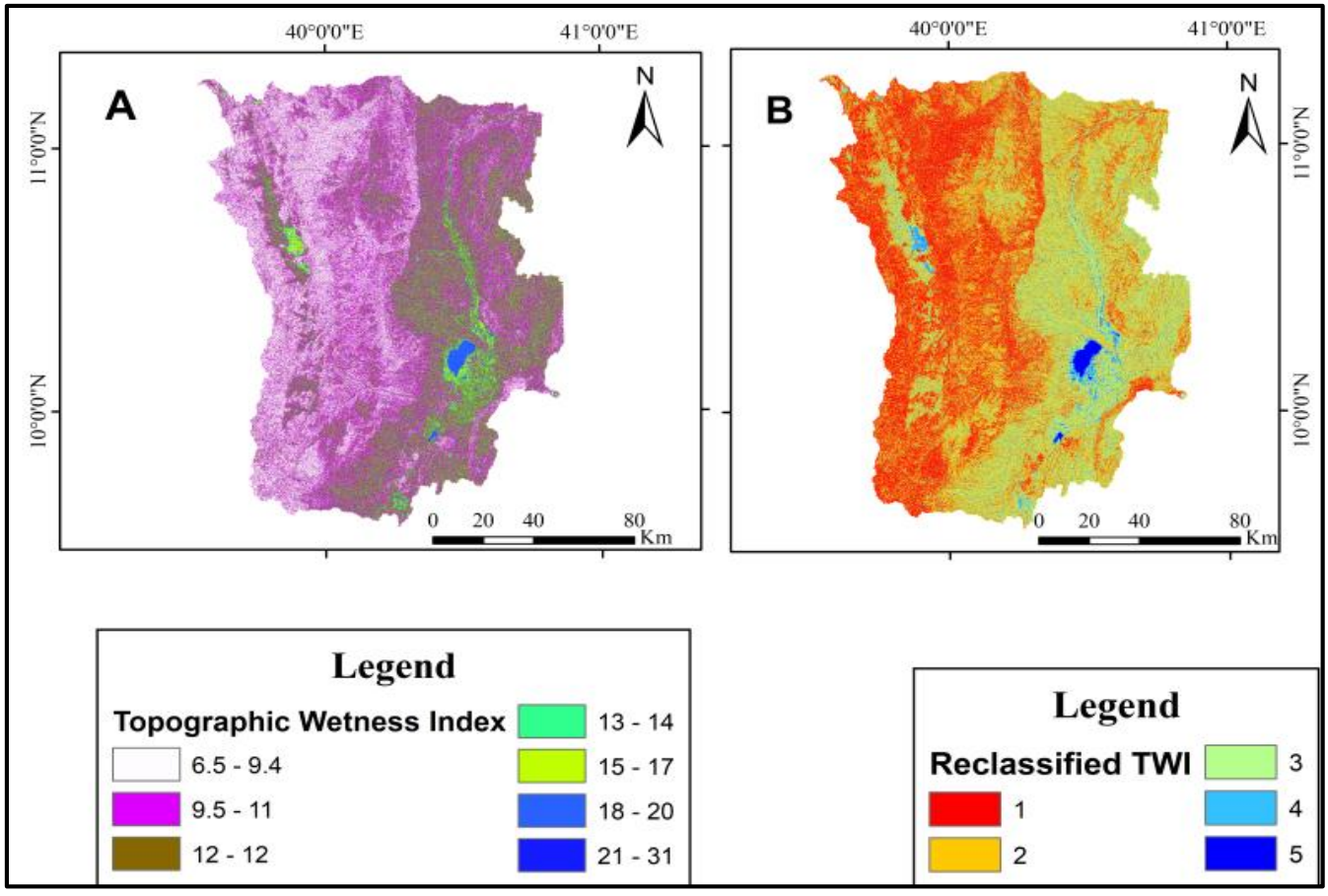


Figure 77: Classified Topographic Wetness Index (A), Reclassified Topographic Wetness Index (B)

5.3 Assigning Percentage of Influence (Weight) for the Thematic Layers

Based on their respective significance for groundwater occurrence, the proportion of influence for the input layers was established(Jhariya et al., 2016, Khan et al., 2022). Using Saaty's Analytical Hierarchy Process (AHP) (SAATY, 1980) paired matrix, and the modified Fuzzy AHP (FAHP) developed by Van-Laarhoven and Pedrycz (1983) (P.J.M. Van-Laarhoven and W.PEDRYCz, 1983), corresponding normalized weights were assigned, by integrating all of the thematic layers against one another in a pairwise comparison matrix(Muralitharan & Palanivel, 2015). Local geological and hydrogeological knowledge, and discussions with professionals regarding the influence of the input layers on the groundwater occurrence especially in the Afar Triangle and Ethiopian Rift Valley, help in assigning the weight of influence to the thematic layers.

The uncertainty during the assigning of the percentages of influence (weight) for the parameters with AHP is controlled by determining the Consistency Ratio(RC) in simple Excel formulated by Saaty(Saaty, 1977), which is determined by the ratio between Consistency Index(CI) and the Random Index(RI(Echogdali et al., 2022)(Equation 30).

Equation 29: $CI = (\lambda_{max} - n)/(n-1)$, Where λ_{max} is the maximum eigenvalue of the comparison matrix and n is the number of factors

Equation 30: $CR = \frac{CI}{RI}$,

For a matrix having more than 5 parameters, the CR value less than 0.1 indicates that the weighting coefficients obtained can be used for water resources potentiality mapping(Razandi et al., 2015). In this study, the consistency ratio (CR) of the pairwise comparison matrix is determined to be 0.06(6%), hence the matrix can be used for groundwater potential mapping. According to Bozdag et al., 2003, Chang, 1996 and Das & Pal, 2019, incorporating FAHP into multi-criteria judgments in addition to AHP enhances the accuracy of groundwater potential mapping. This is because, the Fuzzy-AHP (FAHP) method uses fuzzy numbers with triangular membership functions which are better for solving multi-criteria decision problems instead of crisp numbers used by AHP(Jesiya & Gopinath, 2020, Rahaman et al., 2015). Therefore, FAHP aids in overcoming the inconsistencies that existed in pairwise comparisons, which leads to a better framework for evaluating factors to determine their relative importance, and helps in handling difficult issues(Ahmad, Dar, Teka, et al., 2020, Ben Brahim et al., 2021 Radulović et al., 2022). As a result, the weight determined by FAHP was used to delineate the Groundwater Potential Map of the Study area, and the outcome was then compared with Saaty AHP. Given that a parameter's impact on groundwater potential zones is influenced by its weight value (Gebeyehu & Ayenew, 2023, Gebrie & Getachew, 2019), a layer with a higher weight value has a stronger impact. Accordingly, Lineament density was determined to be the most important component for the presence of groundwater, followed

by Geology, TWI, and Recharge, with normalized weight values of 31.95%, 23.52%, 12.95%, and 12.70%, respectively. Drainage density has the least impact on the presence of groundwater (2.3%) (Figure 78, and Table 45).

Table 44: Analytic Hierarchy Approach (AHP) normalized Pairwise matrix of the thematic layers

Layers	Rate	LD	GG	TWI	Rech	Sl	LULC	Soil	DD	normalized principal Eigenvector (AHP)
		1	2	3	4	5	6	7	8	
LD	1	1	2	3	3	4	4	4	6	28.12
GG	2	½	1	2	3	4	5	5	6	23.25
TWI	3	1/3	½	1	2	3	4	3	5	15.23
Rech	4	1/3	1/3	½	1	3	4	4	5	13.01
Sl	5	¼	¼	1/3	1/3	1	3	3	4	7.99
LULC	6	¼	1/5	¼	¼	1/3	1	1	5	4.95
Soil	7	¼	1/5	1/3	¼	1/3	1	1	5	5.09
DD	8	1/6	1/6	1/5	1/5	¼	1/5	1/5	1	2.35

Table 45: Fuzzy Analytic Hierarchy Approach (FAHP) normalized Pairwise matrix of the layers

Pair-wise comparison matrix for GWPZ with Fuzzy-AHP									
Layers	**LD**	**GG**	**TWI**	**Rech**	**Slope**	**LULC**	**Soil**	**DD**	**FAHP (%)**
LD	(1,1,1)	(1,2,3)	(2,3,4)	(2,3,4)	(3,4,5)	(3,4,5)	(3,4,5)	(5,6,7)	31.95
GG	(1/3,1/2,1/1)	(1,1,1)	(1,2,3)	(2,3,4)	(3,4,5)	(4,5,6)	(4,5,6)	(5,6,7)	23.52
TWI	(1/4,1/3,1/2)	(1/3,1/2,1/1)	(1,1,1)	(1,2,3)	(2,3,4)	(3,4,5)	(2,3,4)	(4,5,6)	12.95
Rech	(1/4,1/3,1/2)	(1/4,1/3,1/2)	(1/3,1/2,1/1)	(1,1,1)	(2,3,4)	(3,4,5)	(3,4,5)	(4,5,6)	12.70
Sl	(1/5,1/4,1/3)	(1/5,1/4,1/3)	(1/4,1/3,1/2)	(1/4,1/3,1/2)	(1,1,1)	(2,3,4)	(2,3,4)	(3,4,5)	6.76
LULC	(1/5,1/4,1/3)	(1/6,1/5,1/4)	(1/5,1/4,1/3)	(1/5,1/4,1/3)	(1/4,1/3,1/2)	(1,1,1)	(1,1,1)	(3,4,5)	5.71
Soil	(1/5,1/4,1/3)	(1/6,1/5,1/4)	(1/4,1/3,1/2)	(1/5,1/4,1/3)	(1/4,1/3,1/2)	(1,1,1)	(1,1,1)	(4,5,6)	4.10
DD	(1/7,1/6,1/5)	(1/7,1/6,1/5)	(1/6,1/5,1/4)	(1/6,1/5,1/4)	(1/5,1/4,1/3)	(1/6,1/5,1/4)	(1/6,1/5,1/4)	(1,1,1)	2.30

LD=Lineament Density, GG= Geology, TWI= Topographic Wetness Index, Rech= Recharge, SL=Slope, LULC= Land use land cover, DD= Drainage Den

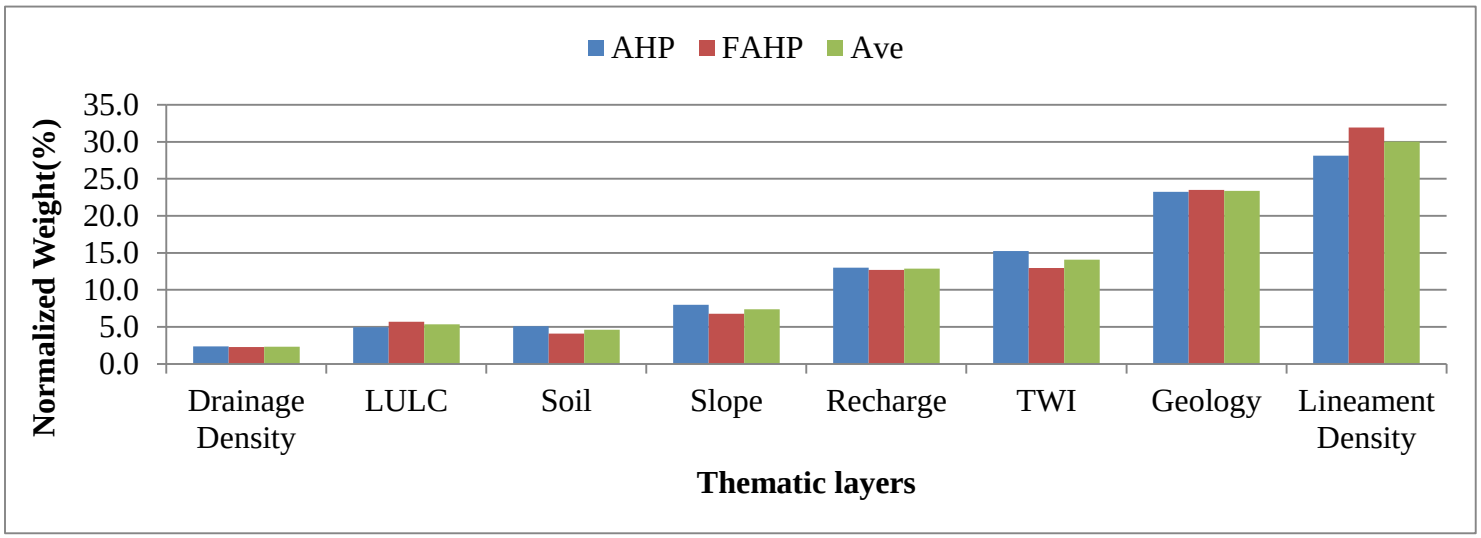


Figure 78: Normalized weights of parameters using AHP and FAHP

5.4 Delineation of Groundwater Potential Zones (GWPZ)

Using a weighted overlay method in the GIS environment, the thematic maps are ranked and weighted according to their significance for the occurrence of groundwater(Xu & Beekman, 2003, Yenehun et al., 2022). The integration of the normalized weighted input parameters to generate a GWPZ map of the study area was calculated using the following equation.

Equation 31:

$$GWPZM=LDWLDWi+GWGwi+TWIwTWIwi+RwRwi+SlwSlwi+LULCwLULCwi+SoilwSoilwi+DDwDDwi$$

Where LD is lineament density, GG is geology, LULC is land use/land cover, SL is the slope, TWI is topographic Wetness Index, R is Recharge, and DD is Drainage Density, while w is the normalized weight of the parameter, and Wi (i = 1 to n) is the normalized weight/Rate of a subclass.

Accordingly, five groundwater potential zone namely Very low, Low, Moderate, High, and Very high with corresponding area coverage of 221.48 Km^2 (1.16%), 9084.46 Km^2 (47.48%), 8281.96 Km^2 (43.29%), 1441.65 Km^2 (7.54%), and 102.45 Km^2 (0.535%) were identified (Table 46). The groundwater potential map has shown that there is a variation in the area coverage for the potential classification done by AHP and FAHP (Figure 79) and (Table 46). This is because the normalized weight of the lineament density in the case of FAHP is increasing while the other parameters are relatively comparable, which shows that the areal groundwater distribution is highly controlled by lineament density as the area is found in the Afar rift and associated escarpments or margins. As a result, when comparing the FAHP approach to the AHP method, the area covered by the Low groundwater potential category is reduced by

1.92% (367.86Km^2), while the area covered by the Moderate groundwater potential zone in the case of FAHP is increased by 1.66% (317.20Km^2).

When evaluating the distribution of groundwater potential in the output (Figure 79), it can be seen that the predominance of thick lacustrine deposits, and the low groundwater recharge are the main causes to have Very low and Low groundwater potential zones along the rift floor. However, from the geological, hydrochemical, and isotope analysis discussed in Chapter Three: Evaluation of the source and mechanisms of Groundwater Recharge, groundwater flows from the marginal grabens to the rift floor due to the presence of transverse faults and lineaments that trend in NE- SW and sometimes W-E directions leads the rift floor can have low to moderate groundwater potential. The presence of intensively faulted Dalha basalt which is regionally interconnected with the marginal grabens as a result of the existence of transverse structures having a trend of NE-SW and sometimes W-E directions orientations that connects the western marginal grabens to the rift floor that commonly occur along the accommodation zones mainly between the adjacent marginal grabens as well as between the two rift arms of main Ethiopian and southern red sea of the western Afar rift margin(Tesfaye et al., 2003, Zwaan, Corti, Keir, et al., 2020) and low to moderate groundwater recharge, the zone between rift margin and rift floor can be called "moderate groundwater potential zone". The presence of transverse faults and lineaments that connect the rift margin to the northwestern plateau, thick alluvial deposits underlain by fractured and weathered volcanic rocks, primarily basalt and ignimbrite, a high Topographic Wetness Index (TWI), and moderate to high groundwater recharge are the primary causes of the high and very high groundwater potential zones that are primarily found in the northwestern, western, and southwestern portions of the western Afar rift margin. Thus, the spatial distribution of groundwater potential zones showed that lineament density and orientations, geology, topographic wetness index (TWI), and recharge are the main factors influencing the presence of groundwater in the region.

Table 46: Groundwater potential zones (GWPZ) coverage variation with AHP and FAHP methods

Groundwater potential zones(GWPZ)	**Area coverage(Km^2)**		**Area coverage (%)**		**Area Variation (km^2) (FAHP-AHP)**	**Area Variation (%)**
	AHP	**Fuzzy AHP**	**AHP**	**Fuzzy AHP**		
Very low	229.96	221.48	1.20	1.16	-8.48	-0.04
Low	9452.32	9084.46	49.41	47.48	-367.86	-1.92
Moderate	7964.76	8281.96	41.63	43.28	317.20	1.66
High	1386.43	1441.65	7.25	7.53	55.22	0.29
Very high	98.53	102.45	0.51	0.53	3.92	0.02

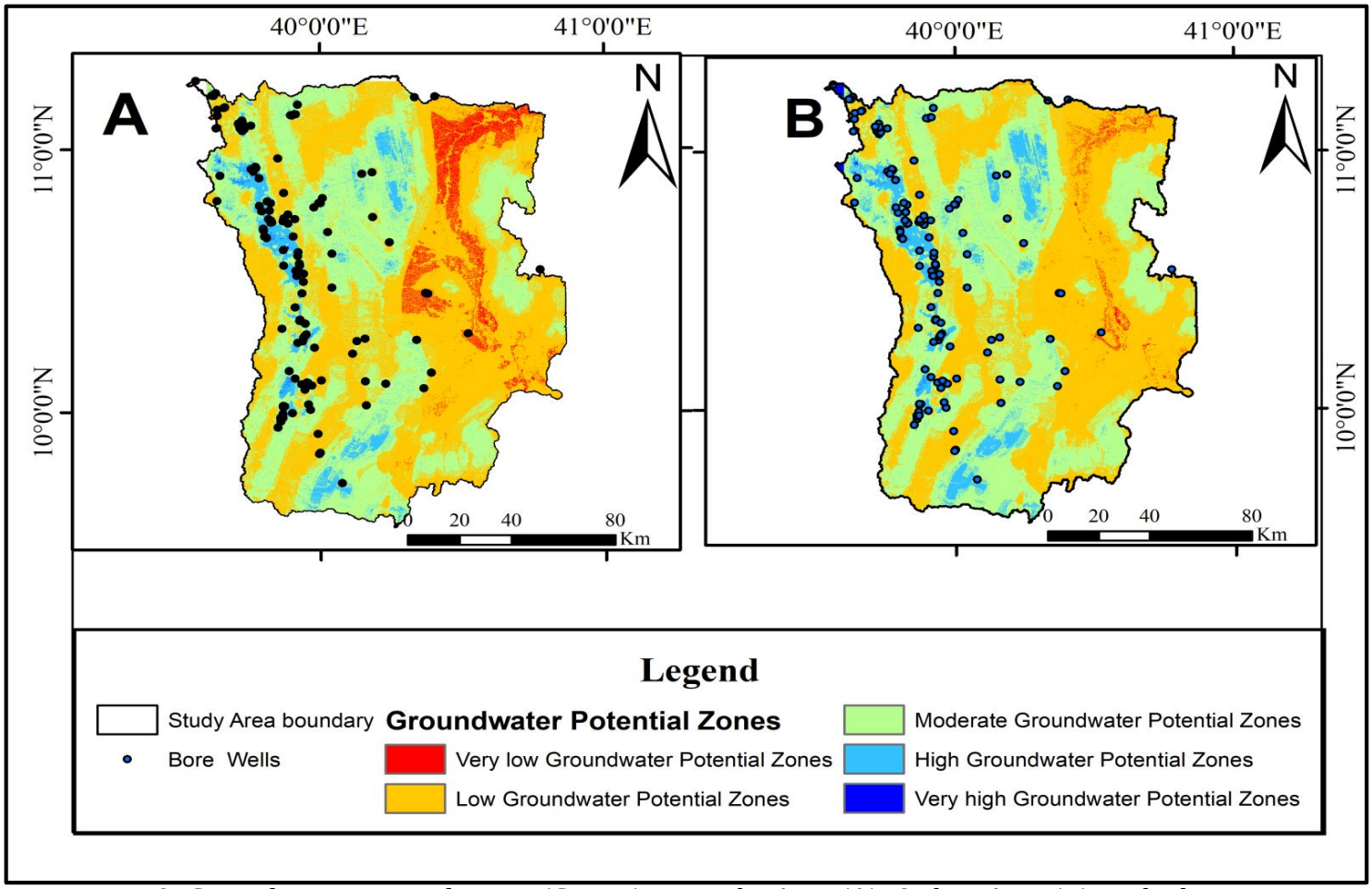


Figure 79: Groundwater potential Zones (GWPZ) Using the AHP (A), & the FAHP (B) methods

5.5 Validation of Groundwater Potential Map (GWPM)

The most crucial phase in the modeling process, according to Ndatuwong & Yadav, 2014, is the validation of the spatially distributed Groundwater Potential zone. Therefore, in this study the spatially distributed groundwater potential zonation was validated by interpretations and the overlaying of data from existing wells, which includes well discharge, transmissivity, and specific capacity. Hence, well yield and aquifer parameters(specific capacity and transmissivity) were combined with the groundwater potential map (raster value) using the extract values to points command in the spatial analyst tools of the GIS working environment(Fetter, 2001, Shen et al., 2015). The correlation process was completed using Microsoft excel. Besides to these parameters, the groundwater flow direction which is controlled by hydraulic gradient, topography, geology, and hydraulic conductivity is a key characteristic(C. B. Pande et al., 2020) and utilized in the evaluation of the groundwater potential of this study.

5.5.1 Validation using Well Discharge

In general, an area having high groundwater potential will give a well of significant yield. In this study, for comparison purposes, the yields of the wells have been categorized into 4 classes (Table 47). According to the well distribution, the vast majority of the wells that were drilled close to low to very low groundwater potential areas mainly in the lacustrine deposit of the rift floor are either dry or have a yield of less than 5 liters/sec. The wells exhibit yields between 5 and 15 liters/sec were found between the rift floor and rift margin. The western rift margins, especially the grabens revealed that the wells drilled along these areas have a yield of more than 15lit/sec. Besides, the correlation of well discharge data and the raster value (GWPZ map) was conducted in the spatial analyst tools with extract values to points command of the GIS working environment. Accordingly, the well yield distribution has a good correlation with the GWPM on the scatter plot having an R^2 value of 0. 81(Figure 80), and the technique used for the current research generated remarkably accurate and dependable results.

Table 47: Well classification based on their yield

S.No	Yield(lit/sec)	Category
1	0-5	Low to very low groundwater potential
2	5-15	Moderate groundwater potential
3	15---25	High groundwater potential
4	≥25	Very high groundwater potential

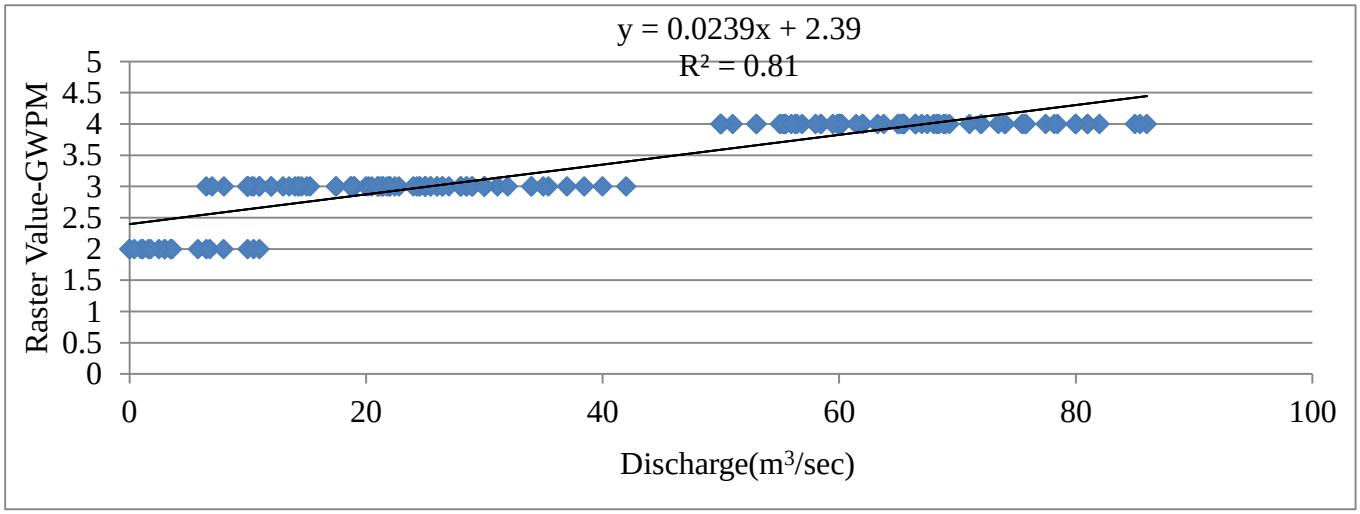


Figure 80: Scatter plot of Discharge VS t Groundwater potential Zone Map (GWPZM)

5.5.2 Validation using Groundwater flow direction

Based on the available hydraulic heads, the groundwater flow direction in the study area is from the SW to NE direction (Figure 81). From the study conducted through geological, Hydrogeological, Hydrochemical, and isotope analysis(Gidafie, Nedaw, Azagegn, et al., 2024), regional groundwater is

flowing from the northwestern plateau to the rift floor through the preferential pathways mainly columnar jointed basalt and transverse structures. Combining these justifications, the rift floor can have moderate groundwater potential, but it is highly controlled by geology and structures. Few borehole data like Amma#1 and #2 in the rift floor, in which the volcanic rocks like Afar stratoid series are the main aquifers, have a yield of more than 20 lit/sec with insignificant drawdown. This shows that the volcanic rocks are regionally interconnected with the western rift margin through the transverse structures, which allows the preferential groundwater flow from the rift margin to the rift floor and supports the conclusion that the rift floor can have moderate groundwater potential. This analysis may help in further evaluation of the groundwater potential after a depth of 500 meters in the rift floor (i.e. below the lacustrine deposit).

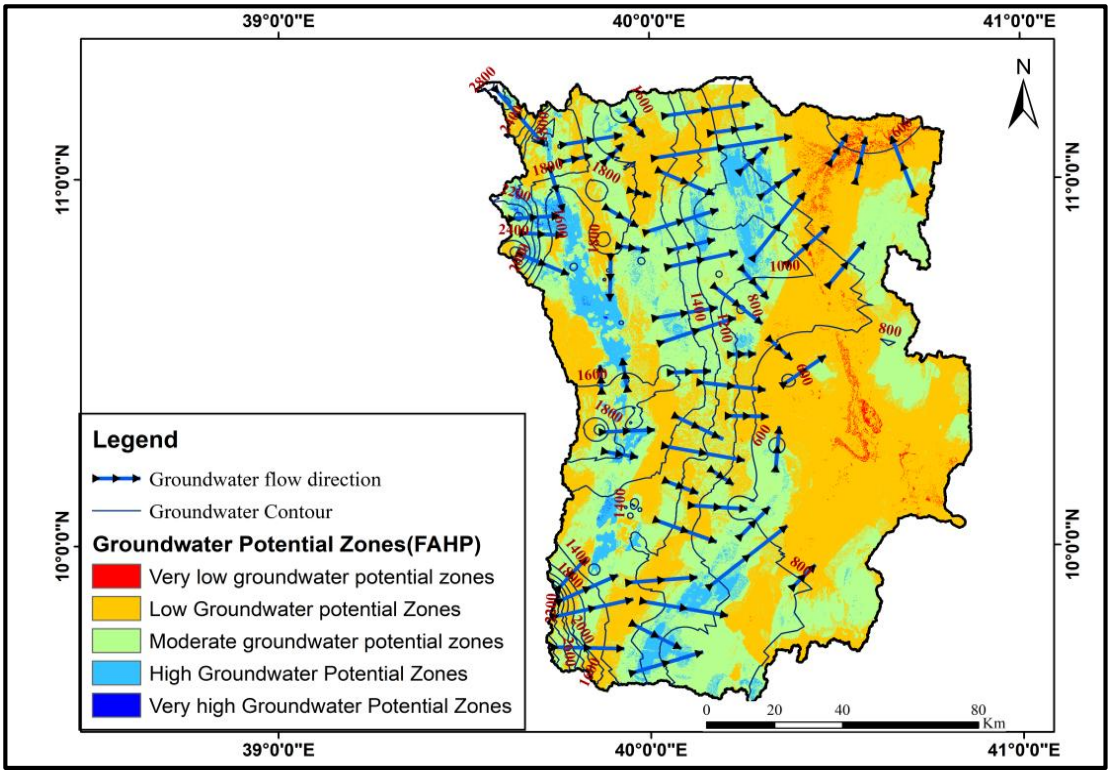


Figure 81: Groundwater flow directions map

5.5.3 Validation using Specific Capacity and Transmissivity

Aquifer characteristics(transmissivity and specific capacity), are crucial in identifying potential zones(T. J. R. Kumar et al., 2016) and are used for the validation of the groundwater potential map of a certain area(Shen et al., 2015, Fetter, 2001). The existing boreholes in the study area have specific capacity and transmissivity values that range from 0.001 m^3/day/m to 792.66 m^3/day/m and 0.00032 m^2/day to 521.76 m^2/day, respectively. The lower values in all cases are primarily found in the rift floor, where the local geology is mainly lacustrine deposits and lesser groundwater structures. The higher values are heavily concentrated at the rift margin, especially along the grabens where the area is covered by alluvial deposits underlain by fractured and weathered basalt and ignimbrites and high lineaments

density. In addition, correlation of transmissivity and specific capacity of the wells and the raster value (GWPZ map) was conducted in the spatial analyst tools with extract values to points command of the GIS working environment. Accordingly, both parameters have a good correlation with the GWPZM on the scatter plot having R^2 values of 0.79 and 0.80 respectively (Figure 82 and Figure 83).

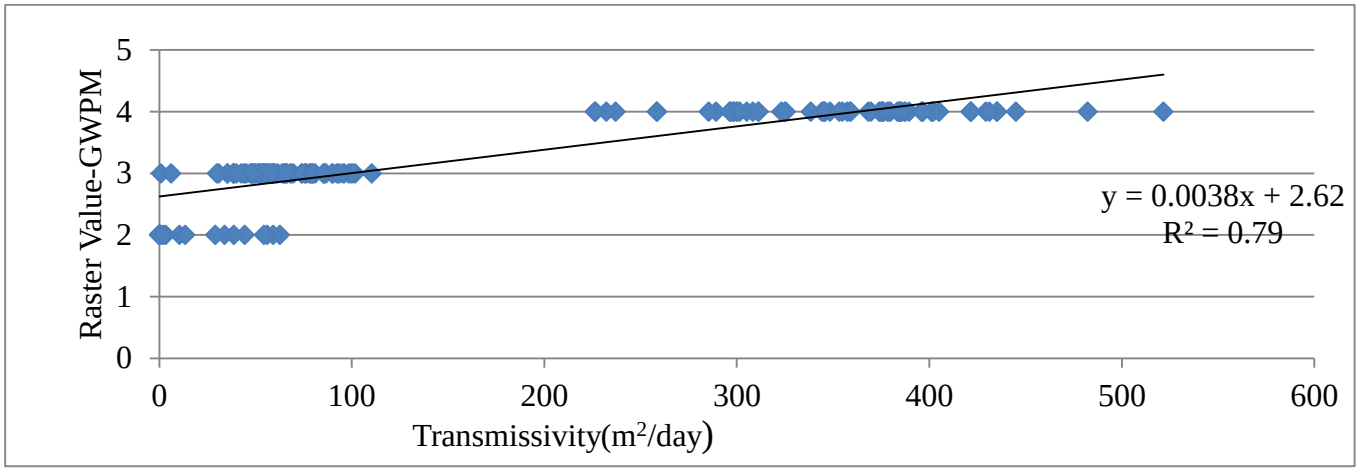


Figure 82: Scatter plot of Transmissivity VS the Groundwater Potential Zone map (GWPZM)

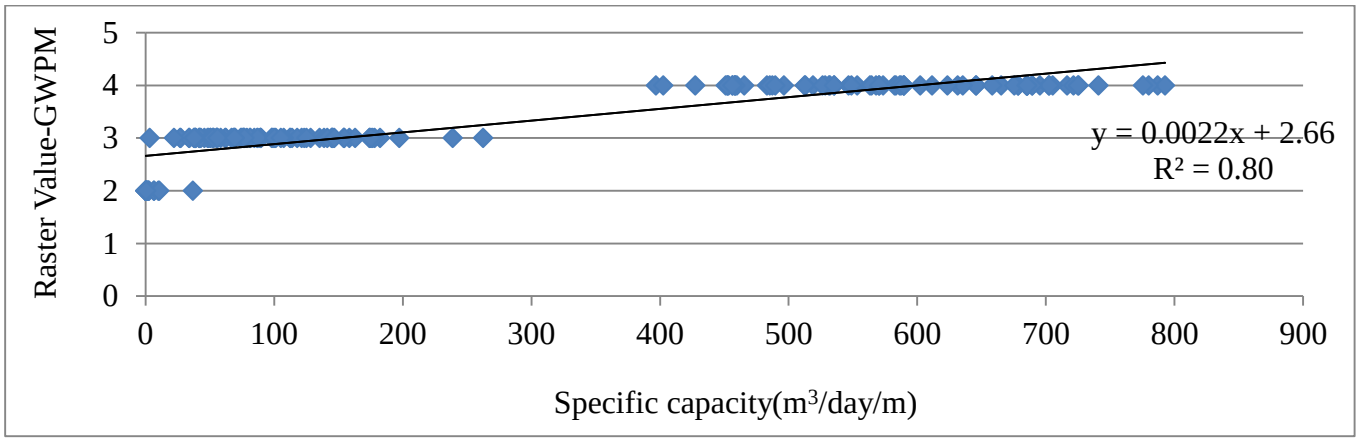


Figure 83: Scatter plot of Specific capacity VS the Groundwater potential Zone map (GWPZM)

5.6 Sensitivity Analysis

The most essential step in any model is performing sensitivity analysis to comprehend both the overall influence and the influence of the ranked and weighted values allocated to each class and parameter (Gebeyehu et al., 2022). Besides, to understand the impact of the input parameters in delineating the GWPM of a certain area, conducting a Sensitivity analysis of the parameters is paramount. For this purpose, the map removal method in the GIS working environment was utilized by eliminating the layers systematically from the GWPZ. Accordingly, the input layer with the greatest Sensitivity Index(SI) is the most sensitive parameter and the input layer with the lowest SI is the least sensitive(Kumar et al., 2016). The influence on the remaining layers in the GWPZ map was expressed as follows(Thapa et al., 2018):

Equation 32, $$\mathbf{SI} = \left[\left[\frac{\left(\frac{\mathbf{GWPI}}{\mathbf{N}}\right)-\left(\frac{\mathbf{GWPI'}}{\mathbf{n}}\right)}{\mathbf{GWPI}}\right]\right] * \mathbf{100}\%$$

Where N and n are the numbers of input parameters/layers used to calculate GWP and GWP', respectively, and SI is the sensitivity index associated with the removal of a single parameter or layer. GWPI is the groundwater potential index calculated using all parameters. GWP' is the groundwater potential index obtained by sequentially excluding each input parameter.

The Sensitivity Index (SI) calculated using Equation 32, shows that Lineament Density and Geology with SI values of 2.08% and 1.74% respectively are the most sensitive parameters, while Drainage Density with SI of -0.89% is the least sensitive parameter (Table 48).

Table 48: Mapping removal sensitivity analysis index

Layers removed	**Sensitivity variation Index (%)**				**Remark**
	Minimum	**Maximum**	**Mean**	**StD**	
Lineament Density	-1.81	6.53	2.08	1.31	High sensitive
Geology	-0.38	5.88	1.74	1.18	
TWI	-1.03	4.43	0.63	1.01	
Recharge	-1.01	3.39	0.24	0.65	
Slope	-2.36	2.53	0.04	0.94	
Soil	-1.43	1.02	-0.55	0.43	
LULC	-1.49	2.16	-0.58	0.47	
Drainage Density	-1.52	0.29	-0.89	0.2	Least Sensitive

Considering the high and the least sensitive parameters respectively (i.e. Lineament and Drainage density), the impact of the removal of these parameters in the areal groundwater distribution is presented in Table 49. Accordingly, removing lineament density will increase the very low groundwater potential area by 0.37%, while moderate, high, and very high groundwater potential areas were decreased by 13.83%, 1.05%, and 0.07% respectively. Removing the drainage density will increase the very low groundwater potential area by 0.08%, while moderate, high, and very high groundwater potential areas were decreased by 0.99%, 0.17%, and 0.01% respectively. This shows that lineament density has a higher impact on the areal groundwater distribution than the drainage density, where the impact is insignificant. So, the availability of groundwater in the study area, particularly on the rift floor is highly controlled by groundwater structures mainly faults and lineaments.

Table 49: Groundwater potential areal distribution with the removal of lineament and drainage density

GWPZ	Fuzzy AHP	Lineament density removal	Difference		Drainage density removal	Difference	
		Area(Km^2)	**(km^2)**	**%**	**Area (Km^2)**	**Km^2**	**%**
Very low	221.48	292.24	70.76	0.37	238.54	17.06	0.08
Low	9084.46	11875.19	2790.73	14.59	9293.4	208.94	1.09
Moderate	8281.96	5635.87	-2646.09	-13.83	8091.47	-190.49	-0.99
High	1441.65	1240.54	-201.11	-1.05	1408.49	-33.16	-0.17
very high	102.45	88.16	-14.29	-0.07	100.09	-2.36	-0.01

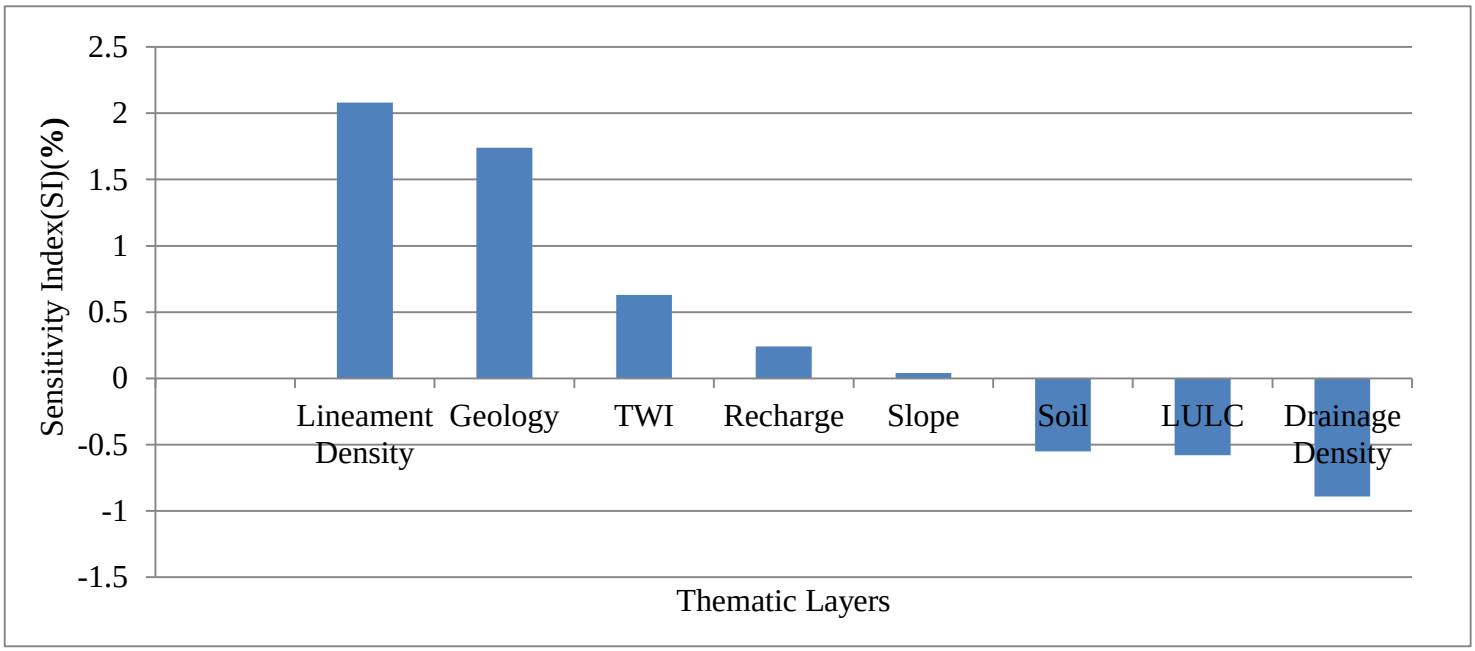


Figure 84: Mapping removal sensitivity analysis index

5.7 Limitations of the study

In this specific study, though the groundwater potential delineation conducted through integrated GIS and Remote Sensing (RS) is found to be effective, there are limitations on the generated Groundwater Potential Map (GWPM). In the first case, few spatially distributed meteorological stations and borehole data were found in the rift floor. As a result, we were obliged to rely on the limited number of observing stations and well data for the preparation of thematic layers, which could potentially skew the mapping

of the spatial distribution of groundwater. Furthermore, local experience and professional judgment were taken into account when choosing and allocating weights to the different thematic layers. Hence, there could be inappropriate selection and insufficient judgment on a parameter that finally can influence the spatial groundwater distribution(Kerdous et al., 2022, Echogdali et al., 2022). In addition, since the approach didn't consider in detail the subsurface geological, structural architecture, and regional groundwater flow dynamics, the output may have limitations in delineating groundwater potential zones. For instance, in this study, the rift floor has shown to have low to very low groundwater potential. However, from the geological, hydrochemical, and isotope analysis, groundwater flows from the rift margin to the rift floor along the preferential pathways, leading the rift floor to have low to moderate groundwater potential. These limitations on the mapping of the spatially distributed groundwater potential of a certain area using integrated GIS and Remote sensing techniques show us that, it is highly recommended to couple and verify the output with the conventional investigation methods besides to hydrochemical and isotope analysis, especially in arid to semi-arid and tectonically active areas like the Afar rift. Last but not the least, the absence of sufficient wells in the rift floor of the study area constitutes an obstacle to GWPM validation, even though the correlation gives 80% satisfaction.

Chapter Six: Steady-state Groundwater Flow Modeling: Jewuha-Robit Catchment

6.1 General

The movement of water through the hydrogeologic units that make up the groundwater flow system can be analyzed using numerical groundwater flow modeling, which aids in forecasting the long-term trends of a hydrogeological system(S. F. R. K. C. Pande, 2016). It is a tool for analyzing how pumping affects water levels, spring flows, and groundwater flow directions(Pagnozzi et al., 2020), as these effects might influence ecosystems that depend on water, and the flow of pollutants(Moneim et al., 2016). The Southern sections of the Western Afar rift margin and associated Rift floor catchment represent a large groundwater system that incorporates many small catchments. Due to its large size and the inherent heterogeneity of the aquifers of the region as well as complex groundwater flow occurrence and dynamics, an attempt is made to develop a simple numerical groundwater flow model for the selected catchment. Taking into account the result of the geological, hydrochemical, and isotope analysis and interpretations, and not conducting repetitive work, especially in the Western Afar rift margin, the Jewuha -Robit catchment was selected as a preliminary modeling work. Simulations are made under steady-state conditions for 1 layer aquifer to obtain a general quantitative representation of the hydrogeological system dynamics.

6.2 Conceptual Model

The previous hydrogeological conceptualization, groundwater occurrence, and flow dynamics analysis conducted through geological, hydrogeological, hydrochemical, and isotope methods were applied to construct the conceptual groundwater flow model of the sub-catchment(Gidafie, Nedaw, Azagegn, et al., 2024, and Gidafie, Nedaw, & Azagegn, 2024). Based on these analyses and interpretations, groundwater in the catchment has got a recharge not only from the local precipitation but also from the adjacent northwestern plateau. The controlling mechanisms are the presence of the extended columnar jointed basalt and transverse structures. Besides, the groundwater is flowing out from the catchment to the rift floor along the transverse structures which trends mainly NE-SW, NW-SE and W- E directions. Generally, groundwater flows from the plateau to the rift margin and finally to the rift floor in SW-NE directions.

6.3 Numerical Model

6.3.1 Model Design

The numerical model domain has an area coverage of 1420 km^2. It is located between the parallels of 1080000 and 1150000 UTM North and 570000 and 630000 UTM East (Figure 85).). The modeling grid consists of 140 rows and 120 columns. Each cell has a dimension of 500m by 500m.

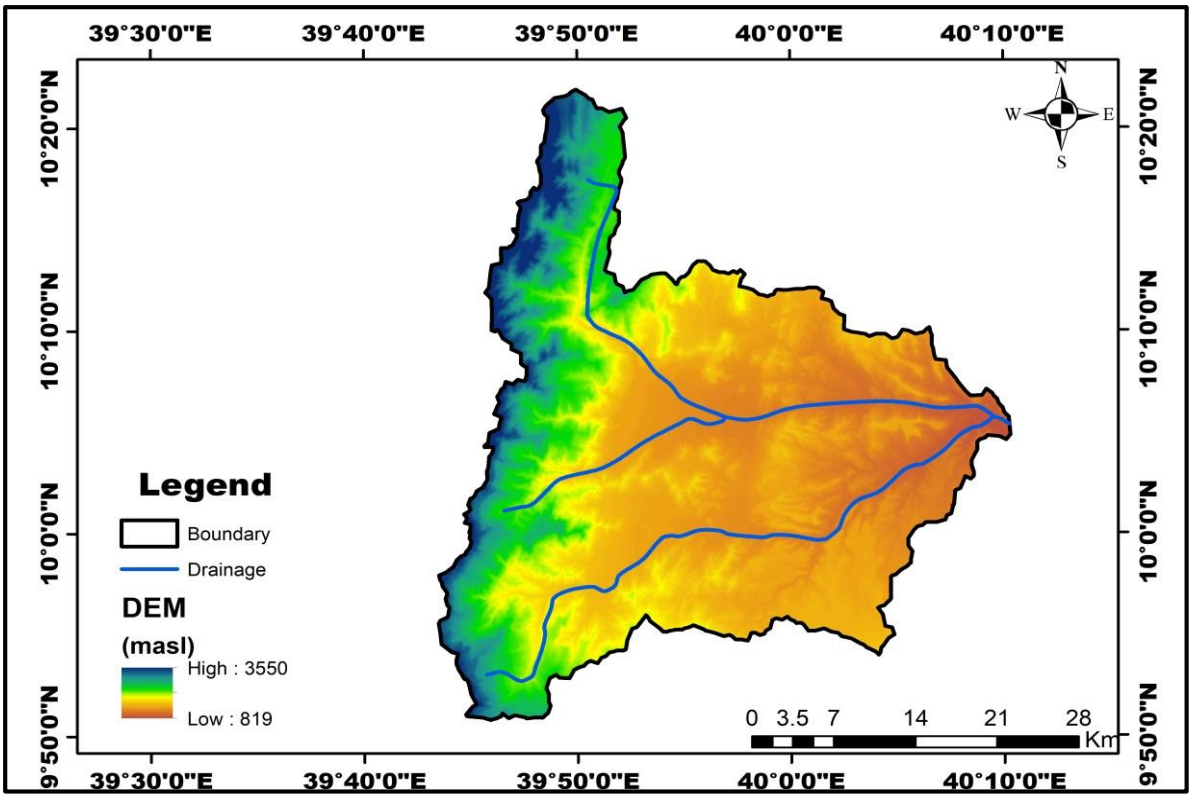


Figure 85: Location map of the model area (Jewuha-Robit catchment)

6.3.2 Model Selection and Governing Equations

Due to its capability, the most widely used numerical groundwater flow model is MODFLOW, which is a modular three-dimensional finite-difference groundwater flow model(Pagnozzi et al., 2020, Mansour et al., 2024, McDonald and Harbaugh,1988, Chiew et al., 1992). In this study, three-dimensional finite-difference MODFLOW computer software is applied to estimate the exploitable groundwater resources and to evaluate groundwater levels in the catchment. The model result will be used as a calibrating and controlling tool for the hydrology output parameters determined by other methods. Hence, the modeling work at this stage focuses more on groundwater flow system analysis, rather than developing a well-calibrated model that can readily be used as a management tool. Mathematical models simulate flow indirectly through a governing equation that represents the physical processes that occur in the system(Anderson and Woessner,1992, Reilly & Harbaugh, 1999, Seeyan, 2020). Groundwater flow

dimensional groundwater movement in a porous medium are developed from the application of Darcy's law and the continuity equation. The concept of the continuity equation explains that the sum of all inflows into and out of the cell equals the rate of change in the storage within the cell(McDonald and Harbaugh,1988). The water balance equation is mathematically combined with Darcy's law to derive the following equation that describes the three-dimensional subsurface groundwater flow process in a porous medium(Anderson and Woessner,1992).

$$\frac{\partial}{\partial x}\left(K_{xx}\frac{\partial h}{\partial x}\right)+\frac{\partial}{\partial y}\left(K_{yy}\frac{\partial h}{\partial y}\right)+\frac{\partial}{\partial z}\left(K_{zz}\frac{\partial h}{\partial z}\right)-W=S_s\frac{\partial h}{\partial t} \qquad \text{(Equation 33)}$$

K_{xx}, K_{yy}, and K_{zz} are values of hydraulic conductivity in the x, y, and z directions along Cartesian Coordinate Axes, which are assumed to align with principal directions of hydraulic conductivity (LT^{-1}),

h is hydraulic head (L),

W is a volumetric flux per unit volume and represents

Sinks and/or sources (T^{-1}),

S_s is the specific storage of the porous material (L^{-1}), and

t is time (T).

6.3.3 Boundary Conditions

In the model area, as most of the topographic divide between the two basins is covered by acidic rocks mainly rhyolite, and tuff and these formations are supposed to have poor hydraulic conductivity, the surface water divides are considered as no-flow boundary. However, as it has been discussed in the conceptual groundwater flow model using the geological, hydrochemical, and isotope analysis(Gidafie, Nedaw, Azagegn, et al., 2024), there is groundwater flow from the adjacent plateau to the western rift margin through the preferential pathways, which shows that the surface water divide and groundwater divides do not coincide in the case of Jewuha-Robit catchment. Hence, to take into account the groundwater flow from the adjacent plateau to the catchment, head dependent boundary (general head boundary) is assigned along the surface boundary mainly along transverse structures that connect the plateau with the rift margin (Figure 86).

Top of layer or surface elevations were extracted from the Digital Elevation Model (DEM) derived from a 30m resolution Shuttle Radar Terrain Model (SRTM). Layer bottom elevations were obtained by subtracting similar aquifer thickness from layer top elevations. An average aquifer thickness of 250m is

considered for the first layer of alluvial deposit from the drilling log. Static water level readings were taken on the ground using a deeper meter and relevant information from pumping test data were used to calculate groundwater heads.

6.3.4 Input parameters and flow packages

The parameters or flow package inputs into the model include initial hydraulic head data, horizontal hydraulic conductivity, recharge, abstractions, conductance of river bed sediments, and General Head Boundary cells (GHB).

6.3.4.1 Hydraulic heads

In this study, the initial hydraulic heads introduced into active cells were defined based on depth to water level from the representative water level measurement at the field, pumping test data interpolations, and understanding of groundwater flow conditions in the area.

6.3.4.2 Horizontal hydraulic conductivity

Hydraulic conductivity values for the water-bearing formations in the model area were derived from the collected existing pumping test data. Interpolation and estimation at unmeasured points were made by geostatistical analysis (kriging) to provide initial estimates for the model. Based on these approaches, the model domain was divided into hydraulic conductivity zones based on similarity in aquifer properties as obtained from the geostatistical predicted hydraulic conductivity map. Accordingly, the horizontal hydraulic conductivity ranges from 0.43 to 8.54 (m/day).

6.3.4.3 General Head boundary

A general head boundary simulates a source of water outside the model area that either supplies water to or receives water from adjacent cells in proportion to the hydraulic-head differences between the source and model cell. The GHB package requires the input of GHB hydraulic conductance and head on the external source. For this model, Cells assigned as GHB are chosen based on the availability of transverse structures, geological formations, groundwater flow direction, and information from ^{222}Rn measurements conducted at the outlets of the tributaries from the marginal grabens. The exchange rate of water between the model cell and the outside source is given by the equation:

Q = C (HB – h) (Equation 34)

, Where Q is the rate of flow into or out of the model cell [L3/T], C is the conductance between the external source and the model cell [L2/T], HB is the head assigned to the external source [L], and h is the hydraulic head within the model cell [L]. Values of C were initially calculated using the equation;

C = K • L (Equation 35)

Where K is the hydraulic conductivity between the model cell and the boundary head [L/T], and L is the length of the general-head boundary within a cell. The input values of hydraulic conductivity have been

obtained from interpolated pumping test data analysis. The length of the GHB within a cell and head on the external source at active vertices of the external sources were considered to calculate the hydraulic conductance of the GHB.

6.3.4.4 Recharge

Recharge, which is water contributing to groundwater passing through the unsaturated zone and reaching the static groundwater table, could be direct, indirect, or localized based on the source and mechanism by which water reaches the water table. In this study, a WetSpass-M model is used to estimate the spatially distributed groundwater recharge rate on a seasonal and annual basis. The principle of the model is that the total water balance for a cell in a spatially distributed grid is split into independent water balances for vegetated, bare soil, open and impervious parts of the grid cell(Aish et al., 2010, Bhattacharya et al., 2021, Martín-Loeches et al., 2018). This makes it possible to take into account the non-uniformity of land use depending on the resolution of the grid cell (Obuobie et al., 2012, Tilahun & Merkel, 2009). Accordingly, the minimum, maximum, and mean groundwater recharge rates assigned to the model cell are 88.43mm/year, 397.45mm/year, and 126.5mm/year respectively.

6.3.4.5 Well package

A pumping well is defined by using the cell-by-cell input methods of assigning a negative sign to model cells. In case more than one pumping wells are located in a given grid cell, the sum of well discharges has been considered for the input. About 12 wells and springs with water level information were used for head observation data, and 40 wells were used to quantify daily and annual abstraction from the aquifer. Accordingly, the total daily abstraction from the aquifer of the Jewuha-Robit groundwater catchment is roughly about 13,000 m3/day.

6.3.4.6 River package

The purpose of the river package is to simulate the effect of exchange between groundwater systems and surface water features. Rivers were defined by using the Cell by-cell input method. The input parameters include hydraulic conductance of river bed material, head in the river, and elevation of the river bed in a cell. Based on some sample site observations and estimations, river bed sediment thickness has been roughly assumed to vary between 0.1 to 0.5m, and river widths range from 10 to 50m. The river length in a cell has been roughly considered to be equal to the side of the cell size (500m). The hydraulic conductivity of river bed sediments was not measured in the field; instead, the hydraulic conductivity of the underlying formation has been considered from the pumping test and interpolated result. The head in the river was taken from surface elevation which is extracted from the Digital Elevation Model (DEM) derived from a 30m resolution Shuttle Radar Terrain Model (SRTM). Elevation of the river bed bottom was modified by subtracting 0.3-0.5m from the top elevation, based on the rough site observation and estimation. The hydraulic conductance of the river bed sediments has been calculated using the relation:

C_{riv}= (K.L.W)/M (Equation 36)
, Where: C_{riv} is the hydraulic conductance of river bed material (m2/d), K is the hydraulic conductivity of the river bed material (m/d), L is the length of the river in the cell (m), W is the width of the river (m), M is thickness of the riverbed (m).

6.4 Model Simulation

After designing the model, and assigning boundary conditions and input parameters and flow packages, the groundwater system of the Jewuha-Robit catchment was simulated under a steady state condition. In steady-state MODFLOW simulation, an equilibrium solution is desired for heads such that all inflows and outflows to the aquifer domain are in perfect balance (Anderson and Woessner, 1992). The steady-state solution provides one set of head fields that represent the long-term and average boundary conditions of the model domain.

6.5 Model Results and Calibration

The primary calibration target in groundwater modeling is the hydraulic head (water level). Hence, field observations of groundwater levels were compared with simulated heads to minimize the model discrepancy, and finally to have a realistic groundwater flow model. Therefore, adjusting and fine-tuning of input parameters and flow packages is necessary for calibration to get the best possible match between simulated and measured hydraulic heads (McDonald and Harbaugh 1988). In this model, a manual trial and error method based on head information has been used for calibration. Field-measured water levels or heads at 12 wells, and springs were used for head observation during calibration. The final simulation result gives head distribution as shown below (Figure 86).

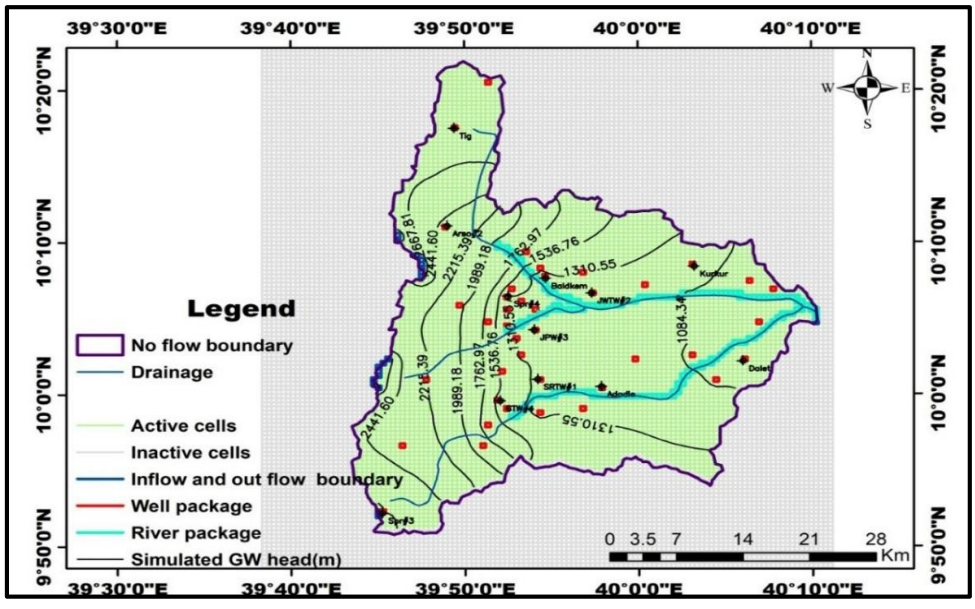


Figure 86: Model result

6.5.1 Evaluation of Calibration Results

Performance metrics, both qualitative and quantitative are used to assess calibration outcomes. The following presentation is a comparison and evaluation of the measured and simulated heads.

6.5.1.1 Qualitative evaluation

Using pattern/visual matching of measured and simulated heads (Figure 87 and Figure 88), the calibrated results are qualitatively evaluated. The qualitative analysis so demonstrates that the simulated and observed ones have good matching.

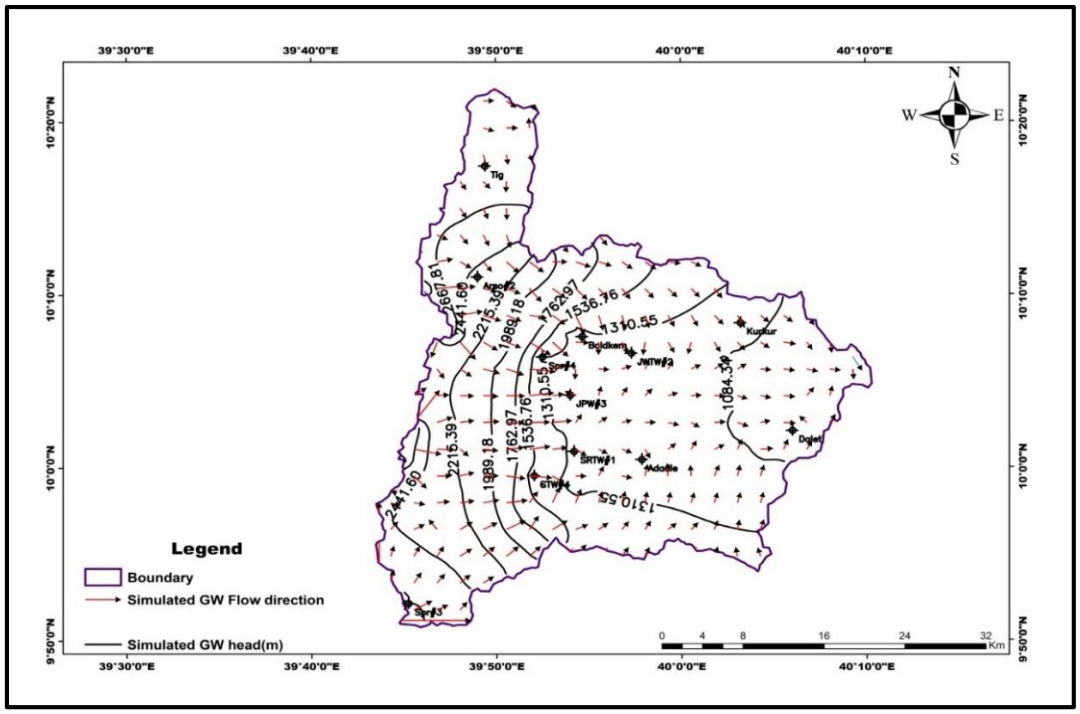


Figure 87: Simulated hydraulic heads (m)

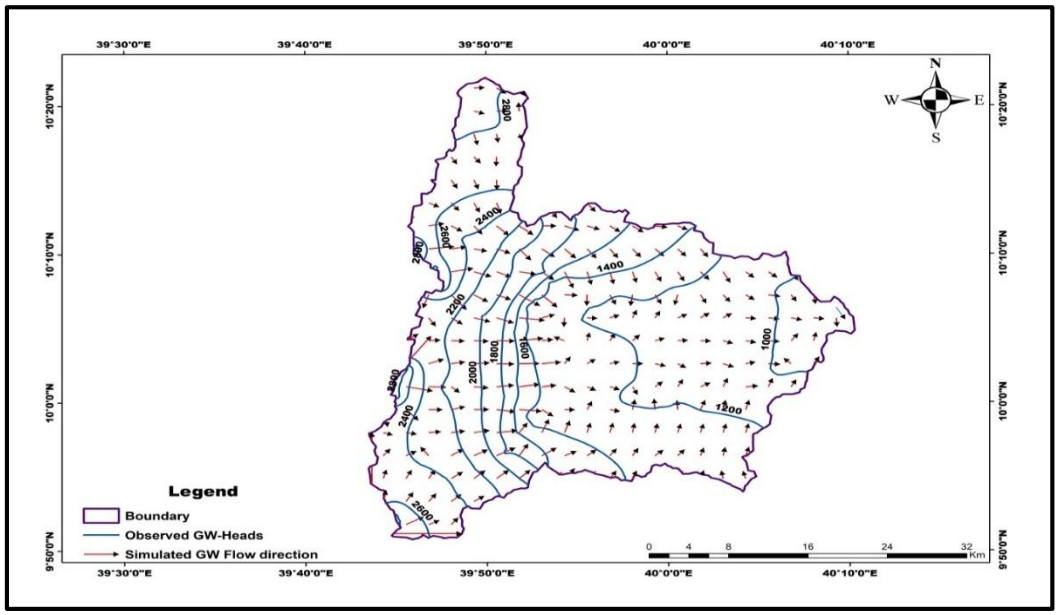


Figure 88: Observed hydraulic heads

6.5.1.2 Quantitative evaluation

In quantitative performance evaluation, water balance errors and residuals are described statistically or mathematically(Cameron & Middlemis, 1994).

Lumped-Sum comparison: These techniques are the most widely used quantitative metrics for calculating the average residual difference. Nevertheless, these performance metrics offer aggregated calibration measurements that do not reveal the error's temporal or spatial dispersion(Anderson and Woessner,1992). These methods included the Mean Error (ME), the Mean Absolute Error (MAE), and the Root Mean Square Error (RMSE).

The Mean Error (ME) is the mean of the differences between measured heads (hm) and simulated heads (hs): Equation 37: $$ME = \frac{1}{n}\sum_{i=1}^{n}(\mathbf{hm} - \mathbf{hs})\mathbf{i}$$

Where n is the number of calibration measurements. Because both positive and negative residuals are used in the calculation, this value should be close to zero for a good calibration(Seeyan, 2020). In other words, the positive and negative errors should balance each other.

The Mean Absolute Error (MAE) is the mean of the absolute value of the differences between measured heads and simulated heads. Because a lower MAE implies that the model's predictions are more closely aligned with the average observed values, it is indicative of better model performance(Pagnozzi et al., 2020).

Equation 38: $$MAE = \frac{1}{n}\sum_{i=1}^{n} |(hm - hs)i|$$

The Root Mean Square Error (RMSE) is used as the basic measure of calibration for heads. The root mean square (RMS) error is the square root of the average of the squared differences between measured heads and simulated heads:

Equation 39: $$RMS = \left|\frac{1}{n}\sum_{i=1}^{n}(\mathbf{hm} - \mathbf{hs})^{2}\right|^{0.5}$$

Using Equation 37, 38 and 39, model performance measures values Mean error (ME) of 0.01m, Mean Absolute error (MAE) of 5.33m, and Root Mean Square error (RMS) of 6.57m^2 were calculated (Table 50). Base on the quantitative evaluation methods, the values of MAE and RMSE looks lager which arise from some uncertainty in head measurements which can be resulted from many factors including, measurement errors, scale errors, and various types of averaging errors, both spatial and temporal. With all the uncertainties, the calibration work can be taken as a good startup for the upcoming groundwater modeling both in the rift margin and rift floor areas.

Table 50: Summary of calibration errors

Statistical parameters	Values, m
Mean Error	0.01
Mean Absolute Error(MAE)	5.33
Root Mean Square Error(RMSE)	6.57

In addition to visual matching of simulated contours to those of observed contours, and Lumped-sum comparison methods, scatter plots are used in assessing the quality of calibration simulations. The degree of scatter about this theoretical line is a measure of overall calibration quality (Anderson and Woessner, 1992). For this purpose, observed head versus simulated head measurements are plotted in Excel. In an ideal calibration, the points will fall on a straight line with a 45-degree slope; i.e., the computed value equals the measured value(Moneim et al., 2016). In our case, the correlation coefficient (R^2) (Figure 89) between the observed and simulated values was 0.95 and can be taken as a good calibrating model

Table 51: Observed vs simulated heads

S.No	Observation Name	Simulated head(m)	Observed Head(m)	Head Difference(m) (Sim-Obs)
1	ADADLE	1196.031	1183	13.031
2	JWTW#2	1188.17	1158	30.17
3	STW#4	1636.076	1515.82	120.256
4	ARSO#2	2373.469	2319	54.469
5	BALDKEM	1294.99	1315	-20.01
6	SRTW#1	1351.58	1325.1	26.48
7	SPR#3	2844.526	2860	-17.474
8	SPR#4	1570.024	1624	-53.976
9	DALETI	1025.323	965	60.325
10	JPW#3	1274.498	1233.48	41.018
11	KURKUR	1144.832	1108	36.832
12	TIG	2588.59	2585	3.59

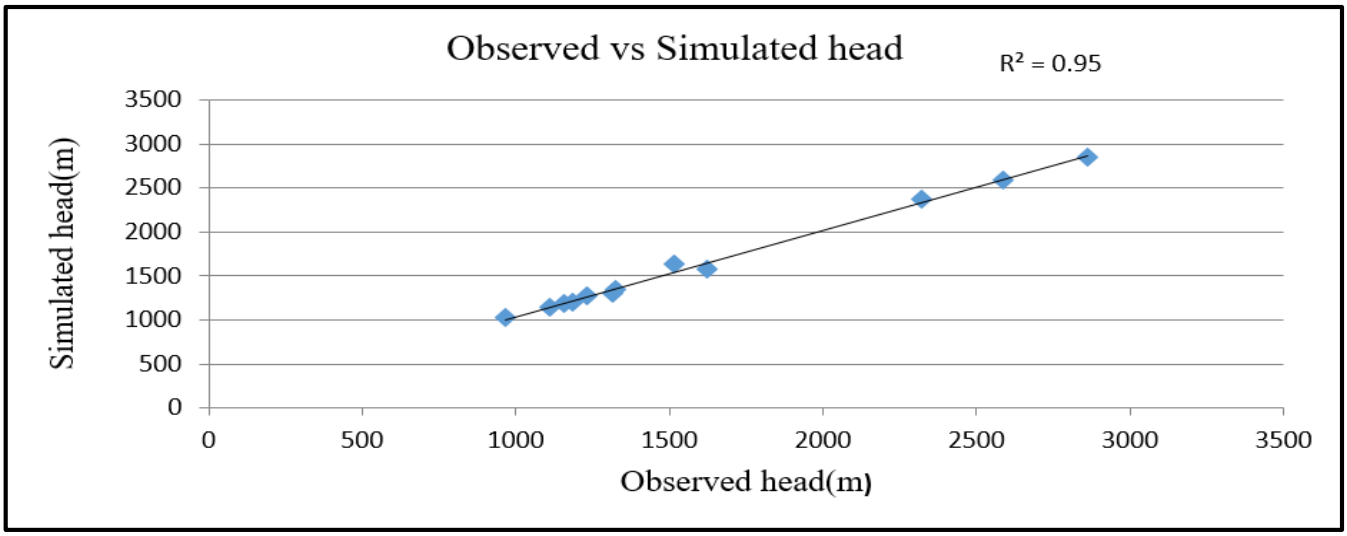


Figure 89: Observed vs simulated heads (m)

Water budget: One of the quantitative performance metrics used to compare the total simulated inflows and outflows and assess the simulation accuracy in the calibrated model is the water budget(Chiew et al., 1992). It shows whether the generated numerical model is generally acceptable or not. For this purpose, MODFLOW computes a volumetric water budget for the entire model at the end of each time step to verify the accuracy. For this specific model as displayed in Table 52, the outflow from and the inflow into the groundwater system are nearly equal, with a percent discrepancy of 0.001%. This very low calculated water balance error, assures a good level of the model calibration, as calibration quality is ensured for steady-state models when storage changes in a water balance approach near zero(Mansour et al., 2024).

Table 52: Water budget of the entire model

Components	Inflow(m3/year)	Outflow(m3/year)	Net(m3/year)	mm/year
Recharge	1.61E+08	0.00E+00	1.61E+08	113.37
River leakage	3.61E+06	2.33E+08	-2.29E+08	(161.22)
Head dependent	1.09E+08	3.61E+07	7.27E+07	51.20
Wells	0.00E+00	4.75E+06	-4.75E+06	(3.34)
Net	2.73E+08	2.73E+08	1.86E+04	0.01

DISCREPANCY [%] 0.001

In addition to the evaluation of the calibration quality, the water budget of the model also presents the contribution of the input parameters for the total water budget. Accordingly, as displayed in Table 52, recharge from local precipitation, and inflows from the adjacent plateau (head-dependent flow) are the major inflow components of the system. Groundwater flow from the system to the river followed by head-dependent inflow to the rift floor and abstraction through springs mainly found in the escarpment like SPR#3 and wells for domestic and agricultural purposes are the major outflow components. In addition, the water budget can also be used as a mechanism to make, and evaluate a comparison between the model outputs and the parameters that were determined by other methods. For instance, the recharge rate obtained from the precipitation in the modeling simulation is 113.37 mm/year, and from the WetSpass method, the estimated recharge is 126.5 mm/year. The two results look comparable, showing that the simulated model is properly calibrated. In addition, from the 20 years of recorded data on river flow, the total flow at the outlet of the Jewuha-Robit Catchment is calculated as 798.08mm/year, and the base flow contribution is 179.77mm/year, which is nearly equal to 22.52% of the total flow. So, subtracting the precipitation recharge from the baseflow, the contribution of the adjacent plateau through base flow is 53.27mm/year which is nearly equal to 30% of the baseflow contribution. From the model simulation result, the groundwater that flows from the adjacent plateau is calculated to be 51.2mm/year which looks somewhat comparable to the baseflow flow determined by baseflow separation methods. So, the model output can be taken as a good simulation.

Besides to the whole model domain, three sub-regions were generated for better evaluation and understanding of the inflow and outflow components along the groundwater flow directions, and their respective water budgets are presented in Table 53, Table 54 and Table 55

Sub region I: This region is created along the escarpment near the boundary between the plateau and the Awash basin. In this sub region, the groundwater inflow from the adjacent plateau is 92.6mm/year, and the recharge from the precipitation is 213mm/year. In addition, from the river leakage inflow and outflow components, groundwater is flowing from the system to the river, and the river can be taken as a gaining river (Table 53).

Sub region II: This region is created in the middle of the catchment by including the marginal grabens. In this sub region, the groundwater inflow from the adjacent catchment is showing an increased value (101mm/year), due to the wide coverage of the extended columnar jointed basalt and transverse structures. While the surface recharge from the precipitation is 135mm/year which is lower than Region I. This is because, as the elevation is decreased, the annual precipitation is decreased leading the recharge value to be lower (Table 54).

Sub region III: This region is created near the outlets of the catchment. At this sub region, the inflow value is 46mm/year which is lower than sub region I and sub region II. This is because, since the area is found near the outlet there is a mechanism of the groundwater outflow from the system to the rift floor. Besides, the recharge from the precipitation in this sub region is 109mm/year (Table 55).

Table 53: Water budget of sub-region-I

	IN (m3/day)	OUT (m3/day)	IN-OUT (m3/day)	m/day	mm/day	mm/year
STORAGE	0	0	0	0	0	0
CONSTANT HEAD	0	0	0.00E+00	0.00E+00	0.00E+00	0.00E+00
HORIZ. EXCHANGE	3.44E+05	2.24E+05	1.20E+05	2.54E-04	2.54E-01	9.26E+01
EXCHANGE (UPPER)	0	0	0.00E+00	0.00E+00	0.00E+00	0.00E+00
EXCHANGE (LOWER)	0	0	0.00E+00	0.00E+00	0.00E+00	0.00E+00
WELLS	0	3.45E+03	-3.45E+03	-7.29E-06	-7.29E-03	-2.66E+00
DRAINS	0	0	0.00E+00	0.00E+00	0.00E+00	0.00E+00
RECHARGE	2.76E+05	0	2.76E+05	5.83E-04	5.83E-01	2.13E+02
ET	0	0	0.00E+00	0.00E+00	0.00E+00	0.00E+00
RIVER LEAKAGE	6.07E+02	3.93E+05	-3.92E+05	-8.29E-04	-8.29E-01	-3.03E+02
HEAD DEP BOUNDS	0	0	0.00E+00	0.00E+00	0.00E+00	0.00E+00
STREAM LEAKAGE	0	0	0.00E+00	0.00E+00	0.00E+00	0.00E+00
INTERBED STORAGE	0	0	0.00E+00	0.00E+00	0.00E+00	0.00E+00
RESERV. LEAKAGE	0	0	0.00E+00	0.00E+00	0.00E+00	0.00E+00
	6.20E+05	6.20E+05	-4.30E+01	-9.09E-08	-9.09E-05	-3.32E-02

Table 54: Water budget of sub region-II

	IN(m3/day)	OUT (m3/day)	IN-OUT (m3/day)	m/day	mm/day	mm/year
STORAGE	0	0	0	0	0	0
CONSTANT HEAD	0	0	0	0	0	0
HORIZ. EXCHANGE	1.60E+05	2.10E+04	139000	2.77E-04	2.77E-01	1.01E+02
EXCHANGE (UPPER)	0	0	0	0.00E+00	0.00E+00	0.00E+00
EXCHANGE (LOWER)	0	0	0	0.00E+00	0.00E+00	0.00E+00
WELLS	0	8.23E+03	-8.23E+03	-1.64E-05	-1.64E-02	-5.98E+00
DRAINS	0	0	0	0.00E+00	0.00E+00	0.00E+00
RECHARGE	1.85E+05	0	1.85E+05	3.69E-04	3.69E-01	1.35E+02
ET	0	0	0	0.00E+00	0.00E+00	0.00E+00
RIVER LEAKAGE	4.35E+04	1.57E+05	-1.14E+05	-2.26E-04	-2.26E-01	-8.25E+01
HEAD DEP BOUNDS	0	0	0	0.00E+00	0.00E+00	0.00E+00
STREAM LEAKAGE	0	0	0	0.00E+00	0.00E+00	0.00E+00
INTERBED STORAGE	0	0	0	0.00E+00	0.00E+00	0.00E+00
RESERV. LEAKAGE	0	0	0	0.00E+00	0.00E+00	0.00E+00
	3.89E+05	1.86E+05	2.02E+05	4.27E-04	4.27E-01	1.56E+02
			2.02E+05	4.27E-04	4.27E-01	1.56E+02

Table 55: Water budget of sub region-III

	IN (m3/day)	OUT (m3/day)	IN-OUT (m3/day)	m/day	mm/day	mm/year
STORAGE	0	0	0	0	0	0
CONSTANT HEAD	0	0	0	0	0	0
HORIZ. EXCHANGE	5.84E+04	2.30E+04	35400	1.26E-04	1.26E-01	4.60E+01
EXCHANGE (UPPER)	0	0	0	0.00E+00	0.00E+00	0.00E+00
EXCHANGE (LOWER)	0	0	0	0.00E+00	0.00E+00	0.00E+00
WELLS	0	2.32E+03	-2.32E+03	-8.26E-06	-8.26E-03	-3.01E+00
DRAINS	0	0	0	0.00E+00	0.00E+00	0.00E+00
RECHARGE	8.40E+04	0	8.40E+04	2.99E-04	2.99E-01	1.09E+02
ET	0	0	0	0.00E+00	0.00E+00	0.00E+00
RIVER LEAKAGE	3.40E+03	1.20E+05	-1.17E+05	-4.17E-04	-4.17E-01	-1.52E+02
HEAD DEP BOUNDS	0	0	0	0.00E+00	0.00E+00	0.00E+00
STREAM LEAKAGE	0	0	0	0.00E+00	0.00E+00	0.00E+00
INTERBED STORAGE	0	0	0	0.00E+00	0.00E+00	0.00E+00
RESERV. LEAKAGE	0	0	0	0.00E+00	0.00E+00	0.00E+00
	1.46E+05	1.46E+05	-1.00E+01	-2.11E-08	-2.11E-05	-7.71E-03

6.6 Model Sensitivity

Finding the model parameter that affects the model calibration to a greater extent is called sensitivity analysis. A sensitivity analysis includes the procedure of methodically changing model input parameters (such as abstraction, boundary conditions, recharge, hydraulic conductivity, etc.) over a suitable range

and tracking the relative change in the model's response(McCuen, 1973). The amount that the head deviates from the calibrated one indicates how sensitive a certain model parameter is(Gillham & Farvolden, 1974). In this particular model, sensitivity analysis is carried out using hydraulic conductivity, recharge, and abstraction typically by changing one parameter value at a time. The model shows different trends of sensitivity by decreasing and increasing with 25%, 50 %, and 75% of the calibrated model. Based on the sensitivity result displayed in Table 56 and Figure 90, the model is highly sensitive to hydraulic conductivity in both scenarios followed by recharge, and less sensitive to abstraction or pumpage, but the impact is more pronounced during the decreasing scenarios.

Table 56: Sensitivity Parameters

Multipliers (%)	Hydraulic head difference (m)		
	Hydraulic conductivity(K)	R(Recharge)	Abstraction(Q)
75	80.98	14.35	1.38
50	61.46	11.53	1.08
25	33.42	7.14	0.83
0	0	0	0
-25	27.09	12.69	1.02
-50	54.27	39.32	1.59
-75	120.63	68.42	1.89

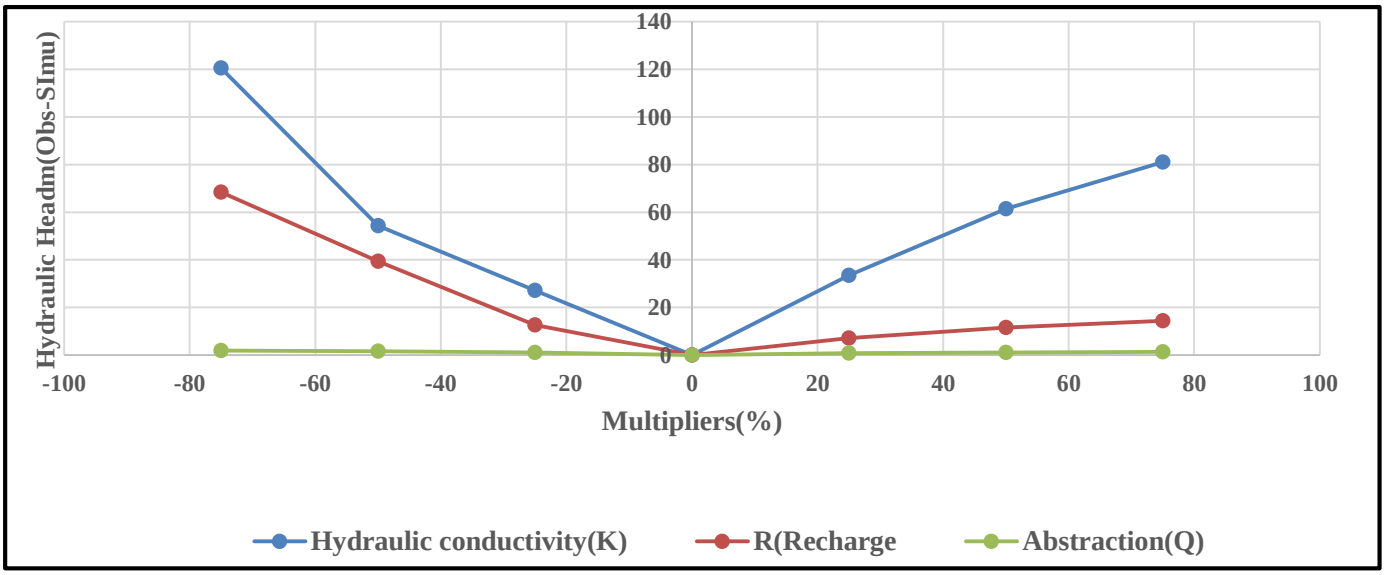


Figure 90: Sensitivity graph

6.7 Scenario analysis

An aquifer system's reactions to possible future stresses can be assessed and contrasted using a calibrated flow model. It is possible to compare the aquifer system's response to assess how well these likely stress changes work to meet management objectives. Even while simulated water levels for a particular

situation might not be an exact match for actual system values, the relative variations in water levels can be compared to offer helpful information for planning and decision-making in the future. In this model, a scenario analysis using abstraction was conducted to see and forward rough management practices by looking at the simulated aquifer-system response to increased and decreased withdrawals. Accordingly, all model parameters were unchanged from those specified in the steady-state simulation, while abstraction is increased by 25, 50, 75, 100, 150, and 200 percent multiplies. Therefore, the output might be used to study the effects of water-management techniques that could lessen the potential negative consequences of higher water withdrawals or to reflect potential future changes in the catchment's water use. Accordingly, the heads calculated for the increment of withdrawal by 25 percent show a maximum decline of the water level by 1.45 meters and a minimum of 0.21 meters, a maximum decline by 1.68m and 2.01m, and a minimum decline by 0.45m and 0.74m were created by 50% and 75% increase of withdrawal scenarios respectively (Table 57 and Figure 91). Up to a maximum of 3.41m, 4.14m, and 4.67m and a minimum decline of 1.02m, 1.24m, and 1.45m have been observed for 100%, 150%, and 200 % increment of abstraction respectively. From the available borehole sittings, the wells which have been drilled in the marginal grabens, have shown minimum average drawdown. This is related to the availability of thick alluvial deposits underlain by fractured and weathered trap series mainly basalt and ignimbrite, besides the transverse structures. The maximum drawdown is recorded in shallow wells and boreholes that have been located far from the groundwater structures. This shows that the boreholes have groundwater recharge from the local sources, which might not sustain the high abstraction rate.

Table 57: Scenario analysis with different abstraction rates

Scenarios	**Drawdown (m)**			**Percentage of increase**	**Abstraction (m3/day)**
	Minimum Drawdown	**Maximum Drawdown**	**Average Drawdown**		
1	0.21	1.45	0.83	25	16,250.00
2	0.45	1.68	1.07	50	19,500.00
3	0.74	2.01	1.38	75	22,750.00
4	1.02	3.41	2.22	100	26,000.00
5	1.24	4.14	2.69	150	32,500.00
6	1.45	4.67	3.06	200	39,000.00

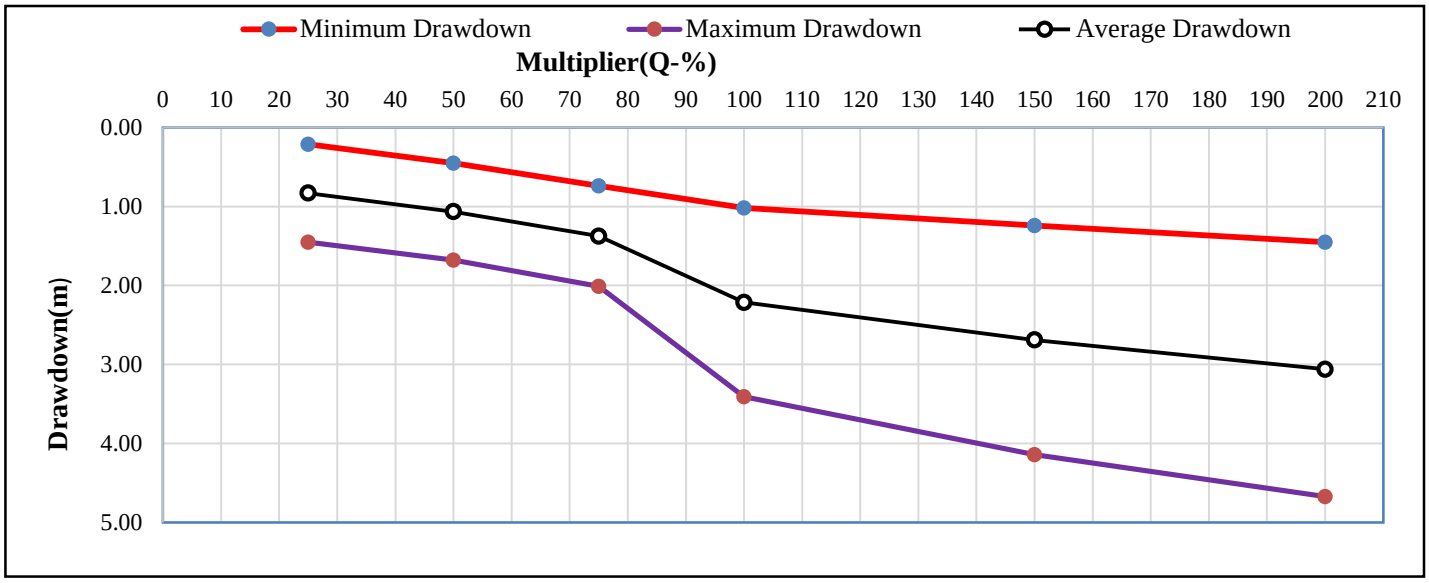


Figure 91: Graph showing scenario analysis with increasing abstractions

6.8 Limitations of the model

An understanding of model limitation is essential to effectively use flow and hydraulic head simulation, and forwarding appropriate recommendations. There are limitations with the modeling work which arise from different scenarios. Aquifer parameters like the hydraulic conductivity data were taken from pumping test data for certain locations of the model area. However, as it is well known most of the pumping test work in Ethiopia has been conducted on the production well itself, hence there could be some distortions in the aquifer parameters. Besides, the hydraulic conductivity value for the rest of the model area is assigned based on interpolation from the nearby data or with estimations, which might not be the actual value. The other limitation of the modeling work is the assigned recharge does not consider inter-basin groundwater flow, as it is determined using WetSpass model. Furthermore, the modeling work was conducted for a single layer by taking the average thickness of the layer to be 250m, which is mainly for the alluvial deposit. However, from the actual drilling data, the thickness of the deposit is variable from place to place. Besides, there is a gap in assigning river packages. This arises from assigning river bed conductivity, the thickness of the river bottom sediments, the width of the river, the elevation of the river bottom, and the assigning of the river length in the model cell. Furthermore, the surface water divide is assigned as a no-flow boundary. However, as has been described above, there is groundwater inflow from the adjacent catchment to the Awash basin due to the favorable geological and structural architectures. This shows that the surface water and groundwater divides are not the same. Generally, in tectonically active areas like the Afar rift, aquifer geometry, aquifer thickness, and hydraulic conductivity can change at intervals smaller than the current model resolution, especially where structures are extensive. Model uncertainty could also come from water level measurement in the field used for model calibration.

Chapter Seven: Conclusions and Recommendations

7.1 Conclusions

This study employed a comprehensive, multi-disciplinary approach—integrating geological, hydrogeological, hydro-meteorological, hydrochemical, and isotopic analyses with GIS and remote sensing techniques. A steady-state groundwater flow model was also developed for Jewuha-Robit catchment, serving as a calibration tool for understanding the flow system.

Based on the geological study and lithostratigraphic correlations constructed from the available boreholes, the trap series mainly the columnar jointed basalt was extended consistently from the plateau to the rift margin, however, in the case of the rift floor there is a lack of a plausible extended layer, because of the strong interruption of the multilayered aquifers by various deep-seated faults and siliceous volcanic. Structurally, transverse structures with NW-SE, NE-SW, and W-E trends link the plateau to the Western Afar rift margin, and finally to the rift floor. The hydrochemical analysis and interpretation indicate that most of the plateau samples and groundwater sources from the rift margin near the escarpment in the northern part of the study area are related to the Ca-(Mg)-HCO3 water type, with low TDS values. Furthermore, data from the analyses of stable isotopes from these sources were plotted close to and along the local meteoric water line (LMWL). Integrating the hydrochemical and isotope results reveals that these water groups correspond to freshly recharged groundwater and/or water in the early geochemical evolution stages that have not yet undergone major water-rock interactions, and is mainly precipitation and local groundwater flow. Correlating the preferential orientation of highland springs along the escarpments, their constant flow and significant yield from the small recharging catchment, Ca-(Mg)-HCO3 water type, and relatively depleted isotopic signature with respective of LMWL, mirrors the influx of groundwater from the adjacent plateau but has not undergone much water-rock interactions serves as the primary source of recharge through the transverse structures, in addition to local precipitation. The deep groundwater in the rift margin is associated with moderately mineralized, Na-Ca-HCO3 and Na-HCO3 water type and depleted isotope content similar to the deep groundwater of the plateau area. This indicates that deep circulating groundwater is present from the Northwest Plateau (NWP) in the Blue Nile Basin to the western rift margin of the Awash Basin. This is due to the presence of continual columnar jointed lower basalt connecting the two basins and transverse structures trending NE-SW and NW-SE. In addition, the increase in TDS and EC values from the plateau to the rift margin and high Radon values is due to the fact that the groundwater has undergone prolonged residence time along the flow directions. Mixed water types are also present along the rift margin, suggesting that there is the mixing of groundwater from different sources, mainly from precipitation, and local to intermediate

flow from the surrounding volcanic mountains, besides the regional flow. This is due to the presence of the overlying porous alluvial deposits and highly fractured volcanic rocks that surround the marginal grabens and facilitate infiltration of groundwater as well as circulation of deep groundwater from the plateau area.

In the rift floor, the groundwater from the shallow aquifers exhibits Ca-HCO3 water type and isotopically enriched, revealing local recharge sources that have been affected by evaporation before joining the aquifer. In contrast, the deep thermal groundwater boreholes in the rift floor are predominantly Na-$HCO3/SO_4/Cl^-$ water type, isotopically depleted, highly mineralized, and higher Radon values which distinguishes them from the shallow systems, suggesting different recharge sources and mechanisms, mainly from the western Afar rift margin through the transverse structures.

The hydrochemical parameters along with the isotopic signatures of the deep aquifers in all the physiography and radon measurements conducted at the rift floor and rift margin in conjunction with geological and lithostratigraphic correlations demonstrate that deep circulating groundwater from the plateau area across the rift margin with little addition of local sources is the main source of recharge for the deep groundwater systems of the Western Afar rift margin and associated rift floor. The main controlling mechanisms are the columnar jointed lower basalt and transverse structures that connect the plateau to the rift margin, and the rift margin to the rift floor which can be taken as preferential pathways. Hence, the plateau area serves as the primary source of groundwater recharge for the deep aquifers for both the rift margin and rift floor. The flow of groundwater from the rift margin to the rift floor leads to the conclusion that the marginal grabens are not hydrogeologically isolated from the rift floor.

From the multiple recharge estimation approaches and Keeping all their limitations, the spatially distributed groundwater recharge determined by the WetSpass model and Base-flow separation method complemented by geological, hydrochemical, and isotope analysis, deliver reliable results in tectonically active areas such as the Afar Rift and in arid to semi-arid climatic regions. Hence, to effectively apply recharge estimation using multiple methods for a specific catchment, a proper understanding of each method and its limitations, data acquisition and management, and geological and hydrogeological conceptualization should be fundamental considerations.

From RS and GIS overlay analysis techniques, five spatially distributed groundwater potential zones were delineated having area coverage of 221.48 km^2 (1.16%), 9084.46 km^2 (47.48%), 8281.96 km^2 (43.29%), 1441.65 km^2 (7.54%), and 102.45 km^2 (0.535%) corresponds to very low, low, moderate, high and very high respectively. Along the rift margin particularly the marginal grabens, thick alluvial deposits and fractured volcanic rocks, with transverse structures, and moderate to higher recharge favor zones

with moderate, high, and very high groundwater potential. In contrast, the presence of thick lacustrine deposits and fewer recharge means that the rift floor and surrounding area exhibit low to very low groundwater potential distribution. However, from the hydrochemical, stable isotope and Radon analysis and interpretations, there is deep circulating groundwater flowing from the plateau to the rift floor via preferential pathways, leading the latter to have low to moderate groundwater potential, showing that the availability of groundwater in the rift floor is highly dependent on structure and geology. Using a multi-criteria decision-making (MCDM) technique, namely the Analytic Hierarchical Process (AHP) and modified Saaty called Fuzzy Analytical Hierarchical Process (FAHP), from the eight thematic layers, the structures followed by geology have a bigger impact on the occurrence of groundwater in the area, consistent with the hypotheses mentioned above. So, combining Remote Sensing (RS) and GIS techniques with other conventional groundwater investigation methods will help to improve the accuracy of the outputs in defining the groundwater potential zones, especially in arid to semi-arid and tectonically affected regions like the Afar rift.

A steady-state numerical groundwater flow model for the Jewuha-Robit catchment was developed and provided valuable information on the groundwater balance, groundwater-surface water interactions, and groundwater flow dynamics. Based on the quantitative and qualitative evaluations of the model result, the output can be taken as a good simulation. However, at this stage the model cannot be used for detailed groundwater management practices, but rather for the evaluation of the different hydrologic parameters. From the sensitivity analysis, hydraulic conductivity and abstraction are the most and the least sensitive parameters that control the flow of groundwater in the catchment respectively. Therefore, having all the uncertainties in the estimation of model input parameters, the overall water balance parameters can be used for the groundwater system analysis of the area.

In conclusion, the integrated approach utilized in this research underscores the importance of using multiple techniques and approaches for the accurate analysis of groundwater flow dynamics; mainly for the assessments of the source and mechanisms of groundwater recharge, the estimation of the rate of recharge, and the delineation of groundwater potential zones in arid to semi-arid regions and tectonically active areas like the Afar Triangle.

7.2 Recommendations

Based on the accomplished work, the following recommendations have been forwarded.

- From the geological, hydrogeological, hydrochemical, and isotope analysis, and interpretations, the groundwater flow dynamics of the western Afar rift margin and the associated rift floor, and its relation with the adjacent Blue Nile basin have been outlined. This will have a better contribution to the further groundwater development, abstraction, and management both at the rift margin and rift floor.
- From the recharge estimation techniques, the results highlight that multiple methods of estimating groundwater recharge are highly recommended to understand and capture the potential recharge mechanisms and to arrive at an acceptable estimate of groundwater recharge, especially in tectonically active areas like the Afar depression.
- With its limitations, GIS and RS techniques have been found effective for the groundwater potential evaluation of the study area. However, for a better assessment of the groundwater potential of a certain basin especially in tectonically active areas like the Afar triangle, and arid to semiarid climatic zones, it is highly recommended to couple the techniques with other conventional methods like geological, and hydrogeological besides to isotope and hydrochemical analysis, and interpretations.
- For a better evaluation of the contribution of groundwater to the river in the ungauged areas mainly between the rift margin and rift floor, it is highly recommended to install additional river gauging stations in these areas.
- Besides, most of the river gauging stations in the study area were not properly functioning, which resulted in a big impact on evaluating the present water level and total flow of the river. So, all the stakeholders should give a solution soon.
- Conducting depth-specific and seasonal water sampling and analysis is highly recommended for a better understanding and assessment of the impact of evaporation on the source of recharge in the water's isotopic signatures, particularly on the rift floor.
- It is highly recommended to conduct a multi-layer aquifer system, a more thorough estimate of model input parameters in a finer model grid, and handling temporal fluctuations under transient circumstances with a proper delineation of the groundwater and surface water divide which could all help to increase the model's accuracy in the future.
- Last but not least, it is highly recommended to have properly established and well-organized data management records both for groundwater and surface water at the national and regional levels.

Reference

Abbate, E., Bruni, P., & Sagri, M. (2015). Geology of Ethiopia: A Review and Geomorphological Perspectives World Geomorphological Landscapes book series (WGLC) Landscapes, DOI 10.1007/978-94-017-8026-1_2, © Springer Science+Business Media Dordrecht 2015. In *World Geomorphological Landscapes, DOI 10.1007/978-94-017-8026-1_2, © Springer Science+Business Media Dordrecht 2015* (Vol. 53, Issue 02). https://doi.org/10.1007/978-94-017-8026-1

Abbate, E., Passerini, P., & Zan, L. (1995). Strike-slip faults in a rift area: a transect in the Afar Triangle, East Africa. *Tectonophysics*, *241*(1–2), 67–97. https://doi.org/10.1016/0040-1951(94)00136-W

Abdalla, F. (2012). Mapping of groundwater prospective zones using remote sensing and GIS techniques: A case study from the Central Eastern Desert, Egypt. *Journal of African Earth Sciences*, *70*, 8–17. https://doi.org/10.1016/j.jafrearsci.2012.05.003

Abdi, H., & Williams, L. J. (2010). Principal component analysis. *Wiley Interdisciplinary Reviews: Computational Statistics*, *2*(4), 433–459. https://doi.org/10.1002/wics.101

Abebe, B., Dramis, F., Fubelli, G., Umer, M., & Asrat, A. (2010). Landslides in the Ethiopian highlands and the Rift margins. *Journal of African Earth Sciences*, *56*(4–5), 131–138. https://doi.org/10.1016/j.jafrearsci.2009.06.006

Abijith, D., Saravanan, S., Singh, L., Jennifer, J. J., Saranya, T., & Parthasarathy, K. S. S. (2020). GIS-based multi-criteria analysis for identification of potential groundwater recharge zones - a case study from Ponnaniyaru watershed, Tamil Nadu, India. *HydroResearch*, *3*, 1–14. https://doi.org/10.1016/j.hydres.2020.02.002

Achraf, M., Khodayar, A., Rouhallah, F., & Habib, A. (2017). Groundwater recharge estimation under semi arid climate: Case of Northern Gafsa watershed, Tunisia. *Journal of African Earth Sciences*. https://doi.org/10.1016/j.jafrearsci.2017.04.020

Acocella, V., Gudmundsson, A., & Funiciello, R. (2004). Acocella_2000_Interaction and linkage of extension_Journal of Structural Geology. *Journal of Structural Geolog*, *22*, 1–14. papers3://publication/uuid/D9D69A42-728B-4112-874E-E7925364AFBF

Adeyeye, J. A., Akinyemi, O. D., Awomeso, J. A., Bada, B. S., & Akintan, O. B. (2021). Geo-chemical investigation of groundwater salinity status in selected coastal areas of south western Nigeria.

Sustainable Water Resources Management, *7*(4), 1–15. https://doi.org/10.1007/s40899-021-00541-9

Adeyeye, O. A., Ikpokonte, E. A., & Arabi, S. A. (2019). GIS-based groundwater potential mapping within Dengi area, North Central Nigeria. *Egyptian Journal of Remote Sensing and Space Science*, *22*(2), 175–181. https://doi.org/10.1016/j.ejrs.2018.04.003

Adimalla, N., Vasa, S. K., & Li, P. (2018). Evaluation of groundwater quality, Peddavagu in Central Telangana (PCT), South India: an insight of controlling factors of fluoride enrichment. *Modeling Earth Systems and Environment*, *4*(2), 841–852. https://doi.org/10.1007/s40808-018-0443-z

ADSWE. (2010). *Eastern Amhara hydrology Report*.

Afrifa, G. Y., Sakyi, P. A., & Chegbeleh, L. P. (2017). Estimation of groundwater recharge in sedimentary rock aquifer systems in the Oti Basin of Gushiegu District, Northern Ghana. *Journal of African Earth Sciences*. https://doi.org/10.1016/j.jafrearsci.2017.02.035

Aghazadeh, N., & Mogaddam, A. A. (2011). Investigation of hydrochemical characteristics of groundwater in the Harzandat aquifer, Northwest of Iran. *Environmental Monitoring and Assessment*, *176*(1–4), 183–195. https://doi.org/10.1007/s10661-010-1575-4

Agostini, A., Bonini, M., Corti, G., Sani, F., & Mazzarini, F. (2011). Fault architecture in the Main Ethiopian Rift and comparison with experimental models: Implications for rift evolution and Nubia-Somalia kinematics. *Earth and Planetary Science Letters*, *301*(3–4), 479–492. https://doi.org/10.1016/j.epsl.2010.11.024

Ahmad, I., Dar, M. A., Andualem, T. G., & Teka, A. H. (2020). GIS-based multi-criteria evaluation of groundwater potential of the Beshilo River basin, Ethiopia. *Journal of African Earth Sciences*, 103747. https://doi.org/10.1016/j.jafrearsci.2019.103747

Ahmad, I., Dar, M. A., Fenta, A., Halefom, A., Nega, H., Andualem, T. G., & Teshome, A. (2021). Spatial configuration of groundwater potential zones using OLS regression method. *Journal of African Earth Sciences*, *177*(September 2020), 104147. https://doi.org/10.1016/j.jafrearsci.2021.104147

Ahmad, I., Dar, M. A., Teka, A. H., Teshome, M., Andualem, T. G., Teshome, A., & Shafi, T. (2020). GIS and fuzzy logic techniques-based demarcation of groundwater potential zones: A case study from Jemma River basin, Ethiopia. *Journal of African Earth Sciences*, *169*(April), 103860.

https://doi.org/10.1016/j.jafrearsci.2020.103860

Ahmad, S., & Mazhar, S. N. (2020). Hydrochemical Characteristics, Groundwater Quality and Sources of Solute in the Ramganga Aquifer, Central Ganga Plain, Bareilly District, Uttar Pradesh. *Journal of the Geological Society of India*, *95*(6), 616–625. https://doi.org/10.1007/s12594-020-1488-y

Ahmed, A. A., & Shabana, A. R. (2020). Journal of African Earth Sciences Integrating of remote sensing , GIS and geophysical data for recharge potentiality evaluation in Wadi El Tarfa , eastern desert , Egypt. *Journal of African Earth Sciences*, *172*(February), 103957. https://doi.org/10.1016/j.jafrearsci.2020.103957

Ahmed, A. A., Shabana, A. R., & Saleh, A. A. (2019). Using hydrochemical and isotopic data to determine sources of recharge and groundwater evolution in arid region from Eastern Desert, Egypt. *Journal of African Earth Sciences*, *151*, 36–46. https://doi.org/10.1016/j.jafrearsci.2018.11.024

Aish, A. M., Batelaan, O., & De Smedt, F. (2010). Distributed recharge estimation for groundwater modeling using wetspass model, case study - gaza strip, palestine. *Arabian Journal for Science and Engineering*, *35*(1), 155–163.

Ako, A. A., Shimada, J., Hosono, T., Ichiyanagi, K., Nkeng, G. E., Eyong, G. E. T., & Roger, N. N. (2012). Hydrogeochemical and isotopic characteristics of groundwater in Mbanga, Njombe and Penja (Banana Plain) - Cameroon. *Journal of African Earth Sciences*, *75*, 25–36. https://doi.org/10.1016/j.jafrearsci.2012.06.003

Al-hallaq, A. H., Sofyan, B., & Elaish, A. (2008). *Determination of Mean Areal Rainfall in the Gaza Strip Using Geographic Information System (GIS) Technique*. *5*(2), 105–126.

Al-Timimi, Y. K., Al-Lami, A. M., & Al-Shamarti, H. K. (2020). Calculation of the mean annual rainfall in iraq using several methods in gis. *Plant Archives*, *20*, 1156–1160.

Alemayehu, S., & Asefa, J. (2023). A Review of Earthquake Source Parameters in the Main Ethiopian Rift. *International Journal of Geophysics*, *2023*(Figure 1). https://doi.org/10.1155/2023/8368175

Ali Rahmani, S. E., Chibane, B., & Boucefiène, A. (2017). Groundwater recharge estimation in semi-arid zone: a study case from the region of Djelfa (Algeria). *Applied Water Science*, *7*(5), 2255–2265. https://doi.org/10.1007/s13201-016-0399-y

Ali, S. A., & Ali, U. (2018). Hydrochemical characteristics and spatial analysis of groundwater quality

in parts of Bundelkhand Massif, India. *Applied Water Science*, *8*(1), 1–15. https://doi.org/10.1007/s13201-018-0678-x

Aliran, M., Air, M., & Tanah, B. (2013). *Estimating Groundwater Recharge Using Empirical Method : A Case Study in the Tropical Zone*. *42*(5), 553–560.

Allafta, H., Opp, C., & Patra, S. (2021). Identification of groundwater potential zones using remote sensing and GIS techniques: A case study of the shatt Al-Arab Basin. *Remote Sensing*, *13*(1), 1–28. https://doi.org/10.3390/rs13010112

Almond, D. C. (1986). Geological evolution of the Afro-Arabian dome. *Tectonophysics*, *131*(3–4), 301–332. https://doi.org/10.1016/0040-1951(86)90180-0

Anderson, M. P., Woessner, W. W., & Hunt, R. J. (n.d.). *APPLIED MODELING Simulation of Flow and Advective Transport Second Edition*.

Arnold, J. G., & Allen, P. M. (1999). Automated methods for estimating baseflow and ground water recharge from streamflow records. *Journal of the American Water Resources Association*, *35*(2), 411–424. https://doi.org/10.1111/j.1752-1688.1999.tb03599.x

ArRajehi, A., McClusky, S., Reilinger, R., Daoud, M., Alchalbi, A., Ergintav, S., Gomez, F., Sholan, J., Bou-Rabee, F., Ogubazghi, G., Haileab, B., Fisseha, S., Asfaw, L., Mahmoud, S., Rayan, A., Bendik, R., & Kogan, L. (2010). Geodetic constraints on present-day motion of the Arabian Plate: Implications for Red Sea and Gulf of Aden rifting. *Tectonics*, *29*(3), 1–10. https://doi.org/10.1029/2009TC002482

Arshad, A., Zhang, Z., Zhang, W., & Dilawar, A. (2020). Mapping favorable groundwater potential recharge zones using a GIS-based analytical hierarchical process and probability frequency ratio model: A case study from an agro-urban region of Pakistan. *Geoscience Frontiers*, *11*(5), 1805–1819. https://doi.org/10.1016/j.gsf.2019.12.013

Arulbalaji, P., Padmalal, D., & Sreelash, K. (2019). GIS and AHP Techniques Based Delineation of Groundwater Potential Zones: a case study from Southern Western Ghats, India. *Scientific Reports*, *9*(1), 1–17. https://doi.org/10.1038/s41598-019-38567-x

Asfaw, L. M. (2000). Tensional fissures in sediments as signature of rift tectonics in the Main Ethiopian Rift. In *SINET: Ethiopian Journal of Science* (Vol. 23, Issue 1). https://doi.org/10.4314/sinet.v23i1.18160

Atawneh, D. Al, Cartwright, N., & Bertone, E. (2021). Climate change and its impact on the projected values of groundwater recharge: A review. *Journal of Hydrology*, *601*(June), 126602. https://doi.org/10.1016/j.jhydrol.2021.126602

Augustin, N., Devey, C. W., Van der Zwan, F. M., Feldens, P., Tominaga, M., Bantan, R. A., & Kwasnitschka, T. (2014). The rifting to spreading transition in the Red Sea. *Earth and Planetary Science Letters*, *395*, 217–230. https://doi.org/10.1016/j.epsl.2014.03.047

Awash Basin Authority. (2017). *Awash River Basin Integrated Participatory Watershed Management Strategic & Detail Action plan*. *June*.

Ayenew, T., Demlie, M., & Wohnlich, S. (2008). Hydrogeological framework and occurrence of groundwater in the Ethiopian aquifers. *Journal of African Earth Sciences*, *52*(3), 97–113. https://doi.org/10.1016/j.jafrearsci.2008.06.006

Ayenew, T., Kebede, S., & Alemyahu, T. (2008). *Environmental isotopes and hydrochemical study applied to surface water and groundwater interaction in the Awash*. *1563*(August 2007), 1548–1563. https://doi.org/10.1002/hyp

Azagegn, T. (2014). *Groundwater Dynamics in the Left Bank Catchments of the Middle Blue Nile and the Upper Awash River Basins , Central Ethiopia Tilahun Azagegn A Thesis Submitted to The School of Earth Sciences Presented in Partial Fulfillment of the Requirement for the Deg*.

Azevedo da Silva, T., Ferreira do Rosário, F., & Cardoso da Silva Júnior, G. (2020). Environmental isotopes and hydrochemical tracers applied to hydrogeological conceptual modeling of the southwest portion of the Amazon Aquifer System (Acre, Brazil). *Applied Geochemistry*, *120*(July). https://doi.org/10.1016/j.apgeochem.2020.104670

Babu, M. A. H., Islam, M. R., Farzana, F., Uddin, M. J., & Islam, M. S. (2020). Application of GIS and Remote Sensing for Identification of Groundwater Potential Zone in the Hilly Terrain of Bangladesh. *Grassroots Journal of Natural Resources*, *3*(3), 16–27. https://doi.org/10.33002/nr2581.6853.03032

Bajjali, W. (2006). Recharge mechanism and hydrochemistry evaluation of groundwater in the Nuaimeh area, Jordan, using environmental isotope techniques. *Hydrogeology Journal*, *14*(1–2), 180–191. https://doi.org/10.1007/s10040-004-0352-2

Bajjali, W. (2008). Evaluation of groundwater in a three-aquifer system in Ramtha area, Jordan:

Recharge mechanisms, hydraulic relationship and geochemical evolution. *Hydrogeology Journal*, *16*(6), 1193–1205. https://doi.org/10.1007/s10040-008-0284-3

Barberi, F., Bonatti, E., Marinelli, G., & Varet, J. (1974). Transverse tectonics during the split of a continent: Data from the afar rift. *Tectonophysics*, *23*(1–2), 17–29. https://doi.org/10.1016/0040-1951(74)90108-5

Barberi, F., Tazieff, H., & Varet, J. (1972). Volcanism in the Afar Depression: Its Tectonic and Magmatic Significance. *Developments in Geotectonics*, *7*(C), 19–29. https://doi.org/10.1016/B978-0-444-41087-0.50007-5

Barbot, S., Fialko, Y., & Sandwell, D. (2008). Effect of a compliant fault zone on the inferred earthquake slip distribution. *Journal of Geophysical Research: Solid Earth*, *113*(6), 1–10. https://doi.org/10.1029/2007JB005256

Baskaran, S., Ransley, T., Brodie, R. S., & Baker, P. (2009). Investigating groundwater-river interactions using environmental tracers. *Australian Journal of Earth Sciences*, *56*(1), 13–19. https://doi.org/10.1080/08120090802541887

Bastow, I. D., Booth, A. D., Corti, G., Keir, D., Magee, C., Jackson, C. A. L., Warren, J., Wilkinson, J., & Lascialfari, M. (2018). The Development of Late-Stage Continental Breakup: Seismic Reflection and Borehole Evidence from the Danakil Depression, Ethiopia. *Tectonics*, *37*(9), 2848–2862. https://doi.org/10.1029/2017TC004798

Bastow, I. D., Keir, D., & Daly, E. (2011). The Ethiopia Afar Geoscientific Lithospheric Experiment (EAGLE): Probing the transition from continental rifting to incipient seafloor spreading. *Special Paper of the Geological Society of America*, *478*(04), 51–76. https://doi.org/10.1130/2011.2478(04)

Batelaan, O., & De Smedt, F. (2007). GIS-based recharge estimation by coupling surface-subsurface water balances. *Journal of Hydrology*, *337*(3–4), 337–355. https://doi.org/10.1016/j.jhydrol.2007.02.001

Baye, A. Y. (2009). Université de Poitiers ANDARGE YITBAREK BAYE Hydrogeological and hydrochemical framework of complex volcanic system in the Upper Awash River basin , Central Ethiopia : with special emphasis on inter-basins groundwater transfer between Blue Nile and Awash. *PhD Thesis*, 1–233.

Ben Brahim, F., Boughariou, E., & Bouri, S. (2021). Multicriteria-analysis of deep groundwater quality using WQI and fuzzy logic tool in GIS: A case study of Kebilli region, SW Tunisia. *Journal of African Earth Sciences*, *180*(July 2020), 104224. https://doi.org/10.1016/j.jafrearsci.2021.104224

Bense, V. F., Gleeson, T., Loveless, S. E., Bour, O., & Scibek, J. (2013). Fault zone hydrogeology. *Earth-Science Reviews*, *127*, 171–192. https://doi.org/10.1016/j.earscirev.2013.09.008

Bera, A. and Das, S., 2021. (1990). Water resource management in semi-arid Purulia district of West Bengal, in the context of sustainable develop- ment goals. In: P. K. Shit, G. S. Bhunia, P. P. Adhikary, Ch. J. Dash, eds. Groundwater and society. Cham: Springer, 501–519. *Workshop on Percolation Ponds, Conducted by Center for Water Resources, Anna University, Chennai*, 23–27.

Berehanu, B., Azagegn, T., Ayenew, T., & Masetti, M. (2017). Inter-Basin Groundwater Transfer and Multiple Approach Recharge Estimation of the Upper Awash Aquifer System. *Journal of Geoscience and Environment Protection*, *05*(03), 76–98. https://doi.org/10.4236/gep.2017.53007

Bersi, M., & Saibi, H. (2020). Groundwater potential zones identification using geoelectrical sounding and remote sensing in Wadi Touil plain, Northwestern Algeria. In *Journal of African Earth Sciences* (Vol. 172). Elsevier Ltd. https://doi.org/10.1016/j.jafrearsci.2020.104014

Beutel, E., van Wijk, J., Ebinger, C., Keir, D., & Agostini, A. (2010). Formation and stability of magmatic segments in the Main Ethiopian and Afar rifts. *Earth and Planetary Science Letters*, *293*(3–4), 225–235. https://doi.org/10.1016/j.epsl.2010.02.006

Beyene, A., & Abdelsalam, M. G. (2005). Tectonics of the Afar Depression: A review and synthesis. *Journal of African Earth Sciences*, *41*(1–2), 41–59. https://doi.org/10.1016/j.jafrearsci.2005.03.003

Bhattacharya, S., Das, S., Das, S., Kalashetty, M., & Warghat, S. R. (2021). An integrated approach for mapping groundwater potential applying geospatial and MIF techniques in the semiarid region. *Environment, Development and Sustainability*, *23*(1), 495–510. https://doi.org/10.1007/s10668-020-00593-5

Biswas, S., Mukhopadhyay, B. P., & Bera, A. (2020). Delineating groundwater potential zones of agriculture dominated landscapes using GIS based AHP techniques: a case study from Uttar Dinajpur district, West Bengal. *Environmental Earth Sciences*, *79*(12). https://doi.org/10.1007/s12665-020-09053-9

Bonetto, S. M. R., Caselle, C., de Luca, D. A., & Lasagna, M. (2021). Groundwater Resources in the Main Ethiopian Rift Valley: An Overview for a Sustainable Development. *Sustainability (Switzerland)*, *13*(3), 1–15. https://doi.org/10.3390/su13031347

Bonini, M., Corti, G., Innocenti, F., Manetti, P., Mazzarini, F., Abebe, T., & Pecskay, Z. (2005). Evolution of the Main Ethiopian Rift in the frame of Afar and Kenya rifts propagation. *Tectonics*, *24*(1), 1–21. https://doi.org/10.1029/2004TC001680

Bretzler, A., Osenbrück, K., Gloaguen, R., Ruprecht, J. S., Kebede, S., & Stadler, S. (2011). Groundwater origin and flow dynamics in active rift systems – A multi-isotope approach in the Main Ethiopian Rift. In *Hydrology* (Vol. 402). https://doi.org/10.1016/j.jhydrol.2011.03.022

Caine, Jonathan, S., Evans, James, P., & Forster, Craig, B. (1996). Fault zone architecture and permeability structure. *Geology*, *24*(11), 1025–1028.

Calvo-Alvarado, J. C. (1986). An evaluation of thornthwaite's water balance technique in predicting stream runoff in costa rica. *Hydrological Sciences Journal*, *31*(1), 51–60. https://doi.org/10.1080/02626668609491027

Cameron, R. I., & Middlemis, H. (1994). Computer modelling of dewatering a major open pit mine: Case study from Nevada, USA. *Geological Society Special Publication*, *79*(79), 207–217. https://doi.org/10.1144/GSL.SP.1994.079.01.18

Carter, C., & Liang, S. (2019). Evaluation of ten machine learning methods for estimating terrestrial evapotranspiration from remote sensing. *International Journal of Applied Earth Observation and Geoinformation*, *78*(January), 86–92. https://doi.org/10.1016/j.jag.2019.01.020

Chanasyk, D. S., Mapfumo, E., & Chaikowsky, C. L. A. (2006). Estimating actual evapotranspiration using water budget and soil water reduction methods. *Canadian Journal of Soil Science*, *86*(4), 757–766. https://doi.org/10.4141/S05-063

Chang, D. Y. (1996). Applications of the extent analysis method on fuzzy AHP. *European Journal of Operational Research*, *95*(3), 649–655. https://doi.org/10.1016/0377-2217(95)00300-2

Chebotarev, I. I. (1955). Metamorphism of natural waters in the crust of weathering-3. *Geochimica et Cosmochimica Acta*, *8*(4), 198–212. https://doi.org/10.1016/0016-7037(55)90053-3

Chiew, F. H. S., Mcmahon, T. A., & Neill, I. C. O. (1992). *Estimating groundwater recharge using an integrated surface and groundwater modelling approach*. *131*, 151–186.

Chorowicz, J. (1990). Dynamics of the different basin-types in the East African rift. *Journal of African Earth Sciences*, *10*(1–2), 271–282. https://doi.org/10.1016/0899-5362(90)90060-R

Chung, I. M., Sophocleous, M. A., Mitiku, D. B., & Kim, N. W. (2016). Estimating groundwater recharge in the humid and semi-arid African regions: review. *Geosciences Journal*, *20*(5), 731–744. https://doi.org/10.1007/s12303-016-0001-5

Clark, I. D., & Fritz, P. (2013). Environmental Isotopes in Hydrogeology. In *Environmental Isotopes in Hydrogeology*. https://doi.org/10.1201/9781482242911

Cloutier, V., Lefebvre, R., Therrien, R., & Savard, M. M. (2008). Multivariate statistical analysis of geochemical data as indicative of the hydrogeochemical evolution of groundwater in a sedimentary rock aquifer system. *Journal of Hydrology*, *353*(3–4), 294–313. https://doi.org/10.1016/j.jhydrol.2008.02.015

Cook, P. (2017). *Title Page Introduction to Isotopes and Environmental Tracers as Indicators of Groundwater Flow i*.

Cook, P. G., Favreau, G., Dighton, J. C., & Tickell, S. (2003). Determining natural groundwater influx to a tropical river using radon, chlorofluorocarbons and ionic environmental tracers. *Journal of Hydrology*, *277*(1–2), 74–88. https://doi.org/10.1016/S0022-1694(03)00087-8

Cooper, M. (2010a). Advanced Bash-Scripting Guide An in-depth exploration of the art of shell scripting Table of Contents. *Okt 2005 Abrufbar Uber Httpwww Tldp OrgLDPabsabsguide Pdf Zugriff 1112 2005*, *2274*(November 2008), 2267–2274. https://doi.org/10.1002/hyp

Cooper, M. (2010b). Advanced Bash-Scripting Guide An in-depth exploration of the art of shell scripting Table of Contents. *Okt 2005 Abrufbar Uber Httpwww Tldp OrgLDPabsabsguide Pdf Zugriff 1112 2005*, *2274*(November 2008), 2267–2274. https://doi.org/10.1002/hyp

Corti, G., Bastow, I. D., Keir, D., Pagli, C., & Baker, E. (2015). Rift-Related Morphology of the Afar Depression. *World Geomorphological Landscapes*, 251–274. https://doi.org/10.1007/978-94-017-8026-1_15

Curewitz, D., & Karson, J. A. (1997). Structural settings of hydrothermal outflow: Fracture permeability maintained by fault propagation and interaction. *Journal of Volcanology and Geothermal Research*, *79*(3–4), 149–168. https://doi.org/10.1016/S0377-0273(97)00027-9

D. Parkhurst and C.Appelo. (2002). *User's guide to PHREEQC (ver 2) - A computer program for*

speciation, batch-reaction, one-dimensional transport, and inverse geochemical calculations. *Version 2*, 54 pp. https://pubs.usgs.gov/wri/1999/4259/report.pdf

Danso, S. Y., & Ma, Y. (2023). Geospatial techniques for groundwater potential zones delineation in a coastal municipality, Ghana. *Egyptian Journal of Remote Sensing and Space Science*, *26*(1), 75–84. https://doi.org/10.1016/j.ejrs.2022.12.004

Das, B., & Pal, S. C. (2019). Combination of GIS and fuzzy-AHP for delineating groundwater recharge potential zones in the critical Goghat-II block of West Bengal, India. *HydroResearch*, *2*, 21–30. https://doi.org/10.1016/j.hydres.2019.10.001

Das, S. (2019a). AC SC. *Groundwater for Sustainable Development*. https://doi.org/10.1016/j.gsd.2019.03.003

Das, S. (2019b). Comparison among influencing factor, frequency ratio, and analytical hierarchy process techniques for groundwater potential zonation in Vaitarna basin, Maharashtra, India. *Groundwater for Sustainable Development*, *8*(April 2018), 617–629. https://doi.org/10.1016/j.gsd.2019.03.003

Das, S., & Pardeshi, S. D. (2018). Integration of different influencing factors in GIS to delineate groundwater potential areas using IF and FR techniques : a study of Pravara basin , Maharashtra , India. *Applied Water Science*, *8*(7), 1–16. https://doi.org/10.1007/s13201-018-0848-x

Dawana, Y. D. (2020). *Groundwater Recharge Estimation in Ethiopia*. *December*, 145.

de Vries, J. J., & Simmers, I. (2002). Groundwater recharge: An overview of process and challenges. *Hydrogeology Journal*, *10*(1), 5–17. https://doi.org/10.1007/s10040-001-0171-7

Demlie, M. (2015). Assessment and estimation of groundwater recharge for a catchment located in highland tropical climate in central Ethiopia using catchment soil–water balance (SWB) and chloride mass balance (CMB) techniques. *Environmental Earth Sciences*, *74*(2), 1137–1150. https://doi.org/10.1007/s12665-015-4099-y

Dennis Risser, B. W., Geological Survey, U., Gburek, W. J., & Folmar, G. J. (2005). Ground-Water Resources Program Comparison of Methods for Estimating Ground-Water Recharge and Base Flow at a Small Watershed Underlain by Fractured Bedrock in the Eastern United States Scientific Investigations Report 2005-5038. *Usgs Sir 2005-5038*.

Dere Gidafie, N. (2016). *Estimation of Groundwater Recharge Using Water Balance Model : A Case*

Study in the Gerado Basin , North Central Ethiopia.

Dereje, B., & Nedaw, D. (2019). Groundwater Recharge Estimation Using WetSpass Modeling in Upper Bilate Catchment, Southern Ethiopia. *Momona Ethiopian Journal of Science*, *11*(1), 37. https://doi.org/10.4314/mejs.v11i1.3

Detto, M., Montaldo, N., Albertson, J. D., Mancini, M., & Katul, G. (2006). Soil moisture and vegetation controls on evapotranspiration in a heterogeneous Mediterranean ecosystem on Sardinia, Italy. *Water Resources Research*, *42*(8), 1–16. https://doi.org/10.1029/2005WR004693

Diouf, O. C., Weihermüller, L., Ba, K., Faye, S. C., Faye, S., & Vereecken, H. (2016). Estimation of Turc reference evapotranspiration with limited data against the Penman-Monteith Formula in Senegal. *Journal of Agriculture and Environment for International Development*, *110*(1), 117–137. https://doi.org/10.12895/jaeid.20161.417

Doke, A. B., Zolekar, R. B., Patel, H., & Das, S. (2021). Geospatial mapping of groundwater potential zones using multi-criteria decision-making AHP approach in a hardrock basaltic terrain in India. *Ecological Indicators*, *127*(September 2020), 107685. https://doi.org/10.1016/j.ecolind.2021.107685

Doubre, C., Déprez, A., Masson, F., Socquet, A., Lewi, E., Grandin, R., Nercessian, A., Ulrich, P., De Chabalier, J. B., Saad, I., Abayazid, A., Peltzer, G., Delorme, A., Calais, E., & Wright, T. (2017). Current deformation in Central Afar and triple junction kinematics deduced from GPS and InSAR measurements. *Geophysical Journal International*, *208*(2), 936–953. https://doi.org/10.1093/gji/ggw434

Dragon, K., & Gorski, J. (2015). Identification of groundwater chemistry origins in a regional aquifer system (Wielkopolska region, Poland). *Environmental Earth Sciences*, *73*(5), 2153–2167. https://doi.org/10.1007/s12665-014-3567-0

Duah, A. A., Akurugu, B. A., Darko, P. K., Manu, E., & Mainoo, P. A. (2021). Journal of African Earth Sciences Groundwater recharge and potential exploitation in the Densu basin , Southwestern Ghana. *Journal of African Earth Sciences*, *183*(June), 104332. https://doi.org/10.1016/j.jafrearsci.2021.104332

Dziuban, C. D., & Shirkey, E. C. (1974). When is a correlation matrix appropriate for factor analysis? Some decision rules. *Psychological Bulletin*, *81*(6), 358–361. https://doi.org/10.1037/h0036316

Ebinger, C., & Belachew, M. (2010). Geodynamics: Active passive margins. *Nature Geoscience*, *3*(10), 670–671. https://doi.org/10.1038/ngeo972

Ebrahim, G. Y., Lautze, J. F., & Villholth, K. G. (2020). Managed aquifer recharge in Africa: Taking stock and looking forward. *Water (Switzerland)*, *12*(7). https://doi.org/10.3390/W12071844

Echogdali, F. Z., Boutaleb, S., Bendarma, A., Saidi, M. E., Aadraoui, M., Abioui, M., Ouchchen, M., Abdelrahman, K., Fnais, M. S., & Sajinkumar, K. S. (2022). Application of Analytical Hierarchy Process and Geophysical Method for Groundwater Potential Mapping in the Tata Basin, Morocco. *Water (Switzerland)*, *14*(15). https://doi.org/10.3390/w14152393

Edet, A. E., Okereke, C. S., Teme, S. C., & Esu, E. O. (1998). Application of remote-sensing data to groundwater exploration: A case study of the Cross River State, southeastern Nigeria. *Hydrogeology Journal*, *6*(3), 394–404. https://doi.org/10.1007/s100400050162

El Ayady, H., Mickus, K. L., Boutaleb, S., El Morjani, Z. E. A., Ikirri, M., Echogdali, F. Z., Ekoa Bessa, A. Z., Abdelrahman, K., Id-Belqas, M., Essoussi, S., Fnais, M. S., & Abioui, M. (2023). Investigation of groundwater potential using geomatics and geophysical methods: Case study of the Anzi sub-basin, western Anti-Atlas, Morocco. *Advances in Space Research*, *72*(9), 3960–3981. https://doi.org/10.1016/j.asr.2023.08.044

Ethiopia_Sentinel2_LULC2016. (n.d.).

FAO. (2009). *DSMW*.

Farnham, I. M., Johannesson, K. H., Singh, A. K., Hodge, V. F., & Stetzenbach, K. J. (2003). Factor analytical approaches for evaluating groundwater trace element chemistry data. *Analytica Chimica Acta*, *490*(1–2), 123–138. https://doi.org/10.1016/S0003-2670(03)00350-7

Faulds, J. E., & Varga, R. J. (1998). The role of accommodation zones and transfer zones in the regional segmentation of extended terranes. *Special Paper of the Geological Society of America*, *323*, 1–45. https://doi.org/10.1130/0-8137-2323-X.1

Fentaw, B., Birhanu, B., Azagegn, T., & Abebe, B. (2024). *Journal of African Earth Sciences Groundwater recharge sources and mechanisms in the Ethiopian central Afar rift : Insights from isotopic and hydrogeochemical tracers* . *216*(April).

Ferede, M., Haile, A. T., Walker, D., Gowing, J., & Parkin, G. (2020). Multi-method groundwater recharge estimation at Eshito micro-watershed, Rift Valley Basin in Ethiopia. *Hydrological*

Sciences Journal, *65*(9), 1596–1605. https://doi.org/10.1080/02626667.2020.1762887

Fetter, C. . (2001). Applied Hydrogeology (4th Edition). In *Applied Hydrogeology* (Vol. 4, pp. 4–615).

Fiedler, F. R. (2003). Simple, Practical Method for Determining Station Weights Using Thiessen Polygons and Isohyetal Maps. *Journal of Hydrologic Engineering*, *8*(4), 219–221. https://doi.org/10.1061/(asce)1084-0699(2003)8:4(219)

Filgueiras, R., Almeida, T. S., Mantovani, E. C., Dias, S. H. B., Fernandes-Filho, E. I., da Cunha, F. F., & Venancio, L. P. (2020). Soil water content and actual evapotranspiration predictions using regression algorithms and remote sensing data. *Agricultural Water Management*, *241*(June), 106346. https://doi.org/10.1016/j.agwat.2020.106346

Fisher, R. S., & Mullican, W. F. (1997). Hydrochemical evolution of sodium-sulfate and sodium-chloride groundwater beneath the Northern Chihuahuan Desert, Trans-Pecos, Texas, USA. In *Hydrogeology Journal* (Vol. 5, Issue 2, pp. 4–16). https://doi.org/10.1007/s100400050102

Fritz, S. . et. a. (1994). Survey of CBE on Piblished Analyis of Potable Ground and Surface Waters. In *Groundwater* (Vol. 32, Issue 4, pp. 539–546).

Gaillardet, J., Dupre, B., Louvat, P., & Allegre, C. J. (1999). <van Rie et al. (1999).pdf>. *Chemical Geology*, *159*(8), 3–30.

Galliari, J., Santucci, L., Misseri, L., Carol, E., & Alvarez, M. del P. (2021). Processes controlling groundwater salinity in coastal wetlands of the southern edge of South America. *Science of the Total Environment*, *754*, 141951. https://doi.org/10.1016/j.scitotenv.2020.141951

Gamachu, D. (1977). *Aspects of Climate and Water Budget in Ethiopia*. Addis Ababa University Press. https://books.google.com.et/books?id=pTYLAQAAIAAJ

Ganvir, P. S. (2023). Hydro-Geochemical Plots : An Efficient Tool for the Elucidation of Groundwater Chemistry. *International Journal of Innovative Science and Research Technology*, *8*(2), 95–100.

Gebeyehu, A., & Ayenew, T. (2023). *Delineation of groundwater potential zones of the transboundary aquifers within the semiarid Bulal*. 1–25.

Gebeyehu, A., Ayenew, T., & Asrat, A. (2022). Journal of African Earth Sciences Hydrogeochemistry of the groundwater system of the transboundary basement and volcanic aquifers of the Bulal catchment , Southern Ethiopia. *Journal of African Earth Sciences*, *194*(May), 104622.

https://doi.org/10.1016/j.jafrearsci.2022.104622

Gebeyehu, A., Ayenew, T., & Asrat, A. (2023). Delineation of groundwater potential zones of the transboundary aquifers within the semiarid Bulal catchment, Southern Ethiopia. *Environmental Monitoring and Assessment*, *195*(4), 1–25. https://doi.org/10.1007/s10661-023-11088-x

Gebre, T., Ahmad, I., Dar, M. A., Gadissa, E., & Teka, A. H. (2018). *Mapping of groundwater potential zones using remote sensing and geographic information system : A case study of parts of Tigray , Ethiopia*. *4*(4), 133–140. https://doi.org/10.1306/eg.06181818001

Gebrie, T., & Getachew, G. (2019). Journal of Hydrology : Regional Studies Groundwater potential assessment using GIS and remote sensing : A case study of Guna tana landscape , upper blue Nile Basin , Ethiopia. *Journal of Hydrology: Regional Studies*, *24*(April), 100610. https://doi.org/10.1016/j.ejrh.2019.100610

Gidafie, D., Nedaw, D., & Azagegn, T. (2024). Groundwater for Sustainable Development Integrated remote sensing and geographic information system overlay analysis for groundwater potential evaluation using AHP and fuzzy AHP : Southern sections of the western Afar rift margin and associated rift floor. *Groundwater for Sustainable Development*, *26*(August), 101310. https://doi.org/10.1016/j.gsd.2024.101310

Gidafie, D., Nedaw, D., Azagegn, T., Abebe, B., & Baba, A. (2024). Journal of Hydrology : Regional Studies Evaluation of the source and mechanisms of groundwater recharge for the southern sections of the western Afar rift margin and associated rift floor. *Journal of Hydrology: Regional Studies*, *56*(September), 102037. https://doi.org/10.1016/j.ejrh.2024.102037

Gidafie, D., Tafesse, N. T., & Hagos, M. (2016). Estimation of groundwater recharge using water balance model: A case study in the Gerado basin, North Central Ethiopia. *International Journal of Earth Sciences and Engineering*, *9*(3), 942–950.

Gillham, R. W., & Farvolden, R. N. (1974). Sensitivity analysis of input parameters in numerical modeling of steady state regional groundwater flow. *Water Resources Research*, *10*(3), 529–538. https://doi.org/10.1029/WR010i003p00529

Giovanni, A., & Donnell, O. (2001). Impact of Human Activity on Groundwater Dynamics The International Association of Hydrological Sciences General Assembly of the International Union of. In *Iahs* (Vol. 269).

Glen, J. M. G., Egger, A. E., Ippolito, C., & Athens, N. (2013). Correlation of Geothermal Springs with Sub-Surface Fault Terminations Revealed by High-Resolution, UAV-Acquired Magnetic Data. *PROCEEDINGS, Thirty-Eighth Workshop on Geothermal Reservoir Engineering*, 1233–1242. http://pangea.stanford.edu/ERE/db/GeoConf/papers/SGW/2013/Glen.pdf

Glendon, W. G. E. E. (1988). *GROUNDWATER RECHARGE IN ARID REGIONS : REVIEW AND CRITIQUE OF ESTIMATION METHODS*. *2*(November 1987).

Glenn, E. P., Neale, C. M. U., Hunsaker, D. J., & Nagler, P. L. (2011). Vegetation index-based crop coefficients to estimate evapotranspiration by remote sensing in agricultural and natural ecosystems. *Hydrological Processes*, *25*(26), 4050–4062. https://doi.org/10.1002/hyp.8392

Glynn, P. D., & Plummer, L. N. (2005). Geochemistry and the understanding of ground-water systems. *Hydrogeology Journal*, *13*(1), 263–287. https://doi.org/10.1007/s10040-004-0429-y

Godfrey, S., & Hailemichael, G. (2016). Three-phase approach to improve deep groundwater supply availability in the Elidar District of Afar region of Ethiopia. *Journal of Water Sanitation and Hygiene for Development*, *6*(3), 414–424. https://doi.org/10.2166/washdev.2016.021

Gonzales, A. L., Nonner, J., Heijkers, J., & Uhlenbrook, S. (2009). Comparison of different base flow separation methods in a lowland catchment. *Hydrology and Earth System Sciences*, *13*(11), 2055–2068. https://doi.org/10.5194/hess-13-2055-2009

González-Trinidad, J., Pacheco-Guerrero, A., Júnez-Ferreira, H., Bautista-Capetillo, C., & Hernández-Antonio, A. (2017). Identifying groundwater recharge sites through environmental stable isotopes in an alluvial aquifer. *Water (Switzerland)*, *9*(8), 1–12. https://doi.org/10.3390/w9080569

Gouin, P. (1970). Seismic and gravity data from Afar in relation to surrounding areas. *Philosophical Transactions for the Royal Society of London. Series A, Mathematical and Physical Sciences*, *358*(May 1961), 339–358.

Grolander, S. (2009). R-09-47 Radon as a groundwater tracer in Forsmark and Laxemar. *Waste Management*.

GSE, G. of the W. area. (2010). *Basic Geoscience Mapping Core Process Geology of Debre Birhan Area*. *February*.

Hagag, W., & Obermeyer, H. (2017). Active Structures in Central Upper Rhine Graben, SW Germany: New Data from Landau Area using Electromagnetic Radiation (EMR) Technique and Cerescope.

Journal of Geology & Geophysics, *6*(5). https://doi.org/10.4172/2381-8719.1000303

Hagos, M., Konka, B., & Ahmed, J. (2016). A preliminary Geological and Generalized Stratigraphy of Western Margin of Northern Afar Depression, Dallol Area, Northern Ethiopia. *Momona Ethiopian Journal of Science*, *8*(1), 1. https://doi.org/10.4314/mejs.v8i1.1

Haile, M. M., Tafesse Yadeta, J., & Amena Gambe, L. (2022). Delineation of groundwater potential zones using geo-spatial and AHP techniques: Ambo area, Blue Nile Basin, Ethiopia. *Sustainable Water Resources Management*, *8*(1), 36. https://doi.org/10.1007/s40899-022-00622-3

Hamada, H. (1999). Analysis of the interaction between surface water and groundwater using radon-222. *Japan Agricultural Research Quarterly*, *33*(4), 261–265.

Hammond, J. O. S., Kendall, J. M., Stuart, G. W., Keir, D., Ebinger, C., Ayele, A., & Belachew, M. (2011). The nature of the crust beneath the Afar triple junction: Evidence from receiver functions. *Geochemistry, Geophysics, Geosystems*, *12*(12). https://doi.org/10.1029/2011GC003738

Hayward, N. J., & Ebinger, C. J. (1996). Variations in the along-axis segmentation of the Afar Rift system. *Tectonics*, *15*(2), 244–257. https://doi.org/10.1029/95TC02292

Healy, R. W., & Cook, P. G. (2002). Using groundwater levels to estimate recharge. *Hydrogeology Journal*, *10*(1), 91–109. https://doi.org/10.1007/s10040-001-0178-0

Hegeu, H., & Kshetrimayum, K. S. (2019). Hydrochemical characterization of groundwater in geomorphic units using graphical and multivariate statistical methods in the Dimapur valley, Northeast India. *Groundwater for Sustainable Development*, *8*, 484–500. https://doi.org/10.1016/j.gsd.2019.01.004

Hoffmann, J., & Sander, P. (2007). Remote sensing and GIS in hydrogeology. *Hydrogeology Journal*, *15*(1), 1–3. https://doi.org/10.1007/s10040-006-0140-2

Hofmann, C., Courtillot, V., Féraud, G., Rochette, P., Yirgu, G., Ketefo, E., & Pik, R. (1997). Timing of the ethiopian flood basalt event and implications for plume birth and global change. *Nature*, *389*(6653), 838–841. https://doi.org/10.1038/39853

Hsuen-chun, Y. I. N. (2009). *A composite method for estimating annual actual evapotranspiration*. *October 2014*, 37–41. https://doi.org/10.1080/02626668809491258

Huang, D., Wang, J., & Khayatnezhad, M. (2021). Estimation of Actual Evapotranspiration Using Soil

Moisture Balance and Remote Sensing. *Iranian Journal of Science and Technology - Transactions of Civil Engineering*, *45*(4), 2779–2786. https://doi.org/10.1007/s40996-020-00575-7

Huang, P., & Wang, X. (2017). Applying environmental isotope theory to groundwater recharge in the Jiaozuo mining area, China. *Geofluids*, *2017*. https://doi.org/10.1155/2017/9568349

Huizenga, J. M. (2011). Characterisation of the inorganic chemistry of surface waters in South Africa. *Water SA*, *37*(3), 401–410. https://doi.org/10.4314/wsa.v37i3.68491

Ibrahim-Bathis, K., & Ahmed, S. A. (2016). Geospatial technology for delineating groundwater potential zones in Doddahalla watershed of Chitradurga district, India. *Egyptian Journal of Remote Sensing and Space Science*, *19*(2), 223–234. https://doi.org/10.1016/j.ejrs.2016.06.002

Ikirri, M., Boutaleb, S., Ibraheem, I. M., Abioui, M., Echogdali, F. Z., Abdelrahman, K., Id-Belqas, M., Abu-Alam, T., El Ayady, H., Essoussi, S., & Faik, F. (2023). Delineation of Groundwater Potential Area using an AHP, Remote Sensing, and GIS Techniques in the Ifni Basin, Western Anti-Atlas, Morocco. *Water (Switzerland)*, *15*(7). https://doi.org/10.3390/w15071436

Imes, J. L., Plummer, Ln., Kleeschulte, M. J., & Schumacher, J. G. (2007). Recharge Area, Base-Flow and Quick-Flow Discharge Rates and Ages, and General Water Quality of Big Spring in Carter County, Missouri, 2000-04. *Scientific Investigations Report. U.S. Geological Survey*, 80. http://search.proquest.com/docview/904488741?accountid=13360%5Cnhttp://purdue-primo-prod.hosted.exlibrisgroup.com/openurl/PURDUE/purdue_services_page?url_ver=Z39.88-2004&rft_val_fmt=info:ofi/fmt:kev:mtx:book&genre=report&sid=ProQ:Aquatic+Science+%26+Fishe

Ishaku, J. M., Ahmed, A. S., & Abubakar, M. A. (2011). Assessment of groundwater quality using chemical indices and GIS mapping in Jada area, Northeastern Nigeria. *Journal of Earth Sciences and Geotechnical Engineering*, *1*(1), 1792–9660.

Jaafarzadeh, M. S., Tahmasebipour, N., Haghizadeh, A., Pourghasemi, H. R., & Rouhani, H. (2021). Groundwater recharge potential zonation using an ensemble of machine learning and bivariate statistical models. *Scientific Reports*, *11*(1), 1–18. https://doi.org/10.1038/s41598-021-85205-6

Jasechko, S. (2019). Global Isotope Hydrogeology—Review. *Reviews of Geophysics*, *57*(3), 835–965. https://doi.org/10.1029/2018RG000627

Jesiya, N. P., & Gopinath, G. (2020). A fuzzy based MCDM–GIS framework to evaluate groundwater

potential index for sustainable groundwater management - A case study in an urban-periurban ensemble, southern India. *Groundwater for Sustainable Development*, *11*, 100466. https://doi.org/10.1016/j.gsd.2020.100466

Jhariya, D. C., Kumar, T., Gobinath, M., Diwan, P., & Kishore, N. (2016). Assessment of groundwater potential zone using remote sensing, GIS and multi criteria decision analysis techniques. *Journal of the Geological Society of India*, *88*(4), 481–492. https://doi.org/10.1007/s12594-016-0511-9

Jie, Z., van Heyden, J., Bendel, D., & Barthel, R. (2011). Combination of soil-water balance models and water-table fluctuation methods for evaluation and improvement of groundwater recharge calculations. *Hydrogeology Journal*, *19*(8), 1487–1502. https://doi.org/10.1007/s10040-011-0772-8

Justin-Visentin, E., & Zanettin, B. (1974). Dike swarms, volcanism and tectonics of the western Afar margin along the Kombolcha-Eloa traverse (Ethiopia). *Bulletin Volcanologique*, *38*(1), 187–205. https://doi.org/10.1007/BF02597810

Kaewdum, N., & Chotpantarat, S. (2021). Mapping Potential Zones for Groundwater Recharge Using a GIS Technique in the Lower Khwae Hanuman Sub-Basin Area, Prachin Buri Province, Thailand. *Frontiers in Earth Science*, *9*(September), 1–16. https://doi.org/10.3389/feart.2021.717313

Kang, T., Lee, S., Lee, N., & Jin, Y. (2022). Baseflow Separation Using the Digital Filter Method: Review and Sensitivity Analysis. *Water (Switzerland)*, *14*(3), 1–14. https://doi.org/10.3390/w14030485

Karlović, I., Marković, T., & Vujnović, T. (2022). Groundwater recharge assessment using multi component analysis: Case study at the NW edge of the Varaždin Alluvial Aquifer, Croatia. *Water (Switzerland)*, *14*(1). https://doi.org/10.3390/w14010042

Kaur, L., Rishi, M. S., Sharma, S., Sharma, B., Lata, R., & Singh, G. (2019). Hydrogeochemical characterization of groundwater in alluvial plains of river Yamuna in northern India: An insight of controlling processes. *Journal of King Saud University - Science*, *31*(4), 1245–1253. https://doi.org/10.1016/j.jksus.2019.01.005

Kaur, L., Rishi, M. S., Singh, G., & Nath Thakur, S. (2020). Groundwater potential assessment of an alluvial aquifer in Yamuna sub-basin (Panipat region) using remote sensing and GIS techniques in conjunction with analytical hierarchy process (AHP) and catastrophe theory (CT). *Ecological Indicators*, *110*(October 2019), 105850. https://doi.org/10.1016/j.ecolind.2019.105850

Kazmin, V. G. (1991). The position of continental flood basalts in rift zones and its bearing on models of rifting. *Tectonophysics*, *199*(2–4), 375–387. https://doi.org/10.1016/0040-1951(91)90179-V

Kebede, S., Admasu, G., & Travi, Y. (2011). Estimating ungauged catchment flows from Lake Tana floodplains, Ethiopia: An isotope hydrological approach. *Isotopes in Environmental and Health Studies*, *47*(1), 71–86. https://doi.org/10.1080/10256016.2011.556724

Kebede, S., Travi, Y., Alemayehu, T., & Ayenew, T. (2005). Groundwater recharge, circulation and geochemical evolution in the source region of the Blue Nile River, Ethiopia. *Applied Geochemistry*, *20*(9), 1658–1676. https://doi.org/10.1016/j.apgeochem.2005.04.016

Kebede, S., Travi, Y., Asrat, A., Alemayehu, T., Ayenew, T., & Tessema, Z. (2008). Groundwater origin and flow along selected transects in Ethiopian rift volcanic aquifers. *Hydrogeology Journal*, *16*(1), 55–73. https://doi.org/10.1007/s10040-007-0210-0

Keegan-Treloar, R., Irvine, D. J., Solórzano-Rivas, S. C., Werner, A. D., Banks, E. W., & Currell, M. J. (2022). Fault-controlled springs: A review. *Earth-Science Reviews*, *230*(December 2021). https://doi.org/10.1016/j.earscirev.2022.104058

Kehali, A. T., Hagos, M., Anteneh, Z. L., & Bawoke, G. T. (2021). Structural controls on the emplacement of scoria cones and rhyolite domes of the western Afar margin, Ethiopia. *Geosciences Journal*, *25*(6), 831–847. https://doi.org/10.1007/s12303-021-0009-3

Kerdous, S. T., Anti-atlas, W., Benjmel, K., Amraoui, F., Aydda, A., Tahiri, A., & Yousif, M. (2022). A Multidisciplinary Approach for Groundwater Potential. *Water*, *14*(10), 1553. https://doi.org/10.3390/w14101553

Khan, M. Y. A., ElKashouty, M., Subyani, A. M., Tian, F., & Gusti, W. (2022). GIS and RS intelligence in delineating the groundwater potential zones in Arid Regions: a case study of southern Aseer, southwestern Saudi Arabia. *Applied Water Science*, *12*(1), 1–23. https://doi.org/10.1007/s13201-021-01535-w

Kieffer, B., Arndt, N., Lapierre, H., Bastien, F., Bosch, D., Pecher, A., Yirgu, G., Ayalew, D., Weis, D., Jerram, D. A., Keller, F., & Meugniot, C. (2004). Flood and shield basalts from Ethiopia: Magmas from the African superswell. *Journal of Petrology*, *45*(4), 793–834. https://doi.org/10.1093/petrology/egg112

King, A. C., Raiber, M., Cox, M. E., & Cendón, D. I. (2017). Comparaison de techniques d'estimation

de recharge des eaux souterraines pour un système aquifère alluvial lié à un cours d'eau temporaire (Queensland, Australie). *Hydrogeology Journal*, *25*(6), 1759–1777. https://doi.org/10.1007/s10040-017-1565-5

Kopáček, J., Hejzlar, J., & Mosello, R. (2000). Estimation of organic acid anion concentrations and evaluation of charge balance in atmospherically acidified colored waters. *Water Research*, *34*(14), 3598–3606. https://doi.org/10.1016/S0043-1354(00)00109-3

Koptev, A., Gerya, T., Calais, E., Leroy, S., & Burov, E. (2018). Afar triple junction triggered by plume-assisted bi-directional continental break-up. *Scientific Reports*, *8*(1), 1–7. https://doi.org/10.1038/s41598-018-33117-3

Kresic, N. (2009). *Groundwater Resources Sustainability,Management and Restoration*.

Kumar, C. P. (1997). *ISH Journal of Hydraulic ESTIMATION OF NATURAL*. *October 2013*, 37–41. https://doi.org/10.1080/09715010.1997.10514603

Kumar, M., Singh, P., & Singh, P. (2022). Integrating GIS and remote sensing for delineation of groundwater potential zones in Bundelkhand Region, India. *Egyptian Journal of Remote Sensing and Space Science*, *25*(2), 387–404. https://doi.org/10.1016/j.ejrs.2022.03.003

Kumar, T. J. R., Balasubramanian, A., Kumar, R. S., Dushiyanthan, C., Thiruneelakandan, B., Suresh, R., Karthikeyan, K., & Davidraju, D. (2016). Assessment of groundwater potential based on aquifer properties of hard rock terrain in the Chittar–Uppodai watershed, Tamil Nadu, India. *Applied Water Science*, *6*(2), 179–186. https://doi.org/10.1007/s13201-014-0216-4

Ladson, A. R., Brown, R., Neal, B., & Nathan, R. (2013). A standard approach to baseflow separation using the Lyne and Hollick filter. *Australian Journal of Water Resources*, *17*(1), 25–34. https://doi.org/10.7158/W12-028.2013.17.1

Le Gall, B., Daoud, M. A., Rolet, J., & Egueh, N. M. (2011). Large-scale flexuring and antithetic extensional faulting along a nascent plate boundary in the SE Afar rift. *Terra Nova*, *23*(6), 416–420. https://doi.org/10.1111/j.1365-3121.2011.01029.x

Liu, Y., & Yamanaka, T. (2012). Tracing groundwater recharge sources in a mountain-plain transitional area using stable isotopes and hydrochemistry. *Journal of Hydrology*, *464–465*, 116–126. https://doi.org/10.1016/j.jhydrol.2012.06.053

Liu, Z. (2022). Estimating land evapotranspiration from potential evapotranspiration constrained by soil

water at daily scale. *Science of the Total Environment*, *834*(March), 155327. https://doi.org/10.1016/j.scitotenv.2022.155327

Lott, D. A., & Stewart, M. T. (2016). Base flow separation: A comparison of analytical and mass balance methods. *Journal of Hydrology*, *535*, 525–533. https://doi.org/10.1016/j.jhydrol.2016.01.063

Machiwal, D., Jha, M. K., & Mal, B. C. (2011). Assessment of Groundwater Potential in a Semi-Arid Region of India Using Remote Sensing, GIS and MCDM Techniques. *Water Resources Management*, *25*(5), 1359–1386. https://doi.org/10.1007/s11269-010-9749-y

Mahamat, H. B., Coz, M. Le, Abderamane, H., Sardini, P., & Razack, M. (2017). Hydrochemical and Isotopic Characteristics of the Basement Aquifer in the Wadi Fira Area, Eastern Chad. *Journal of Water Resource and Protection*, *09*(13), 1688–1708. https://doi.org/10.4236/jwarp.2017.913105

Makris, J., & Ginzburg, A. (1987). The Afar Depression: transition between continental rifting and sea-floor spreading. *Tectonophysics*, *141*(1–3), 199–214. https://doi.org/10.1016/0040-1951(87)90186-7

Mallick, J., Singh, C. K., Al-Wadi, H., Ahmed, M., Rahman, A., Shashtri, S., & Mukherjee, S. (2015). Geospatial and geostatistical approach for groundwater potential zone delineation. *Hydrological Processes*, *29*(3), 395–418. https://doi.org/10.1002/hyp.10153

Manighetti, I., Zigone, D., Campillo, M., & Cotton, F. (1998). Self-similarity of the largest-scale segmentation of the faults: Implications for earthquake behavior. *Earth and Planetary Science Letters*, *288*(3–4), 370–381. https://doi.org/10.1016/j.epsl.2009.09.040

Mansour, M., Christelis, V., Upton, K., & Hughes, A. (2024). Simulation of Complex Groundwater Flow Processes in Low-Fidelity Radial Flow Model Using a Mathematical Representation of the Variation of Vertical Hydraulic Conductivity With Depth. *Hydrological Processes*, *38*(12), 1–12. https://doi.org/10.1002/hyp.70039

Manta, W. F., Hendrayana, H., & Amijaya, D. H. (2022). Determination of groundwater recharge area using environmental isotopes and hydrochemical data in Raimanuk area, East Nusa Tenggara. *IOP Conference Series: Earth and Environmental Science*, *1039*(1). https://doi.org/10.1088/1755-1315/1039/1/012006

Marandi, A., & Shand, P. (2018a). Groundwater chemistry and the Gibbs Diagram. *Applied*

Geochemistry, *97*(August), 209–212. https://doi.org/10.1016/j.apgeochem.2018.07.009

Marandi, A., & Shand, P. (2018b). Groundwater chemistry and the Gibbs Diagram. *Applied Geochemistry*, *97*, 209–212. https://doi.org/10.1016/j.apgeochem.2018.07.009

Margareth, H. (2017). No Title طرق دريس لغة الـ عربـ ية. *Экономика Региона*, 32.

Mart, P. (2019). *8a2Beff6535D2F3Cfd2Fe6Cbd0F1264B.Pdf*. https://doi.org/https://doi.org/10.1007/s10040-019-02001-3

Martín-Loeches, M., Reyes-López, J., Ramírez-Hernández, J., Temiño-Vela, J., & Martínez-Santos, P. (2018). Comparison of RS/GIS analysis with classic mapping approaches for siting low-yield boreholes for hand pumps in crystalline terrains. An application to rural communities of the Caimbambo province, Angola. *Journal of African Earth Sciences*, *138*, 22–31. https://doi.org/10.1016/j.jafrearsci.2017.10.025

Martínez, D. E., & Bocanegra, E. M. (2002). Hydrogeochemistry and cation-exchange processes in the coastal aquifer of Mar Del Plata, Argentina. *Hydrogeology Journal*, *10*(3), 393–408. https://doi.org/10.1007/s10040-002-0195-7

Mattivi, P., Franci, F., Lambertini, A., & Bitelli, G. (2019). TWI computation: a comparison of different open source GISs. *Open Geospatial Data, Software and Standards*, *4*(1). https://doi.org/10.1186/s40965-019-0066-y

Maxwell, S. L., & Culligan, B. K. (2009). Rapid separation method for emergency water and urine samples. *Journal of Radioanalytical and Nuclear Chemistry*, *279*(3), 901–907. https://doi.org/10.1007/s10967-008-7387-0

McCleskey, R. B., Nordstrom, D. K., Ryan, J. N., & Ball, J. W. (2012). A new method of calculating electrical conductivity with applications to natural waters. *Geochimica et Cosmochimica Acta*, *77*, 369–382. https://doi.org/10.1016/j.gca.2011.10.031

McCuen, R. H. (1973). The role of sensitivity analysis in hydrologic modeling. *Journal of Hydrology*, *18*(1), 37–53. https://doi.org/10.1016/0022-1694(73)90024-3

McDonald and Harbaugh. (n.d.). *A MODULAR THREE-DIMENSIONAL FLOW MODEL o o o o A MODULAR THREE-DIMENSIONAL*.

Mechal, A., Birk, S., Dietzel, M., Leis, A., Winkler, G., Mogessie, A., & Kebede, S. (2017).

Dynamique de l'écoulement des eaux souterraines dans le système aquifère complexe du bassin de la Rivière Gidabo (Rift éthiopien): une approche multi-proxy. *Hydrogeology Journal*, *25*(2), 519–538. https://doi.org/10.1007/s10040-016-1489-5

Mekonen, A. A., Berlie, A. B., & Ferede, M. B. (2020). Spatial and temporal drought incidence analysis in the northeastern highlands of Ethiopia. *Geoenvironmental Disasters*, *7*(1). https://doi.org/10.1186/s40677-020-0146-4

Mohamed, M. M., Parimalarenganayaki, S., Khan, Q., & Murad, A. (2021). Review on the use of environmental isotopes for groundwater recharge and evaporation studies in the GCC countries. *Groundwater for Sustainable Development*, *12*(January), 100546. https://doi.org/10.1016/j.gsd.2021.100546

Mohan, C., Western, A. W., Wei, Y., & Saft, M. (2018). Predicting groundwater recharge for varying land cover and climate conditions-a global meta-study. *Hydrology and Earth System Sciences*, *22*(5), 2689–2703. https://doi.org/10.5194/hess-22-2689-2018

Mohr, P. (1983). The morton-black hypothesis for the thinning of continental crust—revisited in western afar. *Developments in Geotectonics*, *19*(C), 509–528. https://doi.org/10.1016/B978-0-444-42198-2.50034-1

Mohr, P. (1987). Patterns of faulting in the Ethiopian rift valley. *Tectonophysics*, *143*(1–3), 169–179. https://doi.org/10.1016/0040-1951(87)90086-2

Mohr, P. A. (1971). Ethiopian Tertiary dike swarms. *Smithsonian Astrophysical Observatory Special Report 339*, *339*.

Mohr, P. A., & Potter, E. C. (1976). The sagatu ridge dike swarm, ethiopian rift margin. *Journal of Volcanology and Geothermal Research*, *1*(1), 55–71. https://doi.org/10.1016/0377-0273(76)90018-4

Molla, D. D., & Tegaye, T. A. (2019). "Multivariate analysis of baseflow index in complex rift margin catchments: The case of Abaya-Chamo lakes basin, southern Ethiopia." *Groundwater for Sustainable Development*, *9*(May), 100236. https://doi.org/10.1016/j.gsd.2019.100236

Moneim, A. A. A., Fernández-álvarez, J. P., Abu, E. M., Ella, E., & Masoud, A. M. (2016). *Groundwater Management at West El-Minia Desert Area , Egypt Using Numerical Modeling*. *July*, 66–76.

Monjerezi, M., Vogt, R. D., Aagaard, P., & Saka, J. D. K. (2011). Hydro-geochemical processes in an area with saline groundwater in lower Shire River valley, Malawi: An integrated application of hierarchical cluster and principal component analyses. *Applied Geochemistry*, *26*(8), 1399–1413. https://doi.org/10.1016/j.apgeochem.2011.05.013

Moore, I. D., Grayson, R. B., & Ladson, A. R. (1991). Digital terrain modelling: A review of hydrological, geomorphological, and biological applications. *Hydrological Processes*, *5*(1), 3–30. https://doi.org/10.1002/hyp.3360050103

Morley, C.K., Ngenoh, D.K., Ego, J. . (1999). Introduction to the East African Rift System. *Geoscience of Rift Systems - Evolution of East Africa*, *44*, 1–18.

Morton, F. I. (1983). Operational estimates of areal evapotranspiration and their significance to the science and practice of hydrology. *Journal of Hydrology*, *66*(1–4), 1–76. https://doi.org/10.1016/0022-1694(83)90177-4

Mozafari, M. (2022). *Transverse structures.pdf*.

Mueller, A. V. (2012). *Development of a Combined Multi-Sensor/Signal Processing Architecture for Improved In-Situ Quantification of the Charge Balance of Natural Waters*.

Muirhead, J. D., Wright, L. J. M., & Scholz, C. A. (2019). Rift evolution in regions of low magma input in East Africa. *Earth and Planetary Science Letters*, *506*, 332–346. https://doi.org/10.1016/j.epsl.2018.11.004

Muralitharan, J., & Palanivel, K. (2015). Groundwater targeting using remote sensing, geographical information system and analytical hierarchy process method in hard rock aquifer system, Karur district, Tamil Nadu, India. *Earth Science Informatics*, *8*(4), 827–842. https://doi.org/10.1007/s12145-015-0213-7

Naderi Peikam, E., & Jalali, M. (2016). Application of inverse geochemical modelling for predicting surface water chemistry in Ekbatan watershed, Hamedan, western Iran. *Hydrological Sciences Journal*, *61*(6), 1124–1134. https://doi.org/10.1080/02626667.2015.1016947

Nagaraju, A., Thejaswi, A., & Sreedhar, Y. (2016). Assessment of Groundwater Quality of Udayagiri area, Nellore District, Andhra Pradesh, South India Using Multivariate Statistical Techniques. *Earth Sciences Research Journal*, *20*(4), 1. https://doi.org/10.15446/esrj.v20n4.54555

Nampak, H., Pradhan, B., & Manap, M. A. (2014). Application of GIS based data driven evidential

belief function model to predict groundwater potential zonation. *Journal of Hydrology*, *513*, 283–300. https://doi.org/10.1016/j.jhydrol.2014.02.053

Nandimandalam, J. R. (2012). Evaluation of hydrogeochemical processes in the Pleistocene aquifers of Middle Ganga Plain, Uttar Pradesh, India. *Environmental Earth Sciences*, *65*(4), 1291–1308. https://doi.org/10.1007/s12665-011-1377-1

Napitupulu, D., Abdel Kadar, J., & Kartika Jati, R. (2017). Validity testing of technology acceptance model based on factor analysis approach. *Indonesian Journal of Electrical Engineering and Computer Science*, *5*(3), 697–704. https://doi.org/10.11591/ijeecs.v5.i3.pp697-704

Nimmo, J. R., Horowitz, C., & Mitchell, L. (2015). Discrete-storm water-table fluctuation method to estimate episodic recharge. *Groundwater*, *53*(2), 282–292. https://doi.org/10.1111/gwat.12177

Obuobie, E., Diekkrueger, B., Agyekum, W., & Agodzo, S. (2012). Groundwater level monitoring and recharge estimation in the White Volta River basin of Ghana. *Journal of African Earth Sciences*, *71–72*, 80–86. https://doi.org/10.1016/j.jafrearsci.2012.06.005

Okiongbo, K. S., & Douglas, R. K. (2015). Evaluation of major factors influencing the geochemistry of groundwater using graphical and multivariate statistical methods in Yenagoa city, Southern Nigeria. *Applied Water Science*, *5*(1), 27–37. https://doi.org/10.1007/s13201-014-0166-x

Onyekuru, S. O. (2010). *Chemical Characteristics of Groundwater Systems in the Southern Anambra Basin , Nigeria*. *6*(12), 2164–2172.

P.J.M. van LAARHOVEN* and W.PEDRYCz. (1983). Delft University. *Fuzzy Sets and Systems*, *11*, 229–241. https://doi.org/https://doi.org/10.1016/S0165-0114(83)80082-7

Pagli, C., Yun, S. H., Ebinger, C., Keir, D., & Wang, H. (2019). Strike-slip tectonics during rift linkage. *Geology*, *47*(1), 31–34. https://doi.org/10.1130/G45345.1

Pagnozzi, M., Coletta, G., Leone, G., Catani, V., & Esposito, L. (2020). *applied sciences A Steady-State Model to Simulate Groundwater Flow in Unconfined Aquifer*. 1–24.

Pande, C. B., Moharir, K. N., Singh, S. K., & Varade, A. M. (2020). An integrated approach to delineate the groundwater potential zones in Devdari watershed area of Akola district, Maharashtra, Central India. *Environment, Development and Sustainability*, *22*(5), 4867–4887. https://doi.org/10.1007/s10668-019-00409-1

Pande, S. F. R. K. C. (2016). Ground water flow modeling for calibrating steady state using MODFLOW software : a case study of Mahesh River basin , India. *Modeling Earth Systems and Environment*, *2*(1), 1–17. https://doi.org/10.1007/s40808-015-0049-7

Panigrahi, K., & Das, B. (2022). Groundwater quality assessment and hydro-geological investigation in Atal Nagar, Chhattisgarh, India. *Journal of Geosciences Research*, *7*(1), 104–111. https://doi.org/10.1007/987-981-16-7373-3

Pazhuparambil Jayarajan, S. K., Schneider, M., & Lakshmanan, E. (2022). Estimation of natural groundwater recharge in Chennai River basin using multiple approaches. *Hydrological Sciences Journal*, *67*(8), 1165–1184. https://doi.org/10.1080/02626667.2022.2064223

Penkova, N. V, & Shiklomanov, I. A. (2007). Water Balance Methodology for indirect assessment and prediction of basin water yield under human-induced land use changes. *Proceedings of the PUB Kick-off 2002*, *309*, 74–84.

Penner, G. C., Araujo Martins, R. T. A., Rodrigues, S., & Wendland, E. (2023). Uncertainty in groundwater recharge estimation using groundwater level fluctuation and aquifer test. *Revista Brasileira de Recursos Hidricos*, *28*, 1–8. https://doi.org/10.1590/2318-0331.282320220113

Prabu, P., & Rajagopal, B. (2013). Mapping of Lineaments for Groundwater Targeting and Sustainable Water Resource Management in Hard Rock Hydrogeological Environment Using RS- GIS. *Climate Change and Regional/Local Responses*, *1976*. https://doi.org/10.5772/55702

Pradhan, R. M., Behera, A. K., Kumar, S., Kumar, P., & Biswal, T. K. (2022). Recharge and Geochemical Evolution of Groundwater in Fractured Basement Aquifers (NW India): Insights from Environmental Isotopes (δ18 O, δ2 H, and3 H) and Hydrogeochemical Studies. *Water (Switzerland)*, *14*(3). https://doi.org/10.3390/w14030315

Prasad, R. K., Mondal, N. C., Banerjee, P., Nandakumar, M. V., & Singh, V. S. (2008). Deciphering potential groundwater zone in hard rock through the application of GIS. *Environmental Geology*, *55*(3), 467–475. https://doi.org/10.1007/s00254-007-0992-3

Priya, U., Iqbal, M. A., Salam, M. A., Uddin, M. F., Reza, A., Islam, T., & Sarkar, S. K. (2022). *Sustainable Groundwater Potential Zoning with Integrating GIS , Remote Sensing , and AHP Model : A Case from*. https://doi.org/https://doi.org/10.3390/su14095640

Putman, A. L., Fiorella, R. P., Bowen, G. J., & Cai, Z. (2019). A Global Perspective on Local Meteoric

Water Lines: Meta-analytic Insight Into Fundamental Controls and Practical Constraints. *Water Resources Research*, *55*(8), 6896–6910. https://doi.org/10.1029/2019WR025181

Quej, V. H., Almorox, J., Arnaldo, J. A., & Moratiel, R. (2019). *Evaluation of Temperature-Based Methods for the Estimation of Reference Evapotranspiration in the Yucatán Peninsula , Mexico*. *24*(2), 1–10. https://doi.org/10.1061/(ASCE)HE.1943-5584.0001747

Radulović, M., Brdar, S., Mesaroš, M., Lukić, T., Savić, S., Basarin, B., Crnojević, V., & Pavić, D. (2022). Assessment of Groundwater Potential Zones Using GIS and Fuzzy AHP Techniques—A Case Study of the Titel Municipality (Northern Serbia). *ISPRS International Journal of Geo-Information*, *11*(4). https://doi.org/10.3390/ijgi11040257

Rahaman, S. A., Ajeez, S. A., Aruchamy, S., & Jegankumar, R. (2015). Prioritization of Sub Watershed Based on Morphometric Characteristics Using Fuzzy Analytical Hierarchy Process and Geographical Information System – A Study of Kallar Watershed, Tamil Nadu. *Aquatic Procedia*, *4*(Icwrcoe), 1322–1330. https://doi.org/10.1016/j.aqpro.2015.02.172

Raiber, M., White, P. A., Daughney, C. J., Tschritter, C., Davidson, P., & Bainbridge, S. E. (2012). Three-dimensional geological modelling and multivariate statistical analysis of water chemistry data to analyse and visualise aquifer structure and groundwater composition in the Wairau Plain, Marlborough District, New Zealand. *Journal of Hydrology*, *436–437*, 13–34. https://doi.org/10.1016/j.jhydrol.2012.01.045

Rajesh, J., Pande, C. B., Kadam, S. A., Gorantiwar, S. D., & Shinde, M. G. (2021). Exploration of groundwater potential zones using analytical hierarchical process (AHP) approach in the Godavari river basin of Maharashtra in India. *Applied Water Science*, *11*(12), 1–11. https://doi.org/10.1007/s13201-021-01518-x

Rane, N., Choudhary, S. P., & Giduturi, M. (2023). *Efficiency and Capability of Remote Sensing (RS) and Geographic Information Systems (GIS): A Powerful Tool for Sustainable Groundwater Management*. *April*. https://doi.org/10.5281/zenodo.7845332

Ravikumar, P., & Somashekar, R. K. (2017). Principal component analysis and hydrochemical facies characterization to evaluate groundwater quality in Varahi river basin, Karnataka state, India. *Applied Water Science*, *7*(2), 745–755. https://doi.org/10.1007/s13201-015-0287-x

Ravikumar, P., Somashekar, R. K., & Prakash, K. (2015). A comparative study on usage of Durov and Piper diagrams to interpret hydrochemical processes in groundwater from SRLIS river basin,

Karnataka, India. *Elixir Earth Science*, *80*(March), 31073–31077. https://www.researchgate.net/publication/273886861

Razandi, Y., Pourghasemi, H. R., & Neisani, N. S. (2015). *Application of analytical hierarchy process , frequency ratio , and certainty factor models for groundwater potential mapping using GIS*. https://doi.org/10.1007/s12145-015-0220-8

Razi, M. H., Wilopo, W., & Putra, D. P. E. (2024). Hydrogeochemical evolution and water–rock interaction processes in the multilayer volcanic aquifer of Yogyakarta-Sleman Groundwater Basin, Indonesia. *Environmental Earth Sciences*, *83*(6). https://doi.org/10.1007/s12665-024-11477-6

Regasa, M. S., Nones, M., & Adeba, D. (2021). A review on land use and land cover change in ethiopian basins. *Land*, *10*(6). https://doi.org/10.3390/land10060585

Reilly, B. T. E., & Harbaugh, A. W. (1999). *Guidelines for Evaluating Ground-Water Flow Models Different Modeling Approaches to Address*.

Rezende, D., Nishi, L., Coldebella, P. F., Mantovani, D., Soares, P. F., Carlos Valim Junior, N., Vieira, A. M. S., & Bergamasco, R. (2019). Evaluation of the groundwater quality and hydrogeochemistry characterization using multivariate statistics methods: Case study of a hydrographic basin in Brazil. *Desalination and Water Treatment*, *161*, 203–215. https://doi.org/10.5004/dwt.2019.24269

Robson, A. G., Holford, S. P., King, R. C., & Kulikowski, D. (2018). Structural evolution of horst and half-graben structures proximal to a transtensional fault system determined using 3D seismic data from the Shipwreck Trough, offshore Otway Basin, Australia. *Marine and Petroleum Geology*, *89*(October 2017), 615–634. https://doi.org/10.1016/j.marpetgeo.2017.10.028

Rooney, T. O. (2017). The Cenozoic magmatism of East-Africa: Part I — Flood basalts and pulsed magmatism. *Lithos*, *286–287*, 264–301. https://doi.org/10.1016/j.lithos.2017.05.014

Rooney, T. O. (2020). The Cenozoic magmatism of East Africa: Part IV – The terminal stages of rifting preserved in the Northern East African Rift System. *Lithos*, *360–361*, 105381. https://doi.org/10.1016/j.lithos.2020.105381

SAATY, R. W. (1980). *THE ANALYTIC HIERARCHY PROCESS-WHAT AND HOW IT IS USED*. *9*(3), 161–176.

Saaty, T. L. (1977). A scaling method for priorities in hierarchical structures. *Journal of Mathematical Psychology*, *15*(3), 234–281. https://doi.org/10.1016/0022-2496(77)90033-5

Sacchi, G., Dipartimento, I., Universitario, C., Chieti, U., Siena, U., Laterina, V., Vecchi, V. V., Giovanni, S., & Ar, V. (2006). structural and geomorphological constraints lp Ik. *Society*, 191–207.

Salem, Ali et.al, 2019. (n.d.). Assessment of Groundwater Recharge , Evaporation , and Runoff in the Drava Basin in Hungary with the WetSpass Model. *Hydrology*, 1–11. https://doi.org/10.3390/hydrology6010023

Santos, C. N. (2022). *Monthly potential evapotranspiration estimated using the Thornthwaite method with gridded climate datasets for Rio de Janeiro state , Brazil*.

Sayadi, M. H., Rezaei, A., Sayadi, M. H., Rezaei, A., Rezaei, M. R., & Nourozi, K. (2014). Multivariate statistical analysis of surface water chemistry: A case study of Gharasoo River, Iran. *Proceedings of the International Academy of Ecology and Environmental Sciences*, *4*(3), 114–122. www.iaees.org

Sayyed, M. R. G., Wagh, G. S., & Supekar, A. (2013). Assessment of impact on the groundwater quality due to urbanization by hydrogeochemical facies analysis in SE part of Pune city, India. *Proceedings of the International Academy of Ecology and Environmental Sciences*, *3*(2), 148–159. www.iaees.org

Scanlon, B. R., Healy, R. W., & Cook, P. G. (2002). Choosing appropriate techniques for quantifying groundwater recharge. *Hydrogeology Journal*, *10*(1), 18–39. https://doi.org/10.1007/s10040-001-0176-2

Scanlon, B. R., Reedy, R. C., Stonestrom, D. A., Prudic, D. E., & Dennehy, K. F. (2005). Impact of land use and land cover change on groundwater recharge and quality in the southwestern US. *Global Change Biology*, *11*(10), 1577–1593. https://doi.org/10.1111/j.1365-2486.2005.01026.x

Schilling, K. E., Langel, R. J., Wolter, C. F., & Arenas-Amado, A. (2021). Using baseflow to quantify diffuse groundwater recharge and drought at a regional scale. *Journal of Hydrology*, *602*(July), 126765. https://doi.org/10.1016/j.jhydrol.2021.126765

Seeyan, S. (2020). *Groundwater Flow Modeling for Qushtapa Plain Unconfined Aquifer in Southern Erbil Basin , Kurdistan Region , Iraq*. 116–132. https://doi.org/10.4236/gep.2020.83009

Şen, Z., & Altunkaynak, A. (2006). A comparative fuzzy logic approach to runoff coefficient and runoff estimation. *Hydrological Processes*, *20*(9), 1993–2009. https://doi.org/10.1002/hyp.5992

Shen, S. L., Wu, Y. X., Xu, Y. S., Hino, T., & Wu, H. N. (2015). Evaluation of hydraulic parameters from pumping tests in multi-aquifers with vertical leakage in Tianjin. *Computers and Geotechnics*, *68*, 196–207. https://doi.org/10.1016/j.compgeo.2015.03.011

Shkeer, A. S., & Awang, Z. (2019). Exploring the Items for Measuring the Marketing Information System Construct: an Exploratory Factor Analysis. *International Review of Management and Marketing*, *9*(6), 87–97. https://doi.org/10.32479/irmm.8622

Shrestha, N. (2021). Factor Analysis as a Tool for Survey Analysis. *American Journal of Applied Mathematics and Statistics*, *9*(1), 4–11. https://doi.org/10.12691/ajams-9-1-2

Sibanda, T., Nonner, J. C., & Uhlenbrook, S. (2009). Comparison of groundwater recharge estimation methods for the semi-arid Nyamandhlovu area, Zimbabwe. *Hydrogeology Journal*, *17*(6), 1427–1441. https://doi.org/10.1007/s10040-009-0445-z

Somaratne, N., & Smettem, K. R. J. (2014). *Theory of the generalized chloride mass balance method for recharge estimation in groundwater basins characterised by point and di ff use recharge*. 307–332. https://doi.org/10.5194/hessd-11-307-2014

Sørensen, R., Zinko, U., & Seibert, J. (2006). On the calculation of the topographic wetness index: Evaluation of different methods based on field observations. *Hydrology and Earth System Sciences*, *10*(1), 101–112. https://doi.org/10.5194/hess-10-101-2006

Souza, E. L. de, Galvao, P., Almeida, R. de, Pinheiro, C., Baessa, M., & Cabral, M. (2015). Stable Isotopes Studies in the Urucu Oil Province, Amazon Region, Brazil. *Journal of Water Resource and Protection*, *07*(03), 131–142. https://doi.org/10.4236/jwarp.2015.73011

Springer, A. E., Stevens, L. E., Anderson, D. E., Parnell, R. A., Kreamer, D. K., Levin, L., & Flora, S. P. (2008). *A comprehensive springs classification system: Integrating geomorphic, hydrogeochemical, and ecological criteria. In: Stevens, L.E. and V. J. Meretsky, editors. Aridland Springs in North America: Ecology and Conservation. University of Arizona Press, Tucs*. 49–75.

Srivastava, P. K., & Bhattacharya, A. K. (2006). Groundwater assessment through an integrated approach using remote sensing, GIS and resistivity techniques: A case study from a hard rock terrain. *International Journal of Remote Sensing*, *27*(20), 4599–4620. https://doi.org/10.1080/01431160600554983

Stab, M., Bellahsen, N., Pik, R., Quidelleur, X., Ayalew, D., & Leroy, S. (2016). Modes of rifting in

magma-rich settings: Tectono-magmatic evolution of Central Afar. *Tectonics*, *35*(1), 2–38. https://doi.org/10.1002/2015TC003893

Subyani, A., & Sen, Z. (2006). *Refined chloride mass-balance method and its application*. *4380*(October), 4373–4380. https://doi.org/10.1002/hyp.6172

Surinaidu, L., Rahman, A., & Ahmed, S. (2021). Distributed groundwater recharge potentials assessment based on GIS model and its dynamics in the crystalline rocks of South. *Scientific Reports*, 1–16. https://doi.org/10.1038/s41598-021-90898-w

Tadesse, E., Azagegn, T., & Alemayehu, T. (2023). Characterizing groundwater and surface water interaction using geological, environmental tracers (222Rn, EC, δ18O, and δ2H) and baseflow index methods for part of the Upper Awash and the adjacent Blue Nile Basin, Ethiopia. *Journal of African Earth Sciences*, *205*, 104992. https://doi.org/10.1016/j.jafrearsci.2023.104992

Taesombat, W., & Sriwongsitanon, N. (2009). Areal rainfall estimation using spatial interpolation techniques. *ScienceAsia*, *35*(3), 268–275. https://doi.org/10.2306/scienceasia1513-1874.2009.35.268

Tanasković, I., Golobocanin, D., & Miljević, N. (2012). Multivariate statistical analysis of hydrochemical and radiological data of Serbian spa waters. *Journal of Geochemical Exploration*, *112*(14), 226–234. https://doi.org/10.1016/j.gexplo.2011.08.014

Tesfaye, S., Harding, D. J., & Kusky, T. M. (2003). Early continental breakup boundary and migration of the Afar triple junction, Ethiopia. *Bulletin of the Geological Society of America*, *115*(9), 1053–1067. https://doi.org/10.1130/B25149.1

Texier, J., Gonçalvès, J., Stieglitz, T., Vallet-Coulomb, C., Labille, J., Marc[2], V., Poulain[2], A., & Dussouillez[2], P. (2024). *Groundwater-Surface water exchanges in an alluvial plain subjected to pumping: a coupled multitracer and modeling approach*. *January*, 1–28. https://doi.org/10.5194/hess-2023-239

Thapa, R., Gupta, S., Guin, S., & Kaur, H. (2018). Sensitivity analysis and mapping the potential groundwater vulnerability zones in Birbhum district, India: A comparative approach between vulnerability models. *Water Science*, *32*(1), 44–66. https://doi.org/10.1016/j.wsj.2018.02.003

Thomas, J. M., & Rose, T. P. (2003). Environmental isotopes in hydrogeology. In *Environmental Geology* (Vol. 43, Issue 5). https://doi.org/10.1029/99eo00169

Tiercelin, J. J. (1986). The Pliocene Hadar Formation, Afar depression of Ethiopia. *Geological Society Special Publication*, *25*(25), 221–240. https://doi.org/10.1144/GSL.SP.1986.025.01.19

Tilahun, K., & Merkel, B. J. (2009). Estimation of groundwater recharge using a GIS-based distributed water balance model in Dire Dawa, Ethiopia. *Hydrogeology Journal*, *17*(6), 1443–1457. https://doi.org/10.1007/s10040-009-0455-x

Tiouiouine, A., Jabrane, M., Kacimi, I., Morarech, M., Bouramtane, T., Bahaj, T., Yameogo, S., Rezende-Filho, A. T., Dassonville, F., Moulin, M., Valles, V., & Barbiero, L. (2020). Determining the relevant scale to analyze the quality of regional groundwater resources while combining groundwater bodies, physicochemical and biological databases in southeastern france. *Water (Switzerland)*, *12*(12), 1–21. https://doi.org/10.3390/w12123476

Tobias, S., & Carlson, J. E. (1969). Brief report: Bartlett's test of sphericity and chance findings in factor analysis. *Multivariate Behavioral Research*, *4*(3), 375–377. https://doi.org/10.1207/s15327906mbr0403_8

Tyner, J. S., Brown, G. O., Vogel, J. R., & Garbrecht, J. (1999). *C HLORIDE M ASS B ALANCE TO D ETERMINE W ATER F LUXES BENEATH KCl F ERTILIZED C ROPS*. *43*(6), 1553–1559.

Uemura, Y. (1994). *FAULTING IN THE AREA AND ACTIVE SURROUNDING RIFT*. *3*.

Ul Hadia, N., Abdullah, N., & Sentosa, I. (2016). An Easy Approach to Exploratory Factor Analysis: Marketing Perspective. *Journal of Educational and Social Research*, *6*(1), 215–223. https://doi.org/10.5901/jesr.2016.v6n1p215

VANUM, G. (2012). *ISSN : 2249-5894 IDENTIFICATION OF GROUNDWATER TYPE AND ISSN : 2249-5894*. *2*(9), 578–595.

Varade, A. M., Yenkie, R. O., Shende, R. R., Golekar, R. B., Wagh, V. M., Khandare, H. W., & Janardan, M. (2018). Assessment of Water Quality for the Groundwater Resources of Urbanized Part of the Nagpur District, Maharashtra (India). *American Journal of Water Resources*, *6*(3), 89–111. https://doi.org/10.12691/ajwr-6-3-1

Varet, J., & et al. (2018). Geology of Afra (East Africa). In *English* (Vol. 1). https://doi.org/https://doi.org/10.1007/978-3-319-60865-5

Vázquez-Suñé, E., Carrera, J., Tubau, I., Sánchez-Vila, X., & Soler, A. (2010). An approach to identify urban groundwater recharge. *Hydrology and Earth System Sciences*, *14*(10), 2085–2097.

https://doi.org/10.5194/hess-14-2085-2010

Volcke, E. I. P., Hulle, S. Van, Deksissa, T., & Zaher, U. (2005). *Calculation of pH and concentration of equilibrium components during dynamic simulation by means of a charge balance*. *32*(9).

Weatherl, R. K., Henao Salgado, M. J., Ramgraber, M., Moeck, C., & Schirmer, M. (2021). Estimating surface runoff and groundwater recharge in an urban catchment using a water balance approach. *Hydrogeology Journal*, *29*(7), 2411–2428. https://doi.org/10.1007/s10040-021-02385-1

Williams, C. A., Reichstein, M., Buchmann, N., Baldocchi, D., Beer, C., Schwalm, C., Wohlfahrt, G., Hasler, N., Bernhofer, C., Foken, T., Papale, D., Schymanski, S., & Schaefer, K. (2012). Climate and vegetation controls on the surface water balance: Synthesis of evapotranspiration measured across a global network of flux towers. *Water Resources Research*, *48*(6), 1–13. https://doi.org/10.1029/2011WR011586

Wilopo, W., Putra, D. P. E., Setiawan, H., & Susatio, R. (2019). Groundwater flow patterns and hydrochemical facies of Kendal groundwater basin, Central Java Province, Indonesia. *IOP Conference Series: Earth and Environmental Science*, *361*(1). https://doi.org/10.1088/1755-1315/361/1/012002

Wolde, B. (1989). Cenozoic volcanism and riftdevelopment in Ethiopia. *Journal of African Earth Sciences*, *8*(1), 99–105. https://doi.org/10.1016/S0899-5362(89)80014-4

Wolfenden, E., Ebinger, C., Yirgu, G., Renne, P. R., & Kelley, S. P. (2005). Evolution of a volcanic rifted margin: Southern Red Sea, Ethiopia. *Bulletin of the Geological Society of America*, *117*(7–8), 846–864. https://doi.org/10.1130/B25516.1

WWDSE. (2018). *Federal Democratic Republic of Ethiopia DRLSP-I : FEASIBILITY STUDY , DESIGN AND PREPARATION OF CONTRACT DRSLP- I Afar Region Feasibility study VOLUME III - Hydrogeological Study Report*.

WWDSE, 2017. (2017). *Kobo-Chefa HYDROLOGICAL STUDY*.

Xu, Y., & Beekman, H. E. (2003). Groundwater Recharge Estimation in Southern Africa Edited by Printed in Cape Town. In *Challenges* (Vol. 64, Issue 64).

Yang, J., Yu, Z., Yi, P., Frape, S. K., Gong, M., & Zhang, Y. (2020). Evaluation of surface water and groundwater interactions in the upstream of Kui river and Yunlong lake, Xuzhou, China. *Journal of Hydrology*, *583*(1), 124549. https://doi.org/10.1016/j.jhydrol.2020.124549

Yenehun, A., Dessie, M., Nigate, F., Belay, A. S., Azeze, M., Camp, M. Van, Taye, D. F., Kidane, D., Adgo, E., Nyssen, J., Griensven, A. Van, & Walraevens, K. (2022). Spatial and temporal simulation of groundwater recharge and cross-validation with point estimations in volcanic aquifers with variable topography. *Journal of Hydrology: Regional Studies*, *42*(December), 101142. https://doi.org/10.1016/j.ejrh.2022.101142

Yin, L., Hu, G., Huang, J., Wen, D., Dong, J., Wang, X., & Li, H. (2011). Groundwater-recharge estimation in the Ordos Plateau, China: Comparison of methods. *Hydrogeology Journal*, *19*(8), 1563–1575. https://doi.org/10.1007/s10040-011-0777-3

Yitbarek, A., Razack, M., Ayenew, T., Zemedagegnehu, E., & Azagegn, T. (2012). Hydrogeological and hydrochemical framework of Upper Awash River basin, Ethiopia: With special emphasis on inter-basins groundwater transfer between Blue Nile and Awash Rivers. *Journal of African Earth Sciences*, *65*, 46–60. https://doi.org/10.1016/j.jafrearsci.2012.01.002

Younes, A. I., & McClay, K. (2002). Development of accomodation zones in the gulf of Suez-Red Sea rift, Egypt. *AAPG Bulletin*, *86*(6), 1003–1026. https://doi.org/10.1306/61eedc10-173e-11d7-8645000102c1865d

Zwaan, F., Corti, G., Keir, D., & Sani, F. (2020a). A review of tectonic models for the rifted margin of Afar: Implications for continental break-up and passive margin formation. *Journal of African Earth Sciences*, *164*. https://doi.org/10.1016/j.jafrearsci.2019.103649

Zwaan, F., Corti, G., Keir, D., & Sani, F. (2020b). Analogue modelling of marginal flexure in Afar, East Africa: Implications for passive margin formation. *Tectonophysics*, *796*(April). https://doi.org/10.1016/j.tecto.2020.228595

Zwaan, F., Corti, G., Sani, F., Keir, D., Muluneh, A. A., Illsley-Kemp, F., & Papini, M. (2020a). Structural Analysis of the Western Afar Margin, East Africa: Evidence for Multiphase Rotational Rifting. *Tectonics*, *39*(7), 1–25. https://doi.org/10.1029/2019TC006043

Zwaan, F., Corti, G., Sani, F., Keir, D., Muluneh, A. A., Illsley-Kemp, F., & Papini, M. (2020b). Structural Analysis of the Western Afar Margin, East Africa: Evidence for Multiphase Rotational Rifting. *Tectonics*, *39*(7). https://doi.org/10.1029/2019TC006043

Appendices

Appendices 1: Borehole Data

Well_ID	E	N	Elev	Depth (m)	Q (lit/sec)	SWL	DWL	DD	K (m/day)	T (m2/d)	S.cap	Head (m)
Daleti(Gelaelo)	627186	1108376	1003	347	3.5	183.65	196.64	12.99	12	241.75	23.28	819.35
Asaharanadintu	636096	1176883	915	180	10	124.5	126.56	2.06	4.4	144	419.42	790.5
Eablidaar	629641	1187504	1012	85	1.15	16.67	73.75	57.08	0.563	78	1.74	995.33
Adadlehengeg	605695	1106414	1173	172	25	7.32	60.21	52.89	30	89	40.84	1165.68
AFTUHA	634712	1117380	870	414	5.5	135.94	136.81	0.87	600	170	546.21	734.06
HaPW-1	654458	1060694	890	300	0	295	300	5	x	x	0	595
Hugub	617470	1039252	761	136	30	22.24	31.3	9.06	219	72	286.09	738.76
KELAT BURI	643874	1042796	755	101	28.8	18.88	27.1	8.22	1930	68.8	302.72	736.12
Dengelegita	649387	1115566	712	92	3	12	85	73	x	67	3.55	700
Mederale#1	629386	1206345	870	195	0.78	7.6	103.95	96.35	0.266	120	0.7	862.4
Mederale #2	625460	1205803	936	188	14	3.6	51.11	47.51	23	136	25.46	932.4
Mereburi	650880	108740	584	120	22	21.64	22.73	1.09	3460	66	1743.85	562.36
Amma#2	649945	1155557	618	150	16.5	28.15	41.64	13.49	108	102	105.68	589.85
BPW-1	617956	1075548	851	102	13.5	24.6	39.12	14.52	150	86	80.33	826.4
DRLP1W-06-18	666420	1138650	562	408	0	x	x	8	x	x	0	#VALUE!
Elebha	621891	1130065	1167	114	16	24.48	34.86	10.38	159	89.2	133.18	1142.52
Endufo	694087	1165632	792	440	0	430	440	10	xx	x	0	362
Elwaha	653040	1245272	685	554	10	108.3	250	141.7	148	x	6.1	576.7
Woranso	666550	1248762	616	392	6.98	169.98	270	100.02	296	x	6.03	446.02
Aftuha	626783	1118436	1027	88	5	61.18	78	16.82	3240	x	25.68	965.82
Leleeda	623503	1135394	1390	100	10.5	18.3	78	59.7	x	x	15.2	1371.7
Elabeha	626674	1136437	1113	92	10.5	14.2	68.1	53.9	137.376	x	16.83	1098.8
Adaar town	670544	1236166	598	300	7	59.63	137	77.37	x	x	7.82	538.37
Burka	652245	1122051	628	100	11	25.3	101.2	75.9	x	x	12.52	602.7
Elwaha	653040	1245272	783	554	10	108.3	226	117.7	x	x	7.34	674.7
Jeldi-Bedenaforo	645625	1237985	662	100	1	45	85	40	x	x	2.16	617
Woranso Site	658356	1247371	684	260	2.14	40	165	125	x	x	1.48	644
Jeldi	653523	1238360	661	100	3	35	148	113	x	x	2.29	626
Inayto	646576	1135853	626	82	3.4	55.6	68	12.4			23.69	570.4
Amma#1	650815	1155371	630	152	16	31.7	41.64	9.94	2.72	129	139.07	598.3
DRSLPW1-01-18	651283	1252518	723	415.2	17.2	113.1	113.9	0.8	7.61	1040	1857.6	609.9
DRLP1W-04-18	628178	1252687	995	450	20.9	83.94	133.55	49.61	0.089	14.66	36.4	911.06
KCPW-1	579066	1226301	1428	300	65	4.7	41.28	36.58	36.6	172	153.53	1423.3
KCPW-2R	578915	1226614	1838	324	66.17	0	119.19	119.19	6.29	547	47.97	1838
KCPW-4	601433	1164280	1450	300	86	6.58	41.2	34.62	7.27	186	214.63	1443.42
KCPW-5	564079	1227125	2218	300	50	0	8.99	8.99	17.4	163	480.53	2218
KCVTW-01-19	564405	1226806	2282	500	80	0	71.2	71.2	6.34	519	97.08	2282

KCVTW-02-19	578915	1226614	1850	600	75.5	10.24	85	74.76	9.32	978	87.26	1839.76
KCVTW-03-19	586889	1189939	1365	512	75	0	76.06	76.06	1.05	1030	85.2	1365
KCVTW-06-20	589874	1190202	1423	500	30	0	179.91	179.91	0.316	10.4	14.41	1423
ATW-2	601518	1143829	1494	160	26	0	59.59	59.59	0.84	38.8	37.7	1494
Chereti	600859	1171148	1440	50	4.15	14	38	24	x	x	14.94	1426
Arso Amba	597485	1122774	1486	150.5	24	13.23	70.6	57.37	0.727	43.6	36.14	1472.77
Ber giby	594750	1140609	2144	162	22.8	3.32	59.7	56.38	0.5	221	34.94	2140.68
Kolo Margefiya	554641	1060261	2796	230	8	19.38	77.8	58.42	0.145	11.8	11.83	2776.62
Car Assembly	554170	1063347	2580	195	7	23.33	95.28	71.95	0.232	20.2	8.41	2556.67
Debrebrhan BH#1	555009	1066916	2767	180	28.31	12.2	56.95	44.75	0.495	43.1	54.66	2754.8
Habesha	556983	1063474	2778	278	53	6.34	39.73	33.39	0.19	100	137.14	2771.66
Rasa _Well	609116	1087867	1178	246	22	27.42	89.1	61.68	0.352	30.7	30.82	1150.58
Shewarobit#1	595265	1107546	1350	256	38	30.75	106.5	75.75	0.0047	0.393	43.34	1319.25
Shewarobit#2	594400	1101453	1353	150.3	27	3.4	30.7	27.3	5.89	341	85.45	1349.6
Shewarobit#3	598826	1105066	1269	84	28	11.13	28.02	16.89	11.7	328	143.23	1257.87
Tarmaber	579054	89754	3009	143	26.6	78.22	83.6	5.38	7.48	304	427.18	2930.78
Senbete_Awlala	602713	1135272	1430	150	27	3.95	19.5	15.55	1.73	82.1	150.02	1426.05
Boru Selassie	569164	1239609	2609	133	6.8	41.05	42.16	1.11	2.86	119	529.3	2567.95
Chefa Robit Well	601611	1167183	1454	243	30	11.26	62.05	50.79	0.538	45.2	51.03	1442.74
Cheleka-Degan#2	599585	1230832	1511	250	11	39.12	101.05	61.93	0.0539	6.36	15.35	1471.88
Cheleka-Degan#1	598543	1230331	1474	256	28	43.75	60.8	17.05	1.63	147	141.89	1430.25
DGTW1	598023	1230433	1495	208.5	29	36.99	45.03	8.04	7.78	488	311.64	1458.01
Bistima	582705	1249598	1174	165	5	1.5	105	103.5	x	x	4.17	1172.5
Gerado(Haraweb elo)	569303	1224795	2257	109	35	0	40.32	40.32	1.12	51.7	75	2257
Gerbi#4	599618	1186654	1420	254	43	0	94.7	94.7	0.358	32.4	39.23	1420
Gerbi _Borehole	607259	1132604	1421	172	21	15.83	95.33	79.5	0.48	28.8	22.82	1405.17
HCKTW#4	585874	1203916	1457	324	60.2	0	45.35	45.35	9.5	303.8	114.69	1457
HCKPW#7	590425	1186041	1417	280	75	0	14.4	14.4	7.62	1185	450	1417
HCKPW#14	590444	1185133	1417	260	19	0	169.69	169.69	6.4	560	9.67	1417
HCKPW#15	590842	1185334	1415	280	78	0	19.13	19.13	6.8	897	352.28	1415
HCKPW#1	588742	1178663	1454	268	80	10.45	17.11	6.66	11.5	1386.6	1037.84	1443.55
HCKPW#2	588092	1179335	1444	274	81	4.06	15.106	11.046	12.03	1349	633.57	1439.94
HCKTW#1	582838	1207610	1496	268	20	5.04	91	85.96	8.4	258	20.1	1490.96
HCKTW#2	587540	1182640	1449	252	60	8.3	12	3.7	7.7	1251	1401.08	1440.7
HCKPW#4	589618	1186654	1420	332	50	0	25	25	7.7	1251	1401.08	1420
HCKTW#5	595255	1173713	1422	310	19	0.8	135	134.2	17.7	0.221	12.23	1421.2
JRTW#1	600033	1164982	1448	239.1	62	2.15	36.18	34.03	2.01	168	157.41	1445.85
JRTW#2	595313	1167092	1490	302	53	4.55	37.25	32.7	2.49	6.8	1400	1485.45
KCPW#2	579067	1226406	1831	152.5	44	9.53	81.68	72.15	1.55	7.4	526.9	1821.47
Kombolcha_Textile#1	578593	1224844	1846	330	50	12.2	67.4	55.2	0.525	9.8	782.6	1833.8

Kombolcha_Textile#2	578595	1225161	1850	330	52	20.18	73.1	52.92	0.67	7.7	849	1829.82
Kocha_Irr_Far1	583702	1206651	1465	250	39	0.5	79.68	79.18	0.421	7.1	425.6	1464.5
Kocha_Met_Ind	579428	1223639	1820	294	15.5	7.6	124.89	117.29	0.00151	7.2	1141	1812.4
Koch_WA_Sup	577915	1226833	1856	143	56	0	32.62	32.62	3.64	9.7	1483.3	1856
Moha_Soft_Dr	569901	1232663	2528	166	6.8	21.7	69.2	47.5	0.0069	3.1	123.7	2506.3
Rasa _Well#2	608700	1096356	1317	450	13	192.79	239.47	46.68	140	0.0002	24.06	1124.21
Senbete_Twon_WS	604040	1138195	1421	248	32	4.53	24.99	20.46	0.628	5.2	135.13	1416.47
Tita_Well#1	572706	1233646	2450	195	25	76.82	97.13	20.31	1.94	5.1	106.35	2373.18
Wollo_UNIV	568373	1238516	2604	234	26.51	42.72	69.1	26.38	8.2	9.2	868.6	2561.28
STW1	603130	1136770	1446	190	55	3.19	31.97	28.78	2.12	11.3	1651.1	1442.81
STW2	600793	1134590	1761	227	32.98	4.56	103.82	99.26	0.4	3.2	287.8	1756.44
SPW1	603486	1137392	1417	250	40	2.75	85.93	83.18	0.25	8.5	854	1414.25
HCKTW#4	585874	1203916	1457	324	60.2	0	45.35	45.35	303.8	9.6	1141.6	1457
HCKPW#7	590425	1186041	1417	280	75	0	14.4	14.4	1185	7.62	450	1417
HCKPW#14	590444	1185133	1417	260	19	0	169.69	169.69	6.4	5.6	345	1417
HCKPW#15	590842	1185334	1424	280	78	0	19.13	19.13	648.4	4.44	352.28	1424
HCKTW#3	592440	592440	1418	268	66	10.45	17.11	6.66	1386.6	11.5	856.22	1407.55
HCKPW#1	588742	1178663	1454	274	80	4.06	15.106	11.046	1349	12.03	625.75	1449.94
HCKPW#2	588092	1179335	1444	280	81	5.04	91	85.96	34.1	8.5	814.1	1438.96
HCKTW#1	582838	1207610	1496	252	20	8.3	12	3.7	17.7	5.1	674.03	1487.7
HCKTW#2	587540	1182640	1420	332	60	8.32	11.59	3.27	14.7	1410	1585.32	1411.68
HCKPW#4	589618	1186654	1420	332	19	0.8	135	134.2	7.1	221	12.23	1419.2
HCKTW#5	595255	1173713	1410	310	19	0.8	135	134.2	7.1	221	12.23	1409.2
JWTW#1	602305	1117221	1183	195	68	0	25.7	25.7	3.19	9.22	1228.61	1183
JWTW#2	604659	1117744	1660	220	40	5.7	63.3	57.6	0.587	6.8	608.45	1654.3
SRTW#1	595779	1107850	1346	193	50	17.9	63.28	45.38	1.26	11.5	952	1328.1
SRTW#2	604946	1108696	1210	245	15	22.76	139.68	116.92	0.0851	7.15	1108.2	1187.24
SRPW#1	595265	1107546	1350	255.7	37.5	30.55	106.5	75.95	0.231	4.9	426.6	1319.45
SRPW#2	595249	1108085	1357	237	40	31.44	141.2	109.76	0.438	3.9	314.9	1325.56
SRPW#3	594562	1102628	1356	219	60	11.56	30.32	18.76	5.6	7.6	534	1344.44
AKTW1	599826	1149466	1561	247.5	20	5.3	115.9	110.6	0.0957	8.33	1562	1555.7
JRTW#1	600033	1164982	1450	239.1	62	2.15	36.18	34.03	2.01	6.8	1574.1	1447.85
JRTW#2	595313	1167092	1490	302	53	4.55	37.25	32.7	2.49	6.8	1400.4	1485.45
STW-1	595028	1103365	1254	143.5	36.6	11.6	32.26	20.66	5.95	7.4	1530.6	1242.4
STW-2	594653	1103147	1353	122	30	15.9	45.87	29.97	1.31	5.8	864.9	1337.1
STW-3	594280	1102960	1365	119	12	24.75	63.1	38.35	0.232	1.7	270.4	1340.25
STW-4	595060	1104673	1352	151	1.5	31.18	93.84	62.66	0.0365	1.47	121.2	1320.82
STW-6	595104	1103011	1339	117	55	3.75	14.85	11.1	12.7	5.12	428.11	1335.25
DGPW2	566864	1226390	2438	123	22.51	0	23.35	23.35	1.34	5.64	832.9	2438
GKBH1	569303	1224795	2258	109	35	0	40.32	40.32	1.43	6.57	750	2258
DHBH2	569800	1230107	2467	75	41	14.2	27.65	13.45	4.76	11.1	2633.8	2452.8

DGBH1	569755	1194212	2671	121	13.4	4.76	21.66	16.9	3.93	4.2	685.1	2666.24
PW1	578537	1226089	1850	112	14.3	0	15.86	15.86	1.69	8.14	779	1850
PW2	578231	1226297	1866	97.5	14.3	0	12.23	12.23	2.64	3.5	101.02	1866
KBH1	579379	1226203	1841	140	51	0	25.69	25.69	5.18	10.2	1715.2	1841
KBH2	578913	1226081	1842	144	30	2.3	19.28	16.98	3.14	9.4	1526.5	1839.7
HrBH3	584805	1208278	1480	146	26	0	56.67	56.67	1.12	4.05	396.4	1480
HrW4	584465	1208654	1489	121	27	0	53.63	53.63	2.01	8	435	1489
CHBH1	600413	1162829	1464	75	6.98	0	1.62	1.62	9.76	280	372.27	1464
CHBH2	600677	1162923	1465	88	6.98	3	5.07	2.07	9.16	261	291.34	1462
ATEW1	601680	1144280	1508	130	20	0	58.8	58.8	0.943	43.7	29.39	1508
ATEW3	601820	1143997	1504	126	24	0	48.8	48.8	1.55	62.9	42.49	1504
ASBH2	593169	1099019	1486	119	39	8.63	33.69	25.06	7.85	358	134.46	1477.37
RW1	609461	1088380	1230	143	13.5	10.9	22.92	12.02	4.48	168	97.04	1219.1
DNBH1	562106	1070685	2792	108	7	12.79	39.68	26.89	0.35	12.7	22.49	2779.21
DNBH2	562015	1071000	2467	95.56	7	11.68	21.39	9.71	2.13	8.93	62.29	2455.32
DNBH5	563330	1070084	2808	150	2.5	7.33	61.86	54.53	0.04	2.22	3.96	2800.67
DNBH6	560803	1070784	2782	108	12	7.4	40	32.6	3.71	181.44	31.8	2774.6
DNBH7	561594	1071660	2796	72	14.2	9.6	40	30.4	7.25	224.64	40.36	2786.4
BNBH2	559369	1067258	2758	100.49	15.3	5.3	20.3	15	2.21	80.78	88.13	2752.7
BNBH5	559432	1066077	2757	102	17	2.85	40	37.15	2.34	80.93	39.54	2754.15
Delgo	603086	1163687	1440	57	2	3	35	32	x	x	5.4	1437
Kichicho	613895	1172141	1557	131	6	74.36	98.86	24.5	x	x	21.16	1482.64
KW-1	595092	1185850	1454	150	10.35	8.1	83.28	75.18	x	71.12	11.89	1445.9
KW-2	595618	1186473	1471	147.6	5	6.81	69.08	62.27	0.07	4.62	6.94	1464.19
KW-3	595618	1186264	1458	150	13.5	6.25	38.35	32.1	0.53	35.16	36.34	1451.75
KW-4	595373	1186685	1502	146	6.5	6.33	18.49	12.16	0.62	44.64	46.18	1495.67
KW-5	597030	1184800	1522	145	19	9.25	23.27	14.02	1.97	130.2	117.09	1512.75
BH-1	579647	1226175	1835	100	10	0	28	28	x	x	30.86	1835
BH-2	579516	1227116	1844	110.7	10	0	35	35	x	x	24.69	1844
BH-3	579266	1228118	1862	100	5.5	0	45	45	x	x	10.56	1862
BH-4	579345	1226470	1840	110	25	0	28	28	x	333.5	77.14	1840
BH-5	578542	1226092	1847	112	20.5	0	40	40	x	88.4	44.28	1847
BH-6	578233	1226301	1853	97	18.7	0	41	41	x	207.4	39.41	1853
EOC-CCE	578304	1225892	1856	137	10	0	32	32	x	x	27	1856
Poultry	579142	1225700	1841	60	8	0	25	25	x	x	27.65	1841
BGI-1	579280	1224940	1832	180	8.75	0	42	42	x	x	18	1832
BGI-New-1	579290	1224952	1837	240	16	36	125	89	x	x	15.53	1801
BGI-New-2	579474	1224993	1830	240	18	40	132	92	x	x	16.9	1790
ELF-2	579539	1225416	1832	180	11	2	68	66	x	x	14.4	1830
TEX-2	578728	1225475	1847	180	10	1	21	20	x	x	43.2	1846
TEX-3	578679	1225237	1849	180	2.78	0	51	51	x	x	4.71	1849
TEX-4	578655	1224977	1852	120	10	1	54	53	x	x	16.3	1851
TEX-5	578703	1224887	1852	180	10	0.012	37	36.988	x	x	23.36	1851.988
TEX-7	579053	1225221	1842	180	12	19	45	26	x	x	39.88	1823

TEX-1	578959	1225361	1847	71	11	8	56	48	x	x	19.8	1839
Well-2	579513	1225734	1831	120	50	5.57	25.41	19.84	x	x	217.74	1825.43
Aykel-01	580142	1224437	1806	120	50	4.25	50.5	46.25	x	x	93.41	1801.75
Well-one	579376	1226205	1839	140	8	1.66	24.03	22.37	2.98	125.14	676.8	1837.34
Well-Two	578936	1226045	1844	144	7	2.3	14.68	12.38	2.67	125.71	592.2	1841.7
PW2	578528	1226346	1450	105	14.3	0	12.3	12.3	2.61	135	100.45	1450
PW3	579565	1226611	1837	110.7	14.4	0	7.16	7.16	3.89	201	173.77	1837
PW#1	588742	1178663	1450	280	41	7	25	18	x	x	196.8	1443
Gerba	600654	1234847	1712	150	6	12.86	106.65	93.79	x	x	5.53	1699.14
BH-2	603652	1142730	1843	151	7	22.2	77.2	55	x	x	11	1820.8
BHI-3	273764	1208747	1860	200.7	5	13.4	67.97	54.57	x	x	7.92	1846.6
BH-4	595787	1186010	1839	90	5.3	21.59	44.37	22.78	x	x	20.1	1817.41
W/kurkur	604946	1108696	1238	245	15	23.21	139.68	116.47	x	x	11.13	1214.79
Kurkuro	610315	1195479	1423	128	40	2.47	18.4	15.93	x	x	216.95	1420.53
Bora/Kulkula	609847	1118817	1391	74	7.97	6.57	9.1	2.53	x	x	272.18	1384.43
Dipo	582702	1226019	2081	87	25	23.5	33.58	10.08	x	x	214.29	2057.5
Chereti	600930	1172719	1402	144	16.5	9.15	62.9	53.75	x	x	26.52	1392.85
Bora	612266	1181300	1558	110	22	26.71	44.9	18.19	x	x	104.5	1531.29
Shoa Robit well#1	598826	1105066	1300	84	28	11.13	28.02	16.89	x	x	143.23	1288.87
korimeda well field/derensa	602477	1155480	1827	200	10.3	3.17	20.04	16.87	x	x	52.75	1823.83
Harawa	609459	1193404	1465	134	28.53	12.96	23.19	10.23	x	x	156.5	1452.04
Tuche	585980	1192246	1519	166	21	0	68.65	68.65	x	x	26.43	1519
Bilacha	595435	1187105	1544	167.8	30	4.12	16.19	12.07	x	x	214.75	1539.88
Jeweha	606269	1116617	1160	162	22	6.05	63.08	57.03	x	x	33.33	1153.95
Dodo	597026	1188581	1647	176	12	27.45	130.15	102.7	x	x	10.1	1619.55
Balchi/tekure	603637	1114883	1163	203.3	30	5.55	13.49	7.94	x	x	326.45	1157.45
Mushe	579054	1089754	3000	143	26.6	78.22	83.6	5.38	x	x	427.18	2921.78
tissue culture	567663	1238587	2733	220	25	41.9	53.36	11.46	x	x	188.48	2691.1
kutaber	561487	1244816	2894	170.8	28	4.35	18.44	14.09	x	x	171.7	2889.65
S.Gebeya	570798	1204844	2448	140	16	7.2	80.88	73.68	x	x	18.76	2440.8
Mutifecha	604286	1117981	1373	200	32	5.95	46.58	40.63	x	x	68.05	1367.05
Harewa Irrigation well # 1	608911	1193509	1520	216	56	32.83	46.95	14.12	x	x	342.66	1487.17
shekla	590347	1193365	1435	148	25	7.64	78.02	70.38	x	x	30.69	1427.36
Gerbiemudewachu	607259	1132604	1450	164	21	15.83	95.33	79.5	x	x	22.82	1434.17
Harbu	583702	1206651	1521	250	39	0.5	79.68	79.18	x	x	42.56	1520.5
Merwa hadrie	603486	1137392	1493	250	40	2.75	85.93	83.18	x	x	41.55	1490.25
borbode	577915	1226833	1897	143	56	0	33.04	33.04	x	x	146.44	1897
Neti	560559	1190895	2630	180	12.5	7.1	58.36	51.26	x	x	21.07	2622.9
Kobojerit#2	595249	1108085	1537	237.5	40	32.1	141.2	109.1	x	x	31.68	1504.9
Baldekem	599791	1119516	1370	199	30	0.35	17.55	17.2	x	x	150.7	1369.65
Hora	599826	1149466	1730	2475	18	5.99	115.9	109.91	x	x	14.15	1724.01

Fursi	613980	1157848	1636	62	1.23	3.35	43.4	40.05	x	x	2.65	1632.65
merere	602969	1160237	1453	62	1.23	9.55	32.42	22.87	x	x	4.65	1443.45
gula	599049	1179331	1412	242	30	7.62	13.91	6.29	x	x	412.08	1404.38
Harro Baqelo	595340	1197606	1961	178	30	0	34.25	34.25	x	x	75.68	1961
Bati	599958	1230832	1630	250	11	39.2	101.05	61.85	x	x	15.37	1590.8
tita well#2	572389	1233441	2446	180	10	8.12	120.5	112.38	x	x	7.69	2437.88
Boren	607022	1191641	1645	74	2.5	4.19	19.8	15.61	x	x	13.84	1640.81
Mekoy well	587675	1181825	1476	216	30	0	12.22	12.22	x	x	212.11	1476
Adame Town	593144	1212252	1958	160	18	2	122.13	120.13	x	x	12.95	1956
Gachene ws well	596340	1057327	1361	180	3	16.2	140	123.8	x	x	2.09	1344.8
Hulatikuye	601449	1167928	1470	63	4	0.87	14	13.13	x	x	26.32	1469.13
Rasa well	609116	1087867	1247	246	22	27.42	89.1	61.68	x	x	30.82	1219.58
Girma's bh	589089	1194117	1442	150	34	0	31.9	31.9	0.7	110.6	92.09	1442

Appendices 2: Hydrochemical analysis data

Sample ID	phy	E	N	Alt	PH	EC (µs/cm)	TDS	Cl- (mg/l)	NO3 (mg/l)	SO4	HCO3 - (mg/l)	K (mg/l)	Na (mg/l)	Ca (mg/l)	Mg (mg/l)
BH1	Pla	564068	1227122	2241	8.8	420	210	5.3	2.77	4.1	167	1.424	58.936	8.712	1.12
BH2	Pla	564901	1226608	2228	7.84	407	191	7.6	11.63	6.7	229.44	1.298	28.988	41.13	7.57
BH3	Pla	569304	1224792	2264	7.4	403	190	4.5	15.18	4.6	286.79	1.875	43.014	53.95	9.51
BH18	Pla	556555	1063307	2786	7.5	227	107	3.5	5.87	3.2	85.52	1.766	7.456	19.08	3.96
BH19	Pla	558229	1066542	2759	7.4	256	121	3.7	1.89	4.9	98.46	2.884	15.681	18.39	2.57
BH20	Pla	564736	1097280	2889	7.3	175	80	4	7.65	3	75.32	2.007	6.758	17.97	3.56
BH21	Pla	555477	1096784	2717	9	334	158	34	1.84	25	52.36	3.078	47.912	1.605	0.09
DCSP-7	Pla	560001	1215214	2933	7.6	315	150	3.62	9.86	7.7	176.9	4.05	12.1	27.3	13.8
DCSP-8	Pla	552397	1223421	2578	7.31	577	275	12.83	24.92	12.2	300.12	1.27	21.5	73.8	14.7
DCSP-9	Pla	559655	1246384	2743	6.88	524	250	5.39	7.64	10.4	184.22	2.23	10.1	39.9	10.4
CSP-11	Pla	549444	1254991	2059	6.69	417	199	4.89	13.85	18.3	224.48	1.43	16.8	49.3	12.8
DRW-1	Pla	554001	1222972	2407	8.19	261	124	8.15	1.1	9.1	170.8	1.26	15	28.3	8.3
DBH-37	Pla	564494	1225842	2230	7.78	417	199	6.24	5.87	6.91	244	1.42	19.7	48	10
DBH-38	Pla	564050	1226264	2222	8.09	418	199	6.03	1.1	8.16	207.4	1.12	26.4	35.1	7.1
DBH-39	Pla	563411	1226816	2219	8.24	341	162	5.96	1.1	5.09	192.76	1.11	37.5	26	4.2
DBH-16	Pla	537991	1263934	1736	7.57	427	203	9.43	12.08	17.3	217.16	0.94	16.9	57.1	13
Ajbar	Pla	52583	1241594	2887	7.41	518	326	20.5	6.56	20	76.25	0.24	12.75	21.6	4.68
Abamela	Pla	27737	1242321	2904	7.1	515.3	293.19	9.5	17.5	1	195.5	1.4	21.4	42.6	5.8

DDW-9	Pla	564333	1256732	2342	7.14	270	136	9.78	8.97	25.79	100.04	1.99	5.9	26.3	9
BH4	Rm	561478	1244817	2675	7.4	380	179	4.6	8.97	4.9	209.91	2.3	12.765	41.841	11.73
BH5	Rm	579514	1225737	1827	7.5	713	334	20.3	2.11	20.5	281.26	0.921	44.128	50.261	13.48
BH6	Rm	578607	1225157	1855	7.8	533	251	14.9	1.93	9.6	291.68	0.993	59.29	35.363	8.45
BH7	Rm	598023	1230428	1482	7.4	811	382	35.7	20.49	65.8	344.15	1.622	52.598	69.49	21.88
BH8	Rm	601845	1234372	1587	7.2	991	466	36.6	56.82	26.5	499.14	1.193	38.951	131.169	34.76
BH9	Rm	633049	1207692	814.7	8.7	1015	520	394.6	18.72	265	10.35	1.241	327.773	37.407	0.05
BH10	Rm	629027	1195313	999.3	7.9	1208	569	158.4	22.71	141.1	23.47	2.128	127.508	32.969	8.83
BH11	Rm	629441	1187301	1006	7.6	1230	580	125	56.38	86.5	204.36	2.867	56.963	95.627	26.48
BH13	Rm	636093	1176914	917	8	1206	558	119.4	69.67	129.1	206.58	8.291	104.167	72.189	33.32
BH22	Rm	593169	1099019	1521	7.5	757	355	14.1	35.11	15.9	302.56	2.657	29.933	68.745	15.48
BH23	Rm	598830	1105065	1268	7.5	1125	524	56.9	68.34	88.4	347.81	5.651	70.393	102.316	27.82
BH24	Rm	632624	1100348	783.1	8.5	537	252	23.8	11.19	25.1	141.23	4.585	54.857	13.775	7.38
BH25	Rm	609461	1088380	1164	7.9	608	286	14.4	7.65	15.2	224.53	4.889	30.652	41.943	10.01
BH26	Rm	604094	1099221	1309	7.4	1436	675	94.1	24.04	175.7	521.11	9.106	162.666	100.911	23.25
BH27	Rm	606332	1116771	1139	7.8	1276	600	42.2	13.4	209.2	452	4.515	243.459	46.418	11.34
BH28	Rm	603745	1108458	1231	7.6	1250	588	78	3.66	131.2	356.85	6.366	169.148	56.114	11.94
BH29	Rm	607779	1133513	x	7.5	680	320	13.9	7.2	9.2	305.45	3.929	42.694	50.532	12.64
BH30	Rm	603147	1136751	1410	7.4	799	376	15.5	8.09	11.4	405.63	5.86	44.652	79.571	21.15
BH31	Rm	620029	1128996	1136	7.4	1247	583	206.1	4.99	174.6	39.05	1.536	212.521	28.921	0.93
BH32	Rm	621781	1129842	1163	7.7	1001	470	86.7	17.39	47.3	245.63	2.124	51.195	65.523	25.62
BH33	Rm	595252	1173712	1407	8.4	350	164	4.1	1.8	8.1	172.08	0.834	58.517	7.013	1.14
BH34	Rm	597154	1170116	1420	8.5	1035	164	49.8	35.55	35.7	380	0.919	42.81	90.465	36.7
BH35	Rm	612213	1181311	1493	8.1	403	190	15.1	1.75	14.5	108.23	1.388	36.576	11.365	4.49
BH36	Rm	609450	1193407	1481	7.4	690	324	15.8	12.08	12.7	309.21	1.204	19.236	67.326	17.36
BH37	Rm	596904	1184518	1456	7.4	801	377	18.4	12.96	21.4	378.52	10.666	29.599	84.384	17.13
BH38	Rm	590839	1185340	1426	7.9	386	181	4	2.02	4.9	168.56	2.36	48.498	14.458	2.9
BH39	Rm	589880	1190342	1434	7.3	1040	489	31.8	2.59	153.4	305.23	7.548	132.402	38.484	8.34
BH40	Rm	587619	1181821	1447	7.6	545	256	4	1.93	4.9	285.45	1.466	36.29	38.616	13.87

BH41	Rm	585871	1203922	1461	8	1021	483	59.2	1.93	118.3	352.66	1.946	171.507	25.405	6.18
BH42	Rm	570774	1204842	2325	7.6	422	199	5	1.93	4.6	185.84	5.681	13.608	35.802	9.18
S1	Rm	566726	1240199	2615	7.6	361	170	5.9	12.08	6.9	145.26	0.829	9.638	34.526	8.53
S3	Rm	582659	1091057	2862	7.8	151	71	1.9	3.66	2.8	58.46	0.813	4.406	12.323	2.94
S4	Rm	593699	1116174	1423	7.5	726	342	11.2	23.59	17.2	345.56	1.087	35.689	64.569	21.08
S5	Rm	598443	1138501	1560	7.4	443	208	6.9	16.06	5.2	236.56	2.955	20.211	45.332	11.27
S6	Rm	594336	1160020	1656	7.3	309	146	4.8	8.53	6.3	125.45	1.014	24.78	17.956	4.08
S7	Rm	571033	1202626	2467	7.5	367	173	4.4	7.2	15.5	136.74	0.894	10.011	33.611	7.64
S8	Rm	574532	1238550	2363	7.7	365	172	4.9	13.4	4.9	145.63	1.073	12.944	27.641	9.01
R1	Rm	577764	1226837	1858	7.6	606	285	33.6	16.95	16.7	245.63	0.829	9.638	34.526	8.53
DBH-13	Rm	566927	1238698	2609	7.46	344	172	5.67	14.29	11.3	190.32	0.64	21.8	38	12.7
DBH-69	Rm	578230	1224874	1831	7.8	514	257	12.7	1.1	12	232.6	0.73	57.5	44.5	9.7
DBH-70	Rm	578543	1224851	1852	8.14	330	165	10.98	1.1	6.5	152.5	0.44	65.9	11.6	1.7
DBH-71	Rm	578675	1224673	1846	8.24	310	155	5.25	1.1	6.2	155.6	0.37	67	9.8	0.8
DBH-72	Rm	577191	1225245	1863	7.79	562	281	13.61	2.77	13.6	341.6	1.34	66.25	47.2	11.5
DRW-11	Rm	570025	1228657	2368	7.35	757	378.5	56.72	21.37	17.15	305	9.17	46.6	74.2	20.5
DRW-12	Rm	568928	1230048	2453	7.55	655	327.5	35.1	6.32	13.74	292.8	7.76	44.99	69.9	17.9
DRW-13	Rm	567009	1238290	2597	7.67	391	195.5	5.88	1.1	4.92	231.8	2.38	15.5	42.3	15
DCSP-30	Rm	582728	1231280	2257	7.9	496	248	6.09	7.2	8.9	309.88	0.85	14.9	60.9	18
DCSP_37	Rm	569287	1232031	2514	8.06	367	183.5	4.96	12.52	9.4	213.5	1.41	19.1	44.8	11.5
DCSP_38	Rm	568084	1229960	2584	7.81	309	154.5	3.19	3.21	6.4	195.2	0.49	8.6	38.2	8.1
DCSP_40	Rm	583910	1220692	2157	7.49	555	277.5	10.14	63.46	12.8	323.2	0.74	23.6	65.7	20.5
DBH-35	Rm	564670	1225399	2235	8.05	333	166.5	4.96	3.22	5.56	207.4	3.25	30.2	33.9	5.7
DBH-36	Rm	564708	1225536	2233	7.82	419	209.5	7.8	5.43	6.53	248.88	2.74	20.3	52.8	11.2
DBH-40	Rm	568979	1230036	2461	7.84	316	158	34.74	19.16	20.78	305	1.95	32.5	74.5	18.6
DBH-41	Rm	569224	1231526	2490	7.82	659	329.5	11.7	6.76	14.93	275.72	1.68	22.5	62.3	15.6
DBH-42	Rm	568760	1231553	2495	7.7	478	239	6.95	5.43	9.42	195.2	8.97	26.1	40.9	8.9
DBH-49	Rm	579283	1225622	1832	7.62	484	242	15.6	1.89	20.59	378.2	1.84	61	63.4	17.2
DBH-50	Rm	579015	1225653	1837	8.26	666	333	9.93	3.22	29.76	305	1.37	58.1	40.9	11.4

DBH-51	Rm	578907	1227572	1860	8.04	559	279.5	7.8	2.77	7.38	439.2	1.46	35.9	60.3	21.7
DBH-52	Rm	579154	1226670	1843	8.27	676	338	9.5	1.1	7.68	366	1.27	62.7	44.4	10.7
DBH-53	Rm	578982	1225920	1836	8.35	574	287	12.05	5.43	19.62	397.72	1.58	57	79.1	23.6
DBH-54	Rm	577860	1225749	1848	8.15	723	361.5	12.62	4.1	14.53	341.6	2.13	53.1	56.6	14.5
DBH-55	Rm	578170	1225540	1860	8.34	561	280.5	12.76	5.43	17.11	342.82	1.69	58.1	68.3	19.5
SBH-3	Rm	600805	1170977	1445	6.64	369	184.5	20.21	16.58	26.08	161	6.47	16.25	55.8	10.25
SBH-4	Rm	599749	1171529	1415	6.96	1394	697	163.07	22.26	28.95	411.14	6.87	91.8	167.2	24.7
SBH-5	Rm	590812	1187759	1447	6.93	898	449	100.68	63.02	112.85	247	21.38	59.7	132.4	25.4
SBH-6	Rm	586670	1188168	1444	7.23	1050	525	90.18	87.39	102.39	356	3.58	41.9	150.8	41.5
SBH-9	Rm	591099	1190335	1443	6.73	340	170	14.46	17.83	18.64	176.9	9.27	24.5	35	7.5
SBH-10	Rm	589035	1200408	1486	7.35	706	353	34.67	16.5	21.02	406.26	2.34	45	77.5	25.1
BH-4#	Rm	592875	1184375	1425	8.9	272	136	11.06	1.89	7.64	117.12	0.72	64.25	0.3	1.75
BH-5#	Rm	595679	1186467	1466	7.48	678	339	22.76	1.44	28.57	452.62	7.44	60.6	99.9	20.7
BH-6#	Rm	594267	1185353	1439	7.76	641	320.5	18.72	13.4	17.21	429.44	11.41	37	101.8	18.2
BH-7#	Rm	591221	1193425	1463	7.82	720	360	32	5.43	51.6	389.18	8.58	153.5	25.8	6
BH-8#	Rm	585349	1206825	1484	7.89	731	365.5	30.34	2.35	6.1	419.68	1.65	94	58.5	25.6
BH-9	Rm	584559	1208864	x	7.75	784	392	65.58	11.63	32.22	366	2.2	0.2	55.3	19.7
BH-10	Rm	584897	1208484	1489	8.04	515	257.5	28.43	4.1	36.16	270.84	1.83	98.7	22.1	7.2
HSP-1	Rm	601554	1175482	1417	8.1	1025	512.5	48.35	1.44	193	265	4.26	231.8	16.5	1.8
HSP-2	Rm	588396	1208522	1565	8.02	1102	551	32.05	1.1	156.9	464.82	2.82	267.3	11	1.6
CSP-1	Rm	585556	1174709	1722	8.29	188	94	0.57	1.44	15.59	107	0.91	11.22	22.36	7.24
CSP-3	Rm	588396	1183662	1991	7.69	433	216.5	1.91	4.5	7.6	269.62	0.8	17.6	57.3	16.4
CSP-4	Rm	588855	1202670	1473	7.77	330	165	37.65	19.6	36.2	314.76	2.08	79.7	45.3	21.6
SBH-7	Rm	601405	1168458	1456	7.02	506	253	15.03	14.29	20.58	226	6.49	40	26.05	11.4
SBH-8	Rm	603913	1165181	1458	7.49	426	213	10	1.89	17.86	262.23	7.39	47.75	21.85	18.5
SBH-2	Rm	601032	1165645	1449	7.33	561	280.5	7.23	1.4	10.77	363	8.04	39.1	59.2	30.6
BH-1	Rm	601858	1167012	1481	6.72	410	205	12.12	13.85	31.26	203	9.87	33	49.05	9.9
BH-3	Rm	600512	1163039	1466	7.56	308	154	3.4	3.22	4.9	187	4.04	17.8	40.3	11.15
Daleti	Rm	627186	1108376	1003	6.81	805	402.5	13.57	13.86	123.35	313.41	1.08	16	105	29

Eblidear	Rm	629641	1187504	1012	6.9	586	293	50.98	16.4	19.38	385	3.9	152	25.8	2.6
Adadlehengeg	Rm	605695	1106414	1173	7.4	1443	760	179.94	1.16	255.35	425	7.9	375.02	16.1	2.5
AFTUHA	Rm	634712	1117380	870	8.07	803	401.5	121.27	2.03	103	102	3.1	168	12	1.44
Mederale #1	Rm	629386	1206345	870	7.82	1013	506.5	32.53	11.39	240.37	46.36	1.02	122	18	1
Mederale #2	Rm	625460	1205803	936	8.23	1096	548	151.17	1.01	222.8	154.76	5.1	262.5	8.4	2.52
Leleeda	Rm	626732	1139045	1110	7.83	917	458.5	121.15	46.21	107.2	164.7	3.7	123	30.24	4.59
KCPW-1	Rm	588407	1189227	1428	7.72	486	243	12.96	1.13	1	268.4	2.3	96	27.74	5.39
KCPW-2	Rm	579066	1226301	1838	7.48	597	298.5	15.36	1.01	1	307.72	1.4	64	84	4.8
KCPW-2R	Rm	578915	1226614	1850	7.84	415	207.5	14.02	1.13	1	291.82	2	70	29.4	8.7
KCPW-4	Rm	601433	1164280	1450	7.27	486	243	8.86	1	1	283.72	2.5	50	37.6	7.2
Arsoamba	Rm	597485	1122774	1486	7.42	441	220.5	7.9	1.29	7.1	275.4	47.3	27.5	30.5	5.4
Mammed	Rm	610029	1234084	1615	7.2	622	311	17.4	1.5	30.5	189.7	2.13	16.4	45.9	7.45
BH12	RF	644344	1174895	615.4	7.6	1237	618.5	86.8	12.08	123	318.52	4.97	81.394	74.201	37.35
BH14	RF	667303	1097773	585.4	8.1	1105	552.5	61.5	4.54	93.1	384.43	11.85	192.717	11.529	5.47
BH15	RF	663388	1099145	584.2	8.1	1128	564	96	7.65	77	260.06	8.796	174.382	9.946	4.95
BH16	RF	663997	1092193	609.8	8.2	1076	538	113.6	12.96	99.6	165.87	8.656	161.327	7.575	4.64
BH17	RF	663193	1102152	573.8	8.1	1152	576	99.9	4.1	80.7	285.45	11.293	186.926	7.243	1.87
S2	RF	668932	1103097	573.4	8.3	1241	620.5	115.8	7.2	90	308.52	9.94	231.47	3.363	1.34
R2	RF	643148	1174225	628.1	7.6	646	323	33.2	5.87	38.8	285.45	0.829	9.638	34.526	8.53
HDW	RF	669414	1132661	568.9	7.7	813	406.5	18.4	1.58	28.6	353.92	0.829	9.638	34.526	1.34
Amma#1	RF	650815	1155371	x	7.84	794	397	25.84	2.29	54.01	435.54	5.7	160	22.4	9.6
Amma#2	RF	649945	1155557	618	7.52	780	390	42.94	1	65.22	386.5	6.2	140	38.35	10.77
Enayto	RF	646576	1135853	626	7.78	1790	895	351.02	1	226.2	197.64	11.3	260	88.2	22.95
L1	RF	650064	1174674	585	8	665	332.5	60.4	4.1	32.9	302.66	0.829	9.638	34.526	8.53

Appendices 3: Stable Isotope analysis data

Sample ID	E	N	Phy	^{18}O	^{2}H	d-excess
BH1	564068	1227122	Plateau	-6.51	-24.4	27.68
BH2	564901	1226608	Plateau	-5.07	-13.9	26.66
BH3	569304	1224792	Plateau	-5.78	-19	27.24
BH4	561478	1244817	RM	-6.33	-21.6	29.04
BH5	579514	1225737	RM	-6.43	-23.2	28.24
BH6	578607	1225157	RM	-6.97	-29.4	26.36
BH7	598023	1230428	RM	-3.62	-9.4	19.56
BH8	601845	1234372	RM	-3.66	-6.4	22.88
BH9	633049	1207692	RM	-5.68	-21.2	24.24
BH10	629027	1195313	RM	-4.32	-10.5	24.06
BH11	629441	1187301	RM	-4.03	-6.9	25.34

BH12	644344	1174895	RF	-3.94	-8.1	23.42
BH13	636093	1176914	RM	-4.35	-17.4	17.4
BH14	667303	1097773	RF	-6.07	-21.3	27.26
BH15	663388	1099145	RF	-6.6	-26.4	26.4
BH16	663997	1092193	RF	-5.97	-23.6	24.16
BH17	663193	1102152	RF	-6.3	-22.7	27.7
BH18	556555	1063307	Plateau	-6.5	-22.8	29.2
BH19	558229	1066542	Plateau	-7.16	-33.7	23.58
BH20	564736	1097280	Plateau	-6.55	-26.2	26.2
BH21	555477	1096784	Plateau	-9.17	-44	29.36
BH22	593169	1099019	RM	-4.03	-6.8	25.44
BH23	598830	1105065	RM	-4.32	-7.7	26.86
BH24	632624	1100348	RM	-6.48	-19.6	32.24
BH25	609461	1088380	RM	-4.47	-9.7	26.06
BH26	604094	1099221	RM	-4.64	-13.5	23.62
BH27	606332	1116771	RM	-6.07	-22.5	26.06
BH28	603745	1108458	RM	-6.04	-18.3	30.02
BH29	607779	1133513	RM	-5.9	-18.9	28.3
BH30	603147	1136751	RM	-5.66	-16.3	28.98
BH31	620029	1128996	RM	-5.6	-23.6	21.2
BH32	621781	1129842	RM	-4.63	-13.9	23.14
BH33	595252	1173712	RM	-6.27	-19.5	30.66
BH34	597154	1170116	RM	-5.06	-9.9	30.58
BH35	612213	1181311	RM	-6.41	-23.3	27.98
BH36	609450	1193407	RM	-4.99	-9.8	30.12
BH37	596904	1184518	RM	-2.04	-3.2	13.12
BH38	590839	1185340	RM	-3.53	-16.5	11.74
BH39	589880	1190342	RM	-4.74	-24.8	13.12
BH40	587619	1181821	RM	-2.96	-7	16.68
BH41	585871	1203922	RM	-2.76	-14.2	7.88
BH42	570774	1204842	RM	-2.42	-6	13.36
S1	566726	1240199	RM	-2.98	-8.7	15.14
S2	668932	1103097	RF	-2.22	-11	6.76
S3	582659	1091057	RM	-3.63	-12.6	16.44
S4	593699	1116174	RM	-1.43	-0.5	10.94
S5	598443	1138501	RM	-2.17	-4.1	13.26
S6	594336	1160020	RM	-2.58	-6.2	14.44
S7	571033	1202626	RM	-3.12	-8.9	16.06
S8	574532	1238550	RM	-3.16	-8.9	16.38
R1	577764	1226837	RM	-0.44	1.8	5.32
R2	643148	1174225	RF	0.56	11	6.52
L1	650064	1174674	RF	1.64	15.8	2.68
HDW	669414	1132661	RF	0.21	7.45	5.77
CSP_8	552397	1223421	Plateau	-2.75	-8.99	13.01
CSP_9	559655	1246384	Plateau	-3.27	-11.55	14.61
CSP_11	549444	1254991	Plateau	-1.74	-4.07	9.85
CSP_22	574139	1237782	RM	-3.12	-3.43	21.53

CSP_23	562651	1267865	RM	-1.89	3.86	18.98
CSP_37	569287	1232031	RM	-4.73	-15.17	22.67
CSP_38	568084	1229960	RM	-4.59	-12.29	24.43
CSP_41	584094	1221342	RM	-2.04	-1.11	15.21
CSP_7	560001	1215214	Plateau	-4.27	-16.85	17.31
CSP_12	589367	1226447	RM	-1.44	-1.18	10.34
CSP_29	596589	1237831	RM	-2.28	0.7	18.94
CSP_53	517869	1254740	Plateau	-2.14	-7.04	10.08
DBH_36	564708	1225536	Plateau	2.52	15.03	-5.13
DBH_37	564494	1225842	Plateau	-1.72	-1.53	12.23
DBH_38	564050	1226264	Plateau	-2.95	-11.03	12.57
DBH_40	568979	1230036	RM	-1.88	-2.45	12.59
DBH_49	579283	1225622	RM	-2.24	-6.87	11.05
DBH_50	579015	1225653	RM	-2.98	-10.33	13.51
DBH_13	566927	1238698	RM	-2.71	-8.12	13.56
DBH_14	599142	1231220	RM	-1.05	1.5	9.9
DBH_18	573979	1279765	RM	-1.57	0.55	13.11
DBH_39	563411	1226816	RM	-3.33	-14.38	12.26
DBH_41	569224	1231526	RM	-2.11	-5.26	11.62
DBH_51	578907	1227572	RM	-3.32	-10.33	16.23
DBH_52	579154	1226670	RM	-3.59	-14.95	13.77
DBH_53	578982	1225920	RM	-2.2	-4.58	13.02
DBH_55	578170	1225540	RM	-1.38	-2.13	8.91
DBH_62	523376	1238731	Plateau	-3.97	-15.91	15.85
DBH_65	525736	1240584	Plateau	-3.87	-15.52	15.44
DBH_69	578230	1224874	RM	-3.82	-17.92	12.64
DBH_70	578543	1224851	RM	-3.92	-17.26	14.1
Meteka	668743	1102566	RF	-4.94	-13.2	26.32
Adaitu	692286	1230439	RF	-5.06	-10.9	29.58
Gewane	671043	1107612	RF	0.13	6.3	5.26

Appendices 4: Radon values and Distribution

No	Rad name	E	N	Z	EC	T	pH	TDS	Radon values (Bq/m^3)	Physiography
1	Rad#1	580392	1221688	1765	700	30.6	8.44	350	127.13	Rift margin
2	Rad#2	590888	1190370	1433	610	28.2	x	310	184.25	Rift margin
3	Rad#3	632296	1223345	936.1	690	32.6	8.31	340	136.54	Rift margin
4	Rad#4	645220	1227654	680	710	35.21	8.53	350	81.42	Rift margin
5	Rad#5	634417	1207804	844	480	32.2	8.99	240	168.45	Rift margin
6	Rad#6	643727	1209034	828	610	33.54	x	260	101.42	Rift margin
7	Rad#7	626952	1195860	1022	485	31.46	x	241	168.45	Rift margin
8	Rad#8	639687	1182510	915	515	32.55	x	250	143.65	Rift margin
9	Rad#9	643990	1175396	619	600	30.8	8.87	300	0	Rift floor
10	Rad#10	692404	1230561	467	800	31.6	11.3	400	48.53	Rift floor

11	Rad#11	669441	1132661	568.9	780	35.6	11.4	390	0	Rift floor
12	Rad#12	672685	1131428	565.9	790	33.6	11.2	400	26.13	Rift floor
13	Rad#13	594718	1078169	1285	320	21.2	x	160	148.25	Rift margin
14	Rad#14	614216	1075622	926	485	32.1	x	241	186.45	B/n RM& RF
15	Rad#15	652685	1103640	579	580	31.2	x	275	31.45	Rift floor
16	Rad#16	645044	1111808	711	470	30.8	x	240	98.45	Rift floor
17	Rad#17	626337	1116726	942	348	29.7	x	172	169.48	Rift margin
18	Rad#18	635647	1129549	879	560	28.4	x	280	145.68	Rift margin
19	Rad#19	628269	1142987	1096	480	27.45	x	240	221.45	Rift margin
20	Rad#20	648909	1153878	637	520	28.45	x	260	25.46	Rift floor
21	Rad#21	627918	1159147	969	480	27.6	x	240	178.45	Rift margin
22	Rad#22	599031	1105354	1300	340	29.6	10.0	170	135.46	Rift margin
23	Rad#23	603457	1109184	1260	470	31.2	x	240	158.42	Rift margin
24	Rad#24	606972	1116123	1116	270	29.7	x	130	138.47	Rift margin
25	Rad#25	606735	1142965	1438	400	20.6	8.31	200	276.33	Rift margin
26	Rad#26	603954	1162591	1422	470	29.8	x	230	174.86	Rift margin
27	Rad#27	601644	1175548	1406	840	23.5	x	170	288.46	Rift margin

Appendices 5: Areal rainfall determination using arithmetic method

	Location		Months												
exce	E	N	Jan	Fab	Mar	Apr	May	June	July	Aug	Sep	Oct	Nov	Dec	Sum
Artuma	610886	1170188	23.5	31.8	55.3	94.5	67.8	17.2	225.4	354.3	83.5	26.6	54.4	4.9	1039.2
Ashara	606603	1116983	8	24.8	63.5	70.2	36.9	14.2	18.1	98.9	37.2	2	17.8	3.8	395.4
Bati	610764	1237678	27.1	34.7	65.8	82.7	54.1	22.9	216.4	236.7	93.4	31.2	35.6	26.6	927.2
Bora	614071	1181290	8.8	95	52.7	70.7	43.1	17.4	235.8	433	47.3	24.1	4.7	10	1142.6
Boru Meda	566861	1240444	19	32	71.2	96.6	75	30.7	319.5	326.3	130	48.7	15.7	26.7	1191.4
Chefa Robit	588687	1198599	13.6	23.6	45.3	84.8	64.4	21.1	249.3	335.9	108.6	28.1	19.9	11.8	1006.4
Kombolcha	578284	1225144	20.8	27.1	60.9	100.6	58.2	29.8	278.8	272.4	106.3	40.3	17.9	15.4	1028.5
Dessie	569230	1228839	12.4	21.4	42.8	84.2	95.5	43.3	276.6	310.2	116.8	51.9	25.3	6.1	1086.5
Efeson	604654	1109811	35.4	37.8	87.8	92.7	62	20.8	206.1	368.3	115	32.5	25.9	20.9	1105.2
Gerba	601754	1234362	9.3	22.6	53.8	69.6	70.1	38.4	240.4	257.4	86.8	35.6	21.7	10.6	916.3
Gudoberet	574509	1083322	14.3	12.9	37.6	57.7	67.8	81.9	394.8	382.1	133	48.1	20.7	6	1256.9
Harbu	585906	1207412	17.3	26.5	80.6	115.3	36.8	31.2	251.7	276.6	112.4	18.9	15	31	1013.3
Karakore	602186	1152500	4.5	26.2	37.1	99.1	79.2	25.3	270.2	394.4	117	15.6	19	4	1091.6
Kutaber	558232	1246367	10.6	15.8	53	57.4	61.1	45.5	336	370.7	131.8	37.5	15	6.6	114
Majete	596235	1160285	34.5	37.1	72.3	115.7	70.9	32.2	282.3	318.4	123.4	53.2	33.4	22.3	1195.7
Mehal Meda	572199	1140064	15.4	23.6	54.2	54.8	35.5	48.1	288.4	269.1	66.1	16.1	6.5	4.6	882.4
Mezezo	580204	1098200	59.8	61.8	106.1	124	116.7	77.5	389.7	483.6	195.8	92	54.6	54.3	1815.9
Senbete	605750	1140378	35.2	33.2	61.5	77.9	36	17.5	227	269.4	96.5	36.7	24.3	17	932.2
Shewa Robit	597925	1106743	18.7	50.4	58.1	106.4	71	23.8	169.2	214.3	91.9	21.9	31.4	19.8	876.9
Tita	573179	1234191	15.5	31.7	71.8	93.9	87.5	41.7	288.8	326.1	100.2	45.2	24	8	1134.4
Werebabo	583992	1253017	14.7	18	62.2	110.2	92.6	43.3	302.6	312.5	110.7	51.4	26.8	18	1163

Adiytu	691791	1229854	9.6	7.4	32	39.2	19	4.7	71.5	101	27	4.1	5.1	3.6	324.2
Albuko	570763	1202764	16.5	49.3	59	113.1	115.3	60.7	376.2	452.5	153.3	57.3	46.7	25.1	1525.0
Ancharo	569085	1221374	25.4	31.7	91.6	122.6	71.4	28.5	295.6	354	135.7	44.1	19.2	23.6	1243.4
Argoba	597090	1056412	11.4	13.5	90.7	52.8	58.1	22.4	178.7	175.2	122.5	32.8	17.5	15	775.6
Chefa	588683	1198671	12.4	15.1	55.9	73.4	46.9	17.7	234.4	321.6	105.5	26.5	26.5	17.3	953.2
Deber Sina	582906	1088469	63.8	47.1	118.9	162.6	135.4	82.7	374.8	444.1	191.4	110.3	86.4	68.6	1886.1
Eliwuha	650877	1243771	3.6	28.7	10.4	22.2	31.5	3.2	53.7	100.1	15.6	53.4	14.4	0.3	283.7
Endeffo	692412	1163777	0.2	20.3	41.5	29.2	-	15.2	308.3	374.5	98	55.8	36.2	25.3	887.2
Furssi	613631	1158372	18.1	30.6	52.8	81.1	71.5	9.6	219.3	309.4	116.8	58.6	31.2	3.5	1002.5
Gewane	681590	1122837	14	28.3	59.8	50.4	34.3	9.5	112	129.8	36.9	24.7	15.9	10.9	526.5
Hadelela	620820	1128966	2.2	9.3	52.7	20.7	92.7	12	102.6	208.9	108.1	29.7	5.7	3.1	647.7
Jara	601688	1166659	21.6	33.9	69.6	138.5	92.3	51.9	190.1	296.1	156.2	94.2	42.3	31.2	1217.9
Kumame	606603	1116983	2.9	8.6	23.2	59.2	16.7	7.8	138.3	148.4	11.1	26.9	1.5	12.18	444.6
Mean monthly Rainfall			18.2	29.7	60.3	83.0	68.7	30.7	238.9	294.8	102.4	40.4	25.2	16.7	**1009.5**

Appendices 6: Areal rainfall determination using Thiessen Polygon method

S.No	Areal Rainfall determination using Thiessen Polygon Method				
	Station _Name	**Mean annual Rainfall(mm)**	**Area_SQKM**	**Wtd_ Area**	**Wtd_ Rainfall(mm)**
1	Abayater	820.8	2151	0.1124	92.290
2	Ankober	1629.1	59	0.0031	5.031
3	Artuma	690.9	218	0.0114	7.885
4	Ashara	395.4	355	0.0186	7.340
5	Bati	927.2	769	0.0402	37.292
6	Bora	1142.6	1836	0.0960	109.663
7	Boru Meda	1191.4	46	0.0024	2.842
8	Chefa Robit	1006.4	456	0.0238	23.980
9	Combolcha	1028.5	265	0.0138	14.224
10	Dessie	1086.5	34	0.0018	1.910
11	Efeson(Ataye)	1105.2	190	0.0099	10.963
12	Gerba	916.3	468	0.0245	22.422
13	Gudoberet	1256.9	36	0.0019	2.359
14	Harbu	1013.3	383	0.0200	20.287
15	Karakore	1091.6	214	0.0112	12.204
16	Kutaber	1141	9	0.0004	0.511
17	Majete	1195.7	326	0.0170	20.355
18	Mehal Meda	882.4	57	0.0030	2.647
19	Mezezo	1815.9	134	0.0070	12.753
20	Senbete	932.2	450	0.0235	21.933
21	Shewa Robit	876.9	461	0.0241	21.147
22	Tita	1134.4	101	0.0053	6.014
23	Werebabo School	1163	16	0.0008	0.987
24	Adiytu	324.2	1064	0.0556	18.031
25	Albuko	1525	290	0.0152	23.153

26	Ancharo	1243.4	64	0.0033	4.127
27	Argoba	790.6	527	0.0275	21.779
28	Chefa	953.2	213	0.0111	10.625
29	Deber Sina	1886.1	414	0.0217	40.862
30	Eliwuha	283.7	1152	0.0602	17.087
31	Endeffo	887.2	1858	0.0971	86.160
32	Furssi	1002.5	874	0.0457	45.805
33	Gewane	526.5	2206	0.1153	60.710
34	Hadelela	647.7	1144	0.0598	38.736
35	Jara	1217.9	290	0.0151	18.436
	Mean Monthly Rainfall(mm/year)	**1020.90**	**19132**	1.0000	**843**

Appendices 7: Areal rainfall Determination using Isohyetal method

Areal rainfall Determination Using Isohyetal Method					
OBJECTID *	**Isohyetal Range (mm)**	**Rainfall (mm)**	**Area_ SQKM**	**Wtd_ Area**	**Wtd_ Rainfall(mm)**
1	<400	300	174	0.0091	2.7284
2	500-300	400	553	0.0289	11.5618
3	600-400	500	921	0.0481	24.0696
4	700-500	600	2638	0.1379	82.7305
5	800-600	700	3493	0.1826	127.8016
6	900-700	800	3672	0.1919	153.5438
7	1000-800	900	2425	0.1268	114.0759
8	1100-900	1000	1794	0.0938	93.7696
9	1200-1000	1100	1356	0.0709	77.9636
10	1300-1100	1200	1043	0.0545	65.4192
11	1400-1200	1300	343	0.0179	23.3065
12	1500-1300	1400	284	0.0148	20.7819
13	1600-1400	1500	209	0.0109	16.3862
14	1700-1500	1600	94	0.0049	7.8612
15	1800-1600	1700	66	0.0034	5.8645
16	1900-1700	1800	62	0.0032	5.8332
17	200-1800	1900	5	0.0003	0.4966
Total			**19,132**	**1.0000**	**834.2**

Appendices 8: Max, Min and Mean Temperature of the study area

Months	**T_ Max(°c)**	**T_ Min(°c)**	**T_ Mean(°c)**
Jan	26.09	11.20	18.65
Feb	27.37	12.20	19.79
Mar	28.27	13.34	20.81
Apr	28.67	14.14	21.40
May	29.66	14.66	22.16
Jun	30.64	15.30	22.97
Jul	28.60	14.75	21.68

Aug	27.38	14.48	20.93
Sep	27.67	14.10	20.88
Oct	27.31	12.61	19.96
Nov	26.75	11.52	19.14
Dec	26.12	11.22	18.67
Mean	**27.88**	**13.29**	**20.59**

Appendices 9: Mean monthly sun shine hours (hrs/d).

Station Name	Location		Months												Mean Annual
	E	N	Jan	Feb	Mar	Apr	May	Jun	Jul	Aug	Sep	Oct	Nov	Dec	
Debre Berhan	556193	1068793	9.49	8.2	7.73	7.09	7.59	6.5	4.24	4.5	5.85	7.26	8.6	9.1	7.18
Gewane	681590	1122837	7.83	8.02	8.6	8.69	8.91	5.6	5.29	6.6	6.73	8.1	8.3	6.4	7.43
Majete	596235	1160285	7.3	7.15	8.34	7.96	8.46	6.9	5.79	6.2	7.6	8.59	8.7	8.4	7.62
Metehara	601180	979845	9.16	9.23	8.81	8.36	8.96	8.5	7.2	7.2	7.73	8.79	9.4	9.2	8.55
Shewa Robit	597925	1106743	8.39	8.39	7.68	7.07	7.59	6.1	4.8	4.4	5.97	8.01	8.4	6.6	6.95
Wereilu	547683	1169310	8.85	8.2	7.9	7.56	8.94	6.6	4.35	5.4	5.97	7.97	9.1	8.6	7.46
Kombolcha	578284	1225144	8.01	8.12	7.76	7.79	8.35	7.4	5.78	6.1	6.73	8.07	8.9	8.6	7.63
Eneware	517052	1094552	9.17	8.76	7.49	7.5	7.51	5.7	4.09	3.9	6.16	8.97	8.8	9.2	7.28
Mehal Meda	601180	979845	8.99	8.63	8.3	8.39	8.86	7.2	4.81	5.5	7.77	9.16	8.9	9.3	7.98
Shola Gebeya	568750	1100449	8.39	8.39	7.68	7.07	7.59	6.1	4.8	4.4	5.97	8.01	8.4	6.6	6.95
Wegel Tena	524025	1281058	9.44	9.26	8.45	8.19	8.36	6.8	4.1	5.5	7.55	9.26	9.3	9.7	7.98
Sirinka	566840	1298886	7.08	7.63	7.83	8.19	8.19	7.2	5.62	6.1	6.8	8.04	8	7.7	7.37
Bati	610764	1237678	7.13	6.82	7.28	7.89	8.78	7.76	6.22	6.96	6.58	7.89	8.79	7.80	7.49
Mean monthly			8.40	8.22	7.99	7.83	8.31	6.79	5.16	5.60	6.72	8.32	8.74	8.26	**7.53**

Appendices 10: Mean monthly and annual wind speed (m/s).

Station Name	Location		Months												**Mean Annual**
	X	Y	Jan	Feb	Mar	Apr	May	Jun	Jul	Aug	Sep	Oct	Nov	Dec	
Bati	40.01539	11.19639	0.82	0.91	0.96	0.96	0.95	1.15	1.26	1.08	0.76	0.66	0.74	0.79	0.92
Kombolcha	39.71763	11.0839	0.66	0.72	0.70	0.67	0.73	0.85	0.78	0.63	0.46	0.41	0.44	0.53	0.63
Debreberehan	39.51306	9.670278	2.36	2.57	2.60	2.27	2.31	2.09	1.49	1.37	1.52	1.62	1.94	2.22	2.03
Eneware	39.15639	9.903611	3.01	3.45	3.39	3.55	3.51	2.60	1.83	1.65	1.97	3.01	2.42	2.54	2.74
Majete	39.88028	10.49694	1.04	1.19	1.19	1.14	1.18	1.23	1.13	1.14	0.86	0.96	1.05	1.07	1.10
Mehal Meda	39.66025	10.3146	1.89	2.14	2.28	2.44	2.83	2.34	1.61	1.61	2.13	2.55	2.26	2.00	2.17
Shewa Robit	39.89436	10.0127	0.59	0.71	0.94	0.90	0.95	0.93	0.91	0.73	0.59	0.66	0.57	0.68	0.76
Metehara	39.921	8.865	1.69	1.84	1.74	1.59	1.56	2.11	2.22	1.83	1.45	1.40	1.48	1.55	1.71
Shola Gebeya	39.62806	9.956389	1.76	1.97	2.21	2.20	2.40	1.87	1.64	1.46	1.49	1.94	1.73	1.67	1.86
Sirinka	39.61428	11.751	1.33	1.42	1.38	1.26	1.30	1.50	1.31	1.15	0.99	0.92	1.08	1.37	1.25
Wegel Tena	39.22122	11.59034	1.38	1.54	1.62	1.59	1.70	1.66	1.47	1.32	1.25	1.40	1.36	1.39	1.48
Mean monthly wind speed			1.50	1.68	1.73	1.69	1.77	1.67	1.42	1.27	1.22	1.41	1.37	1.44	1.51

Appendices 11: Mean monthly and annual Relative Humidity (%)

Stations Name	Location		Months												Mean Annual
	X	Y	Jan	Feb	Mar	Apr	May	Jun	Jul	Aug	Sep	Oct	Nov	Dec	
Bati	40.015	11.2	72.97	69.72	67.2	64.83	56.51	49.08	61.33	69.51	66.92	62.18	61.96	66.66	64.07
Debre Berhan	39.513	9.67	61.08	59.14	61.89	64.19	57.22	59.96	79.37	81.55	73.59	63.38	61.36	60.21	65.25
Gewane	40.658	10.16	55.21	52.27	51.66	50.52	50.55	39.05	51.74	60.97	52.87	45.84	48.76	53.16	51.05
Majete	39.88	10.5	65.92	64.38	62.56	62.09	56.11	49.07	64.65	72.02	71.13	63.02	60.43	64	62.95
Metehara	39.921	8.865	55.91	55.29	53.49	54.48	51.63	47.92	59.02	63.02	58.51	52.43	52.55	53.38	54.80
Shewa Robit	39.894	10.01	49.6	58.4	51.35	54.15	58.1	47.44	61.8	71.07	73.3	57.27	59.85	56.6	58.24
Wereilu	39.437	10.58	59.05	58.92	60.68	61.57	58.2	58.4	78.19	82.35	74.89	62.41	60.07	57.19	64.33
Combolcha	39.718	11.08	62.98	60.44	59.24	59.79	51.33	43.14	59.45	65.97	64.61	59.81	58.37	60.58	58.81
Eneware	39.156	9.904	53.5	51.37	53.93	56.06	58.3	63.29	88.63	88.8	76.79	63.77	57.97	52.94	63.78
Mehal Meda	39.921	8.865	55.5	54.67	58.73	61.8	59.73	57.34	75.73	78.96	69.5	64.93	63.24	57	63.09
Shola Gebeya	39.628	9.956	66.23	64.83	63.49	72.45	71.6	69.31	81.84	84.52	78.32	68.93	69.81	70.41	71.81
Wegel Tena	39.221	11.59	55.21	54.51	58.67	60.98	57.97	55.66	80.08	84.51	73	67.18	61.94	55.87	63.80
			59.43	58.66	58.57	60.24	57.27	53.31	70.15	75.27	69.45	60.93	59.69	59.00	741.98

Appendices 12: Published papers

Journal of Hydrology: Regional Studies 56 (2024) 102037

Contents lists available at ScienceDirect

Journal of Hydrology: Regional Studies

journal homepage: www.elsevier.com/locate/ejrh

Evaluation of the source and mechanisms of groundwater recharge for the southern sections of the western Afar rift margin and associated rift floor

Dereje Gidafie [a,*], Dessie Nedaw [a], Tilahun Azagegn [a], Bekele Abebe [a], Alper Baba [b]

[a] School of Earth Sciences, Addis Ababa University, Addis Ababa, Ethiopia
[b] Department of International Water Resources, Izmir Institute of Technology, Izmir, Turkey

ARTICLE INFO

Keywords:
Groundwater recharge
Hydrochemical
Isotopes
Transverse structures

ABSTRACT

Study area: Southern Sections of Western Afar rift margin and associated rift floor.
Study focus: The purpose of this study is to identify the source and mechanisms of groundwater recharge based on geological, hydrochemical, and environmental isotope studies.
New hydrogeological insights: The investigation illustrate that the columnar jointed basalt was extended from the plateau to the rift margin. In addition, transverse structures trending NW-SE and NE-SW connect the plateau to the rift margin and the marginal grabens to the rift floor. The hydrochemical interpretations with EC and TDS shows that the groundwater from the plateau has evolved from Ca-dominated and slightly mineralized to Na-dominated and highly mineralized to the rift floor. Isotopically, the deep groundwater systems are depleted in the entire physiography in contrast to the shallow groundwater systems. Radon measurements are higher at the outlets of the marginal grabens and between the rift margin and the rift floor, suggesting groundwater feeds the river. A comprehensive analysis of the aforementioned results suggests that the deep circulating groundwater is recharged in the plateau and escarpment and chemically altered with increasing depth and along its preferential flow path into the rift floor. Therefore, the plateau area is the main source of recharge for the western Afar rift margin and associated rift floor, due to the presence of preferential pathways, mainly the columnar jointed basalts and cross-structures.

Groundwater for Sustainable Development 26 (2024) 101310

Contents lists available at ScienceDirect

Groundwater for Sustainable Development

journal homepage: www.elsevier.com/locate/gsd

Research paper

Integrated remote sensing and geographic information system overlay analysis for groundwater potential evaluation using AHP and fuzzy AHP: Southern sections of the western Afar rift margin and associated rift floor

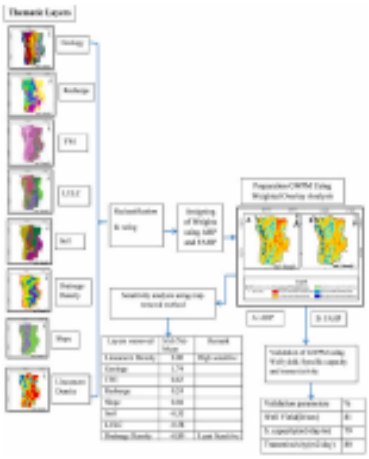
Dereje Gidafie *, Dessie Nedaw, Tilahun Azagegn

Schools of Earth Sciences, Addis Ababa University, Addis Ababa, Ethiopia

HIGHLIGHTS

- GWPM is delineated using integrated RS, GIS, and FAHP techniques.
- Lineament density, Geology, TWI, and Recharge are the dominant factors for the occurrence of groundwater.
- Very low (1.16%), Low (47.48%), Moderate (43.29%), High (7.54%), and Very High (0.535%) GWP zones are delineated.
- The GWPZ map was validated using Discharge, Transmissivity, and Specific capacity
- The map can be used as a rapid reference for groundwater development and future planning.

GRAPHICAL ABSTRACT



ARTICLE INFO

Keywords:
Groundwater potential zones
Overlay analysis
RS and GIS
Thematic layers
FAHP

ABSTRACT

A persistent drought commonly affects the southern sections of the western Afar rift margin and the associated rift floor, leaving the populace concerned about their access to food. A comprehensive assessment and usage of the local groundwater resource is therefore essential to overcoming the ongoing drought and meeting the area's increasing demand for sustainable water. With the aid of RS, GIS, AHP, and Fuzzy AHP methods, this study aims to assess the area's groundwater potential. Lineament density, Geology,Topographic Wetness Index (TWI), Recharge, Slope, Land Use and Land Cover, Soil, and Drainage Density were created using GIS and RS techniques and are the thematic layers taken into consideration for this purpose. The weight of these themes for their relative significance to groundwater occurrence was determined using AHP and Fuzzy AHP (FAHP). Lineament density is the primary factor influencing the presence of groundwater, followed by geology, TWI, and recharge. The Very low (221.48 km^2), Low (9084.46 km^2), Moderate (8281.96 km^2), High (1441.65 km^2), and Very High (102.45 km^2) groundwater potential zones (GWPZs) were delineated using the GIS-overlay analysis technique. The validation of the groundwater potential zone map was completed using the well discharge, transmissivity,

Environmental Earth Sciences (2025) 84:32
https://doi.org/10.1007/s12665-024-11999-z

ORIGINAL ARTICLE

Estimating groundwater recharge through multiple methods: southern sections of the western Afar rift margin and associated rift floor

Dereje Gidafie[1] · Dessie Nedaw[1] · Tilahun Azagegn[1] · Bekele Abebe[1] · Alper Baba[2]

Received: 29 July 2024 / Accepted: 23 November 2024
© The Author(s), under exclusive licence to Springer-Verlag GmbH Germany, part of Springer Nature 2024

Abstract

This study quantifies groundwater recharge in the southern sections of the western Afar Rift margin and associated rift floor by employing multiple methods, including Water balance, Chloride Mass Balance, WetSpass modeling, and Base-flow separation controlled by radon measurement. The mean annual groundwater recharge rates obtained from the first two methods are 114.39 mm/year, and 92.37 mm/year respectively. The spatially distributed recharge determined from the WetSpass model shows the rift margin has higher values than the rift floor, and results in a mean recharge of 100.88 mm/year. The baseflow separation method calculates 136.7 mm/year and 17.86 mm/year at the outlets of the marginal grabens and inside the rift floor respectively. The higher value suggests additional groundwater flows from the adjacent plateau to the rift margin, driven by the extended columnar basalt and transverse structures. In contrast, the presence of highly faulted Dalha basalt along the Arcuate Accommodation Zones (AAZ) promotes groundwater seepage, leading to lower values in the rift floor. However, from the previous hydrochemical and isotope analysis, groundwater flows from the rift margin to the rift floor, due to the presence of transverse structures create preferential pathways that connect these areas. Hence, the rift floor can have moderate recharge. Therefore, the WetSpass model and Base-flow separation methods, supported by other techniques, provide reliable results in tectonically active areas like the Afar Triangle and arid to semi-arid regions. Last but not least, the study underscores the importance of using multiple techniques for accurate assessments of recharge rates and mechanisms in similar areas.

Keywords Recharge estimation · Water balance · Chloride mass balance · WetSpass · Baseflow separation · Fractured media · Afar triple junction